Universidade de São Paulo
Instituto de Física

Nova Física com Mediadores Leves

Ana Luisa Foguel da Silva

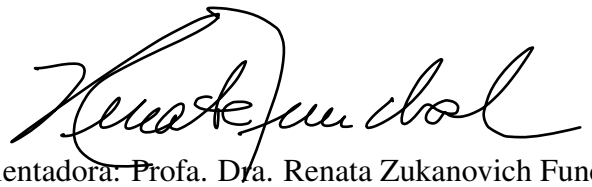

Orientadora: Profa. Dra. Renata Zukanovich Funchal.

Dissertação de mestrado apresentada ao Instituto de Física como requisito parcial para a obtenção do título de Mestre em Ciências.

Banca Examinadora:

Profa. Dra. Renata Zukanovich Funchal (IF/USP)
Prof. Dr. Leandro Salazar de Paula (IF/UFRJ)
Prof. Dr. André Paniago Lessa (UFABC)

São Paulo
2022

FICHA CATALOGRÁFICA
Preparada pelo Serviço de Biblioteca e Informação
do Instituto de Física da Universidade de São Paulo

Silva, Ana Luisa Foguel da

Nova física com mediadores leves / New physics with light mediators. São Paulo, 2022.

Dissertação (Mestrado) – Universidade de São Paulo. Instituto de Física. Depto. de Física Matemática.

Orientador(a): Profa. Dra. Renata Zukanovich Funchal

Área de Concentração: Física de Partículas e Campos

Unitermos: 1. Teoria Quântica de Campo; 2. Física Teórica; 3. Teoria de Campos.

USP/IF/SBI-023/2022

University of São Paulo
Physics Institute

New Physics with Light Mediators

Ana Luisa Foguel da Silva

Supervisor: Prof. Dr. Renata Zukanovich Funchal.

Dissertation submitted to the Physics Institute of the University of São Paulo in partial fulfillment of the requirements for the degree of Master of Science.

Examining Committee:

Prof. Dr. Renata Zukanovich Funchal (IF/USP)
Prof. Dr. Leandro Salazar de Paula (IF/UFRJ)
Prof. Dr. André Paniago Lessa (UFABC)

São Paulo
2022

Acknowledgments - Agradecimentos

Quando em 2020 decidi deixar minha cidade natal para trás para aumentar meus horizontes científicos vindo cursar o Mestrado em São Paulo eu já sabia que o caminho que iria trilhar seria difícil. Entretanto, eu mal poderia imaginar que essa dificuldade seria ainda maior devido ao início de uma pandemia global que nos afetou e afeta até os dias atuais. Em um primeiro momento, a ideia de realizar um Mestrado de forma remota me assustou e me remeteu a uma jornada solitária de isolamento espacial e social.

Hoje, quando olho para trás, penso que, apesar das dificuldades, a minha jornada não foi de forma nenhuma solitária. Ao longo desses dois anos, mesmo que de forma remota, pude conhecer pessoas maravilhosas que marcaram minha história e por quem sempre serei grata.

Gostaria de primeiro agradecer a minha orientadora Renata Funchal. Quando ainda em 2019 conversamos sobre a possível orientação, nenhuma de nós imaginaria o contexto em que tal supervisão se daria. Mesmo apesar de tudo, sei que em nenhum momento ela deixou de acreditar em mim e no nosso trabalho. Obrigada professora, por todas as nossas discussões sobre física, que sempre me motivaram, por todos os ensinamento e, principalmente, por ser uma inspiração para mim. Agradeço também à Fundação de Amparo à Pesquisa do Estado de São Paulo (FAPESP) (processo nº 2020/00174-2) pelo auxílio financeiro durante estes dois anos de Mestrado e também ao apoio do CNPq (Conselho Nacional de Desenvolvimento Científico e Tecnológico - Brasil).

Quero agradecer também aos meus dois principais colaboradores, e amigos, Peter Reimitz e Gabriel Massoni. Ao Peter, queria agradecer não somente por todo conhecimento que aprendi com ele, mas também pelas conversas e debates que tanto acrescentaram. Durante a pandemia, trabalhar em nosso projeto foi um dos fatores que me encorajou a seguir em frente. Aproveito para agradecer também toda a ajuda que ele me deu no processo de revisão desta dissertação. Ao Gabriel, queria primeiro agradecer em específico por ter me procurado para começarmos um projeto juntos. Aquele foi o início de tanta coisa, não apenas no quesito científico, mas também da formação de uma grande amizade. Obrigada pela paciência de me explicar com clareza e didática todas minhas dúvidas. Foi uma honra trabalhar com estes dois colaboradores e espero que muitos e muitos trabalhos ainda venham pela frente.

Dedico agora algumas palavras a dois ex-orientadores meus do Rio e atuais colaboradores também. Sei que só cheguei até aqui devido ao esforço, tempo e dedicação que vocês destinaram a mim. Carla, você foi minha primeira orientadora e meu primeiro contato com a ciência. Eu só

tinha 15 anos naquela época, mas você acreditou no meu potencial, segurou na minha mão e me ajudou a desbravar os caminhos da física. Eduardo, desde que iniciamos nossa pesquisa juntos, não teve um segundo se quer em que eu não me encantei com a física. Com paciência, você me ensinou tanto sobre a física e a vida, e nossa conexão foi tanta que até hoje trabalhamos juntos. Obrigada, de verdade, por todos esses anos.

Também não poderia deixar de dedicar algumas palavras aos meus irmãos Juliana, Vitor e Estevão e aos meus cunhados Celso, Luara e Daiana. Em especial, algumas palavras para minha irmã, que ao longo dos anos se mostrou não só apenas irmã mas também uma grande amiga e companheira. Obrigada por ter sido uma pessoa tão especial na minha vida. Também gostaria de agradecer à minha avó Rosita, que sempre foi uma inspiração para mim.

Quero agora agradecer a uma pessoa muito especial na minha vida. Esta pessoa foi uma das primeiras amizades que fiz durante a pandemia, e tal amizade cresceu tanto, que hoje sou muito feliz em tê-la também como um companheiro. Gustavo, que sorte foi te conhecer, obrigada por ter compartilhado comigo tantos momentos felizes, mas também por ter estado presente nos momentos de desespero, sempre me apoiando.

Agradeço agora a todos as outras amizades que fiz nesses dois anos aqui no Instituto. Matheus, Pedro, Fernanda, Monalisa, Gustavo, Luighi, Antonio, William, Ian, Caue, Pamela, Juliana, tantos nomes, cada um deles com uma participação especial na minha vida. Obrigada pelas conversas, risadas e discussões físicas também. Em especial, queria agradecer ao Mathues, meu companheiro de sala e de escrita de tese, que também se mostrou um grande amigo nesse período. Também quero mencionar duas grandes amizades de longa data que estiveram presentes durante toda minha trajetória acadêmica. Mirlene e Heitor, obrigada por serem pessoas tão maravilhosas e por me apoiarem durantes os altos e baixos desta trajetória.

Por fim, quero concluir dedicando este trabalho ao meus pais Débora Foguel e Jerson Lima da Silva. Palavras nunca serão suficientes para demonstrar toda a gratidão que tenho por vocês. Cientistas brilhantes e pessoas maravilhosas, tudo que conquistei e que sou devo ao empenho, carinho, dedicação e amor que vocês destinaram a mim.

Abstract

Among the possible beyond the Standard Model (SM) extensions, the addition of a new abelian $U(1)$ gauge group is one of the most minimal and simple models that one can think of. In the secluded scenario, the dark vector boson associated with the extra symmetry interacts with the SM sector via a kinetic mixing term with the hypercharge gauge boson, whereas for the generic case we can also afford direct couplings to the SM fermions. In this dissertation we focus on two different studies concerning the $U(1)$ gauge extension. In the first one, following the vector meson dominance approach, we computed, for the first time, vector boson decays into almost arbitrary hadronic final states. The effects of our hadronic improvements lead to substantial modifications on the dark boson decay widths, branching ratios and even on the experimental bounds for some cases. We provide the results of our hadronic implementation in the publicly available python package DELIVER. In the second part of this dissertation, we consider an ultraviolet completion to the $U(1)$ extension where a new scalar singlet that mixes with the SM-like Higgs boson and generates the dark boson mass is added. We study the electroweak precision test constraints of such a model as well as the phenomenological implications of two different kind of searches. In the first one, we simulate the $h \to Z_\gamma Z_\gamma \to 4\mu$ decay signal in order to obtain the ATLAS and CMS bounds on the model parameter space. In the second, we constrain the scalar mixing angle by considering the branching ratio of the invisible kaon decay $K_L^0 \to \pi^0 + \text{inv}$ as limited by the KOTO experiment.

Keywords: Beyond Standard Model physics, Dark Photon, Light Vector Mediators, Dark Higgs, Hidden Abelian Higgs Model.

Resumo

Dentre as possíveis extensões além do Modelo Padrão, a adição de um novo grupo de gauge abeliano $U(1)$ é um dos modelos mais mínimos e simples que se poderia imaginar. No cenário dito oculto, o bóson vetorial escuro associado à simetria extra interage com o setor do MP através de um termo de mistura cinética com o bóson medidor da hipercarga, enquanto que para o caso genérico também podemos permitir acoplamentos diretos com os férmions do MP. Nesta dissertação, iremos focar em dois estudos diferentes relacionados a esta extensão $U(1)$. No primeiro, seguindo a abordagem do modelo VMD (*vector meson dominance*), nós calculamos, pela primeira vez, os decaimentos de bósons vetoriais em estados finais hadrônicos praticamente arbitrários. Os efeitos das melhorias no cálculo hadrônico resultam em modificações substanciais nas larguras de decaimento e nas razões de ramificação do bóson escuro, até mesmo podendo afetar os limites experimentais em certos casos. Os resultados de nossa implementação hadrônica podem ser encontrados no pacote em python DELIVER que foi disponibilizado publicamente. Na segunda parte desta dissertação, nós consideramos uma realização ultravioleta para a extensão $U(1)$ em que um novo singleto escalar que se mistura com o bóson de Higgs do MP e gera a massa do bóson escuro é adicionado. Nós estudamos as restrições dos testes de precisão eletrofracos em tal modelo, bem como as implicações fenomenológicas de dois tipos diferentes de buscas experimentais. Na primeira, nós simulamos o sinal do decaimento $h \to Z_\gamma Z_\gamma \to 4\mu$ para obter os limites dos experimentos ATLAS e CMS no espaço de parâmetros do modelo. Na segunda, restringimos o ângulo de mistura escalar através da razão de ramificação do decaimento invisível do kaon $K_L^0 \to \pi^0 + \mathrm{inv}$, conforme limitado pelo experimento KOTO.

Palavras Chave: Física Além do Modelo Padrão, Fótons Escuros, Mediadores Vetoriais Leves, Higgs Escuro, modelo HAHM.

List of Figures

List of Tables

Contents

Introduction

"Nothing in life is to be feared, it is only to be understood. Now is the time to understand more, so that we may fear less."

(Marie Curie)

Up to this date, the Standard Model (SM) of particle physics can be regarded as the most successful description of the fundamental structure of matter. Almost all SM experimental predictions have been confirmed over the past few decades, with incredible good precision [2]. For instance, the SM predicted the existence of the W and Z bosons, as well as the gluon and top quark, even before the observation of such particles. Recently, the CERN Large Hadron Collider (LHC) confirmed the experimental discovery of the Higgs boson particle, which was arguably the final missing piece of the SM particle content [60, 61].

However, although the great triumph of the SM, nowadays we know that it is still an incomplete theory. The reason for that is due to the increasing number of open questions that continue to arise and cannot be explained within the SM framework. Just for illustration, we can cite, for example, the Hierarchy Problem, the failure to explain neutrino masses and the absence of Dark Matter (DM) candidates. The first issue is related to the huge unnatural discrepancy of 10^{16} orders of magnitude between the characteristic scales of the weak force and gravity [62]. The second concerns the fact that in the SM the neutrinos are massless particles, in contradiction to neutrino oscillation observations [63, 64].

Finally, maybe the major SM open problem is related to the existence of DM. This existence was confirmed by several astrophysical and cosmological observations [65–68], increasing the urge to include a consistent DM theory in the SM framework. Within the SM particle content, the only available candidates for DM would be the neutrinos, but such an option has already been disfavored by all kinds of experimental and observational data [69]. Hence, we rely on the addition of extra Beyond the Standard Model (BSM) particles and interactions in order to explain the DM existence.

All the above mentioned unanswered questions endorse the need of studying new SM extensions as well as searching for experimental BSM signals. In particular, one of the most

simple extensions that we can include in the SM is the addition of an extra $U(1)_Q$ abelian gauge symmetry, where Q is the charge of the symmetry group. In such a model we have a new dark vector boson that kinetically mixes with the hypercharge gauge boson. An important motivation for this kind of theory is that the kinetic mixing (KM) portal is one of the three possible renormalizable portals that one can build in the SM Lagrangian, the others being the Higgs and the neutrino portal. In the secluded $U(1)_Q$ scenario, the coupling between the SM particles and the new dark boson, which we name *dark photon* (DP), can only proceed via the KM portal, while for the generic $U(1)_Q$ case, the dark boson can also enjoy direct couplings to the SM fermionic currents.

The $U(1)_Q$ model can also be embedded into an ultraviolet (UV) completion framework to dynamically explain the origin of the dark boson mass. In the most economical scenario we add a new singlet scalar s that mixes with the SM-like Higgs boson via the quartic term in the scalar potential. After the new scalar acquires a vacuum expectation value (VEV), the *dark photon* mass is generated via the spontaneous symmetry breaking (SSB) of the new abelian group. Note that the scalar mixing term corresponds to the above mentioned renormalizable Higgs portal, which is another feature that makes this minimal UV complete $U(1)_Q$ model so interesting. Let us remark that this model is known in the literature as the Hidden Abelian Higgs Model (HAHM).

In this dissertation, we focused on the study of $U(1)_Q$ extensions with light dark bosons in the MeV-to-GeV mass range. The motivation for this light energy regime is due to the fact that, with the rise of new technologies and several experimental upgrades, many detectors have now the ability and are focused on the search of very low-energy BSM signals. Our study was divided into two distinct parts. In the first part, our goal was to describe the hadronic decays of baryophilic $U(1)_Q$ vector mediators. Since in the generic case the coupling of the dark boson with the SM fermions is not proportional to the electromagnetic (EM) charge, the computation of such hadronic decays can be very challenging. In order to perform this calculation we then stick to the vector meson dominance method. With this method we can compute a specific hadronic channel decay width by dividing the hadronic mode into ρ, ω and ϕ vector meson contributions, which couple with the dark vector bosons. We then improved the previous VMD-based hadronic calculation [1] by including several new hadronic modes, employing recent cross-section experimental data and also performing the correct vector meson division. These improvements lead to effects on the dark boson width and branching ratio computation, which in turn affect the present and future experimental bounds. It is worth mentioning that the hadronic implementation described here was made publicly available in the python package DELIVER [70].

We structured the first part of this dissertation in the following way. In chapter 1 we outline the theoretical background behind the abelian $U(1)_Q$ extension and elaborate on the dark boson production as well as on its decays. In chapter 2 we detail the method we follow in order to describe the dark boson hadronic decays and comment on the improvements of our approach. Finally, in chapter 3 we analyze the effects that our better assessment of the hadronic widths provides on the computation of the dark boson widths, branching ratios, current bounds and future sensitivities.

In the second part of the study, we considered the minimal UV complete $U(1)_Q$ scenario. In chapter 4 we describe the theoretical framework of such a model, including the theory behind the scalar mixing and the interactions and decay widths of the new HAHM particles. The inclusion of the KM and Higgs portal lead to the modification of extremely well-measured EW observables, such as the Z boson and Higgs mass and couplings. Hence, in chapter 5 we investigate the EW precision tests constraints on the HAHM parameters.

Finally, in the last chapter, we consider the phenomenological implications of two different HAHM searches. The first one is related to the $h \to Z_\gamma Z_\gamma \to 4\mu$ decay signal. We explain how we simulate the signal using Monte-Carlo event generator tools and show the obtained ATLAS and CMS experimental sensitivities to probe the HAHM parameter space. The other search we consider in this chapter concerns the upper limit recently set by the KOTO collaboration on the branching ratio of the invisible kaon decay $K_L^0 \to \pi^0 + \text{inv}$. Since this decay can be mimicked by the HAHM decay $K_L^0 \to \pi^0 s$, we can use the KOTO limit to constrain the scalar mixing parameter. We then conclude this last chapter by showing this Higgs portal bound.

Part I

Light Vector Mediators

Chapter 1

General Theoretical Framework

One of the most simple extensions of the Standard Model (SM) is the addition of a new $U(1)_Q$ gauge group, where Q is the symmetry generator or charge of the group. Although this idea was first proposed in the context of supersymmetric theories [71, 72], it was also explored by several authors in different beyond standard model (BSM) frameworks [73–75]. In the minimal model, the new gauge boson associated with the extra $U(1)_Q$ enters in the SM Lagrangian together with the hypercharge gauge boson in a kinetic term that mixes the two fields. This kinetic mixing (KM) always appears as a consequence of adding an extra gauged $U(1)_Q$ group [76], and it is parametrized by a coupling ϵ that needs to be small in order to fulfill several experimental constraints. In this secluded scenario, the only portal with the SM particle content would be due to the mixing with the hypercharge gauge boson, and for this reason the new vector particle is sometimes called *dark photon* (DP) [1], but other common names are also used in the literature, such as dark Z boson, paraphoton and hidden boson [73, 81].

Another interesting feature of this type of model is that the new gauge boson can provide a vector portal to an unexplored hidden sector, and therefore, to new physics. In this scenario, even though the SM fermions do not carry any charge Q, the model can include dark sector particles charged under $U(1)_Q$, implying that the *dark photon* would work as a mediator or a portal to this hidden sector. The new dark particles could also be or constitute a fraction of the dark matter [19, 82–88].

Beyond the minimal *dark photon* model, there are other extensions where some of the SM particles are charged under $U(1)_Q$. In this case, one must be concerned with the correct anomaly-cancellation, which can occasionally result in the need for new particles for a consistent ultraviolet (UV) completion. Some common anomaly-free choices of charges are the dif-

[1] For recent *dark photon* reviews, we refer the reader to [77–80].

ference between the baryonic and leptonic number $U(1)_{B-L}$, the leptonic number differences $U(1)_{L_i-L_j}$ $(i,j = e,\mu,\tau)$ or other combinations, such as $U(1)_{B-3L_i}$ and $U(1)_{B-2L_i-L_j}$.

Another popular model in the literature is the $U(1)_B$ model, where the new gauge boson couple only to the baryon number B. Even though this model is anomalous, and hence requires the introduction of heavier degrees of freedom to cancel the anomalies, it has still plenty of available parameter space, even with the strong constraints due to the non-conserved currents.

A mutual property of these $U(1)_Q$ models is that they can be described very simply. Once we fixed the charge Q of the group, and hence, the fermion couplings, and, also, if we do not add any other dark particles, we can parametrize these models by adding only two parameters to the theory: the dark boson mass m_{Z_Q} and the kinetic mixing ϵ (gauge coupling g_Q) for the case of the *dark photon* (generic vector boson Z_Q). Note that if we want to describe the generic $U(1)_Q$ extensions with only these two parameters (m_{Z_Q} and g_Q) we also need to assume an hierarchy where the KM is very suppressed in comparison with g_Q. Another strong motivation for this type of model is the fact that the vector portal is one of the three renormalizable terms that are allowed in the SM, the others being the Higgs and the neutrino portal.

In this chapter, we will overview the theoretical background of $U(1)_Q$-gauge extensions of the SM. The first section will introduce the concept of kinetic mixing, together with the correct Lagrangian diagonalization to obtain the physical degrees of freedom. After that, we will discuss the anomaly-free gauge extensions and the class of baryophilic models that were considered in the study. In the second and third sections, we will develop the theory behind the production and decays of the new gauge boson.

1.1 Kinetic Mixing and the Dark Portal

We will consider an extension of the SM by a new $U(1)_Q$ gauge group. The dark vector boson Z_Q associated with it will acquire a mass m_{Z_Q} after the SSB of the $U(1)_Q$ symmetry [2]. The abelian gauge boson $\hat{Z}_Q^\mu$ will kinetically mix with the hypercharge boson $\hat{B}^\mu$ through the following Lagrangian [3]

$$\mathcal{L}^0_{\text{gauge}} = -\frac{1}{4}\hat{B}_{\mu\nu}\hat{B}^{\mu\nu} - \frac{1}{4}\hat{Z}_{Q\mu\nu}\hat{Z}_Q^{\mu\nu} - \frac{\epsilon}{2c_W}\hat{Z}_{Q\mu\nu}\hat{B}^{\mu\nu}, \tag{1.1}$$

[2] We will not specify the scalar sector and the mechanism behind this SSB. See chapter 4 for a possible UV completion scenario.

[3] Throughout this dissertation we will always use natural units, *i.e.* $\hbar = c = 1$, the modulus of the electric charge $e > 0$ and the fine-structure constant $\alpha_{\text{em}} = \frac{e^2}{4\pi}$.

where $\hat{Z}_Q^{\mu\nu}$ and $\hat{B}^{\mu\nu}$ are the dark boson and hypercharge boson[4] field strength tensor, respectively, ϵ parametrizes the kinetic mixing and $c_W \equiv \cos\theta_W$ is the cosine of the weak mixing angle. The hatted fields indicate states with non-canonical kinetic terms. In order to recover the physical states we need to perform the proper kinetic and mass diagonalizations. This can be achieved by performing the $GL(2,R)$ rotation

$$\begin{pmatrix} \hat{Z}_Q^\mu \\ \hat{B}^\mu \end{pmatrix} = \begin{pmatrix} \frac{1}{\sqrt{1-(\epsilon/c_W)^2}} & 0 \\ -\frac{\epsilon/c_W}{\sqrt{1-(\epsilon/c_W)^2}} & 1 \end{pmatrix} \begin{pmatrix} \tilde{Z}_Q^\mu \\ B^\mu \end{pmatrix} , \tag{1.2}$$

implying the field redefinitions

$$\hat{Z}_Q^\mu = \eta\ \tilde{Z}_Q^\mu, \tag{1.3}$$

$$\hat{B}^\mu = B^\mu - \frac{\epsilon}{c_W}\eta\ \tilde{Z}_Q^\mu, \tag{1.4}$$

where we defined

$$\eta \equiv \frac{1}{\sqrt{1-\frac{\epsilon^2}{c_W^2}}} . \tag{1.5}$$

With these fields modifications, the gauge Lagrangian eq. (1.1) becomes

$$\mathcal{L}^0_{\text{gauge}} = -\frac{1}{4}B_{\mu\nu}B^{\mu\nu} - \frac{1}{4}\tilde{Z}_{Q\mu\nu}\tilde{Z}_Q^{\mu\nu} . \tag{1.6}$$

Note that in the limit where $\epsilon \ll 1$, which we will focus in this dissertation, we have that $\eta \sim 1$.

Now we need to understand what will happen to interactions after these field redefinitions. Before electroweak (EW) symmetry breaking, the non-diagonalized gauge interaction Lagrangian with the SM chiral fermions f was

$$\mathcal{L}_{\text{int}} = g' J_{B\mu}\hat{B}^\mu + g J_{3\mu}W^{3\mu} + g_Q J_{Q\mu}\hat{Z}_Q^\mu , \tag{1.7}$$

where g, g' and g_Q are the $SU(2)_L$, $U(1)_Y$ and $U(1)_Q$ gauge couplings, respectively, J_Q is an yet unspecified dark current, which will depend on the choice of the $U(1)_Q$ group, and J_B and J_3 are the usual SM currents,

$$\begin{aligned} J_3^\mu &= \bar{f}\gamma^\mu f T^3 , \\ J_B^\mu &= \bar{f}\gamma^\mu f Y , \end{aligned} \tag{1.8}$$

with T^3 the third $SU(2)_L$ generator and Y the $U(1)_Y$ hypercharge generator.

We will first perform the kinetic mixing shift of eq. (1.3) and (1.4) on the interaction La-

[4]Note that, before the electroweak SSB and the kinetic diagonalization, the fields $\hat{Z}_Q$ and $\hat{B}$ cannot yet be defined as the physical dark boson and hypercharge fields.

grangian in eq. (1.7), resulting in

$$\mathcal{L}_{\text{int}} = g' J_{B\mu} B^{\mu} + g J_{3\mu} W^{3\mu} + \left(g_Q J_{Q\mu} - g' J_{B\mu} \frac{\epsilon}{c_W} \right) \eta \tilde{Z}_Q^{\mu} \,. \tag{1.9}$$

After that, we can proceed with the EW symmetry breaking by shifting the B^{μ} and $W^{3\mu}$ fields according to

$$B^{\mu} = A^{\mu} c_W - Z_0^{\mu} s_W \,, \tag{1.10}$$

$$W_3^{\mu} = A^{\mu} s_W + Z_0^{\mu} c_W \,, \tag{1.11}$$

where A^{μ} is the physical photon field, Z_0^{μ} is the SM Z-boson field and $s_W \equiv \sin\theta_W$ is the sine of the weak mixing angle. We then obtain

$$\begin{aligned} \mathcal{L}_{\text{int}} &= g' J_B (A c_W - Z_0 s_W) + g J_3 (A s_W + Z_0 c_W) + \left(g_Q J_Q - g' J_B \frac{\epsilon}{c_W} \right) \eta \tilde{Z}_Q \\ &= (J_B + J_3) g s_W A + g \left(J_3 c_W - \frac{s_W^2}{c_W} J_B \right) Z_0 - g' \eta J_B \frac{\epsilon}{c_W} \tilde{Z}_Q + g_Q J_Q \eta \tilde{Z}_Q \,, \end{aligned} \tag{1.12}$$

where we dropped the μ indexes for simplification. Now we make the usual SM definitions for the electromagnetic current J_{EM} and the neutral current J_Z

$$J_{\text{EM}} = J_B + J_3 \,, \tag{1.13}$$

$$J_Z = J_3 c_W - \frac{s_W^2}{c_W} J_B \,. \tag{1.14}$$

Using these two equations we can also express the hypercharge current as

$$J_B = (J_{\text{EM}} c_W - J_Z) c_W \,. \tag{1.15}$$

Now, if we remember the electric charge e definition in the SM

$$g' c_W = g s_W = e \,, \tag{1.16}$$

we can finally rewrite eq. (1.12) as

$$\mathcal{L}_{\text{int}} = e J_{\text{EM}} A + g J_Z Z_0 - e\epsilon J_{\text{EM}} \eta \tilde{Z}_Q + g' \epsilon J_Z \eta \tilde{Z}_Q + g_Q J_Q \eta \tilde{Z}_Q \,. \tag{1.17}$$

In this last equation we can see that, apart from the first two terms that represent the usual EM and neutral currents that couple fermions to the photon and Z boson, respectively, the KM shift

introduced a coupling of the new gauge boson Z_Q to the EM and the neutral Z currents. These new couplings are both suppressed by the kinetic mixing parameter ϵ. However, this is not the end of the story, there is also a source of mass mixing between Z_0 and $\tilde{Z}_Q$ which depends on the structure of the extended scalar sector.

To illustrate, let us consider that the scalar that breaks $U(1)_Q$ is a singlet (for more details we refer to chapter 4). In this case, from the Higgs doublet H kinetic term $|D_\mu H|^2$, where the covariant derivative $D_\mu H$ is given by

$$D_\mu H = \partial_\mu H - igW_{a\mu}\tau^a H - \frac{1}{2}ig'\hat{B}_\mu H\,, \tag{1.18}$$

we obtain

$$\begin{aligned}
|D_\mu H|^2 &\supset \frac{1}{2}|\partial_\mu h|^2 + \frac{1}{8}(v+h)^2(-gW_3^\mu + g'\hat{B}^\mu)^2 \\
&= \frac{1}{2}|\partial_\mu h|^2 + \frac{1}{8}(v+h)^2\left[-gW_3^\mu + g'\left(B^\mu - \frac{\epsilon}{c_W}\eta\,\tilde{Z}_Q^\mu\right)\right]^2 \\
&\supset \frac{1}{8}(v+h)^2\left[-g(A^\mu s_W + Z_0^\mu c_W) + g'\left(A^\mu c_W - Z_0^\mu s_W - \frac{\epsilon}{c_W}\eta\tilde{Z}_Q^\mu\right)\right]^2,
\end{aligned} \tag{1.19}$$

where v is the Higgs VEV and in the second and last lines we used the field redefinitions given by eq. (1.4) and (1.3) and the EW rotations, respectively. Finally, using the identity in eq. (1.16) we obtain

$$|D_\mu H|^2 \supset \frac{1}{8}(v+h)^2\left[\frac{g}{c_W}Z_0^\mu + g'\frac{\epsilon}{c_W}\eta\tilde{Z}_Q^\mu\right]^2, \tag{1.20}$$

from which we can collect the quadratic terms in v, that correspond to the mass terms

$$|D_\mu H|^2 \supset \frac{1}{2}m_{Z_0}^2 Z_0^2 + \frac{1}{2}\left(\frac{vg'\epsilon\eta}{2c_W}\right)^2\tilde{Z}_Q^2 + \frac{1}{4}\frac{v^2 g g'\epsilon\eta}{c_W^2}Z_0^\mu\tilde{Z}_{Q\mu}\,, \tag{1.21}$$

where m_{Z_0} is the SM Z-boson mass, defined as

$$m_{Z_0} = \left(\frac{vg}{2c_W}\right). \tag{1.22}$$

Similarly, from the spontaneous breaking of $U(1)_Q$ we obtain a mass term for the Z_Q boson. Without focusing on the specific mechanism that generates the SSB [5], we can explicitly add the

[5] For a possible UV completion scenario, see chapter 4.

mass term to the mass mixing Lagrangian

$$\begin{aligned}\mathcal{L}_{\text{mass}}^{Z_0-\tilde{Z}_Q} &= \frac{1}{2}m_{Z_0}^2 Z_0^2 + \frac{1}{2}\left[\left(\frac{vgs_W\epsilon\eta}{2c_W^2}\right)^2 + m_{\tilde{Z}_Q}^2\right]\tilde{Z}_Q^2 + \frac{1}{4}\frac{v^2g^2s_W\epsilon\eta}{c_W^3}Z_0^\mu\tilde{Z}_{Q\mu} \\ &= \frac{1}{2}m_{Z_0}^2 Z_0^2 + \frac{1}{2}m_{Z_0}^2\left[(t_W\epsilon\eta)^2+\delta^2\right]\tilde{Z}_Q^2 + m_{Z_0}^2 t_W\epsilon\eta Z_0^\mu\tilde{Z}_{Q\mu}\,,\end{aligned} \tag{1.23}$$

where $t_W \equiv \tan\theta_W = s_W/c_W$ and we defined

$$m_{\tilde{Z}_Q}^2 = m_{Z_0}^2\delta^2\,. \tag{1.24}$$

In the basis $\mathcal{Z} = (Z_0^\mu, \tilde{Z}_Q^\mu)$ we can write

$$\mathcal{L}_{\text{mass}}^{Z_0-\tilde{Z}_Q} = \frac{1}{2}\mathcal{Z}\mathcal{M}_{ZZ_Q}^2\mathcal{Z}^T\,, \tag{1.25}$$

where the squared mass matrix is given by

$$\mathcal{M}_{ZZ_Q}^2 = m_{Z_0}^2\begin{pmatrix} 1 & t_W\epsilon\eta \\ t_W\epsilon\eta & \delta^2 + t_W^2\epsilon^2\eta^2 \end{pmatrix}\,. \tag{1.26}$$

This is a symmetric matrix and thus can be diagonalized with an orthogonal transformation

$$\begin{pmatrix} Z \\ Z_Q \end{pmatrix} = \begin{pmatrix} \cos\alpha & \sin\alpha \\ -\sin\alpha & \cos\alpha \end{pmatrix}\begin{pmatrix} Z_0 \\ \tilde{Z}_Q \end{pmatrix}\,, \tag{1.27}$$

where

$$\tan 2\alpha = \frac{2t_W\epsilon\eta}{1-\delta^2-t_W^2\epsilon^2\eta^2}\,, \tag{1.28}$$

or, equivalently,

$$\tan\alpha = \frac{-1+\delta^2+t_W^2\epsilon^2\eta^2 \pm \sqrt{4t_W^2\epsilon^2\eta^2 + (1-\delta^2-t_W^2\epsilon^2\eta^2)^2}}{2t_W\epsilon\eta}\,. \tag{1.29}$$

Now, we can finally obtain the mass of the gauge bosons from the mass squared eigenvalues of the matrix $\mathcal{M}_{ZZ_Q}^2$

$$m_{Z,Z_Q}^2 = \frac{1}{2}m_{Z_0}^2\left(1+\delta^2+t_W^2\epsilon^2\eta^2 \pm \text{Sign}(1-\delta^2)\sqrt{(1+\delta^2+t_W^2\epsilon^2\eta^2)^2 - 4\delta^2}\right)\,. \tag{1.30}$$

We can thus consider the limit of suppressed kinetic mixing $\epsilon \ll 1$ ($\eta \sim 1$) and also of light Z_Q masses ($\delta \ll 1$), which is the energy scale we will focus here. The mass eigenvalues then become

$$m^2_{Z_Q} \simeq \delta^2 m^2_{Z_0}(1 - \epsilon^2 t^2_W)\,, \tag{1.31}$$

$$m^2_Z \simeq m^2_{Z_0}(1 + \epsilon^2 t^2_W)\,, \tag{1.32}$$

which means that we can safely approximate $m_{Z_Q} = m_{\tilde{Z}_Q} + \mathcal{O}(\epsilon^2)$ and $m_Z = m_{Z_0} + \mathcal{O}(\epsilon^2)$. Therefore, with this last diagonalization we are ready to write the full Lagrangian of the model. From the $Z - Z_Q$ mass diagonalization we have that

$$Z_0 = Z\cos\alpha - Z_Q \sin\alpha\,, \tag{1.33}$$

$$\tilde{Z}_Q = Z\sin\alpha + Z_Q\cos\alpha\,. \tag{1.34}$$

However, the limit where $\epsilon, \delta \ll 1$ implies that

$$\tan 2\alpha \simeq \frac{2\epsilon t_W}{1-\delta^2} + \mathcal{O}(\epsilon^3) \Rightarrow \tan 2\alpha \simeq 2\alpha \simeq 2\epsilon t_W(1+\delta^2)\,, \tag{1.35}$$

resulting in $\sin\alpha \simeq \alpha \simeq \epsilon t_W(1+\delta^2)$ and $\cos\alpha \simeq 1$. With these approximations it follows that

$$Z_0 = Z - \epsilon t_W Z_Q + \mathcal{O}(\epsilon^2, \delta^2, \epsilon\delta)\,, \tag{1.36}$$

$$\tilde{Z}_Q = Z_Q + \epsilon t_W Z + \mathcal{O}(\epsilon^2, \delta^2, \epsilon\delta)\,. \tag{1.37}$$

Applying these substitutions to the interaction Lagrangian given by eq. (1.17) we get the following terms

$$\begin{aligned}
\mathcal{L}_{\text{int}} &= eJ_{\text{EM}}A + gJ_Z(Z - \epsilon t_W Z_Q) - e\epsilon J_{\text{EM}}(Z_Q + \epsilon t_W Z) + g'\epsilon J_Z(Z_Q + \epsilon t_W Z) \\
&\quad + g_Q J_Q(Z_Q + \epsilon t_W Z) \\
&= eJ_{\text{EM}}A + gJ_Z Z + J_Z(-g\epsilon t_W + g'\epsilon)Z_Q - e\epsilon J_{\text{EM}}Z_Q + g_Q J_Q Z_Q + \mathcal{O}(\epsilon^2, \delta^2, \epsilon g_Q) \\
&= eJ_{\text{EM}}A + gJ_Z Z - e\epsilon J_{\text{EM}}Z_Q + g_Q J_Q Z_Q + \mathcal{O}(\epsilon^2, \delta^2, \epsilon g_Q)
\end{aligned} \tag{1.38}$$

where in the last line we used that $gt_W = g'$. Therefore, neglecting terms of order $\mathcal{O}(\epsilon^2, \epsilon\delta, \delta^2, \epsilon g_Q)$, we obtain the relevant terms involving the new physical Z_Q boson

$$\mathcal{L}_{Z_Q} = eJ_{\text{EM}}A + gJ_Z Z - e\epsilon J_{\text{EM}}Z_Q + g_Q J_Q Z_Q + \frac{1}{2}m^2_{Z_Q}Z^2_Q\,. \tag{1.39}$$

Finally, we can now analyze the new vector current J_Q, which we write as

$$J_Q^\mu = \sum_f \bar{f}\gamma^\mu \, q_Q^f \, f \, , \tag{1.40}$$

where q_Q^f is the Q-charge of fermion f. The secluded case, i.e. the *dark photon* Z_γ case, corresponds to $q_Q^f = 0$ for all fermions, which means that the new gauge boson will couple universally to all charged fermions and the only portal with SM matter will come from the KM portal. Appart from this scenario, the current will depend on the particular gauge group $U(1)_Q$ choice. We will always assume $e\epsilon \ll g_Q$, so when charges are present we will neglect the kinetic mixing contribution.

In the first part of this dissertation, we will focus on the hadronic modes for a light Z_Q with m_{Z_Q} in the MeV-to-GeV range. Hence, we will consider a class of anomaly-free baryophylic models where only three right-handed neutrinos were introduced to the particle content of the SM in order to guarantee the correct anomaly-cancellation. The symmetry generator for these models can be written as [89]

$$Q = B - x_e L_e - x_\mu L_\mu - (3 - x_e - x_\mu) L_\tau \, , \tag{1.41}$$

where B is the baryon number and L_e, L_μ and L_τ are lepton family number operators. To compare with previous works, we will also present our results for the anomalous B model. In table 1.1, we list the models we will use here.

In order to make correct predictions and constraints on the available parameter space of the *dark photon* and other vector mediator models it is important to understand the production mechanisms and the decay widths, along with the branching ratios, of such particles. In the next sections we will focus on the description of the production, decay and detection of the Z_Q gauge boson.

1.2 Z_Q Production

In the *dark photon* case, due to the coupling of Z_γ to the EM current, it can be produced in every process related to ordinary photons. Therefore, the following mechanism are primarily responsible for DP production:

1. **Bremsstrahlung process**, where either an electron or a proton scatters off the target nuclei (A), emitting a DP through the reaction $eA \to eAZ_\gamma$ or $pA \to pAZ_\gamma$, respectively.

x_e	x_μ	Q	q_Q^f			
			quarks	e/ν_e	μ/ν_μ	τ/ν_τ
1	1	$B-L$	$\frac{1}{3}$	-1	-1	-1
3	0	$B-3L_e$	$\frac{1}{3}$	-3	0	0
0	3	$B-3L_\mu$	$\frac{1}{3}$	0	-3	0
0	0	$B-3L_\tau$	$\frac{1}{3}$	0	0	-3
1	0	$B-L_e-2L_\tau$	$\frac{1}{3}$	-1	0	-2
0	1	$B-L_\mu-2L_\tau$	$\frac{1}{3}$	0	-1	-2
–	–	B	$\frac{1}{3}$	0	0	0

Table 1.1: Symmetry generators and fermion charges for the models considered in this dissertation.

2. **Annihilation**, where a DP is produced, together with a photon, via the annihilation of an electron-positron pair, $e^+e^- \to \gamma Z_\gamma$.

3. **Drell-Yan (DY) process**, characterized by the emission of a DP through the annihilation of a quark-antiquark pair, $q\bar{q} \to Z_\gamma$.

4. **Meson Decays**, where a meson M, that could be either π^0, η, K or D, decays into a photon and a DP, $M \to \gamma Z_\gamma$.

5. **Mixing with QCD vector mesons** V ($V - Z_\gamma$ mixing), described by the DP directly mixing with the light dominant mesons $V = \rho, \omega, \phi$.

In the case of production of generic gauge bosons Z_Q, the production mechanisms are the same as the DP, however re-scaled considering the coupling of the model with the SM particles included in the process. For example, if we consider the production by electron bremsstrahlung or e^+e^- annihilation, we have that the following ratio applies

$$\frac{\sigma(eA \to eAZ_Q)}{\sigma(eA \to eAZ_\gamma)} = \frac{\sigma(e^+e^- \to Z_Q\gamma)}{\sigma(e^+e^- \to Z_\gamma\gamma)} = \frac{(g_Q q_Q^e)^2}{(\epsilon e)^2}\,. \tag{1.42}$$

In a similar way, we can recast the production for the other mechanisms always considering the ratio of cross-sections. For more details, we refer to [1].

1.3 Z_Q Decays

After its production, the new gauge boson Z_Q will decay into SM particles proportionally to the KM parameter, in the *dark photon* case, or to the the $U(1)_Q$ gauge group coupling, in the generic case. In the low-energy mass range, which is the focus of this dissertation, the Z_Q can decay into charged or neutral leptons as well as into light hadrons, if kinematically allowed. In the following, we describe its partial decay widths into these channels.

1.3.1 Leptonic Decays

The Z_Q partial decay width into a pair of leptons is given by

$$\Gamma(Z_Q \to \ell\bar{\ell}) = \frac{C_\ell (g_Q q_Q^\ell)^2}{12\pi} m_{Z_Q} \left(1 + 2\,\frac{m_\ell^2}{m_{Z_Q}^2}\right) \sqrt{1 - 4\frac{m_\ell^2}{m_{Z_Q}^2}}\,, \tag{1.43}$$

where m_ℓ is the lepton mass, $C_\ell = 1\,(1/2)$ for $\ell = e, \mu$ (ν_e, ν_μ, ν_τ), g_Q is the $U(1)_Q$ gauge coupling and q_Q^ℓ the corresponding lepton charge of the model according to table 1.1. In the case of the *dark photon*, we need to replace g_Q with $e\epsilon$ and q_Q^ℓ with $q_{\rm em}^\ell = -1$ for all charged leptons and zero for neutrinos.

When the new boson mass is smaller than two times the electron mass, i.e. $m_{Z_Q} < 2\,m_e$, it can also decay into three photons. The decay width for this process is given by [90]

$$\Gamma(Z_Q \to 3\gamma) = \epsilon^2 \frac{\alpha_{\rm em}^4}{2^7 3^6 5^2 \pi^3} \frac{m_{Z_Q}^9}{m_e^8} \left[\frac{17}{5} + \frac{67}{42}\frac{m_{Z_Q}^2}{m_e^2} + \frac{128941}{246960}\frac{m_{Z_Q}^4}{m_e^4} + \mathcal{O}\left(\frac{m_{Z_Q}^6}{m_e^6}\right)\right], \tag{1.44}$$

where $\alpha_{\rm em}$ is the EM fine-structure constant. However, for the models and mass range of interest here, the partial decay width of $Z_Q \to 3\gamma$ is negligibly small and hence, we will refrain from including it into our calculations.

1.3.2 Hadronic Decays

For energies from $\sim 0.2\,\mathrm{GeV}$ up to $\sim 2\,\mathrm{GeV}$, the spectrum is plagued by several hadronic resonances. In this regime, perturbative QCD fails to work and we cannot evaluate the gauge boson hadronic decay rates analytically using the width into quarks.

In the case of the minimal *dark photon* model, there is an easy way to handle these hadronic widths. Since the *dark photon* coupling structure is inherited from the SM photon with a proportionality factor ϵ, in order to obtain the hadronic widths we can directly re-scale the experimental data of e^-e^- annihilation into hadrons, according to

$$\Gamma_{Z_\gamma \to \mathcal{H}} = \Gamma_{Z_\gamma \to \mu^+\mu^-} R_\mu^{\mathcal{H}}[\text{exp}] \,, \tag{1.45}$$

where $\Gamma_{Z_\gamma \to \mathcal{H}}$ represents the *dark photon* decay width into the hadronic channel $\mathcal{H}$, $\Gamma_{Z_\gamma \to \mu^+\mu^-}$ is the DP width into a pair of muons and $R_\mu^{\mathcal{H}}[\text{exp}]$ is the experimentally known ratio [2]

$$R_\mu^{\mathcal{H}}[\text{exp}] \equiv \frac{\sigma(e^+e^- \to \mathcal{H})}{\sigma(e^+e^- \to \mu^+\mu^-)} \,. \tag{1.46}$$

Whereas eq. (1.45) suits very well for the DP model, it cannot be employed anymore when we deal with generic $U(1)_Q$ gauge bosons that do not have coupling structures proportional to the SM photon couplings. Instead, we need to rely on techniques based on chiral perturbation theory, such as the vector meson dominance (VMD) [91–93] approach. The VMD model has recently gained prominence with the application to light vector mediators [1, 94] for the description of vector boson hadronic decays. The basic principle behind the model idea is to provide a low-energy effective theory to describe $Z_Q \to \mathcal{H}$, where $\mathcal{H}$ is a hadronic final state made of light quarks, via the mixing with the QCD vector mesons. Among other advantages, the VMD approach was also used to successfully characterize e^+e^- annihilations into hadrons.

To explain in more details, in the VMD framework we split the EM current of light quarks (u, d, s) into three components: the isospin $I = 0, 1$ and the strange quark current. We then identify these currents with the vector mesons ω, ρ and ϕ, respectively. In order to accomplish that, we treat the vector mesons $V = (\rho, \omega, \phi)$ as dynamical gauge fields of a local hidden symmetry $U(3)_V$. Then, we can describe the hadronic decay channels as arising from a $VV'P$ vertex, where V, V' represents vector mesons and P the pseudoscalar mesons.

To include gauge bosons associated with $U(1)$ symmetries, we need to add them as external fields in the covariant derivative of the pseudoscalar Goldstone Matrix of the chiral Lagrangian. With that, we can obtain the mixing term between the vector meson and the gauge boson, which, in general, has the form [6]

$$\mathcal{L}_{VZ_Q} = 2\, g_Q Z_Q^\mu \text{Tr}\left[V_\mu Q^f\right] \,, \tag{1.47}$$

[6] For the details about the construction of this interaction and also a better description of the VMD model, we refer the reader to appendix A.

where $V^\mu = T^a V^{a,\mu}$ with T^a the $U(3)$ meson generators and Q^f the diagonal light quark matrix, i.e. the matrix with entries equal to the $U(1)_Q$ charges $q_Q^{u,d,s}$. This equation can even be applied in the *dark photon* Z_γ case, where one must take $g_Q \to e\epsilon$ and $q_Q^f \to q_{\rm em}^f$. The relevant $V = (\rho, \omega, \phi)$ vector meson generators are given by

$$\begin{aligned}
\rho: \ \rho^\mu T_\rho &= \rho^\mu \frac{1}{2}\mathrm{diag}(1,-1,0)\,, \\
\omega: \ \omega^\mu T_\omega &= \omega^\mu \frac{1}{2}\mathrm{diag}(1,1,0)\,, \\
\phi: \ \phi^\mu T_\phi &= \phi^\mu \frac{1}{\sqrt{2}}\mathrm{diag}(0,0,1)\,.
\end{aligned} \tag{1.48}$$

As an example, let us consider the baryophilic models of table 1.1 that have quark charges $q_Q^{u,d,s} = 1/3$. From eq. (1.48) we see that the mixing term with the ρ meson is

$$\mathcal{L}_{\rho Z_Q} = g_Q Z_Q^\mu \rho_\mu \mathrm{Tr}[\mathrm{diag}(1,-1,0)\,\mathrm{diag}(1/3,1/3,1/3)] = 0, \tag{1.49}$$

which means that B-coupled models do not mix with the ρ vector meson and hence, only the ω and ϕ mesons will contribute to the description of Z_Q hadronic decays. Therefore, it is of extreme importance an accurate decomposition of the different hadronic channels into ρ, ω and ϕ components, in order to obtain the correct gauge boson mixtures and subsequent decays.

Although some previous works [1, 94] already employed the VMD framework to describe Z_Q decays into hadronic channels, they only considered a limited number of hadronic processes, with several approximations. The focus of the work developed here was exactly to improve the hadronic decay width description of generic $U(1)_Q$ models by including several new hadronic channels, using new experimental data and also dividing the channels into the correct ρ, ω, ϕ contributions with the VMD approach. The exact way we managed to succeed on that is described in more details in chapter 2.

1.3.3 Perturbative Decay into Quarks

In the energy region close to $\sim 2\,\mathrm{GeV}$, we expect that the annihilation processes into hadrons slowly transition into perturbative quark production. In this regime the SM hadronic ratio $R_\mu^{\mathcal{H}}$ will become

$$R_\mu^{\mathcal{H}} \to R_{\rm em} = N_c \cdot \sum_{f=u,d,s} (q_{\rm em}^f)^2 = 2\,,$$

where the number of colors $N_c = 3$ and the EM quark charges are $q_{\rm em}^u = 2/3$ and $q_{\rm em}^{d,s} = -1/3$. Therefore, for the DP case, we expect that in this energy regime the decay width into hadrons

will shift into a fully inclusive decay, such that

$$\Gamma_{Z_\gamma \to \text{quarks}}(m) = R_{\text{em}}(m)\Gamma_{Z_\gamma \to \mu^+\mu^-}(m)\,, \tag{1.50}$$

where $R_{\text{em}}(m) = 2$ if we consider the three light quarks u, d and s. As the energy scale $m = m_{Z_Q}$ gets higher we also need to include in the $R_{\text{em}}(m)$ calculation the charm and bottom quarks. From the R-ratio experimental measurements, the charm quark c will appear after two times the mass threshold of the lightest particle which contains a charm quark, which is the D^0 $(c\bar{u})$ meson. Similarly, the bottom quark b will appear after the Upsilon Υ $(b\bar{b})$ meson mass threshold. Therefore, we have that

$$R_{\text{em}}(m) = \begin{cases} 2, & \text{if } \; m < 2\,m_{D^0} \\ 10/3, & \text{if } \; 2\,m_{D^0} < m < m_\Upsilon \\ 11/3, & \text{if } \; m > m_\Upsilon \end{cases} \tag{1.51}$$

For the other B-coupled models, the strategy is very similar, however the cross-section ratio will be given by

$$R_Q(m) = N_c \cdot \sum_{f=\text{quarks}} (q_Q^f)^2 = N_c \cdot \sum_{f=\text{quarks}} \left(\frac{1}{3}\right)^2 = \begin{cases} 1, & \text{if } \; m < 2m_{D^0} \\ 4/3, & \text{if } \; 2\,m_{D^0} < m < m_\Upsilon \\ 5/3, & \text{if } \; m > m_\Upsilon \end{cases} \tag{1.52}$$

For completeness, we will also add in the perturbative quark width calculation an extra factor δ_{QCD} to account for corrections due to QCD effects [2]. With that, the final decay width of Z_Q into quarks can be written as

$$\Gamma_{Z_Q \to \text{quarks}}(m) = R_Q(m)(1 + \delta_{\text{QCD}}(m))\bar{\Gamma}_{Z_Q \to \mu^+\mu^-}(m)\,, \tag{1.53}$$

where $\bar{\Gamma}_{Z_Q \to \mu^+\mu^-}$ represent the decay into muons, however, normalized to $q_Q^\mu = 1$. This is necessary because in the usual EM R-ratio we need to include the muon charge in order to cancel the quark EM charge factor of e. In the generic case, we do not have this cancellation in the ratio. Actually, the normalized width into muons will only act as an inclusion of the kinematic factors from eq. (1.43) that were cancelled in the R-ratio. This is required even for $U(1)_Q$ models that do not couple with muons, that is why we do not take into account the muon charges of the model in that width.

In the case of the QCD correction factor, according to [2] we take δ_{QCD} to be

$$\delta_{\mathrm{QCD}}(m) = \sum_{n=1}^{4} c_n \cdot \left(\frac{\alpha_s(m^2)}{\pi}\right)^n + \mathcal{O}\left(\frac{\Lambda^4}{m^4}\right), \tag{1.54}$$

where α_s is the QCD fine-structure constant, that was taken from [95], and the first four terms in the expansion are [96]

$$c_n = \begin{cases} 1, & (n=1) \\ 1.9857 - 0.1152\, n_f, & (n=2) \\ -6.63694 - 1.20013\, n_f - 0.00518\, n_f^2 - 1.240\, \xi, & (n=3) \\ -156.61 + 18.775\, n_f - 0.7974\, n_f^2 + 0.0215\, n_f^3 - (17.828 - 0.575\, n_f)\, \xi, & (n=4) \end{cases} \tag{1.55}$$

where n_f is the number of considered quarks in that given energy scale and

$$\xi \equiv \frac{\left(\sum q_Q^f\right)^2}{N_c \sum (q_Q^f)^2}\,.$$

After establishing the general theoretical foundations of the $U(1)_Q$ gauged model, and also discussed the production and decay channels of the the associated new vector boson Z_Q, in the next chapter we will elaborate on how we improved the description of the light mediator hadronic decays.

Chapter 2

Improvements in the Hadronic Calculation

Light vector mediator models have been extensively studied over the years [1, 28, 97, 98], with several experiments constraining the available parameter space (see, for example, Refs. [78, 79, 99]). In general, this type of constraint can be divided into visible and invisible searches. The former relies on detecting dark boson decays into visible SM channels, mainly e^+e^- and $\mu^+\mu^-$ decays, and the latter explores the new boson coupling with invisible signature particles, such as neutrinos, dark matter or other hidden sector particles.

For such searches to be realized, it is important to know the dark boson Z_Q branching ratios. This is not a problem in the case of decays into elementary SM fermions since we can compute the analytical width directly from the Lagrangian, as established by eq. (1.43). However, when considering light mediators, we need to be careful with decays into hadrons, that will dominate in the region between 0.2 GeV and ~ 2 GeV. In the *dark photon* scenario, we saw that the usual strategy is to use the experimental hadronic ratio $R_\mu^{\mathcal{H}}[\text{exp}]$, but when we deal with generic $U(1)_Q$ mediators, that enjoy different couplings to quarks, we cannot employ this technique anymore.

In these generic $U(1)_Q$ scenarios, the best approach is to parametrize the hadronic currents using the vector meson dominance (VMD) model, which considers the mixing of the ρ, ω and ϕ vector mesons with the new Z_Q mediator. With this strategy one can then divide the hadronic current into ρ, ω and ϕ contributions to obtain the separated mixing with the new gauge field and then calculate the new vector mediator hadronic decay width.

Especially when dealing with baryophilic models, such as the ones in table 1.1, the decays into hadronic final states can have a significant contribution to the total width, and hence a great impact on the leptonic branching ratios. Therefore, the correct description of such decays plays a major role that can even affect the experimental constraints. The main purpose of the first part of this dissertation is to show how we can improve this description and provide, for the first time, an almost complete set of Z_Q decays into arbitrary leptonic and hadronic final states.

To this purpose, we explicitly calculated the Z_Q width into several hadronic final states that were not considered in previous studies [1]. To perform the calculation we used a data-driven approach that relies on fits to e^+e^- data using the python package `IMinuit` [100]. The new hadronic channels considered here include some channels already fitted by [19], but also new channels relevant near ~ 2 GeV, for which we performed the fit for the first time. All fits are updated to the most recent data and are based on state-of-the-art hadronic current parametrizations of e^+e^- annihilation processes [101, 102]. We provide the description of hadronic decays of generic Z_Q gauge bosons in the python package DELIVER (**De**cays of **Li**ght **Ve**ctors **R**evised) that is available for public use on GitHub at https://github.com/preimitz/DeLiVeR with a jupyter notebook tutorial. Our results can also be found in the manuscript [70], which was accepted for publication by JHEP .

In this chapter, we will describe the improvements we have implemented in the calculation of the widths and branching ratios of $Z_{\gamma,Q}$ into light hadrons and compare our results with the ones from Ref. [1], that are publicly available in the DARKCAST code. The first section will introduce the calculation method we used to obtain the hadronic widths. After that, we will show the improvements in the description of the low energy hadronic modes. In the third section, we will introduce the new channels that we included in our study. Finally, we will show the results of the vector meson decomposition of all hadronic channels employed, together with the strategy we used to make the transition from the hadronic to the quark width.

2.1 Decay Width calculation

As we explained in the first chapter, in order to calculate the hadronic decay widths for generic light mediators we need to decompose the cross-sections $e^+e^- \to \text{hadrons}$ into ρ, ω, ϕ components according to the VMD approach. In the following discussion, we will first introduce the method that was implemented in a previous work [1] to calculate the hadronic decay width and then we will explain the strategy employed here for the same calculation.

2.1.1 Previous implementation

In the previous work of Ref. [1], the authors performed a fit to the $R_\mu^{\mathcal{H}}$ ratio data, where

$$R_\mu^{\mathcal{H}} \equiv \sigma(e^+e^- \to \mathcal{H})/\sigma(e^+e^- \to \mu^+\mu^-)\,,$$

for the six hadronic channels $\mathcal{H} = \pi\gamma, \pi\pi, 3\pi, 4\pi, KK$ and $KK\pi$.

Their fit was performed according to the following parametrization

$$R_{\mu}^{\mathcal{H}}(m) = \frac{9}{\alpha_{\text{em}}^2}\left| f_{\mathcal{H}}(m) \pm \sum_{V} \mathcal{A}_{\mathcal{H}}^{V}(m) \right|^2 , \tag{2.1}$$

where m is the invariant e^+e^- mass, V correspond to the ground-state resonances ρ, ω, ϕ, the real function $f_{\mathcal{H}}$ accounts for higher resonance effects V^*, which we denote with a 'prime' $V^* = \rho', \rho'', \rho''', \omega', \omega'', \ldots$ and the $\mathcal{A}_{\mathcal{H}}^{V}$ amplitudes have Breit-Wigner forms. They model the $f_{\mathcal{H}}$ function as a bicubic spline and take it to be real in order to neglect possible interference effects between V^* and V.

Using this method, it is easy to translate the SM photon-mediated cross-section ratio into a Z_Q-mediated ratio by simply exchanging the photon couplings for the new vector mediator couplings, according to

$$\begin{aligned}
R_{Z_Q}^{\rho} &= \left(\frac{\text{Tr}\left[T_\rho Q^f\right]}{\text{Tr}\left[T_\rho Q^{\text{em}}\right]} \right)^2 R_{\mu}^{\rho} = \left(2\,\text{Tr}\left[T_\rho Q^f\right]\right)^2 R_{\mu}^{\rho} \\
R_{Z_Q}^{\omega} &= \left(\frac{\text{Tr}\left[T_\omega Q^f\right]}{\text{Tr}\left[T_\omega Q^{\text{em}}\right]} \right)^2 R_{\mu}^{\omega} = \left(6\,\text{Tr}\left[T_\omega Q^f\right]\right)^2 R_{\mu}^{\omega} \\
R_{Z_Q}^{\phi} &= \left(\frac{\text{Tr}\left[T_\phi Q^f\right]}{\text{Tr}\left[T_\phi Q^{\text{em}}\right]} \right)^2 R_{\mu}^{\phi} = \left(-3\sqrt{2}\,\text{Tr}\left[T_\phi Q^f\right]\right)^2 R_{\mu}^{\phi} ,
\end{aligned} \tag{2.2}$$

where $Q^{\text{em}} = \text{diag}(2/3, -1/3, -1/3)$ and Q^f are the SM photon and Z_Q diagonal light quark matrix, respectively, $T_{\rho,\omega,\phi}$ are the vector meson $U(3)$ generators, given by eq. (1.48), and $R_{\mu}^{\rho,\omega,\phi}$ are the ρ, ω, ϕ components of the SM R-ratio. We also used the photon/vector mediator coupling to the vector mesons as given by eq. (1.47).

Nonetheless, the calculation of the total hadronic width cannot be done by directly summing up the three R_{Z_Q} vector meson contributions because we must also take into account the interference terms between the vector mesons. In Ref. [1], the authors calculated the total decay width $\Gamma_{Z_Q \to \text{hadrons}}$ by using the formula

$$\Gamma_{Z_Q \to \text{hadrons}} = \frac{g_Q^2 m_{Z_Q}}{12\pi}\left[\sum_{V} R_{Z_Q}^{V}(m_{Z_Q}) + R_{Z_Q}^{\omega-\phi}(m_{Z_Q}) \right] , \tag{2.3}$$

where the $R_{Z_Q}^{\omega-\phi}$ term accounts for a mixing between these two vector mesons. Even so, this implementation is still incomplete since, apart from the inclusion of only six hadronic channels, they neglected all the other vector meson interference effects.

2.1.2 New implementation

Given that in this dissertation we considered several new hadronic channels, and also included new ρ, ω, ϕ vector meson contributions into the description of the previous and new channels, we did not follow the same approach as in eq. (2.3) for the sake of taking into account all the interference effects. Instead, we explicitly calculate the decay width formulas, and the cross-sections, for each hadronic mode.

Let us now describe here the details of this implementation. The cross-section of the process $e^+e^- \to V \to \mathcal{H}$ (see figure 2.1) can be evaluated by the computation of the matrix element

$$\mathcal{M} = \mathscr{L}^\mu J_\mu \,, \tag{2.4}$$

where J^μ is the hadronic current and $\mathscr{L}^\mu$ is the $e^+(k_+)e^-(k_-)$ leptonic current, given by

$$\mathscr{L}^\mu = e^2 \frac{g^{\mu\nu}}{s} \bar{v}(k_+)\gamma_\mu u(k_-) \,, \tag{2.5}$$

with $s = (k_+ + k_-)^2$ being the square of the center-of-mass (COM) energy and $k_+(k_-)$ is the $e^+(e^-)$ four-momenta. Using the matrix element, we can then write the differential cross-section as

$$\begin{aligned} \mathrm{d}\sigma &= \frac{1}{4\sqrt{(k_+ \cdot k_-)^2 - m_e^4}} \mathrm{d}\Phi_n \left|\overline{\mathcal{M}}\right|^2 \\ &= \frac{1}{2s} \mathrm{d}\Phi_n \frac{1}{12} \left[-\mathscr{L}^\mu \mathscr{L}_\mu\right] \left[-J^\mu J_\mu\right] \,, \end{aligned} \tag{2.6}$$

where $\mathrm{d}\Phi_n$ is the n-body phase-space element

$$\mathrm{d}\Phi_n = \prod_{f=1\ldots n} \frac{\mathrm{d}^3 p_f}{(2\pi)^3 2E_f} (2\pi)^4 \delta^{(4)}\left(k_+ + k_- - \sum p_f\right) , \tag{2.7}$$

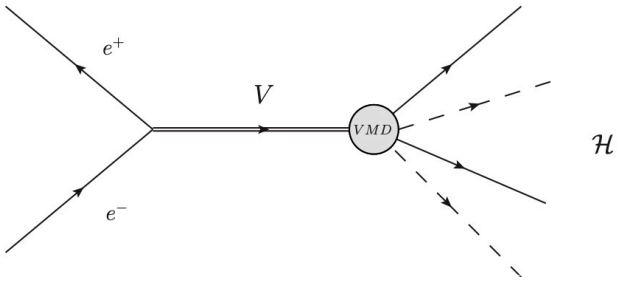

Figure 2.1: Diagrammatic illustration of the $e^+e^- \to V \to \mathcal{H}$ process, where $\mathcal{H}$ represents any hadronic final state.

with $\sum p_f$ representing the sum over the momenta of the final state particles and the factor of $1/12$ comes form the average over the incoming lepton spins $(1/4)$ plus the intermediate vector meson polarizations $(1/3)$. In the cross-section formula we also used the approximation $m_e \sim 0$, since we will consider hadronic decays and the mass of the lightest hadron, *i.e.* the pion mass, is much higher than the electron mass ($m_\pi \gg m_e$).

We can further simplify the cross-section calculation by performing the contraction of the leptonic currents

$$\frac{1}{12}\left[-\mathscr{L}^\mu \mathscr{L}_\mu\right] = \frac{e^4}{3s}\left(1+\frac{2m_e^2}{s}\right) \xrightarrow{m_e=0} \frac{16\pi^2\alpha_{\rm em}^2}{3s}\,, \tag{2.8}$$

such that we end up with

$$\mathrm{d}\sigma = \frac{16\pi^2\alpha_{\rm em}^2}{3s}\frac{1}{2s}\mathrm{d}\Phi_n\left[-J^\mu J_\mu\right]\,. \tag{2.9}$$

Finally, we calculate the vector meson decay width $\Gamma(V\to\mathcal{H})$ from the process $e^+e^-\to V\to\mathcal{H}$ by replacing the leptonic current of the matrix element by the vector meson polarization ε_μ, such that $\mathcal{M}_{V\to\mathcal{H}} = \varepsilon_\mu(V)J^\mu$. The partial decay width can be expressed as

$$\mathrm{d}\Gamma(V\to\mathcal{H}) = \frac{1}{3}\times\frac{1}{2\,m_V}|\mathcal{M}_{V\to\mathcal{H}}|^2\mathrm{d}\Phi_n\,, \tag{2.10}$$

where m_V is the vector meson mass and the $1/3$ factor represents the average over the intermediate vector polarizations.

Until now we were only dealing with the SM cross-section $e^+e^-\to V\to\mathcal{H}$, where $V=\rho,\omega,\phi$ is the intermediate vector meson that will describe the decay into the hadronic mode within the VMD framework. With the purpose of finding an expression for the light mediator decay width, we need to translate this process into $e^+e^-\to Z_Q\to\mathcal{H}$, with the light dark mediator intermediate state. Therefore, to transform the decay width given in eq. (2.10) into a Z_Q hadronic width, we need to multiply the hadronic current by the $U(1)_Q$-SM coupling ratio in order to rescale the vector-meson-quark coupling to the Z_Q-quark coupling. As a result, the decay width matrix element becomes

$$\mathcal{M}_{Z_Q\to\mathcal{H}} = \varepsilon_\mu(Z_Q)\sum_V r(V)J^\mu_{\mathcal{H}}(V)\,,\qquad r(V) = \frac{g_Q\mathrm{Tr}\left[T_V Q^f\right]}{\mathrm{Tr}\left[T_V Q^{\rm em}\right]}\,, \tag{2.11}$$

where now $\varepsilon_\mu(Z_Q)$ is the dark boson polarization, V loops over the vector mesons ρ,ω and ϕ, $T_{V=\rho,\omega,\phi}$ are the vector meson $U(3)$ generators, given by eq. (1.48), and the hadronic current

$J^\mu_{\mathcal{H}}(V)$ is the current associated with the vector meson V [1]. Accordingly, we can write the differential partial decay width, which is given by

$$\mathrm{d}\Gamma(Z_Q \to \mathcal{H}) = \frac{1}{3} \times \frac{1}{2\, m_{Z_Q}} \left|\mathcal{M}_{Z_Q \to \mathcal{H}}\right|^2 \mathrm{d}\Phi_n, \tag{2.12}$$

where the phase-space element depends on the number of final states. For the case of Z_Q decays into two particles, for example $Z_Q \to \pi\pi, \phi\pi, KK$, we can use eq. (B.1) to obtain

$$\Gamma(Z_Q \to 2) = \frac{1}{3} \times \frac{1}{8\pi} \frac{|p_{\mathrm{cm}}|}{m^2_{Z_Q}} \left|\mathcal{M}_{Z_Q \to \mathcal{H}}\right|^2 . \tag{2.13}$$

Now that we succeeded on the decay width formulation we can use eq. (2.12) to individually calculate the decays of the new light mediators into several hadronic final states $\mathcal{H}$. However, this is not the end of the story. For the width calculation there is an essential ingredient that we still need to obtain, which is the hadronic current $J^\mu_{\mathcal{H}}$. The specific form of this current will depend on the hadronic mode that we are interested in. It also includes a form-factor $F_{\mathcal{H}}$, depending on $\mathcal{H}$, that will be responsible for carrying the vector meson structure of the process. Below, we list some of the hadronic currents for different final state configurations $\mathcal{H}$

$$\begin{aligned} J^\mu_{P_1P_2} &= -(p_1 - p_2)^\mu F_{P_1P_2}(q^2), & J^\mu_{P\gamma} &= \varepsilon^{\mu\nu\rho\sigma} q_\nu \varepsilon_{\gamma,\rho} p_{\gamma,\sigma} F_{P\gamma}(q^2), \\ J^\mu_{VP} &= \varepsilon^{\mu\nu\rho\sigma} q_\nu \varepsilon_{V,\rho} p_{1,\sigma} F_{VP}(q^2), & J^\mu_{P_1P_2P_3} &= \varepsilon^{\mu\nu\rho\sigma} p_{1,\nu} p_{2,\rho} p_{3,\sigma} F_{P_1P_2P_3}(p_1, p_2, p_3)\,, \end{aligned} \tag{2.14}$$

where $P_{i=1,2,3}, V$ and γ indicate, respectively, the presence of a pseudoscalar meson, a vector meson, or a photon in the final state. We label the corresponding momenta by p_i for the pseudoscalars and p_γ for the photon. The polarizations are given by $\varepsilon_{\gamma/V}$, for the vector meson and photon. The variable $q = \sqrt{s}$ is the COM energy, such that in the case of $\mathcal{H} = (P_1P_2), (P\gamma)$ and (VP), we have that $q = p_1 + p_2$, $q = p_1 + p_\gamma$ and $q = p_1 + p_V$, respectively.

When the final state contains a vector meson and two pseudoscalars, as, for example $\mathcal{H} = \omega\pi\pi$ and $\phi\pi\pi$, we avoid the inclusion of intermediate structures, such as $\omega f_0 \to \omega\pi\pi$, due to dissenting data observations [54, 55]. As a result, we assume a point-like interaction with hadronic current given by

$$J^\mu_{VP_1P_2} = \left(g^{\mu\nu} - \frac{q^\mu q^\nu}{q^2}\right) \varepsilon^*_{V,\nu} F_{VP_1P_2}(q^2)\,, \tag{2.15}$$

[1] As we explain in appendix B, the form-factors that appear in the hadronic currents are functions of the vector mesons parameters, usually the sum of the V resonances Breit-Wigners. The hadronic current $J^\mu_{\mathcal{H}}(V)$ can then be obtained by considering only the V component of the form-factor.

where $q = p_V + p_1 + p_2$. We also consider some channels with more than three final states. In this case, we directly take expressions from the literature as given in table 2.2.

Last but not least, we need to deal with the form-factor $F_{\mathcal{H}}$ calculation. These form-factors will carry the dependence on the vector meson resonances ρ, ω and ϕ, usually parametrized in the form of Breit-Wigner functions. For the specific formula of these form-factors, and also details about the hadronic current expressions, we refer the reader to appendix B.

2.2 Description of the Hadronic Modes

In the last section we establish the theory behind our method for the light mediator hadronic width calculation. In a more systematic way, we describe below the step-by-step procedure one needs to follow in order to obtain $\Gamma(Z_Q \to \mathcal{H})$

1. First, we identify the specific hadronic channel $\mathcal{H}$ for which we will implement the decay width. We need to check for possible substructures of this channel. For example, it was reported [54, 55] that the 5π channel contains intermediate $\omega\pi\pi$ and $\eta\pi\pi$ states. These two substructures almost saturate the 5π channel, therefore it is more useful to model these two states instead of the 5π. Note that if we took into account these three modes we would end up with duplicate information, and hence a overestimation of the cross-section.

2. After deciding the correct final state we want to model, we need to check if there is some cross-section experimental data available. The method employed here is based on a data-driven approach, so we can only obtain the decay width through the direct fit of the cross-section data.

3. In possession of the experimental cross-section data $\sigma(e^+e^- \to \mathcal{H})$, we need to parametrize the form-factor of that channel in terms of the vector meson ρ, ω, ϕ parameters, such as the vector meson mass m_V and width Γ_V, Breit-Wigner amplitude a_V and phase φ_V, among other parameters (see appendix B).

4. With the analytical expression for the form-factor, and hence for the hadronic current, we perform the fit of the cross-section data according to eq. (2.9). To decide the dominant vector mesons for a particular channel we rely on isospin-symmetry assumptions and G-parity conservation (see section B.2 of appendix B). Recall that in the VMD framework we deal with the neutral intermediate vector mesons, that can either be the ground-state modes ρ, ω, ϕ or their excited versions,which we label with a 'prime' ($\rho', \rho'', \dots$). The fit will give the information of the vector mesons parameters that appear in the description of that particular channel.

5. With the fit information of the vector meson parameters, we have the final expression for the hadronic current $J_\mu^{\mathcal{H}}$, that we can divide into $J_\mu^{\mathcal{H}} = J_\mu^{\mathcal{H}}(\rho) + J_\mu^{\mathcal{H}}(\omega) + J_\mu^{\mathcal{H}}(\phi)$ using the fit values. The final step is to plug the current in eq. (2.12) to obtain the dark mediator decay width, which will depend on the hadronic channel as well as on the phase-space element. In appendix B we give the decay width formulas for several types of hadronic modes. Those formulas represent the SM scenario $V \to \mathcal{H}$, however, to convert to the BSM approach $Z_Q \to \mathcal{H}$ we simply change the squared COM energy s by the squared vector boson mass $s \to m_{Z_Q}^2$ and re-scale the SM quark couplings according to eq. (2.11).

In this dissertation, we included several hadronic channels contributions for the light mediator decay width. Among them, there are six channels that were already considered by [1], that correspond to the dominant contributions close to the ρ, ω, and ϕ ground state masses plus the 4π and $KK\pi$ channels. We list them in table 2.1. We also considered several new hadronic channels as can be seen in table 2.2. For the majority of these new channels, and also for the channels of table 2.1, we took the parametrizations and fits from [19]. However, we also included four new channels that were not considered before in the literature and for which we performed the fit using the python package `IMinuit` [100]. These original channels showed to be very relevant in the energy range close to ~ 2 GeV. For more technical details about the parametrization and fit procedure, we refer the reader to appendix C.

In what follows, we summarize the improvements we achieved by employing the hadronic decay width implementation described above. We first comment on the results concerning the hadronic modes already considered in [1], and then compare the two approaches. After that, we show the results for the new hadronic modes that were added in this dissertation.

channel	resonances	data	parametrization	fit	possible final states
$\pi\gamma$	$\boldsymbol{\rho}, \omega, \boldsymbol{\omega'}, \boldsymbol{\omega''}, \boldsymbol{\phi}$	[3]	[3]	[3]	$\pi\gamma$
$\pi\pi$	$\rho, \rho', ...$	[103–105]	[106]	[106]	$\pi\pi$
3π	$\boldsymbol{\rho}, \boldsymbol{\rho''}, \omega, \omega', \omega'', \phi$	[107]	[108]	[108]	3π
4π	$\rho, \rho', \rho'', \rho'''$	[109, 110]	[111]	[19]	4π
KK	$\boldsymbol{\rho}, ..., \boldsymbol{\omega}, ..., \phi, ...$	[4–13]	[106]	[19]	KK
$KK\pi$	$\boldsymbol{\rho}, \boldsymbol{\rho'}, \boldsymbol{\rho''}, \phi, \phi', \phi''$	[14–18]	[19]	[19]	$KK\pi$

Table 2.1: List of the hadronic channels included in this dissertation and also in the DARKCAST code [1]. The second column shows the resonances that were used in the fit of that particular channel and we emphasize in boldface the ones which were included here, but not in [1]. We denote towers of vector meson resonances with '...'. The other columns display the references that we used for the cross-section data, the parametrization of the hadronic current and the fit, while the last column show the possible final states, composed by low-energy pseudoscalar mesons, π and K, as well as photons.

channel	resonances	data	parametrization	fit	possible final states
$\eta\gamma$	$\rho, \rho', \omega, \phi$	[112]	[112]	[112]	3γ, $3\pi\gamma$,...
$\eta\pi\pi$	ρ, ρ', ρ''	[113, 114]	[115]	[19]	$2\pi2\gamma, 5\pi$,...
$\omega\pi \to \pi\pi\gamma$	ρ, ρ', ρ''	[116]	[116]	[116]	$2\pi\gamma$
$\omega\pi\pi$	ω''	[53–55]	new	new	$5\pi, 3\pi\gamma$
$\phi\pi$	ρ, ρ'	[14, 117]	[19]	[19]	$2K\pi$, 4π,...
$\eta'\pi\pi$	ρ'''	[54]	[115]	[19]	$4\pi2\gamma$,...
$\eta\omega$	ω', ω''	[118]	[19]	[19]	$2\pi2\gamma, 6\pi, \ldots$
$\eta\phi$	ϕ', ϕ''	[14, 119]	[19]	[19]	$KK2\gamma, KK3\pi, \ldots$
$p\bar{p}/n\bar{n}$	$\rho, \rho', \ldots, \omega, \omega'$,...	[120–137]	[138]	[19]	$p\bar{p}/n\bar{n}$
$\phi\pi\pi$	ϕ', ϕ''	[56, 58]	new	new	$KK\pi\pi$
$K^*(892)K\pi$	ρ'', ϕ'	[56, 57]	new	new	$KK\pi\pi$
6π	ρ'''	[59]	[59]	new	6π

Table 2.2: Additional hadronic processes included in this dissertation that are not present in the DARKCAST code [1]. The resonances used to describe the channel are quoted in the second column, where we denote with '...' a tower of resonances. We also show the references from which we extracted the cross-section data, the hadronic current parametrization and the fit. In the $\omega\pi$ channel we only considered the cross-section data coming from the subsequent decay into $\pi\pi\gamma$. The channels marked as 'new' represent the original channels that were implemented here for the first time (for more details see appendix C).

2.2.1 Dominant low-energy hadronic channels

The channels $\mathcal{H} = \pi^0\gamma$, $\pi^+\pi^-$, $\pi^+\pi^-\pi^0$ and KK are the dominant channels close to the ground state vector meson masses $m_\rho = 770\,\text{GeV}, m_\omega = 782\,\text{GeV}$ and $m_\phi = 1020\,\text{GeV}$. We also included the contributions from $\mathcal{H} = 4\pi$ and $KK\pi$, that are more relevant in the higher energy range, close to $1.5\,\text{GeV}$. All of these channels are very precisely measured and were considered before in [1] and included in the DARKCAST code. Table 2.1 lists the resonance contributions for each one of these channels, as well as the references from which we extracted the data, parametrizations and fits.

Figure 2.2 shows the $R_\mu^{\mathcal{H}}$-ratio calculation obtained in this dissertation (solid lines) in comparison with the one from DARKCAST (dashed lines), for the hadronic channels of table 2.1. The black points represent the full $\sigma(e^+e^-) \to \text{hadrons}$ data extracted from PDG [2]. From the figure we can see that, close to the peaks of the ground-state vector meson resonances, the two approaches agree very well, however, we still have several differences in the whole spectrum. It is worth mentioning that, while in DARKCAST they include higher resonances in an approximate way by adding a non-resonant background function to mimic the shape of the data (eq. (2.1)), we stick to the VMD assumption and calculate each channel by considering resonance contributions. Below we enumerate the main improvements from our method and

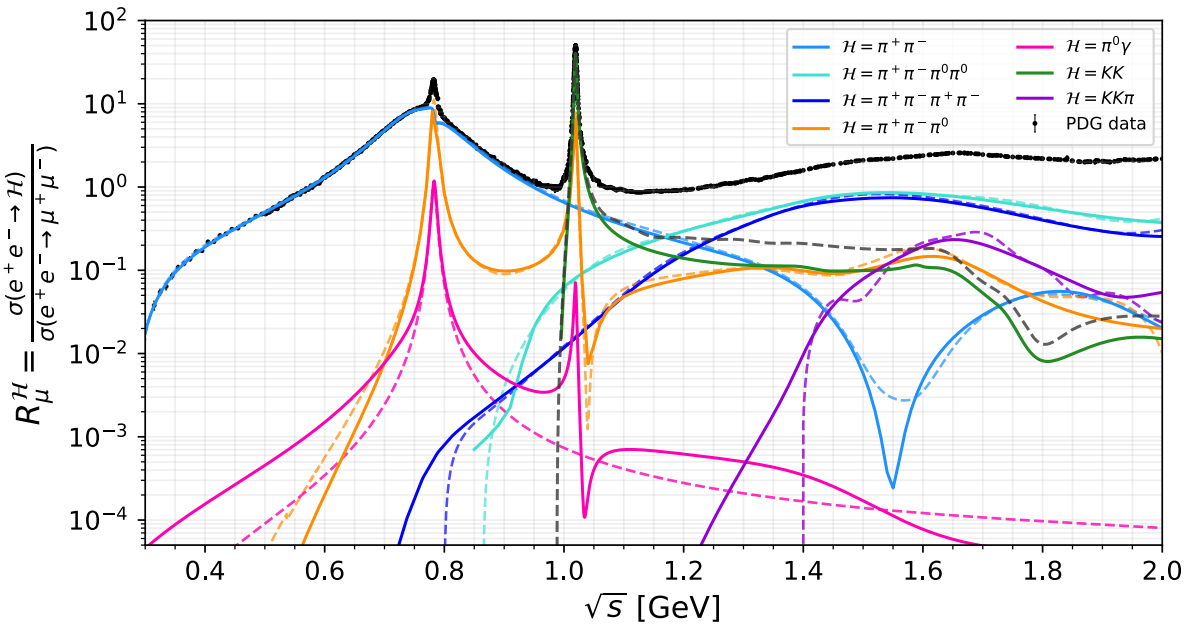

Figure 2.2: Cross-sections for the dominant $e^+e^- \to \mathcal{H}$ channels, normalized by the $e^+e^- \to \mu^+\mu^-$ cross-section. The solid (dashed) lines indicate the results obtained by us (taken from DARKCAST [1]). The data (black points) was taken from the Particle Data Group compilation (PDG) [2]. See text for discussions on the differences.

elaborate on the differences that we introduced here for each hadronic channel:

- $\mathcal{H} = \pi^0\gamma$

  In the case of the $\pi^0\gamma$ channel, DARKCAST only considered the ground state ω contribution, that accounts for the first peak close to $0.8\,\mathrm{GeV}$. In our case, employing the fit from [19], in addition to the inclusion of higher ω resonances, we also consider a ϕ and a small ρ component. The ϕ contribution and the $\omega - \phi$ interference are responsible for the second peak near $1\,\mathrm{GeV}$ and the dip right after it, respectively. The inclusion of these structures results in major improvements on the description of the $\pi\gamma$ data, as can be seen in the left panel of figure 2.3, that shows our (DARKCAST) R-ratio calculation in solid (dashed) pink together with the experimental data points from the SND collaboration [3]. The right panel of the same figure shows the decomposition of the $\mathcal{H} = \pi\gamma$ into ρ (blue), ω (red) and ϕ (green) contributions. The figure highlights that the additional inclusion of the other vector meson structures provides a better description of the data points. Note that this channel is of prime importance since it is the first hadronic channel to appear in the spectrum and the only hadronic mode below the two pion threshold. As a result, we will see in chapter 3 that, in the case of the $U(1)_B$ model, the $\pi\gamma$ discrepancies outlined here will have a great impact on the branching ratios and, consequently, may affect the

model bounds.

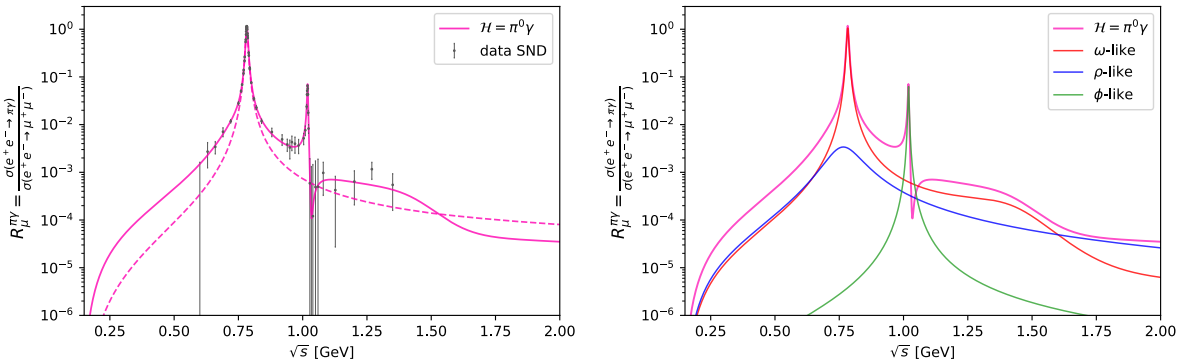

Figure 2.3: Normalized cross-section $R_\mu^{\mathcal{H}}$ for the $\mathcal{H} = \pi^0\gamma$ channel. In the left panel the solid (dashed) pink line indicates our (DARKCAST) calculation, and the gray data points are from SND [3]. In the right panel we show our decomposition of the $\pi\gamma$ channel into ρ (blue), ω (red) and ϕ (green) components.

- $\mathcal{H} = KK$

  The $\mathcal{H} = KK$ channel can be divided into a charged K^+K^- and a neutral K^0K^0 component. Although in DARKCAST they claim that their $\mathcal{H} = KK$ channel is a combination of these two components, their data was taken from [11], which only considered the charged channel. Therefore, they assume that the neutral component is similar to the charged one and took $KK = 2 \cdot K^+K^-$. In contrast, we updated this channel by considering separately the neutral and charged recent cross-section data from several experiments [4–13], such that we have the correct description $KK = K^+K^- + K^0K^0$. In figure 2.4 we highlight this argument by showing the individual normalized cross-sections for the neutral K^0K^0 (light green) and charged K^+K^-(dark green) components, along with the corresponding data points. As one can see, the identification of the neutral mode with the charged one is misleading, since the neutral cross-section is way smaller. This results in an overestimation of the KK contribution in the DARKCAST code, and justifies why their green dashed curve is larger than our solid curve in figure 2.2.

  Besides not taking into account the correct neutral channel contribution, DARKCAST assigned the whole KK channel as a ϕ contribution, while in our approach we also added an $\omega-$ and ρ-like components. As we can see from the right panel of figure 2.4, which shows the vector decomposition for the charged K^+K^- component, although the main peak next to $1\,\mathrm{GeV}$ is originated by the ϕ resonance, the extra features of the curve are mainly a consequence of the other vector mesons. Recall that the correct decomposition of each channel is very important when we deal with the baryophilic $U(1)$ models, since they do not couple with the ρ meson. Thus, for instance, considering the whole KK

channel as an ϕ contribution leads to a wrong overestimation of the $\Gamma(Z_Q \to KK)$ width and branching ratio.

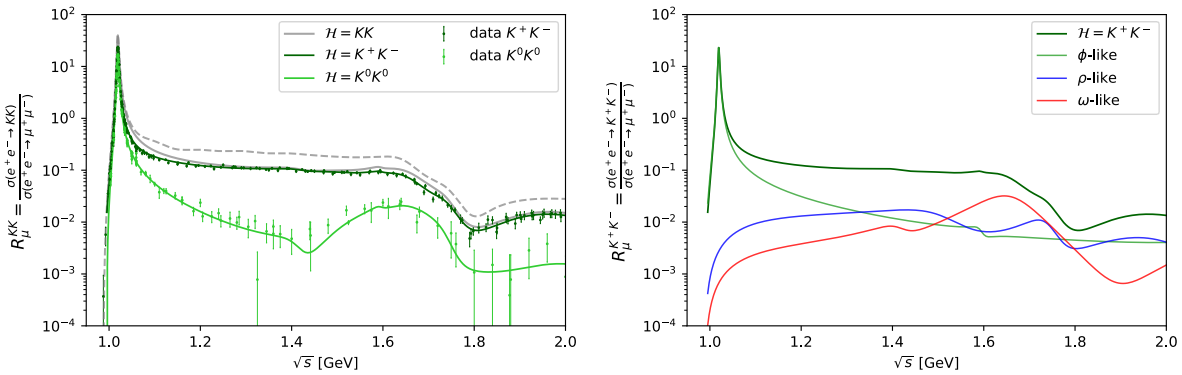

Figure 2.4: Normalized cross-section $R_\mu^{\mathcal{H}}$ for the $\mathcal{H} = KK$ channel. In the left panel the solid (dashed) gray line indicates our (DARKCAST) total KK calculation (same as the green lines in figure 2.2), while the dark (light) green line indicated our fit for the K^+K^- ($K^0\bar{K}^0$) channel. The data points correspond to a compilation from several experiments [4–13]. In the right panel we show the decomposition of the charged K^+K^- channel (dark green) into ρ (blue), ω (red) and ϕ (green) components.

- $\mathcal{H} = KK\pi$

The last crucial difference appears in the $\mathcal{H} = KK\pi$ channel. As in the previous case, we can also divide this channel into three contributions; $K^0K^0\pi^0$, $K^+K^-\pi^0$ and $K^\pm K^0\pi^\mp$. In [1], the authors mention that they considered the isoscalar component of the $KK\pi$ channel. However, the cross-section data they used [14] comes from a $K^\pm K^0\pi^\mp$ analysis, where the collaboration extracted the isoscalar and isovector contributions from the sub-process $e^+e^- \to K^*(892)K$. Hence, in DARKCAST what they call $KK\pi$ contribution is actually the isoscalar component of $K^*(892)K$. The problem of this approach is that $K^*(892)K$ is a two-body process and, hence, enjoys different kinematics compared to the three-body final state $KK\pi$. The correct approach, which we follow here, is actually to consider separately the three components of $KK\pi$. For that, we updated this channel by using data from several experiments [14–18] that considered the individual $KK\pi$ components. This discrepancy in the descriptions is the reason why the two $KK\pi$ curves (solid and dashed purple) in figure 2.2 do not match.

Apart from this, while in DARKCAST they only considered a ϕ-like contribution, here we also included ρ resonances. In figure 2.5 we show the normalized cross-section obtained using the fit from [19] for the individually $KK\pi$ channels, together with the decomposition into ϕ (green) and ρ (blue) contributions and the corresponding data points. The sum

of these three channels results in the total $KK\pi$ channel considered by us, in contrast to the $KK\pi$ used by DARKCAST, which consists only of the isoscalar component and agrees with a different set of data [14].

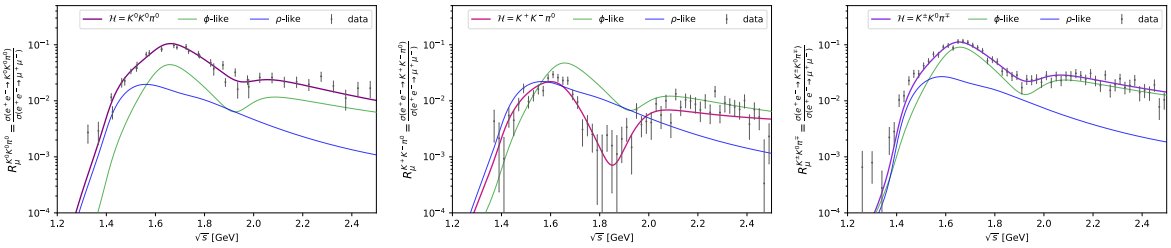

Figure 2.5: Normalized cross-section $R_\mu^{\mathcal{H}}$ for $\mathcal{H} = K^0K^0\pi^0$(left), $K^+K^-\pi^0$ (middle), $K^\pm K^0\pi^\mp$ (right). The purple lines correspond to the channel contribution, whereas the blue and green lines indicate the ϕ and ρ decomposition, respectively. The data points from [14–18] are shown in grey.

- $\mathcal{H} = 3\pi$

The main difference of this channel is that we also included a small ρ component, while in DARKCAST they solely used ω and ϕ. The 3π channel was the only mode which they fit with more than one resonance, and it was due to this channel that they included a $\omega - \phi$ mixing in eq. (2.3).

2.2.2 New hadronic channels

Although the channels already discussed in the last section are the dominant lower energy contributions, there are still several important hadronic modes in the higher resonance region. This region starts right after the ground-state ϕ mass at $1\,\mathrm{GeV}$ and goes up until $\sim 2\,\mathrm{GeV}$ where we transition to the perturbative QCD regime. The problem now amounts to the fact that this higher energy region can be very challenging to describe, due to numerous hadronic modes and poor data available in the literature, especially when dealing with vector mediator decays to currents involving ω and ϕ contributions.

In order to obtain a more robust description of light mediators decays, we introduced a large amount of new channels, as listed in table 2.2. To avoid double counting of any channel, and reduce the possible final states, the first task was to correctly identify the common substructures of each possible process. For instance, we already cover the final state $2\pi 2\gamma$ by including both $\eta\pi\pi$ and $\eta\omega$ contributions, because they are substructures of this channel. In the same way, we do not need to include the 5π channel, because it is covered by $\eta\pi\pi$ and $\omega\pi\pi$.

Initially, we started by the inclusion of all channels considered in [19], since we already had the parametrizations and fits for the currents. However, when we summed them with the old channels, we still could not reach the PDG data points after energies of $\sim 1.5\,\mathrm{GeV}$. The problem was that there were relevant contributions in that regime that were still not taken into account. Due to that we started to search in the literature [2, 139–142] the possible channels that we could be neglecting.

The most important modes that we found, and that had experimental cross-section data, were the $KK\pi\pi$, the 6π and the $\omega\pi\pi$ channels. For the case of the $KK\pi\pi$ final channel, we found two relevant substructures; $\phi\pi\pi$ and $K^*K\pi$. The $\phi\pi\pi$ was divided into a charged ($\phi\pi^+\pi^-$) and a neutral ($\phi\pi^0\pi^0$) component, contributing to $K^+K^-\pi^+\pi^-$ and $K^+K^-\pi^0\pi^0$ states, respectively. For the case of the $K^*K\pi$ mode we have three components, $K^{*0}K^\pm\pi^\mp$, $K^{*\pm}K_S\pi^\mp$ and $K^{*\pm}K^\mp\pi^0$, decaying into $K_SK^\pm\pi^\mp\pi^0$, and one component, $K^{*0}K^\pm\pi^\mp$, decaying into $K^+K^-\pi^+\pi^-$. The 6π channel and $\omega\pi\pi$ channels were also split into a neutral and a charged component. For more details about the parametrization and fit of these channels we refer to appendix C.

In figure 2.6 we show the results of the $R_\mu^{\mathcal{H}}$ ratio for the new implemented channels. The dashed-dot lines indicate the channels which we took the parametrization and fits from other references, according to table 2.2, and the dotted lines indicate the four new channels for which we performed the fit. The solid purple line represents the sum of the contributions of all these new channels, while the cyan solid line is the sum of the old modes from table 2.1. The orange solid line correspond to the sum of all hadronic channels included in this study.

Note that, although the new channels have a minor effect in the lower energy region, their contribution is essential for higher energies, and even reach the old channels curve near $2\,\mathrm{GeV}$. As a result of their inclusion, we can see that for center-of-mass $\sqrt{s} \gtrsim 1.4$ GeV the orange line continues to follow the PDG data to higher energies and almost match with the PDG data points. Thus, we can conclude that without the addition of these new channels we would not describe correctly the effects of the ρ, ω, and ϕ meson excited states.

It is also important to highlight that the inclusion of the four extra channels, especially the 6π and $K^*K\pi$ modes represented by the blue and red dotted lines in figure 2.6, are the major contributions for energies higher than $\sim 1.7\,\mathrm{GeV}$. In fact, their inclusion was crucial to lift the orange curve towards the PDG data.

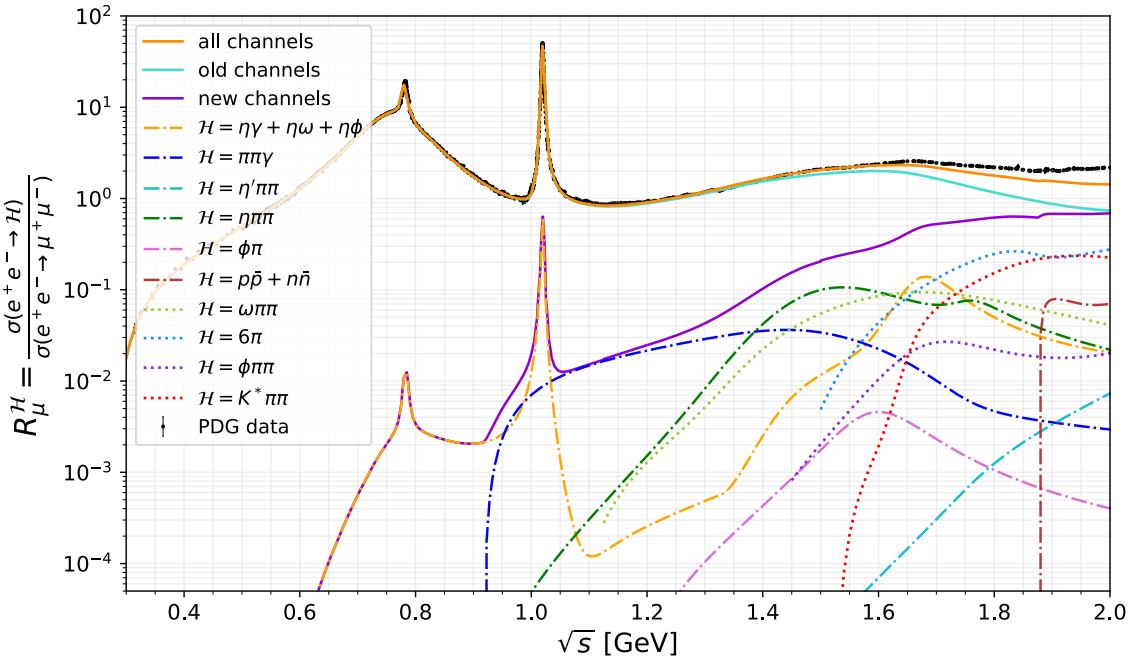

Figure 2.6: Normalized cross-sections $R_\mu^{\mathcal{H}}$ for the new channels included in this dissertation, but not in [1]. The dot-dashed lines indicate the hadronic channels for which we took the parametrization and fit from [19], while the dotted lines indicate channels we have fitted and included here for the first time. The solid lines indicate the total $R_\mu^{\mathcal{H}}$ (summed over all hadronic final states) considering: only the channels shown in figure 2.2 (cyan), only the new channels on table 2.2 (purple), the sum of all contributions we have calculated (orange).

2.3 Final vector meson decomposition

During the hadronic width calculation procedure it was crucial the division of the hadronic current into ρ, ω and ϕ contributions, as given by eq. (2.11). In this same equation, when we re-scale the quark couplings by the ratio of the traces, the model dependent quark matrix Q^f determines if a certain vector meson contribution is present or absent, the latter happening if the trace is zero $\left(\mathrm{Tr}\left[T_V Q^f\right] = 0\right)$.

Figure 2.7 shows the R_μ-ratio decomposed into ρ- (blue), ω- (red) and ϕ-like (green) contributions, considering the sum of all hadronic channels included in this dissertation. The solid lines represent our results while the dashed ones are from DARKCAST. The orange line correspond to the sum of all contributions, which is therefore a γ-like curve, since the photon mixes with all vector mesons, according to the VMD prescription. In the ideal case, we expect that this curve would follow the PDG data points [2].

Let us now analyse the results of figure 2.7. The first two features that call attention are that our ϕ-like curve is lower than the DARKCAST one in the energy range between $(1.1-1.7)$ GeV,

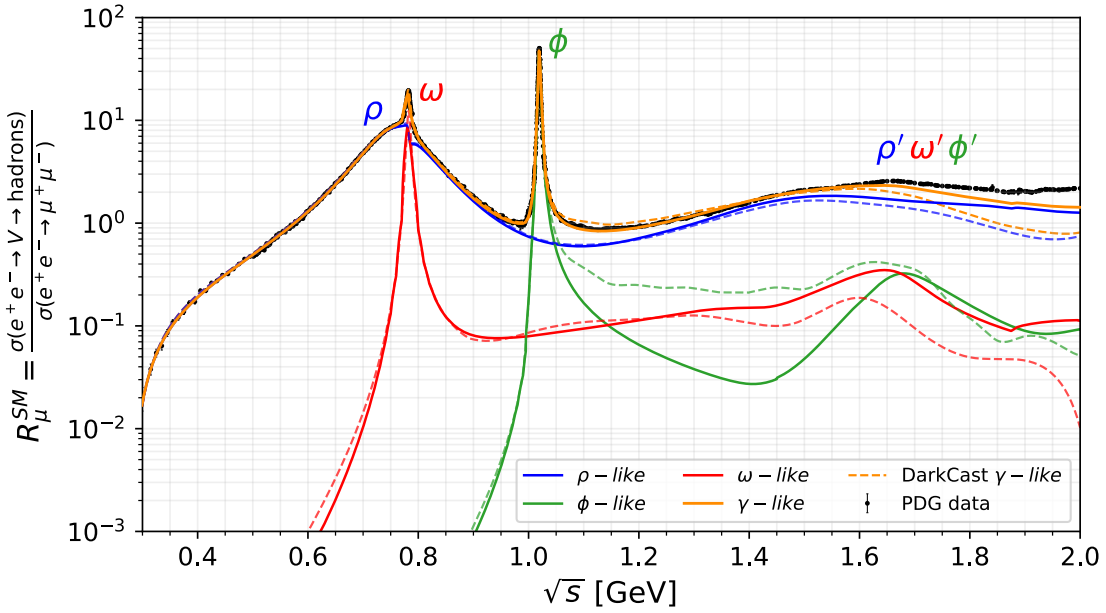

Figure 2.7: Decomposition of the total hadronic cross-section ratio $R_\mu^{\text{SM}} \equiv \sum_{\mathcal{H}} R_\mu^{\mathcal{H}}$ into ρ-, ω- and ϕ-like contributions for the SM. We also show in orange the total γ-like contribution. The dashed lines indicate results obtained with the DARKCAST code [1].

while our ω-like contribution is higher for energies above $\sim 1.3\,\text{GeV}$. This attribute is a consequence of the differences we highlighted before in the KK and $KK\pi$ channels description, since in DARKCAST they assigned these two channels as a ϕ contribution, while we identified ρ and ω components. Hence they end up with an overestimation of the ϕ-like contribution and an underestimation of the others.

The second comment we want to address is that we lift up all the curves for energies above $1.7\,\text{GeV}$. This is an effect of the inclusion of the new channels of table 2.2, that are responsible for the difference we see in the extent of the two orange lines. While in DARKCAST they cannot follow the PDG data points after $\sim 1.6\,\text{GeV}$, in our case the major deviation starts close to $\sim 1.8\,\text{GeV}$. Hence, our hadronic width calculation strategy and the inclusion of new channels and recent data resulted in a better description of the data. Another interesting point is the deviation on the ω-like curve for energies below $\sim 0.7\,\text{GeV}$. This discrepancy comes from the differences in the description of the $\pi\gamma$ mode, and, although small, will have great impact on the B model branching ratios and limits, as we will see next.

A final remark we want to stress again is the importance of the correct vector meson decomposition. Remember that for vector mediator models that do not couple with the ρ current, which correspond to all the baryophilic models considered in this dissertation, and listed in table 1.1, only the ω- and ϕ-like components will matter. This means that the differences we

obtained in comparison with DARKCAST will result in different branching ratios and sometimes even affect model bounds.

2.3.1 Hadron-quark transition

Even though we exhaustively included all the dominant exclusive hadronic modes described in the literature, as listed in PDG [2], for higher masses than $\sim 1.7\,\mathrm{GeV}$ we slightly underestimate the e^+e^- total hadronic cross-section, given by the black points in figure 2.7. The problem is that in this higher energy region several subdominant multi-meson channels start to appear, most of them do not even have experimental description in the literature. Although any possible new channel could be easily added in our approach, the lack of data for these multi-meson processes, combined to the fact that in many modes we still do not have a complete description of the substructures, results in the decline of the $\gamma-$like curve near $2\,\mathrm{GeV}$. Nevertheless, close to this energy we expect that the hadronic decay width slowly transition into perturbative decays into quarks, as described in section 1.3.3.

In order to include a correct and smooth transition, we calculated the intersection point between the hadronic and perturbative quark widths. For the case of the *dark photon* model, this energy point happens at $1.7\,\mathrm{GeV}$, while in the B-coupled models it happens at $1.74\,\mathrm{GeV}$. In the decay calculation, we then directly replaced the hadronic decay width $\Gamma(Z_Q \to \mathrm{hadrons})$ with the total perturbative decay $\Gamma(Z_Q \to \mathrm{quarks})$, given by eq. (1.53), at the corresponding energy thresholds for each model. For instance, in the *dark photon* model this hadron-quark transition represents the replacement of the γ-like curve in figure 2.7 by a perturbative line $R_\mu^{\mathcal{H}} \simeq 2$ [2] at the energy of $1.7\,\mathrm{GeV}$.

In the case of the DARKCAST code, due to the inclusion of a small number of hadronic channels in [1], the authors employed a different strategy to reach the total R_μ^{SM} curve. First, they considered their γ-like contribution as the PDG experimental curve for energies above $1.48\,\mathrm{GeV}$, and the sum of the vector meson curves for energies below this value. The ω-like curve was considered to be their calculation below $1.6\,\mathrm{GeV}$ and the perturbative value $R_\mu^\omega = N_c \cdot (q_u + q_d)^2/2 = 1/6$ above this energy [3]. Similarly, the ϕ-like curve was taken to be equal to $R_\mu^\phi = N_c \cdot (q_s)^2 = 1/3$ above $1.7\,\mathrm{GeV}$. Finally, they define their ρ-like component to be described by the 2π and 4π channels below $1.1\,\mathrm{GeV}$ and equal to the γ-like curve, with the ω and ϕ contributions subtracted, above it. Note that they always use the leading order perturbative value, hence they do not take into account QCD corrections.

[2] It would be exactly $R_\mu^{\mathcal{H}} = 2$ if we did not consider the QCD corrections δ_{QCD} of eq. (1.53).

[3] Recall that the leading order perturbative $R_\mu^{\mathrm{em}} = R_\mu^\rho + R_\mu^\omega + R_\mu^\phi = \frac{3}{2} + \frac{1}{6} + \frac{1}{3} = 2$, where the vector meson components can be calculated according to eq. (A.24).

Although they justify the method above by recognizing that they neglect several hadronic channels, such that it would be necessary to use the PDG data points to include the missing modes, their approximation imply the wrong assumption that all these modes contribute as ρ components. This is a very serious premise, specially for baryophilic $U(1)_Q$ models, since they do not couple to the ρ current. Hence, if on the one hand their γ-like curve match the $R_\mu^{\rm SM}$ experimental calculation, on the other hand all the extra hadronic channels they disregard do not contribute to the baryophilic vector mediator width. This will result in significant consequences on the branching ratios and limits, which is the subject of the next chapter.

In this chapter we have described the hadronic implementation we used in order to improve the light mediator Z_Q decays into hadrons. In the next chapter we will analyze how this hadronic improvement will affect the new mediator width, branching ratios and also experimental bounds.

Chapter 3

Results and Effects on Experimental Bounds

In the last chapter, we focused on the description of the VMD-based method that was used for the calculation of the dark mediator Z_Q hadronic decay width. We compared this method with the previous implementation by [1], that is provided in the paper companion software package DARKCAST. Besides the fact that in our method we explicitly calculate the hadronic width of each channel, and hence took into account all interference terms, we also included several new channels, and updated the previous modes by the inclusion of recent cross-section data and a better decomposition into ρ, ω and ϕ contributions, which is crucial for the correct $U(1)_Q$ boson width determination. As in the case of [1], we provide a numerical package to calculate decay quantities of light vector particles, that can be found at https://github.com/preimitz/DeLiVeR [70].

All these improvements in the hadronic description lead to substantial effects in the calculation of the new light mediator hadronic width, which in turn affects the Z_Q branching ratios into hadrons and leptons and can also modify experimental bounds. This last point is justified since the majority of the available detectors that we employ for dark sector investigation depend on decays into electrons and/or muons. This means that in the calculation of the number of observable events the leptonic branching ratios are a key ingredient. Another important factor is the total decay width of the dark particle. Especially for beam dump experiments, where the particles propagate for a certain distance before reaching the detector, the Z_Q lifetime, together with its mass and the model coupling, will determine if the light mediator will decay inside the detector and, hence, produce an observable signal.

Therefore, in summary, the hadronic width modifications we implemented have a great impact on the leptonic branching ratios and lifetimes, which in turn can influence the model bounds. How exactly the branching ratios and bounds will be affected is the subject of this chapter, which is organized in the following way. In the first section we show the modifications

in the total hadronic decay width for the *dark photon* and baryophilic models (see table 1.1). The second section presents the effect on the Z_Q vector mediator branching ratios. Finally, in the third section, we elaborate on the impact that the hadronic decay width reevaluation generates on the experimental bounds, considering first current limits and then future predictions.

3.1 Hadronic Decay Width

Figure 3.1 shows the total hadronic decay width, normalized by the vector boson mass m_{Z_Q} and coupling g_Q, for the case of the *dark photon* model (blue) and baryophilic models (red) listed in table 1.1. As usual, the solid curve stands for the total hadronic width from this dissertation, which was calculated by the direct sum of all the individual channels widths $\sum_{\mathcal{H}} \Gamma(Z_Q \to \mathcal{H})$, while the dashed one represents DARKCAST calculation given by eq. (2.3). Near $1.7\,\mathrm{GeV}$, the solid colored curves split into two, which indicates the hadron-quark transition described in section 2.3.1. The grey lines correspond to the prolongation of the hadronic width calculation for the corresponding model and the color lines stand for the perturbative quark width given in eq. (1.53). Let us now enumerate the main differences that appear in the figure when comparing our results with DARKCAST ones.

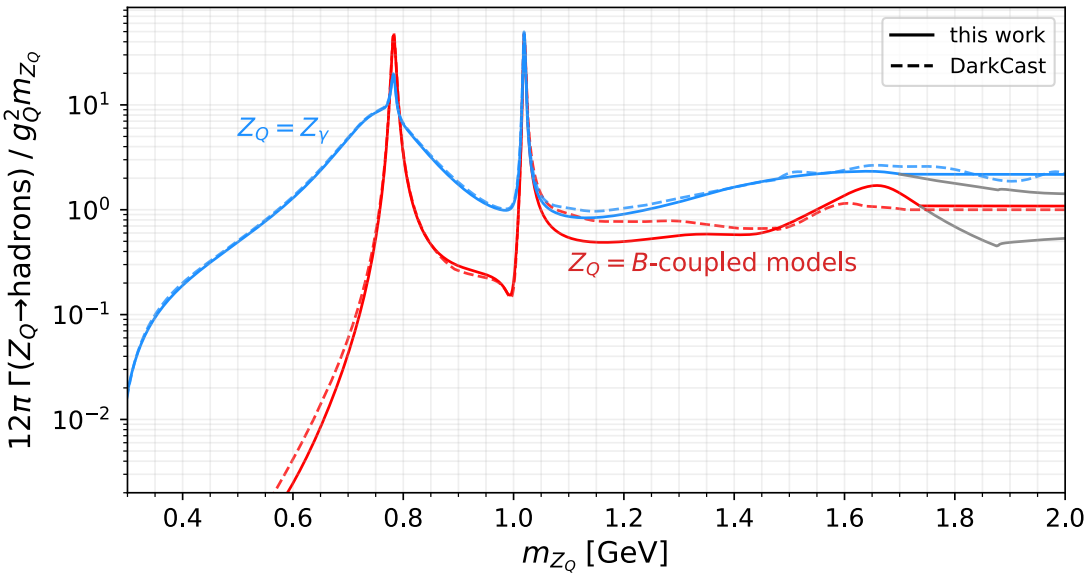

Figure 3.1: Normalized light vector mediator hadronic decay width for the *dark photon* (blue) and B-coupled (red) models. The solid (dashed) curve indicates the results from this dissertation (DARKCAST). The grey curves at higher energies indicate the hadron-quark transition, which happens at $m_{Z_Q} = 1.7\,\mathrm{GeV}$ ($m_{Z_Q} = 1.74\,\mathrm{GeV}$) in the *dark photon* (B-coupled) model.

B-coupled models

- The discrepancies that appear at energies below $0.7\,\mathrm{GeV}$ come from the difference in the calculation of the $\mathcal{H} = \pi\gamma$ channel.

- Between $m_{Z_Q} = (1.1 - 1.5)\,\mathrm{GeV}$, DARKCAST overestimates the hadronic width due to the incorrect exclusive assignment of the KK and $KK\pi$ channels as ϕ-like contributions, while in our description we also included ρ-like components. Thus, as the ρ current does not couple to baryophilic models, in our approach these two channels do not entirely enter in the baryophilic mediator width calculation.

- For energies above $m_{Z_Q} = 1.5\,\mathrm{GeV}$, DARKCAST underestimates the hadronic width due to the absence of several hadronic modes, while in our case we included all the channels listed in table 2.2, many of them contributing with ϕ- and ω- like components. Besides, as described in section 2.3.1, in DARKCAST they considered all the neglected hadronic contributions as ρ-like components, that do not couple to the baryophilic vector mediators.

- At the hadron-quark transition point, we can see that our curve is slightly higher than DARKCAST one. This is a result of our inclusion of QCD corrections in the perturbative quark width given by eq. (1.53).

***Dark photon* model**

- Between $m_{Z_\gamma} = (1.1 - 1.3)\,\mathrm{GeV}$ we can see that DARKCAST width curve is slightly higher than ours. This is a consequence of the misleading assumption that $KK = 2 \cdot K^+K^-$, as we have shown in figure 2.4 the neutral contribution has a smaller cross-section than the charged one. This behavior also appears in the orange dashed curve of figure 2.7 in this same energy region.

- Above the hadron-quark transition, our width calculation transforms into a perturbative quark straight line while in DARKCAST we still see some features. Recall that in DARKCAST calculation they considered their R_μ^ρ curve as being the hadronic ρ-like contribution below $1.1\,\mathrm{GeV}$ and the PDG experimental curve above this energy. As the *dark photon* couples to the ρ current, its width follows the PDG data curve for higher energies. However, although this approach seems to work well, we need to be careful since this method is only a good choice for models that have couplings proportional to the SM photon couplings, which is the case of the *dark photon*. The explanation is that, as stated by eq. (1.45), the *dark photon* hadronic width can be obtained by merely re-scaling the R_μ^{SM} total ratio. Hence, for the specific case of the *dark photon*, we do not need to individually

separate the ρ, ω, ϕ contributions and proceed with the VMD approach, we can just use the PDG data curve [2]. Nevertheless, this is not the case for baryophilic models, or for any model that does not enjoy SM proportional couplings.

3.2 Branching Ratios

With the hadronic and perturbative quark width calculation, it is easy to obtain the branching ratio

$$\mathrm{Br}(Z_Q \to \mathcal{F}) = \frac{\Gamma(Z_Q \to \mathcal{F})}{\Gamma^{\mathrm{tot}}_{Z_Q}} ,$$

where $\mathcal{F}$ represents any hadronic or leptonic channel, $\Gamma^{\mathrm{tot}}_{Z_Q}$ is the total decay width, considering all possible final states, and we use eq. (1.43) to calculate the leptonic decay widths.

In figure 3.2 we show the branching ratios considering the dark vector mediator decay into electrons (light blue), muons (dark blue), hadrons (red) and neutrinos (green) as a function of the vector boson mass and for different $U(1)_Q$ models. The results obtained with the hadronic calculation implemented in this dissertation are shown in solid lines while the results from DarkCast are in dashed lines. In the lower panel of each figure we show the deviation $\Delta\mathrm{Br}$ that is equal to this dissertation branching ratio calculation minus DarkCast one

$$\Delta\mathrm{Br} \equiv \mathrm{Br}^{\mathrm{our}} - \mathrm{Br}^{\mathrm{DarkCast}} ,$$

i.e. it is the subtraction of the dashed lines from the solid ones. The grey vertical dashed line indicates the energy of the hadron-quark transition.

From the figure we can see that, in the case of the *dark photon* model, the differences between the two calculations are always less than 5%. In contrast, for the case of the B model, we see that in the window $0.2 \lesssim m_{Z_B}/\mathrm{GeV} \lesssim 0.4$, the discrepancy in the calculation can be as large as $\sim 30\%$. This is a consequence of the disparities we saw on the $\mathcal{H} = \pi\gamma$ channel description. As we will discuss latter, in the B model the couplings to leptons arise from kinetic mixing loop corrections, and thus are very suppressed in comparison with the couplings to hadrons. Hence, the leptonic branching ratio only is dominant in the kinetically forbidden hadronic region, but when we reach the pion mass threshold the first channel that appears is $\pi\gamma$, and it is the only mode until $m_{Z_Q} \sim 2\, m_\pi$. This is the reason why small modifications on the $\pi\gamma$ channel can lead to major effects on the B model. For energies above $0.3\,\mathrm{GeV}$, the hadrons always dominate, and therefore, although the width calculation has numerical differences, the branching ratio into hadrons is always 100%. Note, however, that the width differences imply modification of the Z_Q lifetime, which in turn can affect the bounds, as we will see.

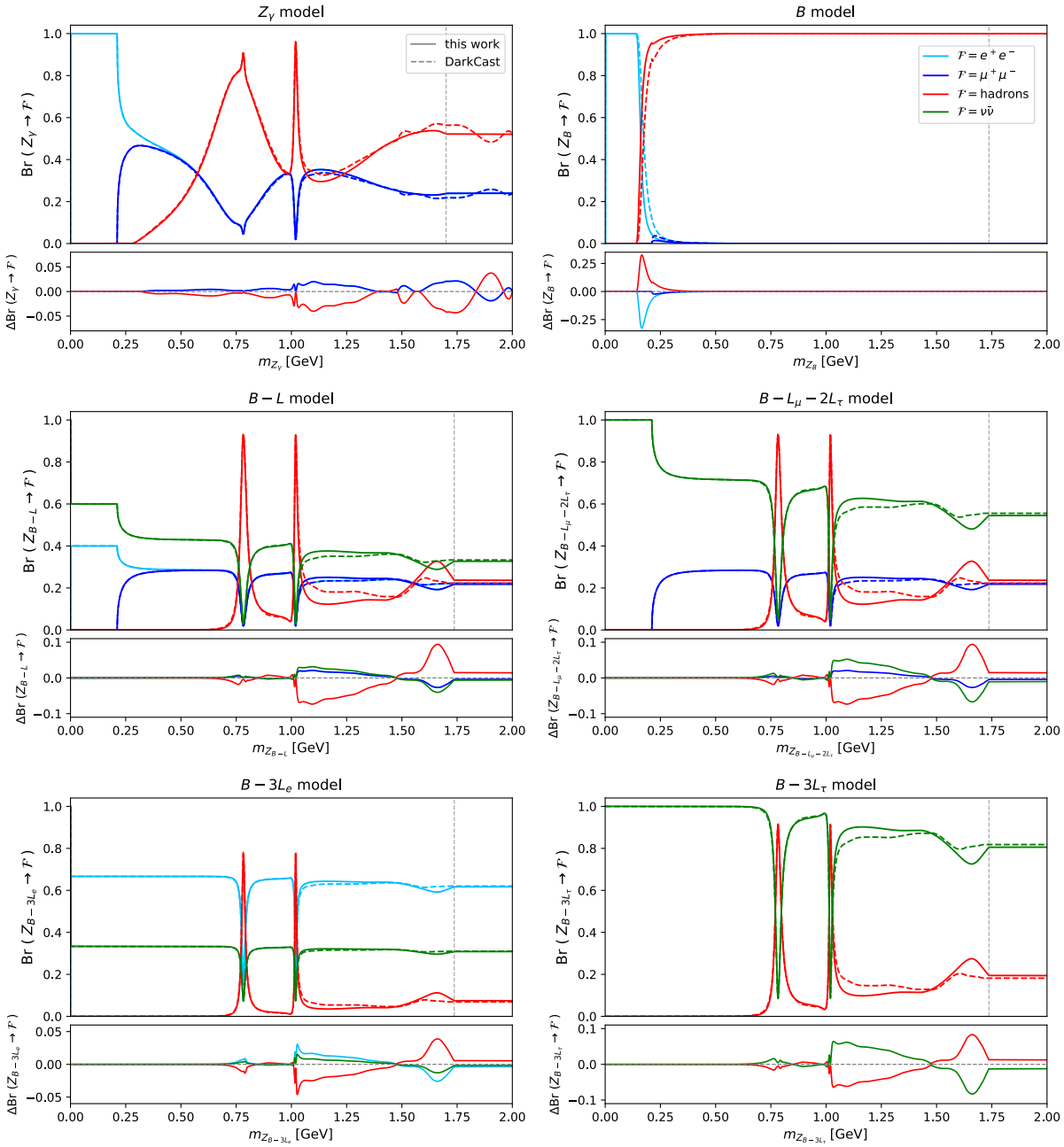

Figure 3.2: Branching ratio of the vector boson mediator Z_Q decaying into electrons (light blue), muons (dark blue), hadrons (red) and neutrinos (green). Each panel represents a specific $U(1)_Q$ model, as the title label indicate. The solid (dashed) lines correspond to this dissertation (DARKCAST) results. In the lower panel of each figure we show the branching ratio difference between the two calculations.

For the other baryophilic models shown in the figure, *i.e.* the $B-L$, $B-L_\mu-2L_\tau$, $B-3L_e$ and $B-3L_\tau$ models, the branching ratio deviation is always at most a 10% effect. The deviations follow the same conclusions from last section; DARKCAST overestimated (underestimated)

the hadronic width in the window $m_{Z_Q} \sim (1.0 - 1.5)\,\mathrm{GeV}$ (above $m_{Z_Q} = 1.5\,\mathrm{GeV}$) as a consequence of the KK and $KK\pi$ modes (new hadronic contributions). We do not show the branching ratios for the $B - 3L_\mu$ and $B - L_e - 2L_\tau$ models since they are similar to $B - 3L_e$ and $B - L_\mu - 2L_\tau$, respectively. A final remark is that the compensation of the hadronic Br numerical modification is split into the leptonic contributions, such that, for example, if we have a $\sim 10\%$ modification on the hadronic branching ratio of the $B - 3L_e$ model, this will effect by $\sim 5\%$ the e^+e^- and $\nu\bar{\nu}$ branching ratios.

Figure 3.3 illustrates the branching ratio modifications of the individual hadronic channels for the B model (left panel) and $B - L$ model (right panel) [1]. The solid and dashed lines indicate this dissertation and DARKCAST results, respectively. The blue line correspond to the sum of all the other hadronic channels not listed in the figure legend. The vertical grey dashed line represents the hadron-quark transition, from which our individual hadronic contributions disappear and are replaced by the perturbative quark contribution. In DARKCAST they do not consider the quark transition, instead, the individual hadronic widths continue growing to account for the u, d, s quark contribution, while the other quark widths are included separately using eq. (1.43) after the respective mass thresholds.

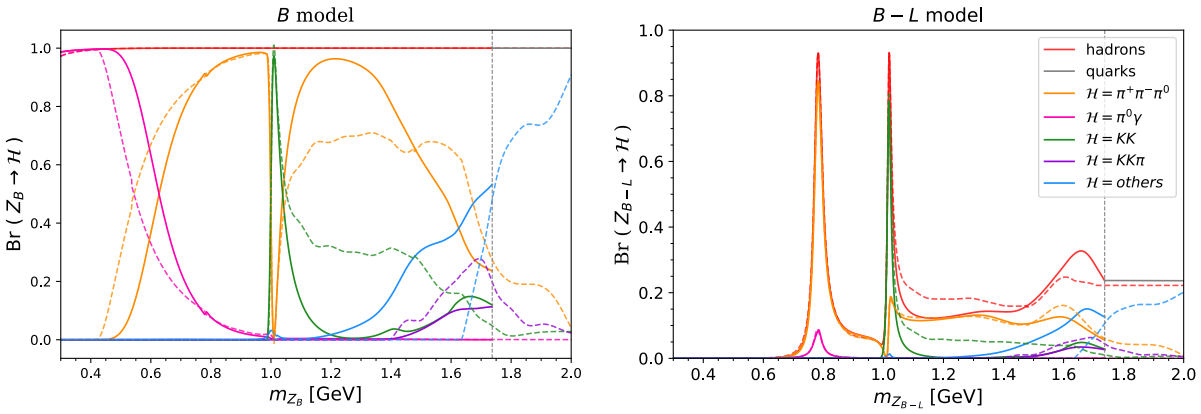

Figure 3.3: Comparison between this dissertation (solid lines) and DARKCAST (dashed lines) individual hadronic branching ratios for the B model (left panel) and $B - L$ model (right panel). We do not show the individual branching ratios for the other B-coupled models, as they behave in a similar way to the $B - L$ model. The vertical dashed gray line indicates the transition from non-perturbative to perturbative calculations as described in the text.

[1] The individual branching ratios for the other baryophilic models are similar to the $B - L$ ones.

3.3 Repercussions on Current Limits and Future Sensitivities

Now that we already distinguished the branching ratio modifications produced by our hadronic implementation, we can explore the effects on the bounds for the different $U(1)_Q$ models in the relevant mass range $100\,\mathrm{MeV} \leq m_{Z_Q} \leq 2\,\mathrm{GeV}$ studied here. In the next two sections we will discuss these effects for the current available experimental bounds and then for the predictions of future experiments and detector upgrades. To obtain these limits, we implemented our hadronic branching ratios in two different software packages, that we describe below.

The first software is the DARKCAST code [1], that was already discussed in previous sections when we compared the hadronic implementation. However, besides the width calculation, this code can also recast *dark photon* searches into generic $U(1)_Q$ model bounds. The recast procedure works in the following way; first one needs to obtain the bound values in the parameter space of the *dark photon* model, *i.e.* the limits on the kinetic mixing vs. mass plane $\epsilon \times m_{Z_\gamma}$; then we can recast these values by re-scaling the dark mediator production, decays and the detector efficiency, as explained in [1]. Therefore, in order to identify the effects on the bounds, we included in DARKCAST our hadronic width calculation, which in turn modified both the decays and the detector efficiency, the latter through the change in the Z_Q lifetime.

The second software we used was the FORESEE (FORward Experiment SEnsitivity Estimator) code [143]. This program can simulate the expected sensitivity reach of experiments placed in the far-forward direction from the interaction point of proton-proton collisions. In particular this code is very useful for predicting FASER (ForwArd Search ExpeRiment) [144–147] sensitivities, and this was exactly the reason why we employed it here.

3.3.1 Current Limits

Table 3.1 shows the experimental searches we considered in the bound plots to constraint the $g_Q \times m_{Z_Q}$ plane for the different $U(1)_Q$ models. In the table we specify each experiment type, the production channel of the dark mediator and the subsequent decay mode.

In all bound plots displayed here, the constraints in blue (green) represent exclusion regions for Z_Q decaying to e^+e^- and $\mu^+\mu^-$ pairs (neutrinos). We start by the current experimental limits we obtained for the B-model, which are shown in figure 3.4. Although this model is not anomaly-free, due to the great differences present in its branching ratios, the bounds highlight the consequences of the improvements of our calculations. We show in gray the regions that were excluded before with DARKCAST hadronic implementation, but are allowed by this dissertation. In the energy region between $0.2 \lesssim m_{Z_B}/\mathrm{GeV} \lesssim 0.4$, we verify that this effect is particularly visible, which is a consequence of DARKCAST underestimation of the $\pi^0\gamma$

Experiment		Z_Q production	Z_Q decay
Fixed Target (electronic)	APEX [20]	e-Bremsstrahlung	$Z_Q \to e^+e^-$
	A1 [21, 22]		$Z_Q \to e^+e^-$
	NA64 [41–43]		$Z_Q \to \nu\bar{\nu}$ (invisible)
Proton Beam Dumps	LSND [27, 28]	$\pi^0 \to \gamma Z_Q$	$Z_Q \to e^+e^-$
	PS191 [23]	$\pi^0 \to \gamma Z_Q$	
	NuCal [25]	$\pi^0 \to \gamma Z_Q$ p-Bremsstrahlung	
	CHARM [26]	$\eta \to \gamma Z_Q$	
Electron Beam Dump	E137 [29, 30]	e-Bremsstrahlung	$Z_Q \to e^+e^-$
e^+e^- Colliders	BaBar [31, 39]	$e^+e^- \to \gamma Z_Q$ (radiative return)	$Z_Q \to e^+e^-,\ \mu^+\mu^-$ $Z_Q \to \nu\bar{\nu}$ (invisible)
	BESIII [44]		$Z_Q \to e^+e^-,\ \mu^+\mu^-$
	KLOE [32, 33, 37, 38]	$e^+e^- \to \gamma Z_Q$ $\phi \to \eta Z_Q$	$Z_Q \to e^+e^-,\ \mu^+\mu^-$
Hadron Collider	LHCb [34, 35]	Meson decays Drell-Yan mechanism	$Z_Q \to \mu^+\mu^-$ (displaced or prompt)
Kaon Decay Experiments	NA48/2 [36]	$\pi^0 \to \gamma Z_Q$	$Z_Q \to e^+e^-$
	NA62 [40]		$Z_Q \to \nu\bar{\nu}$ (invisible)

Table 3.1: Current experimental searches used to constraint the dark mediator models in the relevant mass range from $(0.1 - 2.0)\,\mathrm{GeV}$. In the table we list the production channel and the decay mode of each particular search.

contribution, that implies an enhancement of the $Z_B \to e^+e^-$ signal prediction.

In this same figure, we also have regions where our bounds are more excluding. For instance, we highlight DARKCAST NuCal bound contour with a dashed grey line. We can see that our NuCal limit is more constraining. This is a result of the differences in the mediator lifetime, which is more prominent for the B model and is particularly important in beam dump experiments, due to the considerable propagation of the dark boson. Therefore, as we saw before, although the B model branching ratios are equivalent for masses above $0.4\,\mathrm{GeV}$, if our hadronic width is numerically larger, this will result in a smaller lifetime. Hence, if for a particular mass and coupling, the Z_B boson was decaying outside the detector, now it can decay inside, which increases the bound.

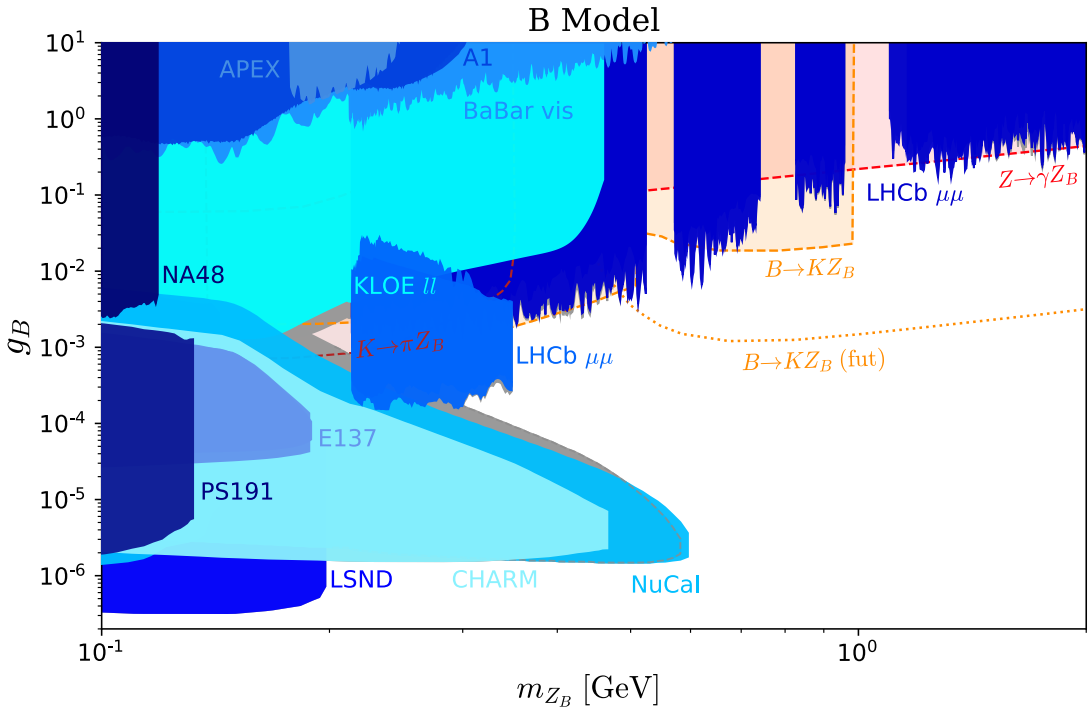

Figure 3.4: The excluded regions in blue show the bounds on the $g_B \times m_{Z_B}$ parameter space for e^+e^- and $\mu^+\mu^-$ decay signatures considering the following experimental searches: the electron fixed target experiments APEX [20] and A1 [21, 22], the proton beam dump experiments PS191 [23], NuCal [24, 25], CHARM [26] and LSND [27, 28], the electron beam dump experiment E137 [29, 30], the e^+e^- colliders BaBar [31] and KLOE [32, 33], the LHCb experiment [34, 35] and the kaon decay experiment NA48 [36]. The grey region indicate the previous bounds from DARKCAST that are still allowed in this dissertation. The dashed lines represent the current limits from $B \to KZ_B$, $K \to \pi Z_B$ and $Z \to \gamma Z_B$ decays, while the dotted orange curve is the future reach of the $B \to KZ_B$ decay search.

We also include in figure 3.4 the limits from the meson decays $B \to K Z_B$ (orange) and $K^{\pm} \to \pi^{\pm} Z_B$ (maroon) and also for the Z boson decay $Z \to \gamma Z_B$ (red), that were extracted from [148, 149]. The dashed lines represent current constraint while the dotted one is a future prediction. It is important to mention that these constraints are enhanced for light vector coupled to non-conserved currents, which is the case of the anomalous B model.

Besides the fact that the B model is anomalous, there is another caveat we need to emphasize. All the experimental searches we used for this model rely on e^+e^- and/or $\mu^+\mu^-$ decay signatures. However, the $U(1)_B$ model does not have direct coupling to leptons. Instead the leptonic coupling is generated via a one-loop induced kinetic mixing between Z_B and the photon, and hence, the magnitude of the coupling to leptons depends on the choice of the renormalization scale and cannot be determined unambiguously. In this dissertation we follow DARKCAST conventions, so we considered the Z_B coupling to leptons to be simply $e g_B/(4\pi)^2$ [94]. Thus, when analyzing limits of the Z_B boson to charged leptons we need to be careful and remember this choice.

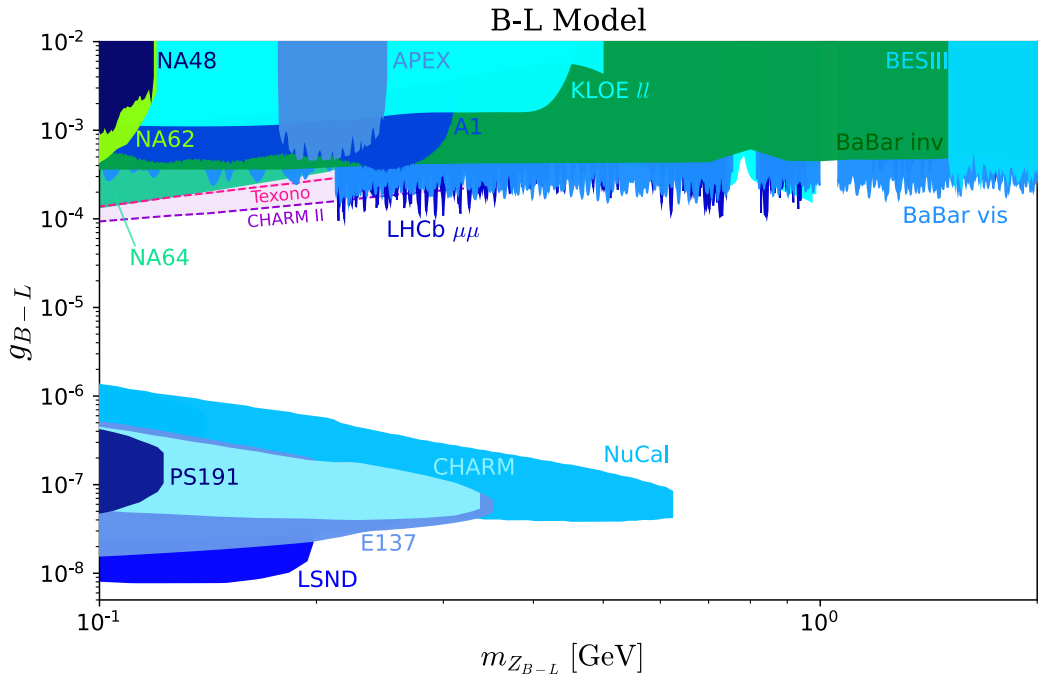

Figure 3.5: Similar to figure 3.4, but for the $B - L$ model. Due to the coupling with neutrinos, in green we add the excluded regions from the invisible searches of the following experiments: KLOE in the $\mu^+\mu^-$ final state [37, 38], BaBar [39], NA62 [40] and NA64 [41–43]. We also include the bound from the e^+e^- collider BESIII [44]. The red and purple dashed lines indicate the limits from the neutrino experiments Texono [45–47] and CHARM-II [46–48] that were extracted from [28].

Apart from the B model, we also compute the bounds for the other baryophilic models. Although the modifications that our hadronic implementation introduced for these models are not sizeable enough to be visible in a plot with several orders of magnitude, they will affect the sensitivity of future experiments as we will see shortly. Despite that, we decided to also show some of the bounds, since these models are very relevant in the literature and we have some recent data from LHCb, NA62 and NA64.

In figure 3.5 we show the bounds for the $B - L$ model. Due to the Z_{B-L} coupling to neutrinos, we also have in the plot bounds from invisible searches, that are the green exclusion regions. We also included, for completeness, the limits from the neutrino experiments Texono [45–47] and CHARM-II [46–48] that were taken from [28]. Note that these neutrino limits come from searches that consider neutrino trident production (CHARM-II) and neutrino-electron scattering (Texono), hence they do not depend on leptonic decays, implying that they are independent of the hadronic branching ratios and cannot be recasted. The limit from the Borexino [150–152] neutrino experiment is omitted from the plot since NA64 and CHARM-II bounds cover it in the mass range considered in this study.

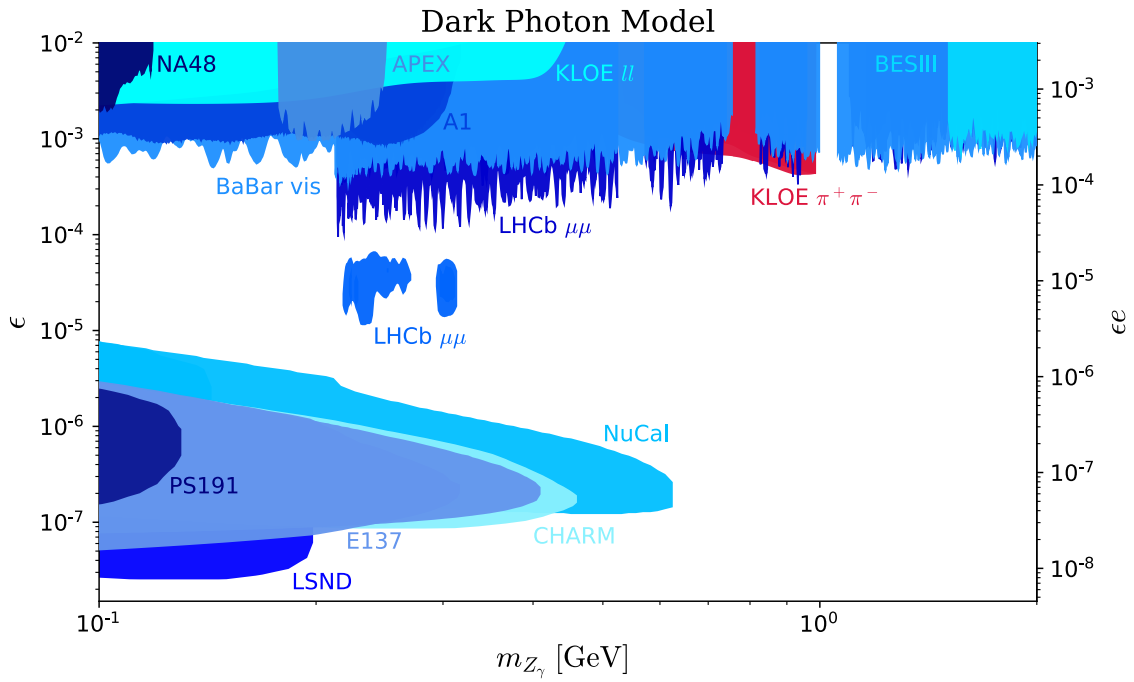

Figure 3.6: The excluded regions in blue show the bounds on the $\epsilon \times m_{Z_\gamma}$ parameter space for e^+e^- and $\mu^+\mu^-$ decay signatures considering the same experimental searches as figure 3.4, plus the bound from the e^+e^- collider BESIII [44]. We also show in red a bound of the e^+e^- collider KLOE coming from a search that considered *dark photon* decays into $\pi^+\pi^-$.

Figure 3.6 shows the experimental bounds of the secluded *dark photon* model in the parameter space that constraints the KM parameter ϵ and the mass of the *dark photon* m_{Z_γ}. Since the *dark photon* does not couple to neutrinos, we do not have any invisible search. Note also, that the KLOE bound from a search of $\pi^+\pi^-$ decay signature is not present in any other baryophilic model bound plot, since the $\pi^+\pi^-$ channel is entirely described by a ρ resonance, that does not couple to such models.

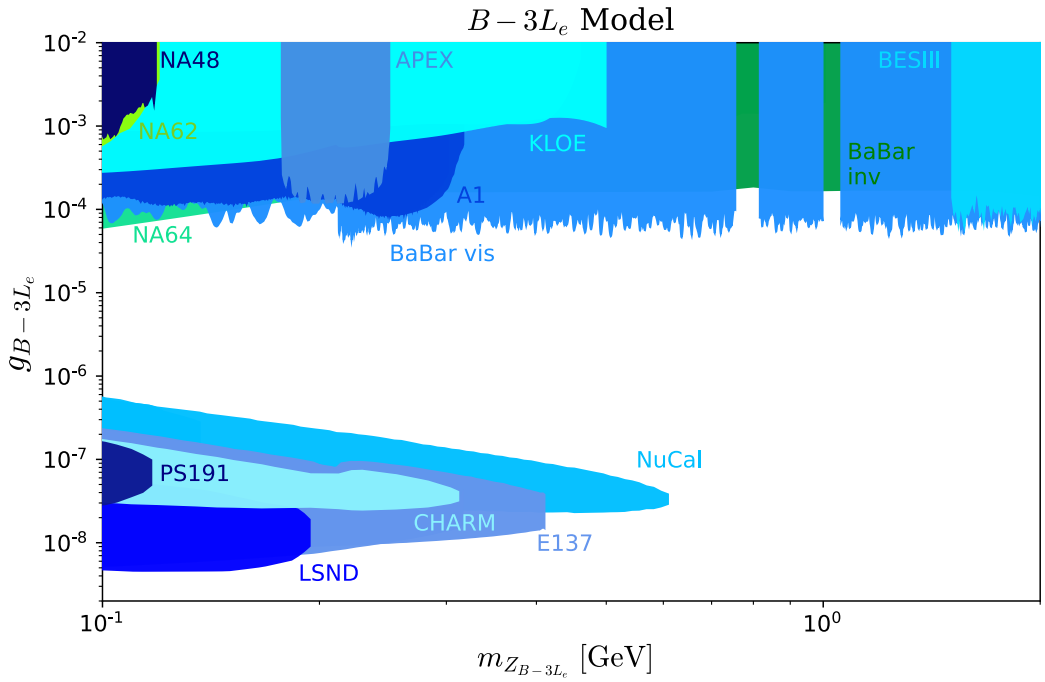

Figure 3.7: Same as figure 3.5, but for the $B-3L_e$ model. Due to the absence of couplings with muons we do not have the constraints from the LHCb experiment and the e^+e^- collider KLOE in the $\mu^+\mu^-$ final state.

Finally, in figures 3.7 and 3.8 we show the bounds for the $B-3L_e$ and $B-L_e-2L_\tau$ models. Since the mediator of these models does not couple to muons, the constraints from LHCb and KLOE in the $\mu^+\mu^-$ final state are absent. We do not display the limits for the $B-3L_\mu$, $B-L_\mu-2L_\tau$ and $B-3L_\tau$ models since the first two only have bounds from LHCb (prompt), NA62 and Belle-II, while the last one only has NA62 limits. Although we omit them here, we refer to [153] for a comprehensive analysis of $B-3L_i$ models.

A final remark we want to make is that, although all experimental searches reported in this dissertation depend on leptonic decay signatures, except from the $\pi^+\pi^-$ KLOE bound showed in red in figure 3.6, hadronic decays could also be probed in other searches (see, *e.g.*, Ref. [154]). This is the case of the future FASER detector [87], as we will see in the next section.

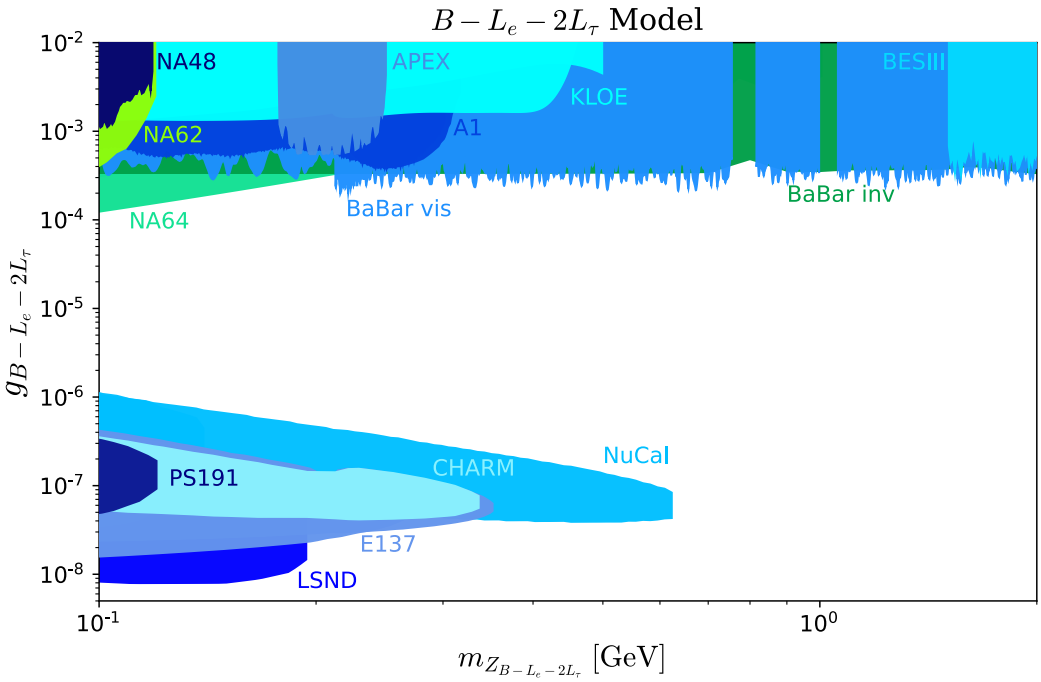

Figure 3.8: Same as figure 3.7, but for the $B - L_e - 2L_\tau$ model.

3.3.2 Future Experimental Sensitivities

In the last section we discussed the bounds obtained using our hadronic implementation with real data from current experimental searches. Now, we will address the predictions for the sensitivities of several high intensity frontier experiments that can probe dark light mediators in the near future.

The first experiment we want to tackle is the ForwArd Search ExpeRiment (FASER) [144–147]. Located approximately 480 m downstream from the interaction point of the ATLAS detector, FASER is a relatively small cylindrical detector whose proposal is the search for new light and weakly coupled long lived particles. The location was specially chosen so the detector could benefit from the LHC luminosity and highly collimated beam. In the experiment schedule, two phases are proposed. In the first one, which we call FASER, the detector dimensions are planned to be 1.5 m long with a diameter of 20 cm and the operation is planned to start during LHC Run 3 in 2022. In the second phase, denoted as FASER 2, the detector size will be 5 m long with a diameter of 2 m. The planned schedule is to start operation in the high luminosity LHC era, which will begin near 2027. While we expect an integrated luminosity of 150 fb^{-1} for FASER, in FASER 2 detector this number increases to 3 ab^{-1}.

In the context of $U(1)_Q$ models, long-lived light mediators, produced in the LHC beam

through meson decays, $pp \to Z_\gamma\, pp$ (Bremsstrahlung) and direct production in hard scattering, can reach the FASER detector. Besides the usual leptonic decay signatures, the experiment will also be sensitive to hadronic final states, such as $\mathcal{H} = \pi\gamma$, 3π and KK [87].

Figure 3.9 shows the expected sensitivity of the FASER 2 detector for the B (left panel) and $B - L$ (right panel) models. We separate the constraints according to the Z_B decay signatures by using different colors: $\pi\gamma$ (pink), 3π (orange), KK (green), total hadronic contribution (red) and leptons (blue). The bounds were obtained by using the FORESEE code [143] with our hadronic branching ratios (solid lines) and also with the default configuration that employs DARKCAST branching ratios (dashed lines). In the lower panel of each plot we show the deviation $\Delta\mathrm{Br}$ that, as before, represents the difference between our and DARKCAST branching ratios.

Note that, although the differences between the final sensitive regions are not so strong, the distinct hadronic approach leads to substantial effects in the individual hadronic channels bounds, specially for the B model. Another interesting feature is the spike that appears near $0.8\,\mathrm{GeV}$, which is a consequence of the ω resonance peak.

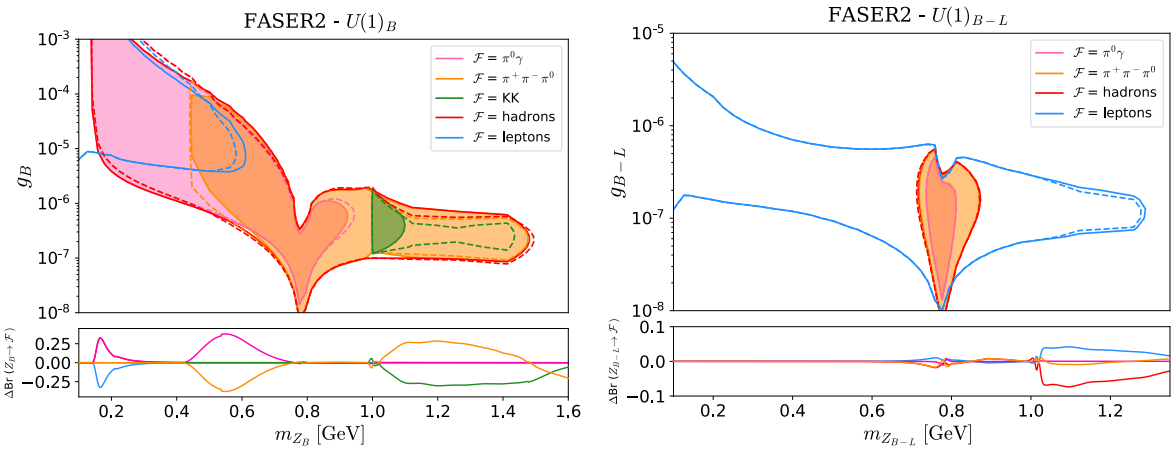

Figure 3.9: FASER 2 forecast for constraints of the B (left panel) and $B - L$ (right panel) models . The solid (dashed) lines indicate the results obtained considering our (DARKCAST) branching ratios together with the FORESEE code. The different colors indicate the decay final states following the conventions from figure 3.3: $\pi\gamma$ (pink), 3π (orange), KK (green), hadrons (red) and leptons (blue). In the lower panels we show the differences between the branching ratio calculations.

The second experiment we will consider here is the proposed SHiP (Search for Hidden Particles) experiment [155]. The SHiP detector is a fixed target facility planned to be installed at the CERN's Super Proton Synchrotron (SPS) 400 GeV proton beam. The experiment goal is exactly the search for hidden sector particles, including *dark photons*, as well as other $U(1)_Q$ vector mediators, in the GeV mass range. The experiment is capable to detect both visible

decays and electron/nuclei scattering signatures through two different instruments, which are the scattering and neutrino detector (SND) and the hidden sector decay spectrometer (HS). Before reaching these detectors, the beam will hit a Molybdenum and Tungsten target and then pass through the hadron absorber and by a system of magnets to sweep muons away. After the SND detector, there is a 50 m long decay volume followed by a tracking system to identify the decay products of the hidden particles. For more details about the experiment configuration, we refer to [156].

In figure 3.10 we display SHiP expected sensitivity for the B (left panel) and $B - L_e - 2L_\tau$ (right panel) models considering proton Bremsstrahlung production followed by $Z_Q \to e^+e^-$ decay. The blue solid bounds (dashed contour) represent the excluded region obtained by using our (DARKCAST) hadronic width calculation in the DARKCAST code for recasting. In the lower panels we show the branching ratio deviation $\Delta\mathrm{Br}$ considering the decay into hadrons (red), electrons (light blue) and neutrinos (green). For the B model, we also show in the right vertical axis the lifetime difference $\delta_\tau = (\tau_{\mathrm{ours}}/\tau_{\mathrm{DarkCast}}) - 1$ represented by an orange line.

With the lifetime evaluation we can appreciate how the differences between our and DARKCAST SHiP exclusion contour follows the same pattern as the lifetime deviation. When the lifetime value in our calculation is smaller, which happens for $m_{Z_B} \lesssim 0.5\,\mathrm{GeV}$, our limits are less stringent since now the Z_B mediator cannot reach anymore the detector for a set of parameter choices $g_B \times m_{Z_B}$. Now, when the lifetime value in our calculation is higher, which happens for $m_{Z_B} \gtrsim 0.5\,\mathrm{GeV}$ according to the figure, we are in the opposite situation, and now our limits are stronger.

In the case of the $B-L_e-2L_\tau$ model, we can see in figure 3.10 that our predicted constraints stop at $m_{Z_B} \sim 1.6\,\mathrm{GeV}$, while in DARKCAST original calculation they end at $m_{Z_B} \sim 1.7\,\mathrm{GeV}$. This is an explicit effect of the inclusion of new channels, as can be seen in the lower panel in the electronic branching ratio difference. Since SHiP rely on e^+e^- signatures, if the hadronic width is larger, the electronic branching ratio will be smaller, which weakens the bound.

Finally, we examine the Belle-II experiment, which is the luminosity upgrade of the B meson factory Belle at the SuperKEKB e^+e^- collider in Japan operating at center of mass energies in the region of the Υ resonances. The detector is sensitive to Z_γ produced via the initial-state radiation (ISR) reaction $e^+e^- \to \gamma_{\mathrm{ISR}}\, Z_\gamma$, followed by the subsequent decay into all kinetically accessible light charged states. The Belle-II upgrade is expected to reach a total integrated luminosity of 50 ab^{-1}. Here, we consider the projected sensitivity of two different searches. The first one is a visible signature search, $Z_\gamma \to e^+e^-, \mu^+\mu^-$, which we recast from figure 211 of ref. [157]. The expected signature of this search is a peak in the distribution of the reconstructed mass of the final lepton pair. Besides the visible final states, Belle-II is also capable

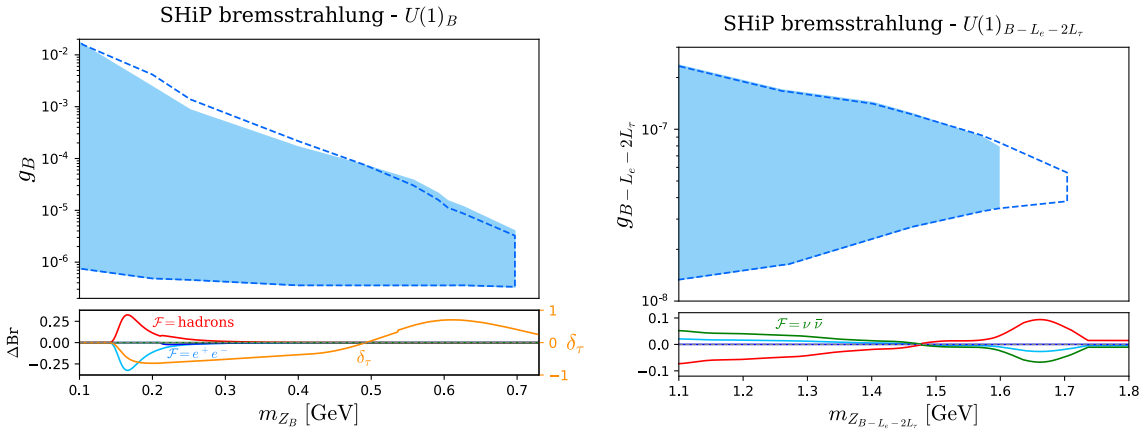

Figure 3.10: Expected reach of the SHiP experiment sensitivity for the B (left panel) and $B-L_e-2L_\tau$ (right panel) models in the Bremsstrahlung production channel. The solid (dashed) lines represent the expected bounds obtained using our (DARKCAST) hadronic implementation. In the lower panel we show the branching ratio deviation and, for the case of the B model, we also show the lifetime difference, as explained in the text.

of searching invisible decays by looking for mono-energetic ISR single photons via the process $e^+e^- \to \gamma_{\rm ISR}\, Z_Q$, $Z_Q \to$ invisible. The projected sensitivity for this invisible decay mode was taken from figure 209 of ref. [157] and recasted for other $U(1)_Q$ models that couple to neutrinos for the purpose of considering the invisible decays $Z_Q \to \nu\bar{\nu}$.

In figure 3.11 we show the predicted sensitivity for Belle-II visible search considering the $B-L$ (top left panel), $B-L_e-2L_\tau$ (top right panel) and $B-3L_e$ (bottom panel) models. In the lower panel we show, as usual, the branching ratio deviation between our and DARKCAST calculations. From the figure, we can see that the same behavior happens in all exposed models, between m_{Z_Q} masses from $1.5\,\mathrm{GeV}$ up to $1.8\,\mathrm{GeV}$ our calculations predict a loss of sensitivity due to the inclusion of the new hadronic modes.

Similarly, we show in figure 3.12 the predicted sensitivity for Belle-II invisible search considering the $B-L$ (left panel) and $B-3L_e$ (right panel) models. The same behavior from the visible search appears here again, for masses between $(1.0-1.5)\,\mathrm{GeV}$ our exclusion region is bigger due to the enhancement of the leptonic branching ratios in comparison to DARKCAST, while for $m_{Z_Q} \gtrsim 1.5$ the opposite happens.

Let us give a brief outlook and summary of the first part of this dissertation. In the first chapter, we have discussed the general theoretical framework of the $U(1)_Q$ gauged group extension of the SM. This extra symmetry introduces a new BSM particle to the SM Lagrangian, that mixes with the hypercharge field through kinetic mixing and can also directly couple to SM fermions. We studied the mechanism of production and decays of such particle, and, in particular, emphasize the difficulties encountered when dealing with hadronic decays. The main

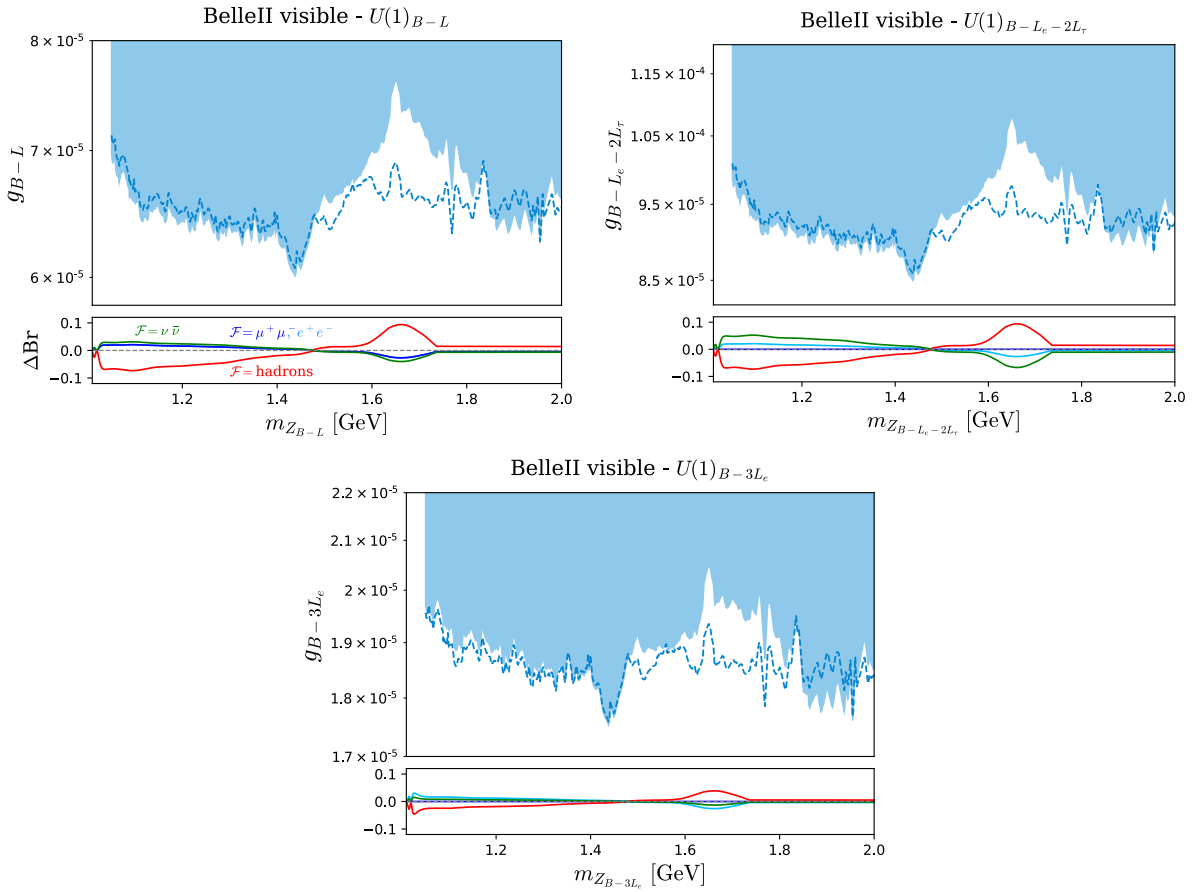

Figure 3.11: Expected sensitivity for the $B-L$ (top left panel), $B-L_e-2L_\tau$ (top right panel) and $B-3L_e$ (bottom panel) models for Belle II visible searches according to our calculation (solid blue) and DARKCAST (dashed lines). In the bottom panels we show for each model the difference of the branching ratio between the two calculations.

purpose of the work develop here was exactly to give a better description of this hadronic decays, which we did by the inclusion of several new channel and data together with the correct VMD-based parametrization and decay width calculation. Finally, we showed the phenomenological consequences of this improved hadronic description by examining the effects on the widths, branching ratios and bound plots. However, as we highlight in the first chapter, although we introduced a mass term to the new light mediator, we did not enter in details about the specific mechanism that generated that mass term. This is exactly the focus of the next part of the work developed in this dissertation.

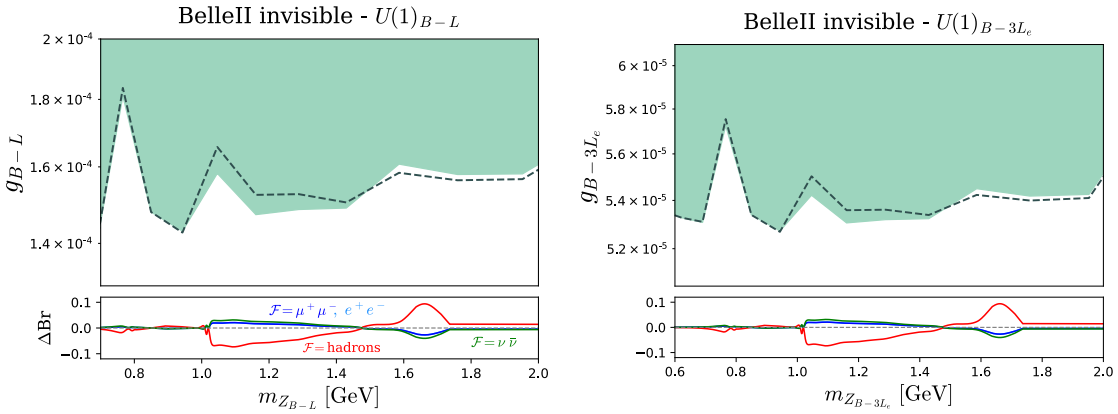

Figure 3.12: Expected sensitivity for the $B-L$ (left panel) and $B-3L_e$ (right panel) models for Belle II invisible searches according to our calculation (solid green) and DARKCAST (dashed lines). In the bottom panels we show for each model the difference of the branching ratio between the two calculations.

Part II

Hidden Abelian Higgs Model (HAHM)

Chapter 4

General Theoretical Framework

In the first part of this dissertation, we provided an overview of the theoretical background of the abelian $U(1)_Q$ gauge extension model. In the theory construction, we explicitly added a mass term to the associated $U(1)_Q$ gauge boson. However, we did not detail the possible mechanisms that could generate that mass term, *i.e.* we did not supply an ultraviolet completion to the $U(1)_Q$ model. In the second part of this dissertation, we will be concerned exactly on studying a possible mass generation mechanism that will complement the $U(1)_Q$ extension.

There are many vector boson mass generation mechanisms reported in the literature, such as, for example, the Stueckelberg Lagrangian [158]. In this dissertation we will focus on an 'Higgs'-like mechanism, where the dark boson mediator will acquire a mass through the spontaneous symmetry breaking of the $U(1)_Q$ group. To this end, we add a new scalar S, which is the responsible for developing a VEV that breaks the $U(1)_Q$ gauge symmetry, and, hence, gives mass to the dark boson. We denote the new scalar by dark Higgs and this mass generation method by the dark Higgs mechanism.

The dark Higgs will couple to the SM sector via a mixing term with the SM-like Higgs boson in the scalar potential. A nice feature of this mechanism is that the new scalar portal, which we call Higgs portal, is also renormalizable and is one of the three possible renormalizable terms that we can include in the SM Lagrangian, the others being the KM portal, addressed in the first part of this dissertation, an the neutrino portal.

Here we will specialize on a scenario where the new mediator is secluded, *i.e.* it is the *dark photon* particle discussed in chapter 1, and the new scalar is a SM singlet that will only couple to the SM sector through the Higgs mixing quartic term in the potential. This model is the well-know Hidden Abelian Higgs Model (HAHM), first introduced by [159] and extensively studied in the literature, in the context of LHC collider searches [51, 160–162] and also in association with dark matter [163–165].

In this first chapter we will introduce the theoretical framework of the HAHM model. In the first section we discuss the scalar sector of the model together with the physics behind the dark Higgs portal. The second section reviews the gauge sector of the model, which is similar to what we describe in chapter 1. In the third section we present the new interactions that arise in this theory and finally, in the last section, we give the decay width formulas for processes involving the new particles.

4.1 The Scalar Sector

Let us begin by introducing the scalar sector of the HAHM model. Besides the SM-like Higgs boson doublet H, now we will also have a new scalar particle S that mixes with H via a quartic term in the scalar potential. The scalar Lagrangian can be written as

$$\mathcal{L}_{\text{scalar}} = |D_\mu H|^2 + |D_\mu S|^2 - V(H,S)\,, \tag{4.1}$$

where the scalar potential $V(H,S)$ is given by

$$V(H,S) = -\mu^2|H|^2 + \lambda|H|^4 - \mu_S^2|S|^2 + \lambda_S|S|^4 + \kappa|H|^2|S|^2, \tag{4.2}$$

with κ parametrizing the scalar mixing and we require that $\mu^2, \mu_S^2, \lambda, \lambda_S > 0$ in order to break both $SU(2)_L \times U(1)_Y$ and $U(1)_\gamma$ spontaneously.

The new scalar S, dubbed 'dark Higgs', is a SM gauge-singlet with $U(1)_\gamma$ charge $q_S \neq 0$, meaning that it does not couple to any SM gauge sector, only with the secluded new vector boson. Since we are in the minimal scenario, the new mediator will be the *dark photon* Z_γ and we will follow the conventions from section 1.1. Hence, we can write the SM-like Higgs and the dark Higgs covariant derivatives according to

$$D_\mu H = \partial_\mu H - igW_{a\mu}\tau^a H - \frac{1}{2}ig'\hat{B}_\mu H\,, \tag{4.3}$$

$$D_\mu S = \partial_\mu S - iq_S g_D \hat{Z}_{\gamma\mu} S\,, \tag{4.4}$$

where g, g' and g_D are the $SU(2)_L$, $U(1)_Y$ and $U(1)_\gamma$ gauge couplings, respectively, and the hatted fields indicate states with non-canonical kinetic terms.

The dark Higgs develops a VEV $\langle S\rangle = v_S/\sqrt{2}$ responsible for the SSB of the $U(1)_\gamma$ gauge symmetry, which in turn results in a mass term for the dark photon, as we will show in the next section. Another consequence of the addition of the new scalar is that the Higgs portal will induce a mixing between the dark Higgs and the SM Higgs. In order to compute this mass

mixing we need to consider the broken phase after both scalars acquire a VEV

$$H \to \begin{pmatrix} 0 \\ (v+h_0)/\sqrt{2} \end{pmatrix} , \tag{4.5}$$

$$S \to \frac{(v_S + s_0)}{\sqrt{2}} , \tag{4.6}$$

where we already transformed the fields according to unitary gauge. Remember that the VEV is exactly the value that minimizes the potential, such that we can express the mass term coefficients as

$$\begin{aligned} &\frac{\partial V}{\partial H}\Big|_{\langle H\rangle,\langle S\rangle} = 0 \Rightarrow -\mu^2 + \lambda v^2 + \kappa \frac{v_S^2}{2} = 0 \\ &\therefore\ \mu^2 = \lambda v^2 + \frac{1}{2}\kappa v_S^2 , \end{aligned} \tag{4.7}$$

$$\begin{aligned} &\frac{\partial V}{\partial S}\Big|_{\langle H\rangle,\langle S\rangle} = 0 \Rightarrow -\mu_S^2 + \lambda_S v_S^2 + \kappa \frac{v^2}{2} = 0 \\ &\therefore\ \mu_S^2 = \lambda_S v_S^2 + \frac{1}{2}\kappa v^2 . \end{aligned} \tag{4.8}$$

In the broken phase, the scalar potential in eq. (4.2) is given by

$$V(h_0, s_0) = -\frac{\mu^2}{2}(v+h_0)^2 + \frac{\lambda}{4}(v+h_0)^4 - \frac{\mu_S^2}{2}(v_S+s_0)^2 + \frac{\lambda_S}{4}(v_S+s_0)^4 + \frac{\kappa}{4}(v+h_0)^2(v_S+s_0)^2 . \tag{4.9}$$

Let us now collect the quadratic terms of this potential to investigate the mass mixing

$$\begin{aligned} V_{\rm m}(h_0, s_0) &= \frac{1}{2}\left(-\mu^2 + 3\lambda v^2 + \frac{\kappa v_S^2}{2}\right) h_0^2 + \frac{1}{2}\left(-\mu_S^2 + 3\lambda_S v_S^2 + \frac{\kappa v^2}{2}\right) s_0^2 \\ &\quad + \frac{1}{2}\, 2\, \kappa\, v\, v_S s_0 h_0 \\ &= \lambda v^2 h_0^2 + \lambda_S v_S^2 s_0^2 + \kappa\, v\, v_S s_0 h_0 , \end{aligned} \tag{4.10}$$

where in the second line we used the conditions imposed by eq. (4.7) and (4.8). Therefore, we find that the mass matrix in the (h_0, s_0) basis is

$$\mathcal{M}_s^2 = \begin{pmatrix} 2\,\lambda v^2 & \kappa\, v\, v_S \\ \kappa\, v\, v_S & 2\,\lambda_S v_S^2 \end{pmatrix} . \tag{4.11}$$

Since this is a symmetric matrix we can diagonalize it with an orthogonal transformation

$$\begin{pmatrix} h \\ s \end{pmatrix} = \begin{pmatrix} \cos\phi & -\sin\phi \\ \sin\phi & \cos\phi \end{pmatrix} \begin{pmatrix} h_0 \\ s_0 \end{pmatrix}, \tag{4.12}$$

where h and s are the physical mass states and ϕ is the scalar mixing angle, defined as

$$\begin{aligned} \tan^2(2\phi) &= \frac{(2\,\kappa\, v\, v_S)^2}{(m_h^2 - m_s^2)^2 - (2\,\kappa\, v\, v_S)^2} \\ &\simeq \left(\frac{2\,\kappa\, v\, v_S}{m_h^2 - m_s^2}\right)^2 + \mathcal{O}\big(\kappa^4\big)\,, \end{aligned} \tag{4.13}$$

assuming the limit of small κ. The Higss and dark Higgs squared masses, m_h^2 and m_s^2, respectively, are the eigenvalues of the mass matrix $\mathcal{M}_s^2$, given by

$$m_{h,s}^2 = \lambda v^2 + \lambda_S v_S^2 \pm \sqrt{v^4\lambda^2 + v_S^4\lambda_S^2 + v^2 v_S^2(\kappa^2 - 2\lambda\lambda_S)}\,, \tag{4.14}$$

where we already considered a specific mass hierarchy $m_h > m_s$, which is the relevant one for our study. Now, in the limit where $\kappa \ll 1$, *i.e.* in the limit of small mixing angles, we have that

$$\tan 2\phi \simeq 2\phi \simeq \frac{2\,\kappa v v_S}{m_s^2 - m_h^2}\,, \tag{4.15}$$

and, hence, $s_h \equiv \sin\phi \simeq \phi$, such that

$$s_h \simeq \frac{\kappa v v_S}{m_s^2 - m_h^2}\,. \tag{4.16}$$

In this limit, the mass eigenvalues become

$$m_h^2 = 2\lambda v^2 + 2s_h^2(\lambda v^2 - \lambda_S v_S^2)\,, \tag{4.17}$$

$$m_s^2 = 2\lambda_S v_S^2 - 2s_h^2(\lambda v^2 - \lambda_S v_S^2)\,, \tag{4.18}$$

up to order κ^2. Note that the SM-like Higgs mass would be only corrected from the SM value $m_h^{\rm SM} = 2\lambda v^2$ by a small factor proportional to the sine of the mixing angle. The fields will also mix according to

$$h_0 = c_h h + s_h s\,, \qquad s_0 = c_h s - s_h h\,, \tag{4.19}$$

where $c_h \equiv \cos\phi \simeq 1 + \mathcal{O}(\kappa^2)$. Now, let us discuss the mass generation in the gauge sector.

4.2 The Gauge Sector

The gauge sector of the model will behave exactly as described in chapter 1 but considering the secluded scenario. The hypercharge portal is realized through a kinetic mixing term

$$\mathcal{L}^0_{\text{gauge}} = -\frac{1}{4}\hat{B}_{\mu\nu}\hat{B}^{\mu\nu} - \frac{1}{4}\hat{Z}_{\gamma\mu\nu}\hat{Z}^{\mu\nu}_{\gamma} - \frac{\epsilon}{2c_W}\hat{B}_{\mu\nu}\hat{Z}^{\mu\nu}_{\gamma}, \tag{4.20}$$

that can be canonically normalized according to the field redefinitions of eq. (1.3) and eq. (1.4), such that

$$\mathcal{L}^0_{\text{gauge}} = -\frac{1}{4}B_{\mu\nu}B^{\mu\nu} - \frac{1}{4}\tilde{Z}_{\gamma\mu\nu}\tilde{Z}^{\mu\nu}_{\gamma}. \tag{4.21}$$

Now, following eq. (1.17), the interaction Lagrangian will be

$$\mathcal{L}_{\text{int}} = eJ_{\text{EM}}A + gJ_Z Z_0 - e\epsilon J_{\text{EM}}\eta\tilde{Z}_\gamma + g'\epsilon J_Z\eta\tilde{Z}_\gamma\,, \tag{4.22}$$

where we took $J_Q = 0$ since we are in the secluded scenario.

In this UV completion framework, we can dynamically originate the *dark photon* mass via the SSB of $U(1)_\gamma$. As in the case of EWSSB, we can extract the dark boson mass term from the dark Higgs kinetic term $|D_\mu S|^2$, where the covariant derivative is given by eq. (4.4)

$$\begin{aligned} |D_\mu S|^2 &= \left|\partial_\mu\left(\frac{s_0+v_S}{\sqrt{2}}\right) - iq_S g_D\hat{Z}_{\gamma\mu}\left(\frac{s_0+v_S}{\sqrt{2}}\right)\right|^2 \\ &= \frac{1}{2}(\partial_\mu s_0)^2 + \frac{1}{2}g_D^2 q_S^2(s_0+v_S)^2\eta^2\tilde{Z}^\mu_\gamma\tilde{Z}_{\gamma,\mu}\,, \end{aligned} \tag{4.23}$$

and η was given in eq. (1.5). In the limit where $\epsilon \ll 1$ we can approximate $\eta \sim 1$, resulting in

$$|D_\mu S|^2 = \frac{1}{2}(\partial_\mu s_0)^2 + \frac{1}{2}m^2_{\tilde{Z}_\gamma}\tilde{Z}^2_\gamma + g_D^2 q_S^2 v_S s_0\tilde{Z}^2_\gamma + \frac{1}{2}g_D^2 q_S^2 s_0^2\tilde{Z}^2_\gamma\,, \tag{4.24}$$

where we defined

$$m_{\tilde{Z}_\gamma} = g_D q_S v_S\,. \tag{4.25}$$

Therefore, the mass of the *dark photon* will depend on the new abelian gauge group coupling, but also on the dark Higgs VEV and charge. After the SSB of both the EW and $U(1)_\gamma$ symmetries, we can proceed with the $Z_0 - \tilde{Z}_\gamma$ mass diagonalization according to eq. (1.23) to obtain the mass eigenstates of eq. (1.30). In the scenario where $m_Z \gg m_{Z_\gamma}$, which is the relevant hierarchy we are interested in, and also for suppressed kinetic mixing, we end up with eq. (1.31)

and (1.32), which we quote here again

$$m_{Z_\gamma}^2 \simeq \delta^2 m_{Z_0}^2 (1 - \epsilon^2 t_W^2)\,, \tag{4.26}$$

$$m_Z^2 \simeq m_{Z_0}^2 (1 + \epsilon^2 t_W^2)\,. \tag{4.27}$$

Hence, we can see that the SM-like Z boson mass will suffer a correction proportional to ϵ^2. Similarly to eq. (1.36) and (1.37), we have that

$$Z_0 \simeq Z - \epsilon t_W Z_\gamma\,, \tag{4.28}$$

$$\tilde{Z}_\gamma \simeq Z_\gamma + \epsilon t_W Z\,. \tag{4.29}$$

4.3 HAHM Interactions

In the last two sections, we discussed the scalar mass mixing that arises from the Higgs portal as well as the *dark photon* mass generation mechanism. Now, we can also compute some of the interaction terms involving the particles of the model. Below we enumerate some of the useful HAHM interactions following a division by particle type.

4.3.1 Gauge Bosons and Scalars

From the H and S kinetic terms we can derive the interactions between gauge bosons and scalars. Let us begin with the dark Higgs kinetic term, that was calculated in eq. (4.24). Due to the scalar and $Z - Z_\gamma$ mixing, this term will originate couplings of the *dark photon* to the dark Higgs and SM-like Higgs as we see below

$$\begin{aligned}
|D_\mu S|^2 &\supset \frac{g_D^2 q_S^2 v_S^2}{2}\left(1 + \frac{s_0}{v_S}\right)^2 \tilde{Z}_\gamma^2 \\
&= \frac{g_D^2 q_S^2 v_S^2}{2}\left(1 + \frac{(s - s_h h)}{v_S}\right)^2 (Z_\gamma + \epsilon t_W Z)^2 \\
&\supset s\left[\left(\frac{m_{Z_\gamma}^2}{v_S}\right) Z_\gamma^2 + \left(\frac{m_{Z_\gamma}^2}{v_S}\epsilon^2 t_W^2\right) Z^2\right] - h\left[\left(\frac{m_{Z_\gamma}^2}{v_S} s_h\right) Z_\gamma^2 + \left(\frac{m_{Z_\gamma}^2}{v_S}\epsilon^2 t_W^2 s_h\right) Z^2\right] \\
&\quad + \frac{2m_{Z_\gamma}^2}{v_S}\epsilon t_W (s - s_h h) Z Z_\gamma \\
&= \left(\frac{m_{Z_\gamma}^2}{v_S}\right) s Z_\gamma^2 - \left(\frac{m_{Z_\gamma}^2}{v_S} s_h\right) h Z_\gamma^2 + \left(\frac{2m_{Z_\gamma}^2}{v_S}\epsilon t_W\right) s Z Z_\gamma + \mathcal{O}(\epsilon^2, s_h\epsilon, s_h\epsilon^2)\,,
\end{aligned} \tag{4.30}$$

where we neglected mass terms and quartic interactions and used that

$$m_{Z_\gamma}^2 \simeq \delta^2 m_{Z_0}^2 + \mathcal{O}(\epsilon^2\delta^2) \simeq m_{\tilde{Z}_\gamma}^2 = g_D^2 q_S^2 v_S^2 \,.$$

Now, we can also compute the Higgs doublet kinetic term in order to find the other gauge boson-scalar interaction terms. From eq. (1.20), we have that

$$\begin{aligned}
|D_\mu H|^2 &\supset \frac{1}{8}(v+h_0)^2\left[\frac{g}{c_W}Z_0^\mu + g'\frac{\epsilon}{c_W}\eta\tilde{Z}_\gamma^\mu\right]^2 \\
&\supset \frac{1}{8c_W^2}(2vh_0)\left[gZ_0^\mu + g'\epsilon\eta\tilde{Z}_\gamma^\mu\right]^2 \\
&= \frac{v}{4c_W^2}(h+s_h s)\left[g(Z^\mu - \epsilon t_W Z_\gamma^\mu) + g'\epsilon\eta(Z_\gamma^\mu + \epsilon t_W Z^\mu)\right]^2 \\
&= \left(\frac{s_h v g^2}{4c_W^2}\right)sZ^2 + \left(\frac{vg^2}{4c_W^2}\right)hZ^2 - \left(\frac{4m_Z^2}{v}\epsilon t_W\right)hZZ_\gamma \\
&\quad + \mathcal{O}(\epsilon^2, \epsilon s_h, \epsilon^3) \times \left(sZ_\gamma^2 + sZ^2 + hZ^2 + hZ_\gamma^2 + hZZ_\gamma + sZZ_\gamma\right),
\end{aligned} \tag{4.31}$$

where in the second line we collect only the term that leads to cubic interactions, we change to the physical fields s, h, Z and Z_γ according to the mixing equations from the last sections and in the last line we neglect interactions of order $\mathcal{O}(\epsilon^2, \epsilon s_h)$ or higher. Finally, joining the results from eq. (4.30) and (4.31), we obtain

$$\begin{aligned}
\mathcal{L}_{\text{GB-S}} = s&\left[\frac{m_{Z_\gamma}^2}{v_S}Z_\gamma^2 + \frac{s_h v g^2}{4c_W^2}Z^2\right] - h\left[\frac{s_h m_{Z_\gamma}^2}{v_S}Z_\gamma^2 - \frac{vg^2}{4c_W^2}Z^2\right] \\
&+ \left(\frac{2m_{Z_\gamma}^2}{v_S}\epsilon t_W\right)sZZ_\gamma - \left(\frac{4m_Z^2}{v}\epsilon t_W\right)hZZ_\gamma \,.
\end{aligned} \tag{4.32}$$

Note that the the interaction of the dark Higgs s with the SM Z boson is identical to the hZZ coupling, but suppressed by an extra s_h factor. Similarly, the $hZ_\gamma Z_\gamma$ coupling is inherited from the scalar mixing in the dark Higgs kinetic term, and, hence, posses an extra s_h suppression in comparison with the $sZ_\gamma Z_\gamma$ interaction. In general, the dark Higgs will inherit all the SM-like Higgs boson couplings to SM particles, but with an extra s_h suppression.

Another interesting feature of that result is that we have a sZZ_γ term among the possible interactions. This coupling will allow the Z boson to decay into s and Z_γ, thus contributing to the Z invisible decay width $\Gamma(Z \to \text{inv})$ at tree-level. However, due to the smallness of ϵ and of m_{Z_γ}, this contribution is sub-leading and below the present sensitivity. Furthermore, loop diagrams contributing to this same channel will always be proportional to ϵ^2, ϵs_h or s_h^2 in the most optimistic scenarios, turning such processes experimentally inaccessible.

4.3.2 Gauge Bosons and Fermions

Let us first investigate how the interactions of the Z boson with fermions will change in the HAHM. To this end, we need to open the terms of the interaction Lagrangian given by eq. (1.17). However, now we want to go up to order $\mathcal{O}(\epsilon^2)$, so we will change to the physical fields Z and Z_γ following eq. (1.33) and (1.34), *i.e.* without expanding the sine and cosine

$$\begin{aligned}
\mathcal{L}_{\text{int}} &\supset g J_Z(Z c_\alpha - Z_\gamma s_\alpha) - e\epsilon\eta J_{\text{EM}}(Z s_\alpha + Z_\gamma c_\alpha) + g'\epsilon\eta J_Z(Z s_\alpha + Z_\gamma c_\alpha) \\
&\supset (\, g c_\alpha J_Z - e\epsilon\eta s_\alpha J_{\text{EM}} + g'\epsilon\eta s_\alpha J_Z) Z \\
&= [\, g c_\alpha J_Z + \epsilon\eta s_\alpha (g' J_Z - e J_{\text{EM}})] Z \\
&= \left[\frac{g}{c_W} c_\alpha (T^3 c_W^2 - Y s_W^2) - \epsilon\eta s_\alpha \frac{g}{c_W} t_W Y \right] \bar{f}\gamma^\mu f Z \,,
\end{aligned} \tag{4.33}$$

where $s_\alpha \equiv \sin\alpha$ and $c_\alpha \equiv \cos\alpha$ and we used equations (1.8), (1.13) and (1.14) for the current expressions and also eq. (1.16) for the electric charge definition. Therefore the interactions between the SM Z boson and the SM fermions f can be written as

$$\mathcal{L}_{Z\bar{f}f} = g_{Z\bar{f}f} Z_\mu \bar{f}\gamma^\mu f \,, \tag{4.34}$$

where

$$g_{Z\bar{f}f} = \frac{g}{c_W} \left[c_\alpha (T^3 c_W^2 - Y s_W^2) - \epsilon\eta s_\alpha t_W Y \right] . \tag{4.35}$$

From this last equation it is easy to obtain the correction to the SM coupling value

$$g^{\text{SM}}_{Z\bar{f}f} = g(T^3 c_W^2 - Y s_W^2)/c_W \,,$$

by considering the limit of small ϵ in eq. (4.35)

$$\begin{aligned}
g_{Z\bar{f}f} &\simeq \frac{g}{c_W}\left[T^3 c_W^2 - Y s_W^2\right] + \frac{g}{c_W}\frac{\epsilon^2 t_W^2}{2(\delta^2-1)^2}\left[-T^3 c_W^2 + Y s_W^2 + 2Y(\delta^2-1)\right] + \mathcal{O}(\epsilon^3) \\
&= g^{\text{SM}}_{Z\bar{f}f} + \frac{g}{c_W}\frac{\epsilon^2 t_W^2}{2(\delta^2-1)^2}\left[T^3 - Q(1+c_W^2) + 2Y\delta^2\right] ,
\end{aligned} \tag{4.36}$$

where we used that $\epsilon\eta \sim \epsilon + \mathcal{O}(\epsilon^3)$ and also the angle approximations

$$c_\alpha \simeq 1 - \frac{t_W^2 \epsilon^2}{2(\delta^2-1)^2} + \mathcal{O}(\epsilon^3) \,, \tag{4.37}$$

$$s_\alpha \simeq \frac{t_W \epsilon}{\delta^2 - 1} + \mathcal{O}(\epsilon^3) \,. \tag{4.38}$$

Therefore, we can see that the correction to the SM Z coupling to fermions is proportional to ϵ^2. Analogously, we can calculate the interaction term between the *dark photon* and the SM fermions starting from the same eq. (4.33), but now collecting the Z_γ terms

$$\begin{aligned}\mathcal{L}_{Z_\gamma \bar{f} f} &= -g s_\alpha J_Z Z_\gamma - e\epsilon\eta c_\alpha J_{\rm EM} Z_\gamma + g'\epsilon\eta c_\alpha J_Z Z_\gamma \\ &\equiv g_{Z_\gamma \bar{f} f} Z_{\gamma\mu} \bar{f}\gamma^\mu f\,,\end{aligned} \tag{4.39}$$

where

$$g_{Z_\gamma \bar{f} f} = \frac{g}{c_W}\left[-s_\alpha(T^3 c_W^2 - Y s_W^2) - \epsilon\eta c_\alpha t_W Y\right]\,. \tag{4.40}$$

It is important to highlight that in the limit where $\epsilon \ll 1$ ($\eta \sim 1$) the $Z_\gamma \bar{f} f$ coupling is 'photon-like' for small δ

$$g_{Z_\gamma \bar{f} f} \simeq e\epsilon Q + \mathcal{O}(\delta^2)\,, \qquad (\delta \ll 1) \tag{4.41}$$

and 'Z-like' for $\delta \simeq 1$

$$g_{Z_\gamma \bar{f} f} \simeq \epsilon\frac{g}{c_W}(T^3 c_W^2 - Y s_W^2) + \mathcal{O}(\delta^2)\,. \qquad (\delta \simeq 1) \tag{4.42}$$

4.3.3 Scalar Interactions

Finally, we can obtain the interactions among the Higgs and dark Higgs scalars by replacing the physical fields h and s of eq. (4.19) in the scalar potential given in eq. (4.9). Below we list the triple interaction terms

$$\mathcal{L}_{hss} = -3hss\left[-v_S\lambda_S c_h^2 s_h + v\lambda c_h s_h^2 + \frac{\kappa}{6}\left(v c_h^3 + 2v_S c_h^2 s_h - 2v c_h s_h^2 - v_S s_h^3\right)\right]\,, \tag{4.43}$$

$$\mathcal{L}_{shh} = -3shh\left[v\lambda c_h^2 s_h + v_S\lambda_S c_h s_h^2 + \frac{\kappa}{6}\left(v_S c_h^3 - 2v c_h^2 s_h - 2v_S c_h s_h^2 + v s_h^3\right)\right]\,, \tag{4.44}$$

$$\mathcal{L}_{hhh} = hhh\left[v\lambda c_h^3 - v_S\lambda_S s_h^3 - \frac{\kappa}{2}\left(v_S c_h^2 s_h - v c_h s_h^2\right)\right]\,, \tag{4.45}$$

$$\mathcal{L}_{sss} = sss\left[v_S\lambda_S c_h^3 + v\lambda s_h^3 + \frac{\kappa}{2}\left(v c_h^2 s_h + v_S c_h s_h^2\right)\right]\,. \tag{4.46}$$

In the mass regime where $m_h > 2m_s$, the decay $h \to ss$ is kinetically accessible and is described by the interaction Lagrangian $\mathcal{L}_{hss}$.

4.4 Decay Widths

Now that we computed the interactions terms which couple the Z and Z_γ gauge bosons with the h and s scalars and also the interactions among the gauge bosons and fermions and between the scalars, we are ready to write down the expressions for the relevant tree-level decay widths.

From the interaction Lagrangian that couples Z_γ to the fermions, given by eq. (4.39) and (4.40), we can obtain the partial width of a *dark photon* decaying into two SM fermions [51]

$$\Gamma(Z_\gamma \to \bar{f}f) = \frac{N_c}{24\pi m_{Z_\gamma}}\sqrt{1-\frac{4m_f^2}{m_{Z_\gamma}^2}}[m_{Z_\gamma}^2(g_L^2+g_R^2) - m_f^2(-6g_Lg_R+g_L^2+g_R^2)]\,, \tag{4.47}$$

where N_c is the number of colors ($N_c = 3$ for quarks and $N_c = 1$ otherwise) and we have divided the $g_{Z_\gamma \bar{f}f}$ coupling into a right-handed g_R and a left-handed g_L component, such that

$$\mathcal{L}_{Z_\gamma \bar{f}f} = g_{Z_\gamma \bar{f}f} Z_{\gamma\mu}\bar{f}\gamma^\mu f = Z_{\gamma\mu}\bar{f}\gamma^\mu(g_L P_L + g_R P_R)f \tag{4.48}$$

where g_L (g_R) is the $g_{Z_\gamma \bar{f}f}$ coupling applied to left-handed (right-handed) fermions. Note that, on the one hand, for a light *dark photon* ($\delta \ll 1$) we are in the 'photon-like' regime, and, hence, the $\Gamma(Z_\gamma \to \bar{f}f)$ decay width will reduce to the expression given in eq. (1.43) for charged fermions and similarly for quarks. Actually, in this regime all the Z_γ decays into leptons, quarks and hadrons follow the same equations described in section 1.3. On the other hand, for a massive *dark photon* ($m_{Z_\gamma} > 10\,\text{GeV}$), we need to rely on eq. (4.47), that also features couplings to neutral particles, inherited from the Z neutral current, such as neutrinos.

In the case of decays involving the SM-like Higgs boson h and the *dark photon*, from eq. (4.32) we can extract the partial decay width for $h \to ZZ_\gamma$ and $h \to Z_\gamma Z_\gamma$

$$\begin{aligned}\Gamma(h \to ZZ_\gamma) =& \frac{\epsilon^2\eta^2 t_W^2 m_Z^2 m_{Z_\gamma}^2}{16\pi v^2 m_h^3 (m_Z^2 - m_{Z_\gamma}^2)^2}[-2m_{Z_\gamma}^2(m_h^2 - 5m_Z^2) + m_{Z_\gamma}^4 + (m_h^2 - m_Z^2)^2] \\ &\times \sqrt{-2m_h^2(m_Z^2+m_{Z_\gamma}^2) + (m_Z^2 - m_{Z_\gamma}^2)^2 + m_h^4}\,,\end{aligned} \tag{4.49}$$

$$\Gamma(h \to Z_\gamma Z_\gamma) = (\kappa')^2 \frac{1}{32\pi}\frac{v^2}{m_h^5}\left[12m_{Z_\gamma}^4 - 4m_h^2 m_{Z_\gamma}^2 + m_h^4\right]\sqrt{1-\frac{4m_{Z_\gamma}^2}{m_h^2}}\,, \tag{4.50}$$

where in the last equation we have defined

$$\kappa' \equiv \kappa \frac{m_h^2}{|m_h^2 - m_s^2|}. \tag{4.51}$$

Finally, our last relevant decay width is for the SM-like Higgs decay into a pair of dark Higgs scalars [166], that can be obtained from eq. (4.43)

$$\Gamma(h \to ss) = \frac{(\kappa')^2 v^2}{32\pi m_h^5}\left(m_h^2 + 2m_s^2\right)^2 \left[1 - \frac{4m_s^2}{m_h^2}\right]^{1/2}. \tag{4.52}$$

To recap what we did so far, in the first part of this dissertation we focused on the study of the decays of a light mediator arising from an additional $U(1)_Q$ gauge symmetry. However, we did not detailed the specific mechanism that dynamically generates this light mediator mass. To give a reasonable UV completion to the $U(1)_Q$ model, we extended the scalar sector by adding a new SM scalar singlet s responsible for the SSB of $U(1)_Q$ and, hence, for the generation of the mediator mass. In particular, we specialize on a model where the dark mediator is the secluded *dark photon* and the new scalar mixes with the SM-like Higgs via the quartic interaction in the scalar potential. This model is known as the Hidden Abelian Higgs Model, and in this chapter we outlined the physics behind the new scalar portal and also elaborate on the interactions and decay widths involving the new particles. Now, we are ready to study some of the phenomenological implications of this model, but first, since we saw in this chapter that the new scalar and KM portals introduce corrections to some of the well-measured SM electroweak observables, such as the Z boson mass and couplings, we first need to investigate the EW constraints of the HAHM, which is the subject of the next chapter.

Chapter 5

Electroweak Constraints

In the last chapter, we developed the theory behind the HAHM, which is, in a few words, a SM extension by two additional renormalizable portals: the KM portal in the gauge sector and the Higgs portal in the scalar sector. By computing the $Z - Z_\gamma$ and $h - s$ mass mixing, as well as the interactions and decay widths involving these particles, we obtained corrections to some of the SM electroweak observables. For example, from the $Z - Z_\gamma$ mixing, we introduced an extra term to the mass of the Z boson, given by eq. (4.27), and also to the coupling with fermions in eq. (4.36). Analogously, due to the extra dark particles, we have two additional invisible decays of the SM-like Higgs boson, which are the decay into a pair of *dark photons* and a pair of dark Higgs. These decays will contribute to the SM Higgs total invisible decay width, which is another well-measured observable.

Hence, since the above mentioned EW observables have been measured extremely well in all sorts of experiments, especially large e^+e^- and pp colliders, such as the Large Electron-Positron Collider (LEP) [167] and the Large Hadron Collider (LHC) [168], the new theory parameters will suffer strong constraint from EW precision data. It is important to investigate these constraints before moving to the phenomenological implications of the HAHM, since the EW precision tests will limit the model parameters that will be used in the next chapter for the simulation of the Higgs Boson decay into two *dark photons*.

This chapter is organized in the following way. In the first and second sections, we compute the constraints that arise from the corrections to the mass and couplings of the Z and Higgs boson, respectively. The third section focuses on the bound from the Higgs boson invisible decay width. Finally, in the last section, we summarize all the computed limits and display the final constraints on the free parameters of the HAHM.

5.1 Z boson mass and couplings

In section 4.2 we computed the $Z - Z_\gamma$ mass mixing and obtained the following expression for the Z boson mass correction

$$m_Z \simeq m_{Z_0}\sqrt{(1+\epsilon^2 t_W^2)}\,. \tag{5.1}$$

The PDG [2] value for the Z boson mass was based on [167] and is given by

$$m_{Z_0} \simeq m_Z^{\text{exp}} = 91.1876 \pm 0.0021 \text{ GeV}\,. \tag{5.2}$$

For the case of the weak mixing angle θ_W, we have [2]

$$s_W^2 = 0.23122 \pm 0.00004\,. \tag{5.3}$$

Joining the mass and mixing angle values we can constraint the KM parameter ϵ by requiring that

$$m_Z^{\text{exp}} - n\, m_{Z,\text{err}}^{\text{exp}} \leq m_Z^{\text{exp}}\sqrt{(1+\epsilon^2 t_W^2)} \leq m_Z^{\text{exp}} + n\, m_{Z,\text{err}}^{\text{exp}}\,, \tag{5.4}$$

where n quantifies the number of standard deviations σ from the experimental value and $m_{Z,\text{err}}^{\text{exp}}$ is the uncertainty on the Z mass calculation, *i.e.* $m_{Z,\text{err}}^{\text{exp}} = 0.0021$. Note that we neglected the s_W uncertainty since the sine of the weak angle appears in the tangent ratio with the cosine. Now, if we consider the limit where $\epsilon \ll 1$, we can express the last equation in terms of the SM deviation value δm_Z

$$|\delta m_Z| \equiv |m_Z^{\text{exp}}\,\frac{\epsilon^2 t_W^2}{2}| \leq n\, m_{Z,\text{err}}^{\text{exp}}\,. \tag{5.5}$$

The constraint on the KM parameter ϵ that arises from this last equation is displayed in the left panel of figure 5.1, which shows the allowed values for the ϵ parameter when varying the number of deviations n. For a 2σ deviation, the allowed interval is

$$-0.0175 \leq \epsilon \leq 0.0175 \quad (2\,\sigma)\,. \tag{5.6}$$

Now, regarding the Z boson coupling to SM fermions, we computed in eq. (4.36) the correction introduced by the HAHM to $g_{Z\bar{f}f}^{\text{SM}}$. The SM reference value can be obtained following the PDG conventions for the vector g_V and axial-vector g_A couplings

$$g_V = g_L + g_R\,, \tag{5.7}$$

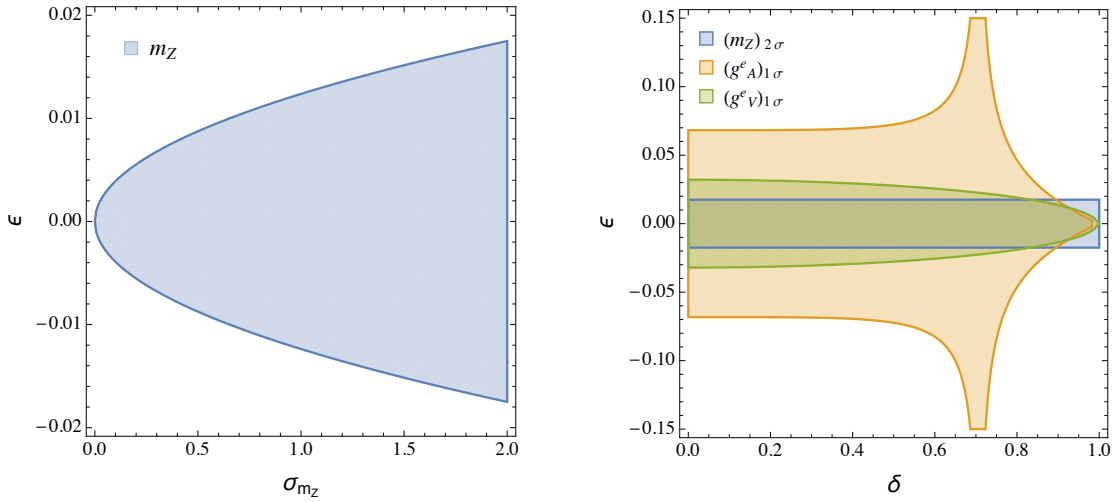

Figure 5.1: In the left panel we show the allowed ϵ values obtained with the constraint of eq. (5.5) as a function of the number of standard deviations from the experimental Z mass given by eq. (5.2). In the right panel, we show the allowed regions on the $\epsilon \times \delta$ plane when considering the Z boson vector (green region) and axial-vector (orange region) electron coupling constraints. The blue area indicates the valid values for ϵ obtained with the Z boson mass constraint at 2 σ.

$$g_A = g_L - g_R\,, \tag{5.8}$$

which enter in the Lagrangian interaction term according to

$$\mathcal{L}_{Zff} = -\frac{g}{2c_W}\bar{f}\gamma^\mu(g_V - g_A\gamma^5)fZ_\mu\,. \tag{5.9}$$

Following this notation, we can extract the HAHM Zff coupling deviation from eq. (4.36)

$$\delta g^{\rm SM}_{Z\bar{f}f} = \frac{\epsilon^2 t_W^2}{2(\delta^2-1)^2}\left[T^3 - Q(1+c_W^2) + 2Y\delta^2\right], \tag{5.10}$$

up to order $\mathcal{O}(\epsilon^2)$. In order to place the bound in the $\epsilon \times \delta$ parameter space, we need to compare with the EW precision value for a specific fermion choice. Here, we will use the coupling with electrons, since it is the most precise coupling measurement in comparison with the other fermions. The PDG values for the vector and axial-vector Z boson coupling to electrons are displayed below

$$g^e_V = -0.03817 \pm 0.00047\,, \tag{5.11}$$

$$g^e_A = -0.50111 \pm 0.00035. \tag{5.12}$$

Now, we can apply the left and right-handed projections on eq. (5.10) to obtain the respective

SM deviations

$$\delta g_L^e \equiv (\delta g_{Z\bar{e}e}^{\text{SM}})_L = \frac{\epsilon^2 t_W^2}{2(\delta^2-1)^2}\left[T_{e_L}^3 - Q_e(1+c_W^2) + 2Y_{e_L}\delta^2\right], \tag{5.13}$$

$$\delta g_R^e \equiv (\delta g_{Z\bar{e}e}^{\text{SM}})_R = \frac{\epsilon^2 t_W^2}{2(\delta^2-1)^2}\left[-Q_e(1+c_W^2) + 2Y_{e_R}\delta^2\right], \tag{5.14}$$

where the LH and RH electron charges are $T_{e_L}^3 = -0.5$, $Y_{e_L} = -0.5$, $Y_{e_R} = -1$ and $Q_e = -1$. Then, using the PDG values and the above definitions we can constraint g_V^e and g_A^e by requiring that

$$|\delta g_V^e| = |\delta g_L^e + \delta g_R^e| \leq (g_V^e)_{\text{err}}\,, \tag{5.15}$$

and

$$|\delta g_A^e| = |\delta g_L^e - \delta g_R^e| \leq (g_A^e)_{\text{err}}\,. \tag{5.16}$$

In the right panel of figure 5.1 we show the allowed regions in the $\epsilon \times \delta$ plane that arise from the g_V^e (green) and g_A^e (orange) constraints considering 1 σ deviation. In blue we show the previous bound from the Z boson mass for a 2 σ standard deviation. We can see from the figure that the mass limit is stronger than the electron coupling bounds. This is a consequence of the fact that the Z mass measurement is more precise than the coupling measurements. For example, while the relative uncertainty of the g_A^e observable is of $\sim 0.06\%$, for m_Z this value reaches $\sim 0.002\%$.

5.2 Higgs boson mass and couplings

In the extended scalar scenario, the physical Higgs boson is a combination of both undiagonalized fields h_0 and s_0, as established by eq. (4.19). Therefore, all the SM-like Higgs coupling are shifted by a factor proportional to c_h, *i.e.* proportional to $\mathcal{O}(\kappa^2)$. This implies that any precision measure on the Higgs boson production and decay can put bounds on the scalar mixing angle.

In particular, in [168] the authors computed the likelihood contours in the Higgs boson coupling (κ_F, κ_V) plane obtained with ATLAS and CMS Run 1 data, where κ_F and κ_V denote the strength of the Higgs coupling to fermions and vector bosons, respectively. In the SM scenario, these two parameters are equal to 1, and the measured region with the combined data lies within a 0.1 unit interval from the SM value. From their results, we can extract the following values for the Higgs coupling strengths [2]

$$\kappa_V = 1.05 \pm 0.04, \quad \kappa_F = 1.05 \pm 0.09\,. \tag{5.17}$$

With this information it is easy to set bounds on the scalar mixing angle, since in order to agree with the LHC data the cosine of ϕ can introduce a correction of at most $\kappa_V - 2\sigma_{\kappa_V} = 0.97$ at two sigma. Therefore,

$$c_h \geq (0.97)_{2\sigma} \tag{5.18}$$

$$\Rightarrow s_h \lesssim (0.24)_{2\sigma}\,, \tag{5.19}$$

where the sine constraint was computed using the identity $c_h^2 + s_h^2 = 1$.

Let us now proceed and consider the bound from the Higgs mass measurement. The PDG value for the Higgs boson mass is

$$m_h^{\text{exp}} = 125.10 \pm 0.14 \text{ GeV}\,. \tag{5.20}$$

In the process of scalar mass diagonalization we obtained the correction δm_h^2 to the SM-like Higgs squared mass

$$\begin{aligned} m_h^2 &= (m_{h_0})^2 + s_h^2[(m_{h_0})^2 - m_S^2] \\ \Rightarrow \delta m_h^2 &\simeq s_h^2[(m_h^{\text{exp}})^2 - m_S^2]\,, \end{aligned} \tag{5.21}$$

as given by eq. (4.17). Therefore, by using the measured mass value of eq. (5.20) we can constraint s_h and $m_s \sim \sqrt{2\lambda_S} v_S$ by requiring that the correction to the experimental Higgs squared mass value should be smaller than the uncertainty on $(m_h^{\text{exp}})^2$

$$|\delta m_h^2| \leq (m_h^{\text{exp}})^2_{\text{err}} = 35.028 \text{ GeV}^2 \tag{5.22}$$

Figure 5.2 shows the allowed regions in the $m_s \times s_h$ plane that meet this requirement at 1 (blue) and 2 (orange) σ. The green region represents the parameter space where the dark Higgs mass is smaller than $m_h/2$, which represents the kinetically accessible region for the $h \to ss$ decay.

5.3 Higgs boson invisible decays

The last EW precision test constraint that we will analyze here is related to the Higgs boson invisible decay width. Recall that to compute a total decay width, all possible final states must be considered, regardless if the final on-shell particles are unstable or not. Following this reasoning, we can consider, as a first approximation, only two-body decays for the calculation of the SM Higgs invisible decay width. Hence, the HAHM introduces three new possible decay channels for h, namely $h \to ss$, $h \to Z_\gamma Z_\gamma$ and $h \to Z Z_\gamma$. The first two contain invisible dark sector final states, and thus contribute to the invisible h decay width, while the last one will only

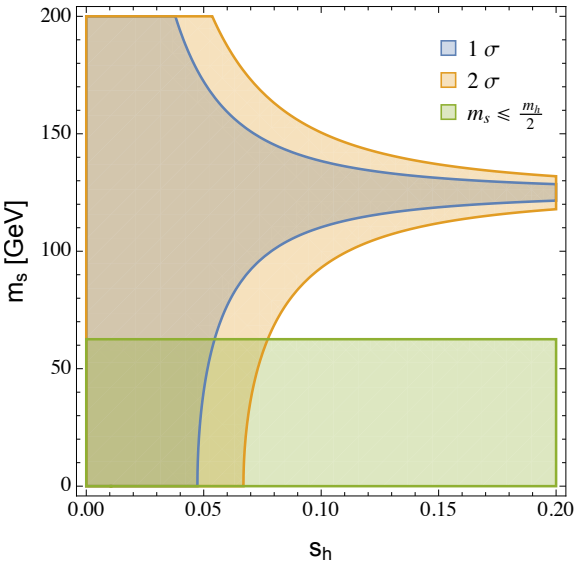

Figure 5.2: Regions in the $m_s \times s_h$ plane that fulfill the requirement that the correction of the SM Higgs squared mass should be smaller than the associated error at 1σ (blue) and 2σ (orange) deviations. The green region indicates the parameter space where the Higgs mass is at least two times higher than the dark Higgs mass.

contribute to the total Higgs decay width due to the Z boson final particle.

In spite of these last comments, we can write down the new invisible branching ratio of the Higgs boson

$$\text{Br}(h \to \text{inv}) = \frac{\Gamma(h \to ss) + \Gamma(h \to Z_\gamma Z_\gamma)}{\Gamma_{\text{tot}}^{\text{exp}}}\,, \tag{5.23}$$

where $\Gamma_{\text{tot}}^{\text{exp}}$ represents the experimental value of the Higgs boson total width and we can use the explicit expressions for the tree-level decays given in equations (4.50) and (4.52) for the new invisible decay widths. Now, we can combine this expression with the measured values [2]

$$\Gamma_{\text{tot}}^{\text{exp}} = 3.2^{+2.8}_{-2.2}\,\text{MeV}, \quad \text{Br}(h \to \text{inv}) < 0.19\,, \tag{5.24}$$

to obtain the allowed regions in the $m_{Z_\gamma} \times m_s$ parameter space that fulfill this branching ratio constraint, which are shown in the left panel of figure 5.3 for different choices of κ. Note that for $\kappa < 6 \times 10^{-3}$ we are safe to choose any (m_{Z_γ}, m_s) combination and still agree with the invisible Br constraint.

In the right panel of figure 5.3 we show the branching ratios of the three decays: $h \to ss$ (red), $h \to Z_\gamma Z_\gamma$ (purple) and $h \to Z Z_\gamma$ (green). Note that the $\Gamma(h \to Z Z_\gamma)$ decay is subdominant in comparison with the others. The fact that the KM parameter only appears in this branching ratio justifies why the invisible SM-like Higgs decay constraint is independent

of ϵ. For this branching ratio calculation we fixed $\kappa = 5 \times 10^{-3}$, $\epsilon = 0.01$ and $m_{Z_\gamma} = 1\,\text{GeV}$.

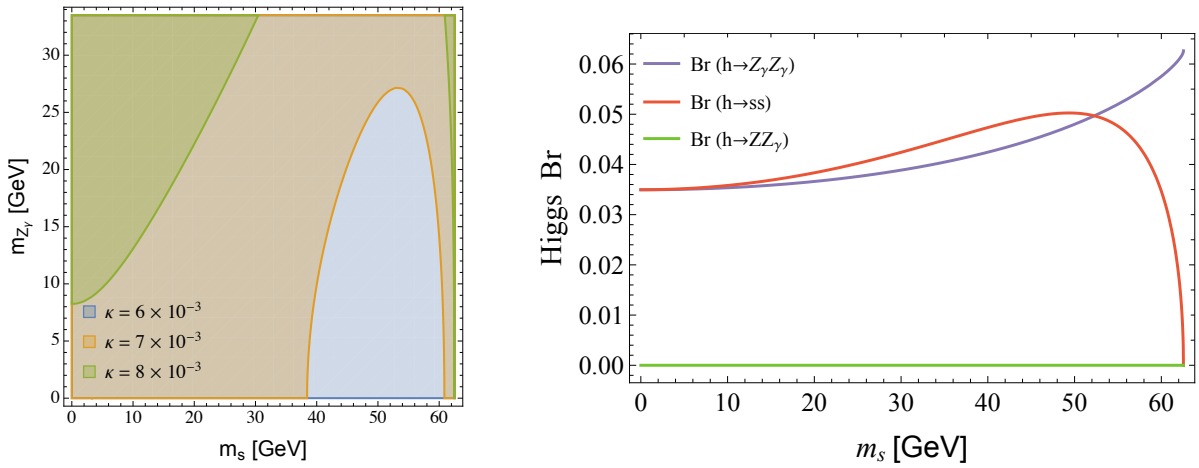

Figure 5.3: In the left panel we show the available regions that agree with the branching ratio constraint $\text{Br}(h \to \text{inv}) < 0.19$ for $\kappa = 6 \times 10^{-3}$ (blue), $\kappa = 7 \times 10^{-3}$ (orange) and $\kappa = 8 \times 10^{-3}$ (green). In the right panel we show the branching ratios for the processes $h \to ss$ (red), $h \to Z_\gamma Z_\gamma$ (purple) and $h \to Z Z_\gamma$ (green) considering $\kappa = 5 \times 10^{-3}$, $\epsilon = 0.01$ and $m_{Z_\gamma} = 1\,\text{GeV}$.

5.4 Summary of EW constraints

Finally, now that we computed and presented all the relevant EW precision constraints, we can combine the results to obtain the final bounds on the HAHM free parameters. Table 5.1 enumerate all the new independent parameters introduced in the model and distinguish which of them we choose to fix (right) and which we leave as free observables (left). We also show the obtained EW constraints on the free parameters and the definitions of the fixed variables in terms of the free ones.

It is important to highlight that, since in this first part of the project we were just focused on obtaining some preliminary constraints on the HAHM parameters for the phenomenological study, we were not concerned on performing a full EW precision test analysis. Hence, we decided to follow the simplified approach presented here and employed some approximations, such as to consider the experimental mass of the Z and Higgs boson very close to the undiagonalized fields Z_0 and h_0, respectively. A better approach would be to perform a global fit or to consider the oblique electroweak corrections.

Let us now make some comments about the parameters. First, we fixed the scalar $U(1)_\gamma$ charge to $q_S = 1$, and from now on, we will always assume this value. Regarding the λ_S quartic coupling, the bound displayed in the table comes from perturbativity and vacuum sta-

bility constraints, as described in [166]. Finally, since in this dissertation we choose to study the mass hierarchy $m_h > m_s > m_{Z_\gamma}$, the dark Higgs and *dark photon* mass should satisfy $0 < m_s < m_h/2$ and $0 < m_{Z_\gamma} < m_s/2$ in order to enable the $h \to ss$ and $s \to Z_\gamma Z_\gamma$ decays.

Parameter	Status	Constraint
ϵ	Free	$\epsilon \leq 10^{-2}$
κ	Free	$0 < \kappa \lesssim 6 \times 10^{-3}$
m_{Z_γ}	Free	-
m_s	Free	-
g_D	Free	-

Parameter	Status	Definition
s_h	Fixed	$s_h = \frac{\kappa v v_S}{m_s^2 - m_h^2}$
v_S	Fixed	$v_S = \frac{m_{Z_\gamma}}{g_D}$
λ_S	Fixed	$\frac{\kappa^2}{4\lambda} < \lambda_S = \frac{m_s^2}{2v_S^2} < 4\pi$
s_α	Fixed	$s_\alpha \simeq -\epsilon t_W$

Table 5.1: Summary of Electroweak precision tests constraints on the HAHM parameters. We choose $\epsilon, m_{Z_\gamma}, m_s, \kappa$ and g_D to be the model free parameters (left table) while v_S, λ_S, s_h and s_α are fixed according to the chosen values of the free parameters (right table). For the case of the free (fixed) variables, we display in the third columns the obtained EW constraints (parameter definitions). We fix the scalar charge $q_S = 1$.

Now that we have a better assessment of the HAHM free parameters and constraints we are ready to move on to practical phenomenological studies. In particular, we are interested in investigating the possible limits we can obtain by considering searches of $h \to Z_\gamma Z_\gamma \to 4\mu$. In order to compute these limits we rely on computational softwares for simulating the specific process we are interested, such as the Monte-Carlo simulation program MADGRAPH [169]. In fact, the specific choice of $\epsilon, m_{Z_\gamma}, m_s, \kappa$ and g_D as our free parameters was motivated by this program, since in the implemented FEYNRULES [170] file these were the available parameters. In the next chapter, we will focus on describing the computational implementation of the HAHM, together with the methodology we follow for the process simulation and phenomenological analysis. We will also investigate another HAHM bound by considering the invisible kaon decay $K_L^0 \to \pi^0 + \text{inv}$ measured by the KOTO experiment.

Chapter 6

Searching the Higgs and $U(1)$ portals

In the second part of this dissertation we introduced a UV complete scenario to the $U(1)_Q$ extension described in the first part. In this model, dubbed HAHM, beside the *dark photon* gauge boson we also add a new scalar s, which develops a VEV and breaks spontaneously the secluded $U(1)_Q$ symmetry. The specific theoretical implications behind the addition of these two portals, *i.e.* the KM and Higgs portal, were described in chapter 4, and we saw that they lead to modifications of very well-measured EW observables. Therefore, in order to agree with the EW precision tests, we explored several constraints on the HAHM parameters in chapter 5. Now, we are concerned with exploring how we can limit the available HAHM parameter space by performing searches on processes that depend on the model free variables.

In particular, we focus on the study of two different searches that can put bounds on the Hidden Abelian Higgs Model. The first one is related to the decay $h \to Z_\gamma Z_\gamma$ which proceeds via the $s-h$ mixing, proportional to κ, followed by $Z_\gamma \to \mu^+\mu^-$ through the KM portal. Hence, any search for this process can constrain both the kinetic and scalar mixing parameters. In the work by [51], the authors considered this same decay in the HAHM framework. However, they did not implement any collider detector simulator to correctly compute the detection efficiency and also only consider the decays of the light *dark photon* inside the MADGRAPH [169] environment, which applies many approximations, such as neglecting hadronic decays and considering massless quarks and leptons. Besides, they perform a different treatment for the background rejection.

Here, we improve their results in several ways. On the one hand, for the computation of the detector efficiency we use the DELPHES [171] collider simulator to describe the muon decays inside CMS and ATLAS experiments at the LHC. On the other hand, for the correct description of the *dark photon* decays, we used a modified version of the MADDUMP [172] software for

the computation of decay probabilities. The modifications we add in the source code include an explicit computation of the light mediator decays into leptons, quarks and hadrons, that follows the implementation described in the first part of this dissertation and is based on the DELIVER [70] package.

The second search we explored is related to the KOTO [173, 174] experiment at JPARC. The goal of this experiment is the observation of the rare Flavor Changing Neutral Current (FCNC) decay $K_L^0 \to \pi^0\nu\nu$. Using data collected during the 2015 run, the collaboration established a new upper limit on the branching ratio $Br(K_L^0 \to \pi^0 + \text{inv})$, where inv represent any invisible final state. If we consider that this invisible particle is the dark Higgs, we can constrain the $s_h \times m_s$ parameter space via the decay $K_L^0 \to \pi^0 s$.

This chapter is divided into two sections. In the first section, we will focus on the ATLAS and CMS bounds obtained with a search in the channel $h \to Z_\gamma Z_\gamma \to 4\mu$. We begin by introducing the considered experiments, then we describe the methodology employed to simulate the decay and, finally, show the exclusion regions in the HAHM parameter space. In the second section, we analyze the KOTO limits obtained with the $Br(K_L^0 \to \pi^0 + \text{inv})$ branching ratio measurement. Similarly, after giving details about the experimental setup we explain the constraints we need to impose so that both Z_γ decay outside the detector and conclude with the final bounds on the $s_h \times m_s$ parameter space.

6.1 LHC bounds through the $h \to Z_\gamma Z_\gamma \to 4\mu$ decay

The first channel we chose to investigate is the $h \to Z_\gamma Z_\gamma \to 4\mu$ decay. This choice is justified since we can probe both the kinetic mixing and the Higgs portal with this kind of search (see figure 6.1). However, to produce the Higgs boson on shell, we need to rely on high-energy experiments, such as the ones currently running at the LHC proton-proton collider. In particular, among the four largest LHC experiments, only the CMS and ATLAS detectors were designed for Higgs particle production and have measured such particles.

This section is divided into three parts. In the first part, we describe the CMS and ATLAS experimental setup. After that, we explain the procedure we follow to correctly simulate the $h \to Z_\gamma Z_\gamma \to 4\mu$ decay via a combination of several computational tools. Finally, we conclude with our results on the exclusion bounds on the HAHM parameter space.

6.1.1 The CMS and ATLAS experiment

In order to exclude the HAHM parameter space, we simulate the search sensitivity of the ATLAS and CMS experiments considering the $h \to Z_\gamma Z_\gamma \to 4\mu$ decay. These two experiments

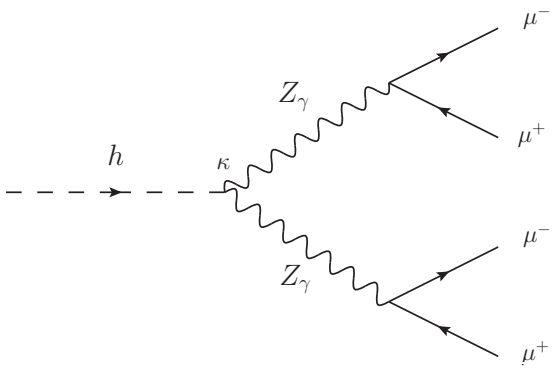

Figure 6.1: Feynman diagram of the $h \to Z_\gamma Z_\gamma \to 4\mu$ decay. The Higgs decay into two Z_γ can be used to probe the Higgs portal, while the *dark photon* decay can probe the KM parameter ϵ.

are the best choice for this kind of search since, up to this date, are the only detectors capable of producing and measuring the Higgs boson, being even known as Higgs factories. The reason is that the LHC is the only collider that can reach total collision energies of the order of $13\,\mathrm{TeV}$. Just for illustration, the second biggest hadron collider, which was the Tevatron accelerator at Fermilab, was only able to reach energies of $980\,\mathrm{GeV}$.

That being said, let us describe in more detail the CMS and ATLAS apparatus. The CMS experiment [175], which stands for Compact Muon Solenoid, is a general-purpose cylindrical detector with dimensions of 21 m long per 15 m in diameter. The experiment contains several layers of detectors sensitive to different kinds of particles, such as electromagnetic and hadronic calorimeters, as well as muon detectors (see left panel of figure 6.2). The detector was built around a huge solenoid magnet, responsible for generating a 4 Tesla magnetic field that deflects the charged particles track, which helps in the calculation of particle momenta and charges. Therefore, the particles can be tracked and their momentum and position are very well-measured. In particular, the efficiency of muon detection, which is relevant for us, is very high [176].

As the largest LHC detector, the ATLAS (A Toroidal LHC ApparatuS) experiment [50] is a 46 m long and 25 m in diameter cylindrical general-purpose detector. Similarly to CMS, the experiment is composed of several detector layers to identify different particles, including calorimeters, a muon spectrometer and a magnet system (see right panel of figure 6.2). Next to the interaction point, where the protons collide, there is a tracking system formed by pixel and silicon detectors. The magnets bend the particle trajectories in order to enable the computation of particle momenta. Together with the CMS experiment, the ATLAS detector participated in the Higgs boson discovery in 2012 [60, 61].

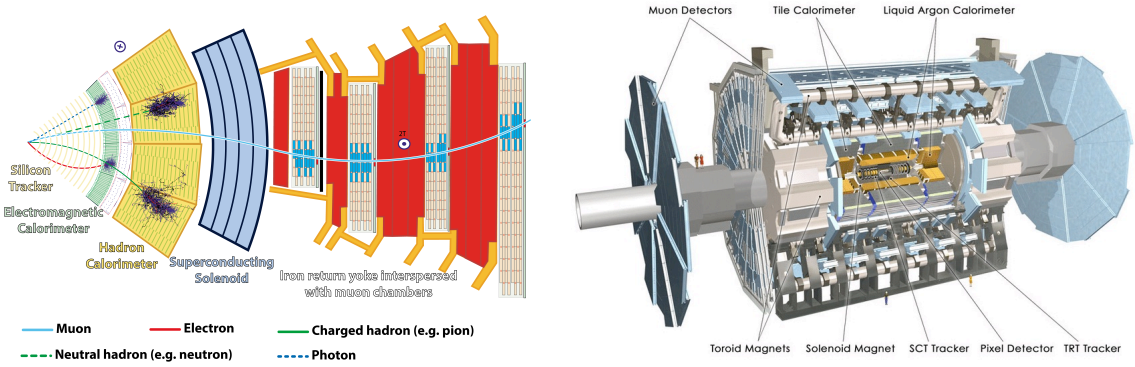

Figure 6.2: Illustration of the different detector layers of CMS (left) and ATLAS (right). Figures extracted from [49] (left) and [50] (right).

6.1.2 Signal Simulation

In order to simulate the $h \to Z_\gamma Z_\gamma \to 4\mu$ decay we used the MADGRAPH5 [169] Monte Carlo event generator, which is a computational tool for simulating high-energy collisions widely employed for LHC physics. A useful feature of this event generator is that it can be used to explore BSM physics as well. The software allows for the importation of user-defined models, created via the FEYNRULES [170] Mathematica package, inside the program interface, such that we can simulate processes with BSM particles. In a nutshell, for creating a new BSM model we simply need to define the new fields, the model parameters and the Lagrangian inside the FEYNRULES file. After that, the package will compute the Feynman rules and vertices of the defined model and output everything into a UFO (Universal FeynRules Output) folder that can be imported to MADGRAPH.

For the particular case of the HAHM, we employed the publicly available UFO implementation created by [51, 177] that can be found at `http://insti.physics.sunysb.edu/~curtin/hahm_mg.html`. After importing the UFO model into the MADGRAPH [1] interface, we simulated a proton-proton collision $p\ p \to Z_\gamma Z_\gamma$ with both *dark photons* decaying into muons $Z_\gamma \to \mu^+\mu^-$. We also included processes with one and two hadronic jets, *i.e.* $p\ p \to Z_\gamma Z_\gamma\ j$ and $p\ p \to Z_\gamma Z_\gamma\ j\ j$, where j is the label for the jet. As usual, after generating the output folder for the relevant process, we can launch it in the MADGRAPH interface and perform several 'runs' in which we can specify a series of variables, such as the HAHM parameters, the number of requested events, and several kinematic details.

In the process of event simulation, we can also run inside the MADGRAPH interface other programs, such as the showering and hadronization tool PYTHIA8 [178] and the fast collider detector simulator DELPHES [171]. In summary, the standard simulation chain begins with

[1] We used MADGRAPH version 2.6.4, which is the version compatible with the MADDUMP plugin.

the MADGRAPH software, which computes the matrix elements and generates Monte-Carlo parton-level events that are exported into a **.lhe** file. After that, PYTHIA8 realizes the parton showering and hadronization, returning the hadron-level events in a **.hepmc** output format. Finally, DELPHES receives the **.hepmc** file as an input and simulates the passage of particles through an LHC-style detector, producing a **.lhco** file. To correctly calculate the detection efficiency we performed this whole simulation chain for the $h \to Z_\gamma Z_\gamma \to 4\mu$ process generation.

However, for the correct $h \to Z_\gamma Z_\gamma \to 4\mu$ event selection, we applied several kinematic cuts in the runs. Essentially, there are two ways we can apply such cuts. The first one is by directly performing the cuts inside the MADGRAPH interface at the event-generation level via the `run_card.dat` file in the output decay folder. This card contain important information about several kinematic variables including the transverse momenta of each particle, the pseudo-rapidity, minimum and maximum invariant mass for pairs, among others. Although this option seems to be an easy solution, there are only a limited number of available cut choices. Besides, when we increase the number of kinematic cuts, we also increase the simulation time.

The second way we can perform the cuts is by using event selection tools after the simulation, such as the MADANALYSIS5 [179] program, or the LHCO_reader [180] python package. The former can be used for analyzing event files produced by Monte Carlo tools at parton level (**.lhe**), hadron level (**.hepmc**) or after detector simulation (**.lhco**). The later is a python module that reads detector-level events in **.lhco** format and allows the user to perform cuts, plots, inspect and manipulate the events.

In this analysis we choose to combine both event-generation level and post-simulation cuts. Below we list the required cuts we apply in the `run_card.dat` file inside the MADGRAPH interface:

- The minimum transverse momenta of the jets must be of $(p_T^j)_{\min} = 20\,\text{GeV}$.

- The maximum pseudo-rapidity for the jets must be of $(\eta^j)_{\max} = 5.0$.

After the conclusion of each run simulation, the remaining necessary cuts were applied at the detector-level events, *i.e.* on the **.lhco** file, by using the MADANALYSIS5 tool. The cuts were divided into two sets, one for the runs with $2\,m_\mu < m_{Z_\gamma} \leqslant 10\,\text{GeV}$ (light *dark photon* cut) and the other for the runs with $m_{Z_\gamma} > 10\,\text{GeV}$ (heavy *dark photon* cut). The lower limit in the *dark photon* mass window is exactly the production threshold of two muons. Below we list the applied cuts divided into the common cuts for the two sets and the specific ones.

Common Cuts

- The number of muons in the final state must be equal to 4.
- The minimum transverse momenta of the muons must be of $(p_T^\mu)_{\min} = 7\,\mathrm{GeV}$.
- The maximum pseudo-rapidity for the muons must be of $(\eta^\mu)_{\max} = 2.4$, where the pseudo-rapidity $\eta \equiv -\ln\tan(\theta/2)$ and θ is the angle between the particle trajectory and the beam axis.
- The reconstructed four-muon invariant mass must satisfy $120\,\mathrm{GeV} < m_{4\mu} < 130\,\mathrm{GeV}$.

Light *dark photon* cut

- We reject the events where the reconstructed invariant mass of the same vertex muon pair is higher than $10\,\mathrm{GeV}$, *i.e.* we select $m_{\mu^+\mu^-} < 10\,\mathrm{GeV}$.

Heavy *dark photon* cuts

- The invariant mass of the same vertex muon pairs must be smaller than $85\,\mathrm{GeV}$, *i.e.* we select $m_{\mu^+\mu^-} < 85\,\mathrm{GeV}$.
- The invariant mass of the state formed by the highest p_T muon and the highest p_T anti-muon must be smaller than $70\,\mathrm{GeV}$.

The muon pairs belonging to the same vertex are selected by looking the transverse momentum hierarchy. Besides these cuts, we also investigated the effect of performing a selection on the minimum leptonic angular separation variable $\Delta R_{\mu\mu} \equiv \sqrt{\Delta\phi^2 + \Delta\eta^2}$, where ϕ is the azimuthal angle. We considered three selection criteria: no cut on the angular separation, an angular separation between all muon pair combinations satisfying $\Delta R_{\mu\mu} > 0.02$ and satisfying $\Delta R_{\mu\mu} > 0.05$. From now on, we will label these three choices as cut A, cut B and cut C, respectively. We choose to add this cut since, in order to correctly detect a muon pair, we must have a minimum angular separation. However, in the literature it is not well established a common criteria for this observable and different studies employ different isolation cuts since the angular separation also depends on the muon momenta.

Regarding the other selection cuts, let us make some relevant remarks. First, all the transverse momentum and pseudo-rapidity cuts are related to the detector geometrical and energetic acceptance, and were motivated by [181, 182]. The cut on the four-muon invariant mass is extremely important in order to identify the Higgs vertex, since the SM-like Higgs mass was measured to $m_h \simeq 125\,\mathrm{GeV}$.

For the case of the light and heavy *dark photon* selection, the choices have different motivations. While the light *dark photon* cut is related to the reconstruction of the Z_γ mass, the heavy cut was based on a background analysis. Let us explain what we mean by this. To correctly investigate 4μ final states that can act as background events to our search, we simulated 1 million events of a proton-proton collision with four muons in the final state $p\,p \to 2(\mu^+\mu^-)$, also including one and two jets. When applying the selected cuts for the light *dark photon* case in this run, we ended with zero events, meaning that we do not have any background effect. However, in the case of the heavy *dark photon* selection, there were still some events that remained after the application of the cuts. The reason for that is because as we increase the mass we approach the Z boson peak, where the decay $h \to ZZ \to 4\mu$ can contaminate our search. Hence, we tried several observable combinations to obtain a cut that maximizes the signal-to-background ratio. The best cut that minimizes the background was related to the rejection of the muon pair masses that are close to the Z boson mass peak, as described above, and this was the chosen cut to the heavy *dark photon* search. Nevertheless, even with this cut we still end up with some background events and we will return to this point later when we discuss the detection efficiency calculation.

Now that we explained our applied cuts, we can compare our approach to the one of reference [51]. In [51], the authors also considered the $h \to Z_\gamma Z_\gamma \to 4\mu$ decay channel, but they did not run any detector simulator tool to properly calculate the detection efficiency. Therefore, they only applied the event selection cuts at the event-generation level inside the MADGRAPH interface. This can be a problem since, for instance, the selection cut we applied requiring four muons in the final state at the detector-level excluded approximately 60% of the generated events.

Another difference that is important to highlight is that in [51] they included an explicitly *dark photon* mass dependent cut which requires the invariant mass of both dimuon pairs to be close to m_{Z_γ}. Although this selection criteria was a great choice for background rejection, this kind of cut is problematic since, even though in the simulation we can fix the *dark photon* mass, in a real life search we do not have this information. Hence, this condition cannot be adapted in practice to a real experimental search. Regarding the background rejection, for high *dark photon* masses they employed a method to estimate the background events that are close to a small signal region on the dimuon mass plane centered at the DP mass. For light *dark photon* they only comment that their *dark photon* mass dependent double dimuon mass cut is so strong that the background can be completely neglected.

After establishing the general methodology we follow in order to simulate the $h \to Z_\gamma Z_\gamma \to 4\mu$ signal, we can explain how we proceed to obtain the bounds on the scalar and kinetic mixing

HAHM parameters. In the case of the Higgs portal constraint, we considered the prompt decay of the *dark photon* into a muon pair. This prompt limit can be achieved by considering a relatively large ϵ. Now, according to the narrow-width approximation, when the Z_γ is on-shell its production and decay can be treated separately. This implies that the cross-section of the process will turn to be a production rate, since, although the decay $\Gamma(Z_\gamma \to \mu^+\mu^-) \propto \epsilon^2$, we will get another ϵ^2 factor in the denominator coming from the total Z_γ decay rate. Hence, in the end, the cross-section of the $h \to Z_\gamma Z_\gamma \to 4\mu$ decay, for prompt Z_γ, is independent of the KM parameter ϵ (we just need to be sure to choose an ϵ which preserves the prompt condition).

Another feature of this search is that the cross-section is proportional to κ^2. Therefore, in the simulation procedure, we just need to change the m_{Z_γ} parameter in each run, but we can fix κ and ϵ as well. The dark Higgs mass can also be fixed since we will show the results as limits on κ', which is the only variable in the cross-section that depend on m_s. Hence, in order to obtain the scalar mixing bound we realized 19 different runs for m_{Z_γ} between $[0.3 - 50]\,\mathrm{GeV}$, each one with 250K generated events. As explained before, in the simulation procedure we used PYTHIA8 and DELPHES tools for the correct hadronization and detector response. After each run, we applied the described cuts using MADANALYSIS5, such that we end up with the final number of events N_f for that specific κ value. In the case of the heavy *dark photon* runs, we need to remember to subtract from N_f the normalized number of background events. Now, in order to re-scale the final number of events for any luminosity it is useful to remember that

$$N = L\,\sigma\,,$$

where N is the number of events, L is the luminosity and σ the cross-section. Hence, the final number of events N_f^L for a luminosity L is given by

$$N_f^L\,(m_{Z_\gamma}) = \frac{N_f(m_{Z_\gamma})\sigma(m_{Z_\gamma})L}{N_i}\,, \tag{6.1}$$

where $N_i = 250\mathrm{K}$ is the initial number of generated events and the cross-section σ is computed in the simulation [2]. Finally, in order to obtain the κ' value that correspond to $N_f^L = 3$ events, where 3 events represent a 95% confidence level bound, we can simple re-scale κ according to

$$\kappa^L\,(m_{Z_\gamma}) = \sqrt{3 \cdot \frac{\kappa^2}{N_f^L(m_{Z_\gamma})}}\,, \tag{6.2}$$

[2] It is worth remarking that, when we run PYTHIA8, the simulation returns the original cross-section σ but also another cross-section σ^m computed after the jet matching. Here we need to be careful since after the matching the number of events also decrease to N_i^m, such that the ratio σ/N_i is equal to σ^m/N_i^m and eq. (6.1) is consistent.

where $\kappa = 2.37 \times 10^{-3}$ is the value we fixed for κ in the simulation. Following this procedure we were able to obtain the bound on the $\kappa' \times m_{Z_\gamma}$ parameter space for different integrated luminosities, as we will show in the next section.

Now, for the case of the constraint in the KM portal, *i.e.* in the $\epsilon \times m_{Z_\gamma}$ plane, we consider the displaced *dark photon* decay in the $h \to Z_\gamma Z_\gamma \to 4\mu$ process. The number of signal events in the detector N_{evts} can be computed via the equation

$$N_{\text{evts}} = N_{Z_\gamma} P_{\text{dec}}\, \varepsilon_\mu \,, \tag{6.3}$$

where N_{Z_γ} is the number of produced *dark photons*, ε_μ is the combined efficiency of detector effects and kinematic cuts and P_{dec} is the probability that the two *dark photons* decay into muons inside the detector, given by

$$P_{\text{dec}} = f_{\text{geom}}\left[\left(e^{-d_1/\lambda_1} - e^{-l_1/\lambda_1}\right)\left(e^{-d_2/\lambda_2} - e^{-l_2/\lambda_2}\right)\right]\left[\text{Br}(Z_\gamma \to \mu^+\mu^-)\right]^2 , \tag{6.4}$$

where f_{geom} is the detector geometrical acceptance, *i.e.* the fraction of events that intersect the detector volume, $i = 1, 2$ labels the *dark photon* particles, d_i and l_i are the distances at which the Z_γ^i enters and exits from the detector, and $\lambda_i = c\beta_i\gamma_i/\Gamma_{Z_\gamma}$ is the *dark photon* decay length, with β the velocity, γ the boost factor and Γ_{Z_γ} the total decay width.

For the correct calculation of this decay probability we employed the MADDUMP [172] plugin. Although originally conceived for beam-dump simulations, this tool can be useful for any search that rely on displaced decays. The python-based source code can be integrated together with MADGRAPH to correctly calculate the decay probability described in eq. (6.4). For the proper use of this program we need to modify the pythonic source code in order to include the specific geometrical configurations of the chosen experiment we are analyzing, as well as to set the explicit decay probability formula for the process we are studying. In our case, we choose to investigate the constraints from the ATLAS experiment, such that we implemented in the code the cylindrical ATLAS geometry as described in section 6.1.1. We also set $d_i = 0$ in the decay probability formula since there is no distance from the interaction point and the detector. It is important to highlight that a more careful analysis would also include boundary effects of the detector geometry (see [183]).

Besides the usual adaptations we need to apply in the MADDUMP displaced decay python code, we also modified the decay width calculation. Originally, the MADDUMP software would read from the MADGRAPH cards the calculated decay widths of the chosen displaced particle. However, since MADGRAPH was created with the purpose of high-energy physics calculations, during the decay width computation it generally considers the massless limit for leptons and

quarks.

In addition to this, except for a few resonances, the MADGRAPH interface does not include any hadronic calculation. This is not a problem for very massive particle decays, since for high energies we are in the perturbative quark limit. However, as we saw in the first part of dissertation, for light particles the hadronic decays are a major component of the particle width and can widely affect the results. Therefore, in order to correctly calculate the *dark photon* total width and branching ratio we wrote an external python program to include the leptonic width calculation as well as the hadronic decay implementation, as described in the first part of this dissertation.

Let us now quickly summarize the simulation procedure we follow. The first step was to generate the $p\ p \to Z_\gamma Z_\gamma$ collision via the MADGRAPH interface. In this case we did not run PYTHIA8 or DELPHES since we only need the **.lhe** files which contain the *dark photon* variables information. We performed several runs for m_{Z_γ} between $[0.3 - 50]\,\text{GeV}$, each one of them producing a **.lhe** file. After that, we simulated the displaced decay of the *dark photon* into muons in the MADDUMP interface for each m_{Z_γ} by importing the corresponding **.lhe** file and also using the modified python code. In the end of the simulation, the program returns to us the decay probability of eq. (6.4).

Finally, to conclude the calculation of the number of events given in eq. (6.3), there are still two elements we need to compute. In the case of the number of produced *dark photons* N_{Z_γ}, we can compute it for a specific luminosity by using the $p\,p \to Z_\gamma Z_\gamma$ cross-section given by MADGRAPH. Now, for the case of the combined efficiency ε_μ, we need to rely on the DELPHES simulation performed in the previous analysis. Recall that, for each m_{Z_γ} simulation, we started with an initial number of events N_i and ended with N_f after the kinematic cuts. We can simply calculate the efficiency as a function of DP mass with the ratio

$$\varepsilon_\mu(m_{Z_\gamma}) = \frac{N_f - N_{\text{BKG}}}{N_i}\,,$$

where $N_{\text{BKG}} = 0$ for the light DP case and vary with m_{Z_γ} for the heavy DP case.

6.1.3 Results and Discussion

After describing the procedure we follow in order to simulate the $h \to Z_\gamma Z_\gamma \to 4\mu$ signal, for both the prompt and displaced searches, we are ready to present the obtained exclusion regions on the HAHM parameter space.

In figure 6.3 we show the exclusion limits in the $\kappa' \times m_{Z_\gamma}$ parameter space for the prompt $h \to Z_\gamma Z_\gamma \to 4\mu$ search described in the last section. We perform the simulation for $m_s =$

$300\,\mathrm{GeV}$ and $m_s = 40\,\mathrm{GeV}$, but, as we explained before, the bounds are independent of this choice. During the simulation we run the DELPHES software for the detector configurations of ATLAS and CMS. The final obtained exclusion bounds were similar for both detector simulations, hence, the results presented in figure 6.3 apply for both ATLAS and CMS.

The left panel of figure 6.3 shows the results considering integrated luminosities of $3000\ \mathrm{fb}^{-1}$ (purple), $300\ \mathrm{fb}^{-1}$ (orange), $139\ \mathrm{fb}^{-1}$ (red) and $10\ \mathrm{fb}^{-1}$ (blue). We also exhibit the constraints for the different muon angular separation cuts, which we divided into a set without the angular cut (cut A in dashed lines), a minimum angular separation of $\Delta R_{\mu\mu} > 0.02$ (cut B in solid lines) and the more restrictive cut with $\Delta R_{\mu\mu} > 0.05$ (cut C in dash-dotted lines). Each one of these cut choices have four different curves which correspond to the above mentioned luminosities. Note that the angular separation cut only has an impact for smaller *dark photon* masses.

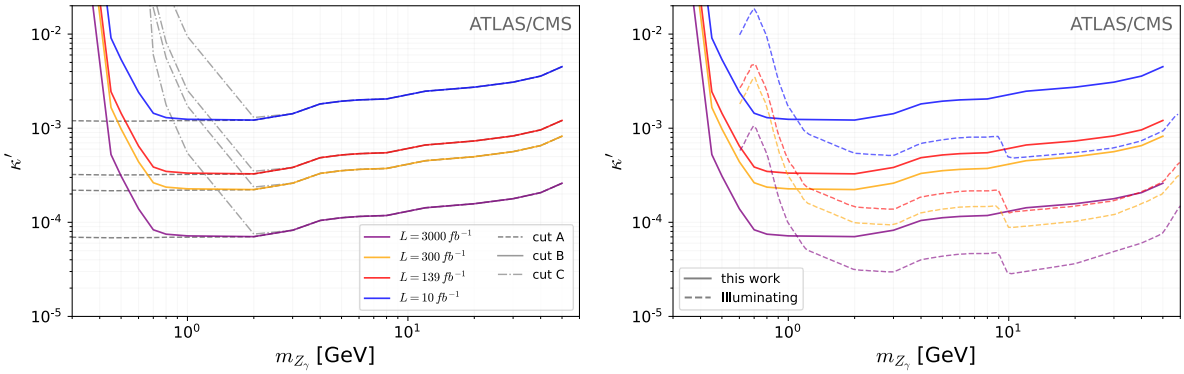

Figure 6.3: In the left panel we show the exclusion bounds on the $\kappa' \times m_{Z_\gamma}$ parameter space for different luminosities and considering the three distinct angular muon cut. In the right panel we compare the results obtained in this dissertation with the use of cut B, with the previous results from [51]. These bounds represent a full simulation of the CMS and ATLAS detector response. The COM energy was fixed to $13\,\mathrm{TeV}$ and the curve with $L = 139\ \mathrm{fb}^{-1}$ (red) corresponds to the current integrated luminosity of ATLAS [52].

The right panel of figure 6.3 shows the comparison between the exclusion bounds obtained in this dissertation with cut B (solid lines) and the results from [51] (dashed lines) following the same color convention for the luminosities. From the figure, we can see that for $m_{Z_\gamma} > 1\,\mathrm{GeV}$ the bounds computed in [51] are stronger than ours. There are several reasons that can explain this difference, for instance, in the simulation procedure we included the detector response and performed the cuts at the detector level events. In particular the four muon cut was very restrictive, since in the DELPHES software the events are reconstructed after passing through the different detector layers, such as the electromagnetic and hadron calorimeters, as well as the muon identification system. Although in this procedure we can lost a lot of final muon states, this must be taken into account since we want to perform a more realistic detector analysis.

Now, for masses $m_{Z_\gamma} < 1\,\mathrm{GeV}$, we can see that our limits are more exclusive. This is a consequence of the fact that we choose to adopt the intermediate angular separation cut B for the final bound. Let us explain this choice. From the left panel of figure 6.3, we can see the importance of applying the angular muon cut, since we expect that for very light Z_γ the detector response starts to decline. Hence, since we need to apply an isolation cut, we cannot employ cut A, which left us with the intermediate cut B and the more restrictive cut C. Based on a CMS muon reconstruction study [176] we chose to select the intermediate $\Delta R_{\mu\mu} > 0.02$ cut.

It is important to mention that during the development of the study described here, the ATLAS collaboration publish a similar analysis [52] were they explored the same $h \to Z_\gamma Z_\gamma \to 4\mu$ signal considering a integrated luminosity of $L = 139\ fb^{-1}$. In particular, in figure 19 of such paper they also present the exclusion bounds on the $\kappa' \times m_{Z_\gamma}$ parameter space. Our bounds show a good agreement with the experimental ATLAS results, which validates the procedure we follow in the simulation.

In figure 6.4 we show the bounds on the $\epsilon \times m_{Z_\gamma}$ parameter space obtained with the $h \to Z_\gamma Z_\gamma \to 4\mu$ displaced decay simulation for a $13\,\mathrm{TeV}$ COM energy collider. As we explained in the last section, we implemented the ATLAS detector geometry inside the MadDump interface, such that the exhibit bounds correspond to the ATLAS experiment sensitivity. The colors indicate different κ choices and the regions in grey are the constraints of other experimental searches on the *dark photon* model parameter space (same as the exclusion regions of figure 3.6).

The first evident feature of the new bounds is that they cover an yet unexplored region of the parameter space. Note also that we have a loss of sensitivity between 0.8 and $1.0\,\mathrm{GeV}$. This is an effect of the inclusion of hadronic decays in the simulation, since in this region we have the peak of the ρ, ω and ϕ resonances. Hence, due to the increase of the *dark photon* hadronic width in this mass window, the branching ratio into muons decreases, which in turn weakens the bound. This effect is not present in the bounds presented in [51], since they do not include hadrons in their computation.

6.2 KOTO bounds

The last bound we want to address concerning the HAHM model is related to the invisible decay of the long-lived neutral kaon $K_L^0 \to \pi^0 + \mathrm{inv}$. The KOTO collaboration recently establish a new upper limit for the branching ratio of such process [173, 174]. By considering the decay $K_L^0 \to \pi^0 s$ we can simple constraint the HAHM scalar mixing parameter by comparing $\mathrm{Br}(K_L^0 \to \pi^0 s)$ with the measured KOTO $\mathrm{Br}_{\mathrm{exp}}(K_L^0 \to \pi^0 \nu\bar{\nu})$ branching ratio.

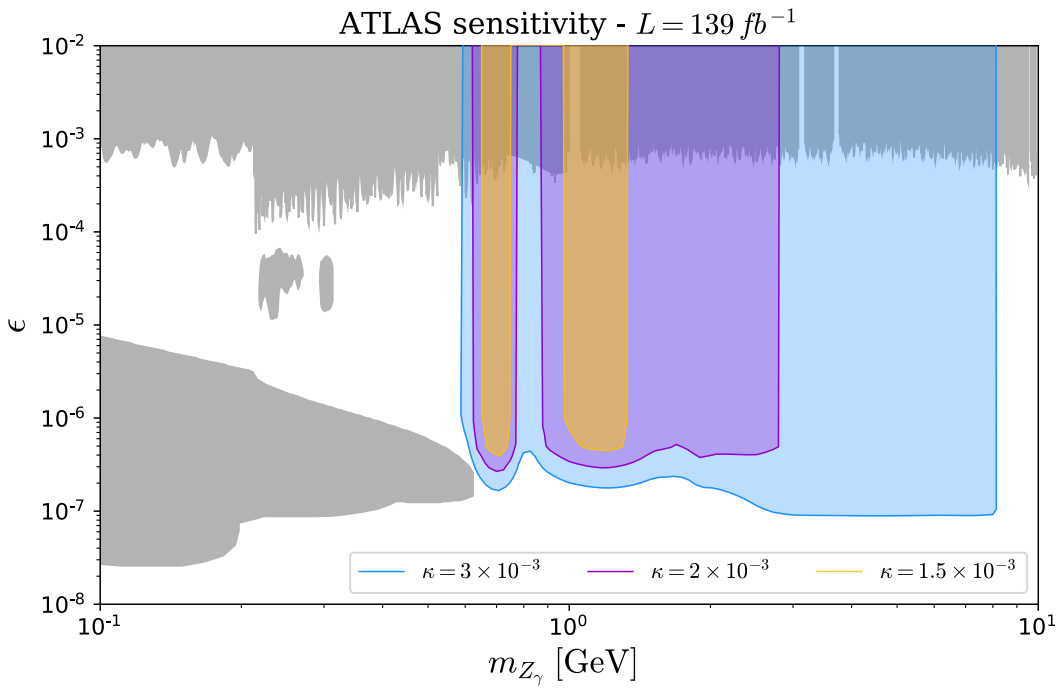

Figure 6.4: Final sensitivity of the ATLAS experiment on the $\epsilon \times m_{Z_\gamma}$ parameter space computed considering the $h \to Z_\gamma Z_\gamma \to 4\mu$ displaced decay search for $\kappa = 3 \times 10^{-3}$ (blue), $\kappa = 2 \times 10^{-3}$ (purple) and $\kappa = 1.5 \times 10^{-3}$ (orange). The grey regions represent other *dark photon* experimental constraints for the searches displayed in figure 3.6. We considered COM energies of $13\,\mathrm{TeV}$ and the ATLAS luminosity of $L = 139\ fb^{-1}$ [52].

However, in order to correctly obtain this constraint we need to be careful with the decay of the dark Higgs into a pair of Z_γ, since the *dark photon* can decay into visible final states spoiling the $K_L^0 \to \pi^0 + \mathrm{inv}$ computation. Hence, for an accurate constraint, we require that the *dark photon* particle is sufficiently long-lived in order to escape the KOTO detector. Only in this case, the $K_L^0 \to \pi^0 s$ can be considered as a truly invisible signal.

In this section we will first introduce some details about the KOTO experiment. After that, we will discuss how we obtained the regions of the DP parameter space that satisfy the long-lived *dark photon* condition. Finally, in the last section we show the computed exclusion bounds.

6.2.1 The KOTO experiment

Located at the J-PARC Hadron Experimental Facility in Japan, the KOTO experiment was conceived for the search of the rare FCNC K_L^0 decay $K_L^0 \to \pi^0 \nu\bar{\nu}$. The SM branching ratio of such process is very suppressed since this decay can only proceed via loop effects. The search is performed by measuring the $\pi^0 \to \gamma\gamma$ decay signal, where the photons are detected with an

EM calorimeter.

Regarding the detector apparatus, the kaons are produced from the collision of a proton beam with a gold target. After that, they travel a distance of $D = 21.5$ m in the decay volume before reaching the detector, which has a length of $L_{\rm det} = 3$ m [184]. Using data collected during the 2015 experimental run, the KOTO collaboration set the following upper limit on the $\mathrm{Br}(K_L^0 \to \pi^0 \nu\bar{\nu})$ branching ratio

$$\mathrm{Br}_{\rm exp} \equiv \mathrm{Br}_{\rm exp}(K_L^0 \to \pi^0 \nu\bar{\nu}) < 3.0 \times 10^{-9}\,. \tag{6.5}$$

In the SM, the theoretical prediction of such branching ratio is

$$\mathrm{Br}_{\rm SM} \equiv \mathrm{Br}_{\rm SM}(K_L^0 \to \pi^0 \nu\bar{\nu}) = 3.0 \times 10^{-11}\,. \tag{6.6}$$

6.2.2 Long-lived *dark photon* condition

The width of the dark Higgs in the HAHM is dominated by the decay into two *dark photons* for any g_D parameter value higher than $\sim 10^{-7}\,\mathrm{GeV}$. Hence, we can assume that s will predominantly decay into *dark photons*. Now, in order to the $K_L^0 \to \pi^0 s \to \pi^0 Z_\gamma Z_\gamma$ process to mimic the search signal in the KOTO experiment, we must require that both the DP particles escape the detector.

Therefore, we need to calculate the probability $P(d > L_{\rm det})$ for the *dark photon* to decay after a distance d outside the detector, which is given by

$$P(d > L_{\rm det}) \equiv P_{Z_\gamma} = e^{-L_{\rm det}/c\beta\gamma\tau}\,, \tag{6.7}$$

where β and γ are the *dark photon* velocity and boost factor, respectively. In order to calculate the DP velocity we can simple compute the kaon and scalar velocities and use a sum rule to obtain β. We then require that the probability for the two *dark photons* decay outside the detector to be higher than 90%, which means that

$$0.9 < P_{Z_\gamma} < 1 \Rightarrow 0.81 < (P_{Z_\gamma})^2 < 1\,. \tag{6.8}$$

In figure 6.5 we show in green the region on the $\epsilon \times m_{Z_\gamma}$ parameter space that satisfies the condition given by (6.8), computed for a scalar mass in the kinematic threshold of the $K_L^0 \to \pi^0 s$ decay, *i.e.* for $m_s = m_{K_L^0} - m_{\pi^0} \sim 360\,\mathrm{MeV}$. Since the scalar s will decay in two *dark photons*, the maximum DP mass is $m_{Z_\gamma} = 180\,\mathrm{MeV}$. The red colored bound represents the region in which at least one *dark photon* decay inside the KOTO detector and, hence, spoils the $K_L^0 \to \pi^0 + \mathrm{inv}$ calculation. Therefore, the results we show in the next section are only

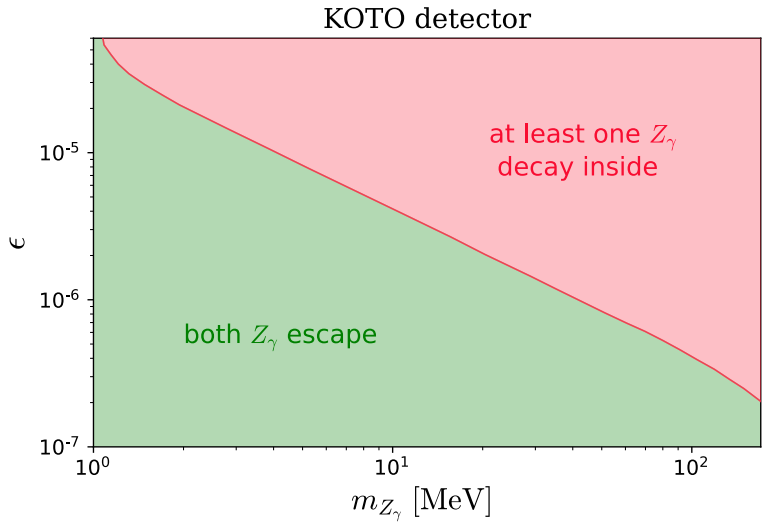

Figure 6.5: The green region represents the *dark photon* parameter values that satisfy the condition given by eq. (6.8), *i.e.* where we have a high probability that both Z_γ escape the KOTO detector such that the decay $K_L^0 \to \pi^0 s$ can mimic the invisible KOTO signal. The red region is the opposite case, for which the probability of at least one *dark photon* particle decays within the detector is dominant.

valid in this green region of the *dark photon* parameter space. Note that, for the mass hierarchy where $m_{Z_\gamma} > m_s$ we do not have this constraint, since, the decay $s \to Z_\gamma Z_\gamma$ is forbidden. But given that in this dissertation we choose to focus on the hierarchy $m_h > m_s > m_{Z_\gamma}$, we will not consider this other scenario.

6.2.3 Results and Discussion

For the calculation of the KOTO exclusion bound we need to use the formula of the $K_L^0 \to \pi^0 s$ decay branching ratio, given by [185]

$$\mathrm{Br}(K_L^0 \to \pi^0 s) = 7.0 \times 10^{-3} \, \frac{2\,\hat{p}(m_K^2, m_\pi^2, m_s^2)}{m_K} s_h^2 \,, \tag{6.9}$$

where $m_K = 497.6\,\mathrm{MeV}$ is the K_L^0 mass, s_h was defined in eq. (4.16) and

$$\hat{p}(m_K^2, m_\pi^2, m_s^2) = \frac{\lambda(m_K^2, m_\pi^2, m_s^2)}{2m_K} \tag{6.10}$$

where the λ function was given in eq. (B.3).

The constraint can be obtained by requiring the above scalar branching ratio to be smaller than the measured KOTO upper limit of eq. (6.5), such that we can exclude the HAHM parame-

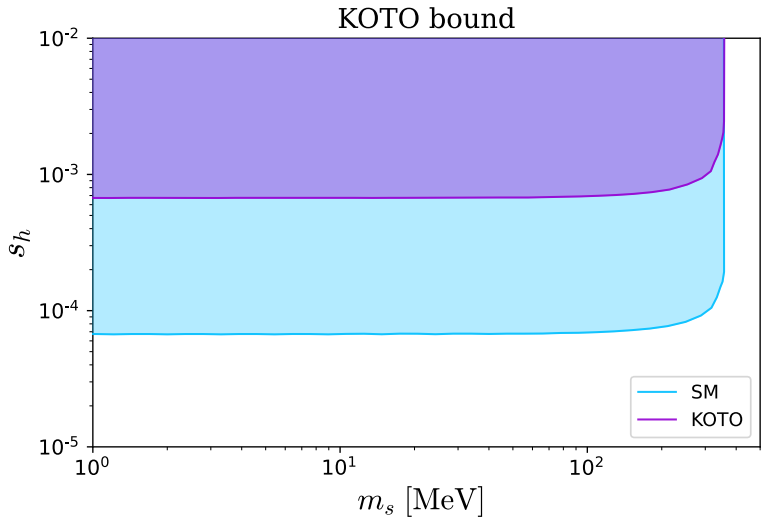

Figure 6.6: Bounds obtained with the $K_L^0 \to \pi^0 + \text{inv}$ branching ratio constraint on the $s_h \times m_s$ parameter space. The purple region represents the limits for the KOTO experiment while the blue region was computed considering the SM prediction for the $K_L^0 \to \pi^0 \nu\bar{\nu}$ branching ratio.

ters that would produce a $\text{Br}(K_L^0 \to \pi^0 s)$ bigger than the value measured by KOTO. Similarly, we can do the same for the SM branching ratio prediction given in eq. (6.6). We expect that, with more data and upgrades, the KOTO experiment will reach the SM upper limit in the future.

Figure 6.6 shows the constraints obtained following the above mentioned method considering the KOTO measurement (purple) and the SM prediction (blue) for the $K_L^0 \to \pi^0 \nu\bar{\nu}$ branching ratio. The SM limit represents the maximum possible sensitivity that the KOTO experiment can reach for such decay. From the figure we can see that this new KOTO limit lowers the previous EW precision test constraint on the scalar mixing angle from $s_h \lesssim 5 \times 10^{-2}$ to $s_h \lesssim 7 \times 10^{-4}$, for dark Higgs masses smaller than $\sim 360\,\text{MeV}$, which corresponds to an improvement of two orders of magnitude.

Conclusions and future perspectives

Up to this date, the Standard Model of particle physics is the most successful theory we have to describe the fundamental structure of matter. However, due to several questions that still remain unanswered, such as the dark matter and hierarchy problems, we know that the SM cannot be the final theory of Nature. As a result, the motivation to study theories that lie Beyond the Standard Model has increased a lot in the last few decades.

In particular, in this dissertation we studied BSM theories that contain a new light vector boson mediator particle. This particle is a consequence of the introduction of an extra $U(1)_Q$ abelian symmetry in the SM gauge sector, where Q represents the symmetry charge. In the secluded case, where the new boson does not enjoy any direct couplings to the SM particles, the portal that connects the dark sector with the SM is generated by a kinetic mixing term with the hypercharge boson, and the new boson particle is called *dark photon*. Besides this minimal scenario, we can also consider the generic $U(1)_Q$ case, where we have an explicit term on the Lagrangian that couples the new boson Z_Q with the SM fermions.

In the first part of this dissertation we investigated the consequences of the decays of the generic dark $U(1)_Q$ vector bosons. In particular, we focused on the hadronic decays of such particles. Although for the secluded case the hadronic decays can be easily calculated due to the *dark photon* photon-like couplings to fermions, in the generic $U(1)_Q$ case this task can become very complicated since we cannot use anymore the experimental $R_\mu^{\mathcal{H}}[\text{exp}] \equiv \sigma(e^+e^- \to \mathcal{H})/\sigma(e^+e^- \to \mu^+\mu^-)|_{\text{exp}}$ ratio. Hence, we rely on VMD-based techniques for the computation of the hadronic Z_Q decays. In a nutshell, in the VMD method we divide each hadronic current into ρ, ω and ϕ vector mesons components and then we proceed with the $Z_Q \to \text{hadrons}$ decay computation by simple considering the mixing between the new vector boson and the vector meson and the subsequent vector meson decay. This approach has been already considered in previous studies [1], however with several approximations and only with the implementation of a limited number of hadronic final states.

The main purpose of the first part of the study developed here was exactly to improve this hadronic decay description. After establishing the theoretical framework of the $U(1)_Q$ model

in chapter 1, we describe the VMD-based hadronic implementation we employed in chapter 2. We showed how we improved the hadronic decay computation by the inclusion of several extra hadronic modes, the use of recent experimental cross-section data and also by dividing the VMD contributions into the correct ρ, ω and ϕ components. For the majority of these new implemented hadronic channels we employed the parametrization and fits of [19], however we also performed the fit for four new hadronic channels that are very relevant in the higher energy region close to $\sim 2\,\mathrm{GeV}$. These channels were modeled for the first time here, and we describe in detail the fit procedure in appendix C.

All the above mentioned improvements on the hadronic calculation, as well as our final results, are summarized in reference [70], which was already accepted for publication by JHEP. We also created a python code for the computation of generic Z_Q decays where we included the hadronic implementation developed here. The code was made publicly available and can be found at https://github.com/preimitz/DeLiVeR.

To conclude this study, we investigated in chapter 3 the consequences of the implemented hadronic improvements in the calculation of the Z_Q hadronic width, branching ratios and also the possible effects on the evaluation of current and future experimental bounds. We saw that, compared to the previous assessment [1], we obtained some relevant differences on the hadronic decay width calculation of B-coupled $U(1)_Q$ models. Since in this kind of model the dark boson do not couple to the ρ current, the correct division of the ρ, ω and ϕ components is essential for a precise description of the baryophilic vector boson decays. For these models, such hadronic width modification lead to differences in the hadronic and leptonic branching ratios, which in turn can affect the experimental bounds. In particular, we saw that, in the case of the B model, the branching ratio reaches, for some mass values, a 30% deviation in comparison with the previous literature computation. Besides the branching ratio calculation, we also had modifications on the Z_Q lifetime, which influenced the B model experimental constraints, especially for beam-dump detectors.

Regarding the future experimental sensitivities, we showed how our hadronic implementation impact the expected reach of FASER, SHiP and Belle II. Let us remark that, although all the other considered searches rely on leptonic signals, the FASER experiment will be able to detect hadronic final states, such as $\pi\gamma$, 3π and KK. Hence, the correct VMD description of these modes is of extreme importance for baryophilic $U(1)_Q$ FASER searches. For more details on this topic, see our contribution to the FPF White Paper [186].

Although we have described in the first chapter the physics behind the $U(1)_Q$ BSM extension, we did not explain the origin of the dark boson mass term. Hence, motivated by the inclusion of a UV complete scenario to the *dark photon* model, in the second part of this disser-

tation we explored some phenomenological consequences of the Hidden Abelian Higgs Model. In this model, besides the *dark photon* boson, we also add a new SM singlet scalar which mixes with the SM-like Higgs doublet in the quartic term of the scalar potential. Hence, in addition to the KM portal we also have a Higgs portal in the HAHM. It is worth mentioning that both these portals are renormalizable. The *dark photon* mass generation mechanism proceeds via the SSB of the $U(1)_Q$ symmetry after the new scalar acquires a VEV.

In order to explore the phenomenology of the HAHM model, we first introduced in chapter 4 the physics behind the scalar mixing along with the new interactions and decay widths of the model. By doing so, we saw that several well-measured EW observables, such as the Higgs and the Z boson mass and couplings, received extra contributions suppressed by the HAHM parameters. Hence, we explored in chapter 5 the EW precision test constraints on the scalar and kinetic mixing variables. This study was important to set the baseline values for the HAHM parameters that were employed for the model simulation.

Finally, in chapter 6 we focused on some phenomenological implications of the HAHM. In particular we decided to study two different searches. The first one was related to the $h \to Z_\gamma Z_\gamma \to 4\mu$ process, which proceeds via the scalar and kinetic mixing vertices. Hence, with such signal we can constraint both the Higgs and the KM portals. For the former constraint, we considered the ATLAS and CMS bounds with a prompt *dark photon* decay search in the $h \to Z_\gamma Z_\gamma \to 4\mu$ channel. For the latter, we performed a Z_Q displaced decay search in the ATLAS experiment.

The methodology we follow in order to obtain such bounds was based on Monte-Carlo event simulator tools, such as MADGRAPH, PYTHIA8, DELPHES and MADDUMP. We described in chapter 6 the details of the signal simulation, as well as the employed kinematic cuts and the detector efficiency evaluation. Compared to the previous analysis of [51] for this same channel, we have implemented several improvements on the signal simulation. First, whereas in [51] the authors did not simulate the detector response, we employed the DELPHES software for the full detector simulation. We also applied the chosen kinematic cuts on the detector-level events, in order to calculate the combined geometric, energetic, and kinematic efficiency of the CMS and ATLAS experiments. Besides, we performed a background study to select the best kinematical cuts that enhance the signal-to-background ratio, while in [51] they used a *dark photon* mass dependent cut which is not the best choice for a real experimental search.

Regarding the simulation of the displaced Z_Q signal, we employed the MADDUMP software for the decay probability computation. We modified the python-based source code of this program to include the geometry of the ATLAS detector and the decay probability of the two *dark photon* displaced decay. In addition, we add the explicit calculation of the Z_γ leptonic

and hadronic decays, following the implementation described in the first part of this dissertation. This was crucial since the MADGRAPH software was primarily conceived for high-energy collision, such that it does not have any hadronic implementation and in general considers leptons and quarks as massless states. Since in [51] the authors only used this software, their results can be misleading for very light *dark photons*. A final remark is that we also included in the displaced search the detector efficiency obtained after applying the kinematical cuts at the detector-level events generated by the DELPHES software.

After performing the simulation and analysis of the prompt and displaced $h \to Z_\gamma Z_\gamma \to 4\mu$ searches, we obtained the final bounds in the $\kappa \times m_{Z_\gamma}$ and $\epsilon \times m_{Z_\gamma}$ parameter spaces, respectively. In the case of the Higgs portal constraint, our results are compatible with the recent published results of the ATLAS collaboration [52]. We also highlighted the main differences when comparing with the previous results from [51]. For the case of the KM constraint, we saw that the ATLAS experiment is capable of probing an unexplored region of the parameter space that extends for KM parameters between $10^{-4} \lesssim \epsilon \lesssim 10^{-7}$ and masses between $0.6\,\mathrm{GeV} \lesssim m_{Z_\gamma} \lesssim 10\,\mathrm{GeV}$, depending on the κ value. Another interesting feature was the appearance of the effects of our hadronic MADDUMP implementation in the final displaced bounds.

The other HAHM phenomenology analysis we investigated was related to the recently measured upper limit on the invisible kaon decay $K_L^0 \to \pi^0 + \mathrm{inv}$ branching ratio [173, 174]. By considering the HAHM decay $K_L^0 \to \pi^0 s$ we were able to set a bound on the $s_h \times m_s$ parameter space. Recall that the obtained EW precision test limit to this mixing angle was $s_h \lesssim 5 \times 10^{-2}$. With the KOTO bound we lowered such constraint to $s_h \lesssim 7 \times 10^{-4}$ for dark Higgs masses smaller than $\sim 360\,\mathrm{MeV}$. We also computed the bound for the SM $K_L^0 \to \pi^0 \nu\bar{\nu}$ branching ratio prediction. This limit represents the upper bound on s_h that the KOTO sensitivity can reach, *i.e.* the KOTO experiments can probe scalar mixing angles down to $\sim 7 \times 10^{-5}$.

Now that we described our main results, let us comment about our future research perspectives. Regarding the study developed in the first part of this dissertation, we plan to extend our work by including also dark matter candidates in the $U(1)_Q$ model framework. The DM candidates, which can be complex scalars, Majorana fermions, Dirac fermions, as well as inelastic DM particles, will couple directly to the dark boson Z_Q. In fact, we already started the study of such model and one can already find in our DELIVER python package the Z_Q decays into DM candidates. Right now we are investigating how the inclusion of this extended dark sector can impact the recast of the experimental *dark photon* bounds for other baryophilic models.

For the case of the HAHM, we are also studying other potential searches than can bound the model parameter space. In particular, we analyzed the sensitivity of the LHCb experiment to the displaced search $B \to Ks \to K Z_\gamma Z_\gamma \to K\ 4l$, where the dark Higgs is produced via B

meson decays into kaons, and then it subsequently decay into a *dark photon* pair which in turn produce a visible leptonic signal. We considered a scenario where the s decay is prompt while the *dark photon* can propagate before the decay. Following the same approach described in chapter 6, the simulations were made using a modified MADDUMP version with the inclusion of the correct width implementation, in this case for both the dark Higgs and the *dark photon* particles. Now, we are investigating the possibility to bound the HAHM with the B-factory experiments BaBar and Belle via the Upsilon decay.

To conclude, we just want to emphasize again the importance of studying and searching for BSM signals. The SM of particle physics was developed more than half century ago, and, although all the theoretical predictions could be verified with an exceptional good precision, several other experimental evidences suggest that there is still missing pieces that we are failing to describe. In this context, we need to rely on SM extensions to shed some light on the yet unanswered questions. In particular, a very good motivation for $U(1)_Q$ models is their simplicity and renormalizability, which makes them valuable candidates for the portal between our world and a possible dark sector. Although the search for this possible new dark boson can be very challenging, there are several future experimental prospects to enlarge the signal sensitivities. We hope that in the (near) future we can finally confront the truth behind the mysteries that Nature reserved for us to unravel.

Appendix A

Chiral Perturbation Theory for Mesons

In this appendix we will discuss in more detail the theoretical background that we used for the description of the hadronic processes in the width calculation. We will start by giving an overview of the effective theory that characterizes the low-energy degrees of freedom of Quantum Chromodynamics (QCD), denoted as Chiral Perturbation Theory (ChPT), that will cover pseudoscalar meson interactions with external fields. After that, we will introduce the couplings with an odd number of pseudoscalar mesons by considering the Wess-Zumino-Witten action. In the third section, we enlarge the ChPT Lagrangian by adding the vector meson interactions through the Hidden Local Symmetry model. Finally, in the last section we will comment on the Vector Meson Dominance (VMD) framework, which we employed in the main analysis of [70] for the decomposition of the hadronic processes into ρ, ω and ϕ components.

A.1 Chiral Perturbation Theory review

The SM of particle physics gives a good description for three of the four forces we have observed in Nature, *i.e.* electromagnetic, strong and weak forces. Within the SM, the theory that describes strong interactions is called QCD and deals with gluon and quark degrees of freedom. However, as the name already suggests, the strong force is strongly coupled, meaning that its perturbativity fails to work in the low-energy regime (energies smaller than $\sim 1\,\mathrm{GeV}$). Due to the phenomenon of confinement, the low energy degrees of freedom cease to be quarks and gluons and become composite states of quarks, called hadrons.

In order to describe this low-energy theory we need to rely on effective field theory (EFT) methods. ChPT is exactly the EFT that will deal with the low-energy dynamics of QCD, such as meson interactions, and the approximate chiral symmetry valid in that regime. In order to

obtain the chiral Lagrangian we start with the pure QCD Lagrangian including only the three lightest quarks u, d and s

$$\mathcal{L}_{\rm QCD} = -\frac{1}{4}(G^a_{\mu\nu})^2 + \bar{q}(i\not{D} - M_q)q\,, \tag{A.1}$$

where $G^a_{\mu\nu}$ is the gluon field strength tensor, q and $\bar{q}$ are the quark and anti-quark triplets $q = (u, d, s)^T$, $\bar{q} = (\bar{u}, \bar{d}, \bar{s})$, M_q is the quark mass matrix $M_q = \mathrm{diag}(m_u, m_d, m_s)$ and D is the covariant derivative

$$D_\mu = \partial_\mu + igG_\mu\,, \tag{A.2}$$

with $G_\mu = G^a_\mu T^a$ the eight gluon fields and T^a the $SU(3)_c$ generators. In order to expose the chiral behaviour of this Lagrangian we can decompose the quarks into their right-handed $P_R\, q = \frac{1}{2}(1+\gamma_5)q \equiv q_R$ and left-handed $P_L\, q = \frac{1}{2}(1-\gamma_5)q \equiv q_L$ projections

$$\mathcal{L}_{\rm QCD} = -\frac{1}{4}(G^a_{\mu\nu})^2 + i\bar{q}_L\not{D}q_L + i\bar{q}_R\not{D}q_R - \bar{q}_R M_q q_L - \bar{q}_L M_q^\dagger q_R\,. \tag{A.3}$$

Note that the mass terms spoil the total decoupling of the right-handed (RH) and left-handed (LH) fields. However, if we remember that the masses of these three quarks are much smaller than the QCD scale $m_u, m_d, m_s \ll \Lambda_{QCD} \sim 1\,\mathrm{GeV}$ [1], we can safely approximate the quark masses to zero, ending with

$$\mathcal{L}_{\rm QCD} = -\frac{1}{4}(G^a_{\mu\nu})^2 + i\bar{q}_L\not{D}q_L + i\bar{q}_R\not{D}q_R\,. \tag{A.4}$$

Now, we can see that this Lagrangian has two independent symmetries, that correspond to the individual rotation of the LH and RH fields, according to

$$q_L \to e^{i\theta^a_L T^a} q_L \equiv L\, q_L \quad (L \in SU(3)_L) \tag{A.5}$$

$$q_R \to e^{i\theta^a_R T^a} q_R \equiv R\, q_R \quad (R \in SU(3)_R) \tag{A.6}$$

where $\theta^a_{L,R}$ parametrize the $SU(3)_{L,R}$ transformation. Hence, we say that $\mathcal{L}_{\rm QCD}$ is symmetric under the chiral $SU(3)_L \times SU(3)_R$, where the word 'chiral' means that the symmetry acts differently on LH and RH fields. In fact, the massless QCD Lagrangian is symmetric under the symmetry group $G = SU(3)_L \times SU(3)_R \times U(1)_V \times U(1)_A$, where the last two groups

[1] Actually, we have $(m_u, m_d, m_s) = (2.15, 4.70, 93.5)/\mathrm{MeV}$, implying that $m_u, m_d \ll m_s$ and hence $SU(2)_L \times SU(2)_R$ is a better symmetry than $SU(3)_L \times SU(3)_R$.

correspond to vector and axial transformations

$$q \to e^{i\theta} q \quad (U(1)_V)\,, \tag{A.7}$$

$$q \to e^{i\theta\gamma_5} q \quad (U(1)_A)\,. \tag{A.8}$$

On one side, the vector $U(1)_V$ symmetry remains even with the inclusion of quark masses and represents the conservation of baryon number. On the other side, the axial symmetry $U(1)_A$ is anomalous, *i.e.* it is broken by quantum effects on what is denoted by the axial anomaly.

Although we have discovered the full symmetry group of the massless QCD Lagrangian, this is not the end of the story. For instance, right after the beginning of the Universe, when the temperatures lowered below the Λ_{QCD} scale, the quarks started to condensate, in what we call 'quark condensation' or 'chiral condensation' phenomenon [187]. The quark condensate acquires a VEV

$$\langle \bar{u}u \rangle = \langle \bar{d}d \rangle = \langle \bar{s}s \rangle = V^3\,, \tag{A.9}$$

which in turn spontaneously breaks the $SU(3)_L \times SU(3)_R$ symmetry into the diagonal subgroup $SU(3)_V$, also called $SU(3)_{\text{isospin}}$

$$SU(3)_L \times SU(3)_R \xrightarrow{\langle \bar{q}q \rangle} SU(3)_V \tag{A.10}$$

Note that, according to the Goldstone Theorem, since $\dim(SU(3)_L \times SU(3)_R) = 16$ and $\dim(SU(3)_V) = 8$, we must have $16 - 8 = 8$ broken generators, and hence, eight Nambu-Goldstone Bosons (NGB) arising from this SSB pattern. These eight pseudoscalars degrees of freedom must transform as an octet under $SU(3)_V$ and can be identified with the SM pseudoscalar mesons, as we will see next. First, let us parametrize the NGBs by the Goldstone matrix

$$\Sigma(x) = e^{i\Phi(x)/f_\pi}\,, \tag{A.11}$$

where f_π is the pion decay constant, which is a parameter with mass dimension,

$$\begin{aligned}\Phi(x) = \sum_{a=1}^{8} \lambda_a \phi_a(x) &\equiv \begin{pmatrix} \phi_3 + \frac{1}{\sqrt{3}}\phi_8 & \phi_1 - i\phi_2 & \phi_4 - i\phi_5 \\ \phi_1 + i\phi_2 & -\phi_3 + \frac{1}{\sqrt{3}}\phi_8 & \phi_6 - i\phi_7 \\ \phi_4 + i\phi_5 & \phi_6 + i\phi_7 & -\frac{2}{\sqrt{3}}\phi_8 \end{pmatrix} \\ &= \begin{pmatrix} \pi^0 + \frac{1}{\sqrt{3}}\eta_8 & \sqrt{2}\pi^+ & \sqrt{2}K^+ \\ \sqrt{2}\pi^- & -\pi^0 + \frac{1}{\sqrt{3}}\eta_8 & \sqrt{2}K^0 \\ \sqrt{2}K^- & \sqrt{2}\bar{K}^0 & -\frac{2}{\sqrt{3}}\eta_8 \end{pmatrix}\,,\end{aligned} \tag{A.12}$$

where λ_a are the Gell-Mann matrices normalized to $\mathrm{Tr}[\lambda_\mathrm{a}\lambda_\mathrm{b}] = 2\delta_\mathrm{ab}$, we identified the eight mesons with linear combinations of ϕ_a, *i.e.* the mesons manifest as excitations of the chiral condensate, and η_8 mixes with a non-NGB resonance η_0 to form the physical η and η' mesons. Note that the π^0, η and η' generators can be expressed as

$$\begin{aligned} T_{\pi^0} &= \frac{\lambda_3}{2} = \frac{1}{2}\mathrm{diag}(1,-1,0)\,, \\ T_\eta &= \frac{\cos\theta}{2}\lambda_8 - \frac{\sin\theta}{\sqrt{6}}\mathbb{1} \approx \frac{1}{\sqrt{6}}\mathrm{diag}(1,1,-1)\,, \\ T_{\eta'} &= \frac{\sin\theta}{2}\lambda_8 + \frac{\cos\theta}{\sqrt{6}}\mathbb{1} \approx \frac{1}{2\sqrt{3}}\mathrm{diag}(1,1,2)\,, \end{aligned} \tag{A.13}$$

where the $\eta - \eta'$ mixing angle θ satisfies $\sin\theta \simeq -1/3$ and $\cos\theta \simeq 2\sqrt{2}/3$ [188].

The Goldstone matrix transforms linearly under $SU(3)_L \times SU(3)_R$

$$\Sigma \to L\Sigma R^\dagger\,, \quad \Sigma^\dagger \to R\Sigma^\dagger L^\dagger\,, \tag{A.14}$$

such that the mesons will transform under infinitesimal transformations according to

$$\phi^a \to \phi^a + \frac{f_\pi}{2}(\theta_L^a - \theta_R^a) - \frac{1}{2}f^{abc}(\theta_L^b + \theta_R^b)\phi^c + \dots\,, \tag{A.15}$$

where f^{abc} are the structure constants of the $SU(3)$ algebra $[\lambda_a, \lambda_b] = 2if^{abc}\lambda_c$. Here we used the Baker–Campbell–Hausdorff formula and that $T^a = \lambda_a/2$. Note that in the broken phase we have $\theta_L^a = \theta_R^a$, confirming that the mesons will transform in the adjoint representation, given that the generators of the adjoint representation are the structure constants f^{abc} themselves. This is what we expected, since, for example, the physical pions transform according to the adjoint representation of the isospin group.

In order to build the chiral Lagrangian we must remember that it should contain the same approximate symmetry as in QCD, meaning that it must be invariant under the chiral transformation (A.14). Another feature of the low-energy effective theory is that it must behave as an expansion of operators suppressed by powers of a mass dimension parameter (cutoff). This cutoff will specify the valid energy regime of the chiral Lagrangian.

Armed with these arguments, we are ready to build the most general consistent chiral Lagrangian. The leading order term is given by [189, 190]

$$\mathcal{L}^0_\mathrm{ChPT} = \frac{f_\pi^2}{4}\mathrm{Tr}\left[(D_\mu\Sigma)(D^\mu\Sigma)^\dagger\right]\,, \tag{A.16}$$

and the complete Lagrangian is [191]

$$\mathcal{L}_{\rm ChPT} = \mathcal{L}^0_{\rm ChPT} + L_1\big(\mathrm{Tr}\left[(D_\mu\Sigma)(D^\mu\Sigma)^\dagger\right]\big)^2 + L_2\mathrm{Tr}\left[(D_\mu\Sigma)(D_\nu\Sigma)^\dagger\right]\mathrm{Tr}\left[(D^\mu\Sigma)(D^\nu\Sigma)^\dagger\right] + \dots \tag{A.17}$$

where the subleading L_i terms have at least four derivatives, resulting in suppressions proportional to an even number of extra f_π^{-1} powers compared to the leading term. We can also observe that all the Σ terms carry derivatives. This is a consequence of the fact that $\Sigma\Sigma^\dagger = \mathrm{I}$ would result in trivial terms.

To include external gauge fields we use a trick where we gauge the $SU(3)_L \times SU(3)_R$ symmetry introducing the associated gauge bosons l_μ and r_μ, respectively. Then, the covariant derivative that appears in eq. (A.16) acting on the Goldstone Matrix is given by

$$D_\mu\Sigma = \partial_\mu\Sigma + il_\mu\Sigma - i\Sigma r_\mu\,, \tag{A.18}$$

such that we have the following transformation laws

$$D_\mu\Sigma \to L(D_\mu\Sigma)R^\dagger\,, \tag{A.19}$$

$$r_\mu \to Rr_\mu R^\dagger + iR\partial_\mu R^\dagger\,, \tag{A.20}$$

$$l_\mu \to Ll_\mu L^\dagger + iL\partial_\mu L^\dagger\,. \tag{A.21}$$

For illustration, we can add the interaction with the photon field. We know that it couples identically to LH and RH quarks, therefore we can assign

$$r_\mu = l_\mu = eQA_\mu\,, \tag{A.22}$$

where e is the EM charge, $Q = \mathrm{diag}(q_u, q_d, q_s) = \mathrm{diag}(2/3, -1/3, -1/3)$ is the quark charge matrix and A_μ is the photon field. The interactions with the quarks then read

$$\begin{aligned}\mathcal{L}_{\rm int} &= \bar{q}_L\gamma^\mu l_\mu q_L + \bar{q}_R\gamma^\mu r_\mu q_R \\ &= eQA_\mu(\bar{q}_L\gamma^\mu q_L + \bar{q}_R\gamma^\mu q_R) = eQA_\mu\bar{q}\gamma^\mu q \\ &= eA^\mu\left(\frac{1}{\sqrt{2}}\left[(q_u - q_d)J_\mu^{I=1(3)} + (q_u + q_d)J_\mu^{I=0}\right] + q_s J_\mu^s\right) \\ &= eA^\mu J_\mu^{\rm had}\,,\end{aligned} \tag{A.23}$$

where we defined the third component of the isospin $I = 1$, the isospin $I = 0$, and the strange-

quark current, respectively, as

$$\begin{aligned} J_\mu^{I=1(3)} &= \frac{1}{\sqrt{2}}(\bar{u}\gamma_\mu u - \bar{d}\gamma_\mu d)\,, \\ J_\mu^{I=0} &= \frac{1}{\sqrt{2}}(\bar{u}\gamma_\mu u + \bar{d}\gamma_\mu d)\,, \\ J_\mu^{s} &= \bar{s}\gamma_\mu s\,. \end{aligned} \tag{A.24}$$

As we will see next, in the VMD approach we will assign these currents to the vector mesons ρ, ω and ϕ.

If we now expand the leading term of the chiral Lagrangian eq. (A.16), including the photon field, we obtain

$$\begin{aligned} \mathcal{L}^0_{\text{ChPT}} &= \frac{f_\pi^2}{4}\text{Tr}\left[(\partial_\mu\Sigma + ieQA_\mu\Sigma - i\Sigma eQA_\mu)(\partial^\mu\Sigma^\dagger - i\Sigma^\dagger A^\mu eQ + iA^\mu eQ\Sigma^\dagger)\right] \\ &= \frac{1}{2}(\partial_\mu\pi^0)^2 + (\partial_\mu\pi^+)(\partial^\mu\pi^-)^\dagger + \cdots + \frac{ief_\pi^2}{2}A_\mu\text{Tr}\left[\Sigma\partial^\mu\Sigma^\dagger Q - \Sigma Q\partial^\mu\Sigma^\dagger\right] + ... \end{aligned} \tag{A.25}$$

where in the second line we collected some kinetic terms for the pions as well as the linear term in A_μ. If we further expand Σ up to quadratic terms, the linear photon coupling becomes

$$\mathcal{L}^{0,\gamma}_{\text{ChPT}} = \frac{ie}{2}A_\mu\text{Tr}\left[Q[\Phi, \partial^\mu\Phi]\right]\,, \tag{A.26}$$

such that we can write down the terms that describe interactions between the photon and the pseudoscalar mesons

$$\begin{aligned} \mathcal{L}_{\gamma PP} =& eA_\mu i\Big((q_u - q_d)\left[\pi^-\partial^\mu\pi^+ - \pi^+\partial^\mu\pi^-\right] + \frac{1}{2}(q_u - q_d)\left[K^-\partial^\mu K^+ - K^+\partial^\mu K^-\right] \\ &+ \frac{1}{2}(q_u + q_d)\left[K^-\partial^\mu K^+ - K^+\partial^\mu K^-\right] - q_s\left[K^-\partial^\mu K^+ - K^+\partial^\mu K^-\right] + \dots\Big)\,, \end{aligned} \tag{A.27}$$

where the dots represent additional couplings to the $K^0, \bar{K}^0$ mesons.

Finally, just for completeness, it is important to include some comments about a possible mass term for the mesons. As we know, the shift symmetry of eq. (A.15) forbids a mass term for the mesons, since it would explicitly break the chiral symmetry. A viable solution would be

to promote the quark mass matrix into a fictitious field that would transform as

$$M_q \to L M_q R^\dagger \,, \tag{A.28}$$

such that we can build a chiral invariant mass term. We then call the mass matrix a *spurion*, *i.e.* an auxiliary field that will be used to determine the invariant operators under the symmetry. The chiral Lagrangian eq. (A.16) can now also include a mass term

$$\mathcal{L}^0_{\text{ChPT}} = \frac{f_\pi^2}{4}\text{Tr}\left[(D_\mu\Sigma)(D^\mu\Sigma)^\dagger\right] + \frac{f_\pi^2}{2}\Lambda_m \text{Tr}\left[M_q^\dagger\Sigma + \Sigma^\dagger M_q\right] , \tag{A.29}$$

where Λ_m is a new parameter with dimensions of mass that need to be fixed by experimental measurements.

A.2 Wess-Zumino-Witten term

Until now, the strategy we follow in the last section allowed us to build a Lagrangian to describe the dynamics of pseudoscalar mesons in conjunction with the interactions of the photon with an even number of pseudoscalars, such as the γPP coupling. However, what happens if we also want to give a description for the processes involving an odd number of pseudoscalars, like the $\pi^0 \to \gamma\gamma$ decay? To solve this question Wess, Zumino and Witten [192, 193] proposed an additional term to the chiral Lagrangian to account for these processes. When considering only the massless NGBs without external fields, this new term was expressed by the addition of the following term to the equations of motion of the chiral Lagrangian

$$\partial_\mu\left(\frac{f_\pi^2}{2}\Sigma\partial^\mu\Sigma^\dagger\right) + \lambda\varepsilon^{\mu\nu\rho\sigma}\Sigma\partial_\mu\Sigma^\dagger\Sigma\partial_\nu\Sigma^\dagger\Sigma\partial_\rho\Sigma^\dagger\Sigma\partial_\sigma\Sigma^\dagger = 0 \,, \tag{A.30}$$

where λ is a constant and $\varepsilon^{\mu\nu\rho\sigma}$ is the completely anti-symmetric Levi-Civita tensor. To formally include this term into the action functional of ChPT it is necessary to extend the field definition adding an extra hypothetical fifth dimension. We will not specialize here on the specific technical construction of the WZW action [2], but only quote the result for the term with the smallest number of NGBs,

$$S^{5\Phi}_{\text{WZW}} = \frac{1}{240\pi^2 f_\pi^5}\int \text{d}^4x\varepsilon^{\mu\nu\rho\sigma}\text{Tr}\left[\Phi\partial_\mu\Phi\partial_\nu\Phi\partial_\rho\Phi\partial_\sigma\Phi\right] \,, \tag{A.31}$$

[2] We refer to [189, 194] for more details about the WZW action construction.

where we already performed the integration over the fifth dimension. Now, if we want to include the external fields, it is necessary to add an extra term to the original WZW action $S^0_{\rm WZW}$, given by [195–197]

$$\begin{aligned} S_{\rm WZW} &= S^0_{\rm WZW} + S^{\rm ext}_{\rm WZW} \\ S^{\rm ext}_{\rm WZW} &= -\frac{iN_C}{48\pi^2}\int \mathrm{d}^4x\, \varepsilon^{\mu\nu\rho\sigma}\mathrm{Tr}\left[Z_{\mu\nu\rho\sigma}\right] , \end{aligned} \tag{A.32}$$

where $N_C = 3$ is the number of colors and $Z_{\mu\nu\rho\sigma}$ contains more than 20 terms which combine powers of $\Sigma, \Sigma^\dagger$, $\partial_\mu\Sigma, \partial_\mu\Sigma^\dagger$, l_μ and r_μ. For the special case of the photon field, where $r_\mu = l_\mu = eQA_\mu$, we can simplify this expression a lot due to symmetry arguments in the presence of the total anti-symmetric tensor. In the end, we obtain [189, 194]

$$\begin{aligned} \mathcal{L}^{\rm ext}_{\rm WZW} =& eA_\mu J^\mu + i\frac{N_C e^2}{48\pi^2}\varepsilon^{\mu\nu\rho\sigma}\partial_\nu A_\rho A_\sigma \mathrm{Tr}\Big[2Q^2(\Sigma\partial_\mu\Sigma^\dagger - \Sigma^\dagger\partial_\mu\Sigma) \\ & - Q\Sigma^\dagger Q\partial_\mu\Sigma + Q\Sigma Q\partial_\mu\Sigma^\dagger\Big] , \end{aligned} \tag{A.33}$$

where the current J^μ is given by

$$J^\mu = \frac{N_C\varepsilon^{\mu\nu\rho\sigma}}{48\pi^2}\mathrm{Tr}\left[Q\partial_\nu\Sigma\Sigma^\dagger\partial_\rho\Sigma\Sigma^\dagger\partial_\sigma\Sigma\Sigma^\dagger + Q\Sigma^\dagger\partial_\nu\Sigma\Sigma^\dagger\partial_\rho\Sigma\Sigma^\dagger\partial_\sigma\Sigma\right] . \tag{A.34}$$

If we further expand $\Sigma = 1 + i\frac{\Phi}{f_\pi} + \ldots$, and use the parametrization of Φ in terms of the NGBs, given in eq. (A.12), we can then obtain the EM interactions with the pseudoscalar mesons. For the case of interactions with three mesons, we find that

$$J^\mu_{3\Phi} = -\frac{i\varepsilon^{\mu\nu\rho\sigma}}{8\pi^2 f_\pi^3}\mathrm{Tr}\left[Q\partial_\nu\Phi\partial_\rho\Phi\partial_\sigma\Phi\right] . \tag{A.35}$$

For instance, we can use this equation to obtain the 3π and $\eta\pi\pi$ currents

$$\begin{aligned} J^\mu_{3\pi} &= -\frac{i\varepsilon^{\mu\nu\rho\sigma}}{4\pi^2 f_\pi^3}\partial_\nu\pi^+\partial_\rho\pi^-\partial_\sigma\pi^0 \\ J^\mu_{\eta\pi\pi} &= -\frac{i\varepsilon^{\mu\nu\rho\sigma}}{4\sqrt{3}\pi^2 f_\pi^3}\partial_\nu\eta\partial_\rho\pi^+\partial_\sigma\pi^- , \end{aligned} \tag{A.36}$$

respectively, which describe $(\gamma\, 3\pi)$ and $(\gamma\,\eta\,\pi^+\pi^-)$ interactions.

The second term in eq. (A.33) covers interaction with two photon fields. It can be used, for

example, to describe the $\pi^0 \to \gamma\gamma$ decay

$$\mathcal{L}_{\pi^0\gamma\gamma} = -\frac{e^2}{32\pi^2}\varepsilon_{\mu\nu\rho\sigma}F^{\mu\nu}F^{\rho\sigma}\frac{\pi^0}{f_\pi}\,, \tag{A.37}$$

where $F^{\mu\nu}$ is the photon field strength tensor.

A.3 Hidden Local Symmetry model

In the last two sections we saw how to build the chiral Lagrangian and we succeed to describe pseudoscalar meson interactions with the photon, now including even and odd number of mesons. Nevertheless, the SM particle spectrum contains also vector mesons aside from pseudoscalar degrees of freedom. So, the question that we are left to ask is how to include these vector mesons and correctly describe their interactions within the ChPT framework?

The most popular theoretical framework that succeeds to answer this question is the Hidden Local Symmetry (HLS) approach [194, 198–202], in which we treat the vector mesons as the dynamical gauge bosons of a hidden $U(3)_V$ local symmetry. In fact, the HLS method can be applied to any system described by a non-linear realization of the symmetry G that is broken spontaneously into a subgroup $H \subset G$. The reason is that we have a gauge equivalence between the nonlinear sigma model, where the NGBs transform non-linear under G/H, and the HLS model with a larger symmetry $G_{\text{global}} \times H_{\text{local}}$, where H_{local} is the HLS.

Let us now explain the idea behind the HLS framework. First, we divide the Goldstone matrix into two fields

$$\Sigma(x) = \xi_L^\dagger(x)\,\xi_R(x)\,, \tag{A.38}$$

where the new fields transform under $G_{\text{global}} \times H_{\text{local}} = [\mathrm{U}(3)_L \times \mathrm{U}(3)_R]_{\text{global}} \times [\mathrm{U}(3)_V]_{\text{local}}$ as

$$\begin{aligned} \xi_L &\to H\xi_L L^\dagger \\ \xi_R &\to H\xi_R R^\dagger\,, \end{aligned} \tag{A.39}$$

and $H \in H_{\text{local}}$. Now, we can introduce the non-Abelian gauge field

$$V_\mu = V_\mu^a T^a\,, \tag{A.40}$$

by including it in the covariant derivatives

$$\begin{aligned} D_\mu \xi_L &= (\partial_\mu - igV_\mu)\xi_L + i\xi_L l_\mu \\ D_\mu \xi_R &= (\partial_\mu - igV_\mu)\xi_R + i\xi_R r_\mu \,. \end{aligned} \tag{A.41}$$

where we also add the external gauge fields l_μ and r_μ. The covariant derivatives will follow the same transformation laws for $\xi_{L,R}$ while the HLS gauge boson will transform according to

$$V_\mu \to H V_\mu H^\dagger + iH\partial_\mu H^\dagger \,. \tag{A.42}$$

Using $\xi_{L,R}$ and $D_\mu \xi_{L,R}$ we can build two invariants under the larger symmetry $G_{\text{global}} \times H_{\text{local}}$

$$\mathcal{L}_{V/A} = -\frac{f_\pi^2}{4}\text{Tr}\left[\left(D_\mu \xi_L \cdot \xi_L^\dagger \pm D_\mu \xi_R \cdot \xi_R^\dagger\right)^2\right] \,, \tag{A.43}$$

such that we can write down the final Lagrangian

$$\mathcal{L} = \mathcal{L}_A + a\mathcal{L}_V + \mathcal{L}_{\text{gauge}}^{\text{kin}} \,, \tag{A.44}$$

where a is an arbitrary parameter and the gauge Lagrangian $\mathcal{L}_{\text{gauge}}^{\text{kin}}$ contains the kinetic terms of the gauge fields

$$\mathcal{L}_{\text{gauge}} = -\frac{1}{2}\text{Tr}(F_{\mu\nu}^V F^{V,\mu\nu}) - \frac{1}{2}\text{Tr}(f_{\mu\nu}^L f^{L,\mu\nu}) - \frac{1}{2}\text{Tr}(f_{\mu\nu}^R f^{R,\mu\nu}) \,. \tag{A.45}$$

with $F_{\mu\nu}^V = \partial_\mu V_\nu - \partial_\nu V_\mu - ig[V_\mu, V_\nu]$ the field strength tensor of the HLS gauge boson. Linear combinations of $\mathcal{L}_V$ and $\mathcal{L}_A$ reproduce the original chiral Lagrangian in eq. (A.16).

The next step is to fix the HLS gauge, by choosing $\xi_L = \xi_R^\dagger \equiv \xi = e^{i\Phi/2f_\pi}$. We will also consider the external field as being the photon field $l_\mu = r_\mu = -eQA_\mu$. The Lagrangian then takes the form

$$\begin{aligned} \mathcal{L}_A =& \frac{f_\pi^2}{4}\text{Tr}\left[\partial_\mu \Sigma \partial^\mu \Sigma^\dagger\right] + ie\frac{f_\pi^2}{2}A_\mu \text{Tr}\left[Q[\xi^\dagger, \partial^\mu \xi]\right] \\ &+ ie\frac{f_\pi^2}{2}A_\mu \text{Tr}\left[Q(\Sigma^\dagger \partial^\mu \xi \xi - \xi \partial^\mu \xi \Sigma^\dagger\right] + \dots \\ \mathcal{L}_V =& g^2 f_\pi^2 \text{Tr}\left[V_\mu V^\mu\right] + e^2\frac{f_\pi^2}{2}A_\mu A^\mu \text{Tr}\left[QQ\right] + e^2\frac{f_\pi^2}{2}A_\mu A^\mu \text{Tr}\left[\Sigma Q \Sigma^\dagger Q\right] \\ &+ ie\frac{f_\pi^2}{2}A_\mu \text{Tr}\left[Q[\xi^\dagger, \partial^\mu \xi]\right] - ie\frac{f_\pi^2}{2}\text{Tr}\left[Q(\Sigma^\dagger \partial^\mu \xi \xi - \xi \partial^\mu \xi \Sigma^\dagger)\right] \\ &- igf_\pi^2 \text{Tr}\left[V_\mu [\xi^\dagger, \partial^\mu \xi]\right] + gef_\pi^2 A_\mu \text{Tr}\left[V_\mu(\xi Q \xi^\dagger + \xi^\dagger Q \xi)\right] + \dots \,, \end{aligned} \tag{A.46}$$

where we can find in $\mathcal{L}_A$ the chiral Lagrangian plus terms that describe photon interactions, while $\mathcal{L}_V$ comprises the terms involving the vector mesons V_μ. We can then expand $\xi = 1 - \frac{i\Phi}{2f_\pi} + ...$ in order to get the interactions terms

$$\begin{aligned}\mathcal{L}_A + a\mathcal{L}_V \supset & -\frac{1}{4} i g_{VPP} 2\mathrm{Tr}\left[V_\mu[\Phi, \partial^\mu \Phi]\right] + \frac{1}{4} g_{\gamma PP} A_\mu 2\mathrm{Tr}\left[Q[\Phi, \partial^\mu \Phi]\right] \\ & + e g_{V\gamma} 2A_\mu \mathrm{Tr}\left[V^\mu Q\right] + ... \,, \end{aligned} \tag{A.47}$$

where we defined the couplings with two pseudoscalars as $g_{VPP} = \frac{1}{2}ag$ and $g_{\gamma PP} = \frac{1}{2}(a-2)e$, while the vector meson-photon mixing is $g_{V\gamma} = agf_\pi^2$.

The gauge field matrix V^μ can be expressed in terms of real vector meson states

$$V^\mu = T^a V^{a,\mu} = \frac{1}{\sqrt{2}} \begin{pmatrix} \frac{\omega^\mu + \rho^\mu}{\sqrt{2}} & \rho^{+,\mu} & K^{*+,\mu} \\ \rho^{-,\mu} & \frac{\omega^\mu - \rho^\mu}{\sqrt{2}} & K^{*0,\mu} \\ K^{*-,\mu} & \bar{K}^{*0,\mu} & \phi \end{pmatrix} . \tag{A.48}$$

Using the last equation we can obtain the vector meson $U(3)$ generators, such as

$$\begin{aligned} T_\rho &= \frac{1}{2}\mathrm{diag}(1, -1, 0) \,, \\ T_\omega &= \frac{1}{2}\mathrm{diag}(1, 1, 0) \,, \\ T_\phi &= \frac{1}{\sqrt{2}}\mathrm{diag}(0, 0, 1) \,. \end{aligned} \tag{A.49}$$

Now, we can use eq. (A.47), together with the vector meson kinetic term of eq. (A.45), to obtain the final Feynman rules of the HLS model, which we explicitly show in figure A.1.

One important remark about the HLS model is that we can recover the original chiral Lagrangian with external photon fields in the limit where the vector meson decouples ($m_V^2 \gg p^2$). For example, we can describe the annihilation of a photon into two pseudoscalar by the process $\gamma \to V \to PP$, where the first vertex arise from the photon-vector-meson mixing (last term of eq. (A.47)) and the second from the VPP interaction (first term of eq. (A.47)). Now, in the limit where $m_V^2 \gg p^2$, or similarly where $p^2 \to 0$, the matrix element of this process, obtained with the HLS approach, reduces to the one from the direct $\gamma \to PP$ interaction from eq. (A.26). This implies that the point-like γPP vertex behaves as a low-energy limit of the vector meson HLS.

Now, what about the terms with odd interactions? On the one hand, analogously to the case of ChPT, we can also add a WZW component to the HLS Lagrangian. On the other hand, the explicitly construction and addition of the terms that create the WZW action requires the intro-

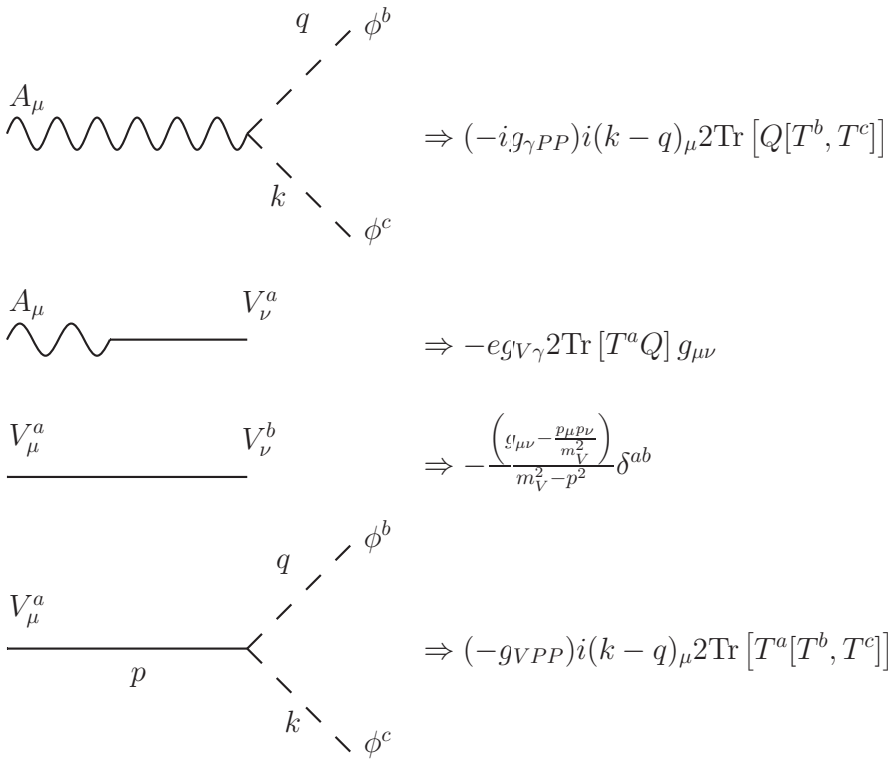

Figure A.1: Feynman rules of the HLS vector meson model with an external photon field A_μ. The V^a_μ fields represent the vector mesons while the ϕ^a fields are the pseudoscalar mesons.

duction of several differential forms and the further assembly of these forms into Lagrangian invariants that contain interactions mixing the vector mesons, photons and pseudoscalars, such as $(V\gamma\Phi), (VV\Phi)$ and $(V\Phi^3)$. Here we will not go into the technical details of the WZW-HLS construction [3], but will only mention that in Ref. [194] the authors present a specific combination of this Lagrangian invariants with the attribute that all interactions with vector mesons can be described using the $VV\Phi$ vertex

$$\mathcal{L}_{VV\Phi} = \frac{3g^2}{4\pi^2 f_\pi}\epsilon^{\mu\nu\rho\sigma}\partial_\mu V^a_\nu \partial_\rho V^b_\sigma \phi^c \mathrm{Tr}\left[T^aT^bT^c\right] \ . \tag{A.50}$$

Now, all the processes that contain vector mesons will be given by the photon-vector-meson mixing and the $VV\Phi$ vertex, that in general will be the $\omega\rho\pi$ coupling

$$\mathcal{L}_{\omega\rho\pi} = g_{\omega\rho\pi}\epsilon^{\mu\nu\rho\sigma}\partial_\mu\omega_\nu\partial_\rho\rho_\sigma\pi^0 + ... \tag{A.51}$$

[3] For further details, we refer the reader to [194].

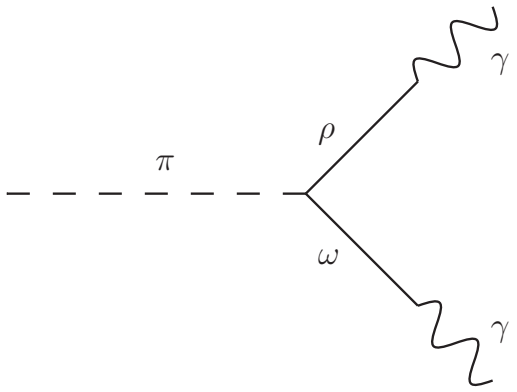

Figure A.2: $\pi^0 \to \gamma\gamma$ decay within the vector meson HLS model.

For illustration, let us consider the $\pi^0 \to \gamma\gamma$ decay. This process can be described by a $\omega\rho\pi$ coupling following two photon-vector-meson mixings, as shown in Figure A.2.

A.4 Vector Meson Dominance framework

In the last section, we showed how to add the vector mesons in the chiral Lagrangian description using the HLS model. When we include the odd interaction terms with the WZW approach we choose a particular choice of Lagrangian invariants, fixed by experimental observations, in order to describe the vector meson interactions only with the VVP vertex and mixing with the photon. This choice already depicts a specific realization in which vector mesons dominate, *i.e.* we shift to a representation of hadronic processes where the vector mesons predominate in the vertices.

The idea behind the VMD framework is that in the regions close to the vector meson masses, *i.e.* where the vector mesons dominate, the hadronic components of the vacuum polarization of the photon consist solely of the know vector mesons [203], as illustrated by Figure A.3.

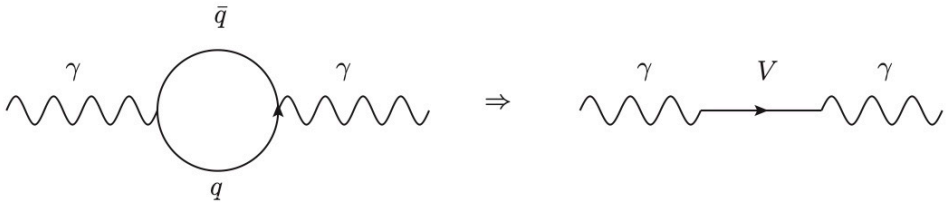

Figure A.3: Close to the vector meson masses the photon propagator receives dominant contributions from hadronic loops that translate into an effective photon-vector-meson mixing.

In a more specific way, in the VMD theory we identify the light neutral vector mesons, such

as ρ^0, ω^0 and ϕ, with the electromagnetic hadronic current $J_\mu^{\rm had}$ through the field current-identity

$$V_\mu \sim J_\mu^{\rm had} \,. \tag{A.52}$$

To show this relation we reduce the gauge symmetry group to $SU(2)$ with the isospin doublets

$$\Psi_q = \begin{pmatrix} u \\ d \end{pmatrix} \quad , \quad \bar{\Psi}_q = \begin{pmatrix} \bar{u} & \bar{d} \end{pmatrix} \,. \tag{A.53}$$

We then write a general Lagrangian invariant under this isospin symmetry and including the isospin $I = 1$ triplet gauge field ρ_μ

$$\begin{aligned} \mathcal{L}_m + \mathcal{L}_{\rm SU(2)} &= -\frac{1}{2}(m_\rho \vec{\rho}_\nu)^2 - \frac{1}{4} G_{\mu\nu}^2 + \bar{\Psi} \not{D} \Psi \\ &= -\frac{1}{2}(m_\rho \vec{\rho}_\nu)^2 - \frac{1}{4} G_{\mu\nu}^2 + \bar{\Psi} \gamma^\mu \left(\partial_\mu + g_0 \vec{\tau} \cdot \vec{\rho}_\mu \right) \Psi \,, \end{aligned} \tag{A.54}$$

where m_ρ is the ρ field mass, $G_{\mu\nu}$ is the ρ strength tensor and $\tau^a = \frac{i}{2}\sigma^a$ are the $SU(2)$ group generators with Pauli matrices σ^a. If we expand the interaction term, we can notice that the third isospin $I = 1$ mode is neutral and also that it couples to a quark content similar to the isospin $I = 1$ component of the EM current in eq. (A.24)

$$\bar{\Psi} g_0 \frac{i}{2} \sigma^3 \rho_\mu^3 \Psi = \frac{g_0}{2} i \rho_\mu^3 (\bar{u} \gamma^\mu u - \bar{d} \gamma^\mu d) \,. \tag{A.55}$$

This suggest that we can shift the third component of the ρ field by

$$\rho_\mu^3 \to \hat{\rho}^3 = \rho_\mu^3 + \frac{e_0}{g_0} A_\mu \,,$$

in order to incorporate the photon field A_μ in the Lagrangian. If we then add the photon kinetic terms and write the photon and ρ fields equations of motion we can arrive to the well know result

$$\frac{1}{\sqrt{2}} J_\nu^{I=1(3)} = -\frac{m_\rho^2}{g_0} \rho_\nu^3 \,, \tag{A.56}$$

which is the field-current equation. Thus, we see that the third component of the isovector EM hadronic current can be identified as the third component of the isospin triplet ρ_μ, which we associate with the physical ρ meson. Similarly, we can identify the isoscalar $I = 0$ component

of J^{had} with the ω meson

$$\omega_\mu \sim J_\mu^{I=0} = \frac{1}{\sqrt{2}}\left(\bar{u}\gamma_\mu u + \bar{d}\gamma_\mu d\right) . \tag{A.57}$$

If we further expand the quark content by adding the strange quark s, we can identify the ϕ vector meson with the strange current

$$\phi_\mu \sim J_\mu^s = \bar{s}\gamma_\mu s\,. \tag{A.58}$$

Thus, we end up with the field-current identity

$$J_\mu^{\text{had}} = \sum_{\mathcal{V}=\rho,\omega,\phi} \frac{m_V^2}{g_V}\mathcal{V}_\mu\,. \tag{A.59}$$

Finally, we can write down the complete Lagrangian of the VMD representation, which takes the form

$$\mathcal{L}_{\text{VMD}} = -\frac{1}{4}F_{\mu\nu}F^{\mu\nu} - \frac{1}{4}\mathcal{V}_{\mu\nu}\mathcal{V}^{\mu\nu} + \frac{1}{2}m_V^2\mathcal{V}_\mu\mathcal{V}^\mu - g_{V\pi\pi}\mathcal{V}_\mu J^{\text{had},\mu} - eA_\mu J^{\text{had},\mu} - \frac{e}{2g_V}F_{\mu\nu}\mathcal{V}^{\mu\nu}\,. \tag{A.60}$$

So, in other words, the whole purpose of the VMD model is to show that the coupling of the photon to the electromagnetic quark current can be replaced by a coupling to vector mesons, with each vector representing a specific component of the EM current.

A.5 Light $U(1)_Q$ vector mediators in ChPT

Now that we establish the ideas behind the HLS and VMD models, we can generalize these theories to a BSM framework by the inclusion of a light $U(1)_Q$ vector mediator, such as the *dark photon* or any baryophilic boson. This mediator will enter in the ChPT Lagrangian in the same way as the photon field, *i.e.* it will behave like an external gauge field as described in eq. (A.18).

The theoretical details about the extension of the SM by a new $U(1)_Q$ gauge symmetry can be found in chapter 1. Following eq. (A.22), now, in addition to the photon field, we will add the new vector mediator Z_Q via the l_μ, r_μ prescription

$$r_\mu = l_\mu = Q^f Z_{Q,\mu} + eQA_\mu\,, \tag{A.61}$$

where Q^f is the diagonal light quark matrix $Q^f = \mathrm{diag}(q_Q^u, q_Q^d, q_Q^s)$ and $q_Q^{u,d,s}$ are the $U(1)_Q$ quark charges. In this equation we also used the fact that the new mediator will couple to LH and RH fields in the same way. With the addition of the new mediator, the covariant derivative that acts on the Goldstone Matrix will become

$$D_\mu \Sigma = \partial_\mu \Sigma + i(Q^f Z_{Q,\mu} + eQA_\mu)\Sigma - i\Sigma(Q^f Z_{Q,\mu} + eQA_\mu)\,. \tag{A.62}$$

The theoretical outcomes of this inclusion will be the simply addition of new terms for the Z_Q boson that are similar to the photon terms, but replacing $eQA_\mu \to Q^f Z_{Q,\mu}$, and also some extra terms mixing the photon and new mediator fields. For instance, the chiral Lagrangian given by eq. (A.25) will be

$$\begin{aligned}\mathcal{L}_{\mathrm{ChPT}} =& \frac{f_\pi^2}{4}\mathrm{Tr}\left[D_\mu\Sigma(D_\mu\Sigma)^\dagger\right] \\ =& \cdots - \frac{if_\pi^2}{4}Z_{Q,\mu}\Big(\mathrm{Tr}\left[\Sigma(\partial^\mu\Sigma^\dagger)Q^f + \Sigma^\dagger(\partial^\mu\Sigma)Q^f\right] \\ &+ 4eA^\mu\mathrm{Tr}\left[QQ^f\right] - 2eA^\mu\mathrm{Tr}\left[Q\Sigma Q^f\Sigma^\dagger\right] - 2eA^\mu\mathrm{Tr}\left[Q^f\Sigma Q\Sigma^\dagger\right] \\ &- 2Z_Q^\mu\mathrm{Tr}\left[(Q^f)^2\right] + 2Z_Q^\mu\mathrm{Tr}\left[Q^f\Sigma Q^f\Sigma^\dagger\right]\Big) + \ldots\end{aligned} \tag{A.63}$$

Note that the couplings of the new mediator to quarks play a major role here, since the interactions with the pseudoscalar mesons will be determined via traces involving the quark matrix Q^f. Now, analogously to what we did before, we can also generalize eq. (A.27)

$$\begin{aligned}\mathcal{L}_{Z_Q PP} =& Z_{Q,\mu}\, i\Big((q_Q^u - q_Q^d)\left[\pi^-\partial^\mu\pi^+ - \pi^+\partial^\mu\pi^-\right] + \frac{1}{2}(q_Q^u - q_Q^d)\left[K^-\partial^\mu K^+ - K^+\partial^\mu K^-\right] \\ &+ \frac{1}{2}(q_Q^u + q_Q^d)\left[K^-\partial^\mu K^+ - K^+\partial^\mu K^-\right] - q_Q^s\left[K^-\partial^\mu K^+ - K^+\partial^\mu K^-\right] + \ldots\Big)\,.\end{aligned}$$

We could also include interactions with an odd number of pseudoscalar mesons. In this case we would obtain similar expressions to eq. (A.36), but with the new vector field Z_Q.

Finally, if we want to describe interactions involving vector mesons, we need to follow the same approach of the HLS section. Recall that, after including the WZW term to the chiral Lagrangian, we ended with a formulation where all the processes with vector mesons could be described by combining the $VV\Phi$ vertex with the mixing between the photon and the vector meson. Now, if we want the same description but for a new vector mediator Z_Q, we simply exchange the photon field by the new boson field, such that now we will use the $VV\Phi$ vertex

and the vector mediator-vector meson mixing

$$\mathcal{L}_{VZ_Q} = 2\, g_Q Z_Q^\mu \mathrm{Tr}\left[V_\mu Q^f\right] \,. \tag{A.64}$$

This term is the $U(1)_Q$ version of the last term of eq. (A.47), and is exactly the equation that we use for the formulation of Z_Q decays into hadrons (eq. (1.47)) depicted in section 1.3.2. Therefore, the hadronic decays proceed in the following manner: after its production, the new vector mediator Z_Q converts into a vector meson, according to eq. (1.47), and then the subsequent vector meson decays into other mesons via the $VV\Phi$ vertex. The vector mesons can also decay into photons, in this case we will use the photon-vector meson mixing.

Appendix B

Hadronic Current Calculation

The main purpose of this appendix is to explain and derive the formulas of the hadronic currents that appear in equations (2.14) and (2.15) for several types of hadronic channels, such that we can obtain the final cross-section and decay width expressions. To this end, we will first introduce in the next section some kinematic details about the calculation of the phase space element and then we will make some comments about the underlying symmetry assumptions that help in the determination of which vector meson will contribute to a certain hadronic current. Finally, in the last section we give the complete expression of each hadronic current type, together with the correspondent form-factor.

B.1 Kinematic Details

In order to calculate the cross-section and decay width formulas of equations (2.9), (2.10) and (2.12), we need to obtain the expressions for the phase-space element $\mathrm{d}\Phi_n$, as we describe below.

B.1.1 Phase-space element

In the case of e^+e^- annihilation into two particles, *i.e.* $k_+ + k_- \to p_1 + p_2$, in the center-of-momentum frame the phase-space element will be

$$\begin{aligned} \mathrm{d}\Phi_2 &= \prod_{i=1,2} \frac{\mathrm{d}^3 p_i}{(2\pi)^3 2E_i} (2\pi)^4 \delta^{(4)}(k_+ + k_- - p_1 - p_2) = \frac{1}{16\pi^2} \frac{p_f}{\sqrt{s}} \mathrm{d}\Omega \\ \Rightarrow \Phi_2 &= \frac{1}{4\pi} \frac{p_f}{\sqrt{s}}\,, \end{aligned} \tag{B.1}$$

where $s = (k_+ + k_-)^2$ and $p_f = |\vec{p}_1| = |\vec{p}_2|$ is the magnitude of the final state particle momenta

$$p_f = \hat{p}(s, m_1^2, m_2^2) = \frac{1}{2\sqrt{s}}\lambda(s, m_1^2, m_2^2) \tag{B.2}$$

and λ is the Callan function, which is given by

$$\begin{aligned} \lambda(m_0^2, m_1^2, m_2^2) &= \sqrt{m_0^4 + m_1^4 + m_2^4 - 2m_0^2m_1^2 - 2m_0^2m_2^2 - 2m_1^2m_2^2} \\ &= \sqrt{(m_0^2 - (m_1 + m_2)^2)\,(m_0^2 - (m_1 - m_2)^2)}\,. \end{aligned} \tag{B.3}$$

Similarly, for a e^+e^- annihilation into a three-body final state $k_+ + k_- \to p_1 + p_2 + p_3$, the phase-space element will be [2]

$$\mathrm{d}\Phi_3 = \prod_{i=1,2,3} \frac{\mathrm{d}^3 p_i}{(2\pi)^3 2E_i}(2\pi)^4\delta^{(4)}(k_+ + k_- - p_1 - p_2 - p_3) = \frac{1}{(2\pi)^3}\frac{1}{16s}\mathrm{d}m_{12}^2\mathrm{d}m_{23}^2\,, \tag{B.4}$$

where $m_{ij}^2 = (p_i + p_j)^2$ $(i, j = 1, 2, 3)$. If the integrand (that also includes the hadronic current) only depends on one mass variable, m_{12} for example, we can integrate over the other one, resulting in

$$\mathrm{d}\Phi_3 = \frac{\mathrm{d}m_{12}^2}{32\pi^3 s^{\frac{1}{2}} m_{12}}\hat{p}^3(s, m_{12}^2, m_3^2)\hat{p}^3(m_{12}^2, m_1^2, m_2^2)\,, \tag{B.5}$$

where

$$\hat{p}(m_0^2, m_1^2, m_2^2) = \frac{\lambda(m_0^2, m_1^2, m_2^2)}{2m_0}\,. \tag{B.6}$$

B.2 Symmetry Assumptions

In order to obtain the correct vector mesons that mediate a specific hadronic channel current, we need to rely on symmetry arguments. In what follows, we will discuss the two most relevant symmetries in the context of hadronic interactions that will be useful for us.

B.2.1 G-parity

G-parity is a multiplicative quantum number used in the context of strong interactions, specially valuable when dealing with pion processes. We define the G-parity number for a particle p as

$$G(p) = (-1)^{L+S+I}\,, \tag{B.7}$$

where L, S and I are the orbital angular momentum, spin and isospin of the particle p, respectively. The G-parity operation is a symmetry of low-energy strong interactions, meaning that all meson composed of *up* and *down* quarks and anti-quarks are eigenstates of the G-parity number G. This is the case of pions, that have G-parity equals to -1, according to

$$G(\pi) = (-1)^{0+0+1} = -1\,, \tag{B.8}$$

where the L, S and I quantum numbers can be extracted from PDG [2]. When the meson state has $G = -1$ we call it G-parity *odd*, while when $G = 1$, we call it G-parity *even*.

The G-parity number will be useful when dealing with processes with mesons states composed of u and d quarks and anti-quarks, since it will be conserved in such reactions. So, if we want to guess which vector meson mediate this type of process we can use G-parity conservation. Using the quantum numbers from PDG we have that for the vector mesons V

$$\begin{aligned} &G(V) = (-1)^{0+1+I} = (-1)(-1)^I \\ &\Rightarrow G(\rho) = (-1)(-1)^1 = +1 \\ &\Rightarrow G(\omega) = (-1)(-1)^0 = -1 \\ &\Rightarrow G(\phi) = (-1)(-1)^0 = -1\,. \end{aligned} \tag{B.9}$$

For illustration, let us consider the two pion final state $\mathcal{H} = \pi^+\pi^-$. Since G-parity is a multiplicative number we have that

$$G(\pi\pi) = G(\pi)G(\pi) = (-1)(-1) = +1\,. \tag{B.10}$$

Hence, due to G-parity conservation, in order to mediate this current we need a vector meson with isospin $I = 1$, such that the only candidate is the ρ meson that also has $G = +1$.

However, it is important to emphasize that this symmetry is only approximately conserved in strong interactions, which means that G-parity violating, or 'isospin breaking', minor contributions can appear in the description of a given channel. For instance, as we will see in the next section, the $\mathcal{H} = \pi^+\pi^-\pi^0$ channel, which has $G(3\pi) = -1$, has a small G-parity violating contribution coming from the ρ vector mediator. Therefore, we can use G-parity arguments to determine the dominant contributions for a certain current, that in the case of $\mathcal{H} = \pi^+\pi^-\pi^0$ will be $V = \omega, \phi$. However, we cannot discard possible small G-parity violation components.

Another interesting feature is that we can identify substructures in the hadronic channels by using G-parity assumptions. For example, in the $\mathcal{H} = \pi^+\pi^-\pi^0$ channel, we can combine two pions to create a $G = +1$ state. This state will be mediated by the ρ meson, such that we can

describe the 3π process with $\phi, \omega \to \rho\pi^0 \to \pi^+\pi^-\pi^0$ (see figure B.3).

In summary, we can use G-parity in low-energy strong interactions involving hadronic states with u and d quarks as a guiding principle to determine with vector mesons will dominate. Nevertheless, for final state channels that include photons, such as $\mathcal{H} = \pi\gamma$ or $\eta\gamma$, we cannot rely in G-parity conservation anymore since the interactions involved are not purely governed by the strong force. For these pseudoscalar photon modes $\mathcal{H} = P\gamma$ we need to include all vector mesons in the hadronic current description, and the dominant ones will be determined by considering the dominant branching ratios $\mathrm{Br}(V \to P\gamma)$. Similarly, for mesons that contain s quarks and anti-quarks, such as the kaons, G-parity fails to work. In this case, we will need to consider purely isospin symmetry arguments, as we will see next.

B.2.2 Isospin Symmetry

For mesons that are bound states of strange quarks and carry the 'strangeness' quantum number, dubbed as 'strange mesons', we cannot use G-parity assumptions anymore. Instead, we will use isospin symmetry considerations to determine their vector contributions [204, 205]. Unlike in the G-parity case, we will not establish which mesons are forbidden and which are allowed in each reaction. Rather than this, we will determine the magnitude of the contribution of each vector meson to the hadronic current. To this end, we first need to express the mesons as isospin eigenstates. For the kaons we have

$$\left|K^+\right\rangle = |1/2, +1/2\rangle\,, \quad \left|K^0\right\rangle = |1/2, -1/2\rangle\,, \tag{B.11}$$

$$\left|\bar{K}^0\right\rangle = |1/2, +1/2\rangle\,, \quad \left|K^-\right\rangle = |1/2, -1/2\rangle\,, \tag{B.12}$$

and similarly for $K^*(892)$

$$\left|K^{*+}\right\rangle = |1/2, +1/2\rangle\,, \quad \left|K^{*0}\right\rangle = |1/2, -1/2\rangle\,, \tag{B.13}$$

$$\left|\bar{K}^{*0}\right\rangle = |1/2, +1/2\rangle\,, \quad \left|K^{*-}\right\rangle = |1/2, -1/2\rangle\ . \tag{B.14}$$

The pion states are expressed as

$$\left|\pi^+\right\rangle = |1, +1\rangle\,, \quad \left|\pi^0\right\rangle = |1, 0\rangle\,, \quad \left|\pi^-\right\rangle = |1, -1\rangle\ . \tag{B.15}$$

For instance, let us consider the $\mathcal{H} = KK\pi$ channel. In order to obtain the isospin contributions to this channel, we first need to describe the $K^*(892)$ decays by combining the different isospin states. For example, consider the decays $K^*(892) \to \pi^0 K^+$ and $K^*(892) \to \pi^+ K^0$.

Combining the final states, we obtain

$$\begin{aligned}\left|\pi^0\right\rangle \otimes \left|K^+\right\rangle &= |1,0\rangle \otimes |1/2,+1/2\rangle \\ &= \sqrt{\frac{2}{3}}\,|3/2,+1/2\rangle - \sqrt{\frac{1}{3}}\,|1/2,+1/2\rangle \\ &= \sqrt{\frac{2}{3}}\,|3/2,+1/2\rangle - \sqrt{\frac{1}{3}}\left|K^{*+}\right\rangle\,, \end{aligned} \tag{B.16}$$

and

$$\begin{aligned}\left|\pi^+\right\rangle \otimes \left|K^0\right\rangle &= |1,+1\rangle \otimes |1/2,-1/2\rangle \\ &= \sqrt{\frac{1}{3}}\,|3/2,+1/2\rangle + \sqrt{\frac{2}{3}}\,|1/2,+1/2\rangle \\ &= \sqrt{\frac{1}{3}}\,|3/2,+1/2\rangle + \sqrt{\frac{2}{3}}\left|K^{*+}\right\rangle\,, \end{aligned} \tag{B.17}$$

where we used Clebsch-Gordon coefficients in the isospin tensor product. Therefore our calculations show that the weight of the $\pi^0 K^+$ and $\pi^+ K^0$ final states are $\sqrt{1/3}$ and $\sqrt{2/3}$, respectively. In a similar way, we can extract the weights of all $K\pi$ final state combinations

$$\begin{aligned} K^{*+} &\to \pi^0 K^+, \pi^+ K^0 : \sqrt{\frac{1}{3}}, \sqrt{\frac{2}{3}} \\ K^{*0} &\to \pi^0 K^0, \pi^- K^+ : \sqrt{\frac{1}{3}}, \sqrt{\frac{2}{3}} \\ \bar{K}^{*0} &\to \pi^0 \bar{K}^0, \pi^+ K^- : \sqrt{\frac{1}{3}}, \sqrt{\frac{2}{3}} \\ K^{*-} &\to \pi^0 K^-, \pi^- \bar{K}^0 : \sqrt{\frac{1}{3}}, \sqrt{\frac{2}{3}} \end{aligned} \tag{B.18}$$

Now that we have the K^* decays, we can follow the same strategy to obtain the isospin $I = 0$ and $I = 1$ contributions of the $\bar{K}K^*$ combinations. For instance

$$\begin{aligned}\left|K^-\right\rangle \otimes \left|K^{*+}\right\rangle &= |1/2,-1/2\rangle \otimes |1/2,+1/2\rangle \\ &= \sqrt{\frac{1}{2}}\,|1,0\rangle - \sqrt{\frac{1}{2}}\,|0,0\rangle \\ &= \sqrt{\frac{1}{2}}(A_1 - A_0)\,, \end{aligned} \tag{B.19}$$

where A_0 and A_1 represent isospin $I = 0$ and $I = 1$ amplitudes, respectively. Hence, for

example

$$\begin{aligned} K^- K^{*+} :& \frac{1}{\sqrt{2}}(A_1 - A_0) \\ \bar{K}^0 K^{*0} :& \frac{1}{\sqrt{2}}(A_1 + A_0)\,. \end{aligned} \tag{B.20}$$

Finally, we can join the results of eq. (B.18) and (B.20) to obtain the relative signs and coefficients of the isospin $I = 0$ and $I = 1$ amplitudes in the $KK^* \to K(K\pi)$ process cross-sections

$$\begin{aligned} \sigma(K^+(K^-\pi^0) + K^-(K^+\pi^0)) :& \quad \frac{1}{6}|A_0 - A_1|^2, \\ \sigma(K_S^0(K_L^0\pi^0) + K_L^0(K_S^0\pi^0)) :& \quad \frac{1}{6}|A_0 + A_1|^2, \\ \sigma(K^0(K^-\pi^+) + \bar{K}^0(K^+\pi^-)) :& \quad \frac{1}{3}|A_0 + A_1|^2, \\ \sigma(K^+(\bar{K}^0\pi^-) + K^-(K^0\pi^+)) :& \quad \frac{1}{3}|A_0 - A_1|^2\,. \end{aligned} \tag{B.21}$$

Following this same method we can also describe, for example, the $\mathcal{H} = KK\pi\pi$ channel. This mode is one of the new channels that we performed the parametrizations and fit and we refer to appendix C for more details.

B.3 Final Hadronic Current Expression

Now that we already have the expressions for the phase-space element, and have explored the symmetry arguments that help identifying the vector meson contributions, we can finally obtain the formulas of the hadronic currents, given by equations (2.14) and (2.15), for several types of hadronic channels. We will also elaborate on the expressions of the corresponding form-factors. Recall that for all the hadronic channels listed in table 2.2, and not marked as 'new' [1], we follow the parametrization and used the fits from [19]. For more details on the parametrization and the explicit values of the fit parameters for each hadronic channel, including the modes not considered below, we refer to appendix A of [19]. All the calculations described below, including the form-factor formulas for all the considered hadronic channels, can be found in the package DELIVER [70], available at https://github.com/preimitz/DeLiVeR.

[1] Regarding the 'new' channels of table 2.2, we give a detailed description on appendix C.

B.3.1 Two pseudoscalar mesons

The relevant two pseudoscalar channels $\mathcal{H} = P_1P_2$ which we considered in this dissertation are $e^+e^- \to \pi^+\pi^-$ and $e^+e^- \to K^+K^-, K^0_S K^0_L$ neutral modes. The former is described by an isospin $I = 1$ current mediated by the ρ resonance, while the latter is described by isospin $I = 0, 1$ currents mediated by ρ, ω and ϕ vector mesons, as we show in figure B.1. We can obtain an expression for the $\mathcal{H} = P_1P_2$ hadronic current by using the HLS Feynman rules for the diagram in figure A.1. In this case, the useful rule is the one for the VPP vertex, from which we can conclude that

$$J^\mu = -(p_1 - p_2)^\mu F_{\pi/K}(q^2) \,, \tag{B.22}$$

where $q = \sqrt{s} = p_1 + p_2$, resulting in

$$-J^\mu J_\mu = q^2 \left(1 - \frac{4m^2_{\pi/K}}{q^2}\right) \left|F_{\pi/K}(q^2)\right|^2 , \tag{B.23}$$

where $F_{\pi/K}$ is the $\pi\pi$ / KK form-factor. Thus, we can use this hadronic current, combined with the 2-body phase-space element given in eq. (B.1), in the cross-section formula of eq. (2.9) to get

$$\sigma(e^+e^- \to \pi\pi/\, KK) = \frac{\pi\alpha^2_{\text{em}}}{3\, q^2} \left(1 - \frac{4m^2_{\pi/K}}{q^2}\right)^{3/2} \left|F_{\pi/K}(q^2)\right|^2 . \tag{B.24}$$

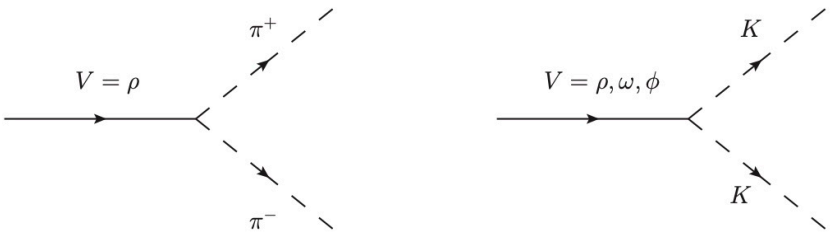

Figure B.1: $V \to \pi^+\pi^-$ and $V \to KK$ currents mediated by $V = \rho$ and $V = \rho, \omega, \phi$ vector mesons, respectively.

Similarly, we can use eq. (2.10) to obtain the partial vector meson decay width

$$\Gamma(e^+e^- \to V \to \pi\pi/\, KK) = \frac{1}{48\pi} m_V \left(1 - \frac{4m^2_{\pi,K}}{m^2_V}\right)^{3/2} |F_{\pi,K}|^2 . \tag{B.25}$$

Now, regarding the form-factors, for the case of the $\pi\pi$ channel, we took as in [19] the

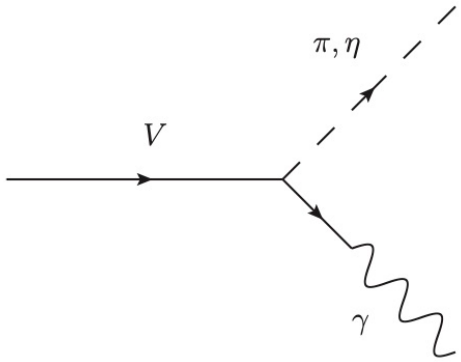

Figure B.2: The decay of a vector meson into a pseudoscalar meson and a photon proceeds via the VVP vertex followed by the vector meson-photon mixing in one leg.

F_π form-factor from [106], which considers a sum of Breit-Wigner propagators plus a $\rho - \omega$ mixing contribution. The KK channel form-factor F_K was also taken from [106] with a similar parametrization.

B.3.2 Pseudoscalar meson and photon

For the case of the production of a photon together with a pseudoscalar meson, we consider the two channels $\mathcal{H} = \pi^0\gamma$ and $\mathcal{H} = \eta\gamma$. The production will proceed via a VVP vertex plus a photon-vector meson mixing, as illustrated in figure B.2. From eq. (A.50) we can obtain the hadronic current

$$J^\mu = \epsilon^{\mu\nu\rho\sigma} q_\nu \epsilon_{\gamma,\rho} p_{\gamma,\sigma} F_{P\gamma}(q^2)\,, \tag{B.26}$$

where q is the sum of the final state momenta, $q = \sqrt{s} = p_1 + p_\gamma$, and all the HLS parameters where absorbed in the form-factor $F_{P\gamma}$ in the form of an effective coupling. The current contraction will be given by

$$-J^\mu J_\mu = 2\, q^2\, p_f^2 \left|F_{P\gamma}(q^2)\right|^2\,, \tag{B.27}$$

with final momenta $p_f = (q^2 - m_P^2)/(2\,q)$, where we used eq. (B.2) with the pseudoscalar meson mass $m_1 = m_P$ and the massless photon $m_2 = 0$.

Plugging the hadronic current contraction and the two-body phase-space eq. (B.1) in the cross-section formula of eq. (2.9) and the decay width given in eq. (2.10), we get

$$\sigma(e^+e^- \to P\gamma) = \frac{4\pi\alpha_{\rm em}^2}{3s^{3/2}} p_f^3 |F_{P\gamma}(s)|^2\,, \tag{B.28}$$

$$\Gamma(e^+e^- \to V \to P\gamma) = \frac{1}{12\pi} p_f^3 |F_{P\gamma}(s)|^2 \,. \tag{B.29}$$

The form-factor of the $\pi\gamma$ channel was based on the model by [3], where they fit the cross-section measured by the SND experiment. The explicit form-factor formula can be expressed by the conventional sum of Breit-Wigner resonances

$$F = \sum_V a_V e^{i\varphi_V} \, \mathrm{BW}_V(s) \,, \tag{B.30}$$

where a_V and φ_V are the vector meson resonance amplitude and phase, respectively, and the Breit-Wigner function is given by

$$\mathrm{BW}_V(s) = \frac{m_V^2}{m_V^2 - s - i\sqrt{s}\,\Gamma_V(s)}, \tag{B.31}$$

where m_V and Γ_V are the vector meson mass and width. Remember that this decay width is related to the process $e^+e^- \to V \to P\gamma$, such that $s = q^2$ corresponds to the squared COM energy of the system. Hence, when the COM energy approaches the resonance mass we have a peak, represented in the Breit-Wigner function.

For the particular case of $F = F_{P\gamma}$, we have the form-factor sum over $V = \rho, \omega, \phi, \omega', \omega''$ resonance Breit-Wigner functions. In the case of the $\eta\gamma$ channel the form-factor was taken from [112], and has the same form as in eq. (B.30), but with $V = \rho, \omega, \phi, \rho'$. For more details on the form-factor parametrization, we refer to [19].

B.3.3 Pseudoscalar meson and vector meson

In this dissertation we considered the following pseudoscalar plus vector meson production channels: $\pi\rho$, $\pi\omega$, $\pi\phi$, $\eta\rho$, $\eta\omega$ and $\eta\phi$. However, since ρ is a broad resonance, it is better to consider the $\rho \to \pi\pi$ subsequent decay. Hence, we used only the $\pi\omega$, $\pi\phi$, $\eta\omega$ and $\eta\phi$ final states, and included the two modes with the ρ vector meson, *i.e.* $\pi\rho$ and $\eta\rho$, as 3π and $\eta\pi\pi$ contributions, respectively.

For the $\mathcal{H} = VP$ hadronic current calculation, we can directly use the VVP vertex, eq. (A.50), together with the generators from eq. (A.13) and eq. (A.49), to obtain

$$J^\mu = \varepsilon^{\mu\nu\rho\sigma} q_\nu \varepsilon_{V,\rho} p_{P,\sigma} F_{VP}(q^2) \,, \tag{B.32}$$

following the conventions of eq. (2.14). The current contraction will be

$$-J^\mu J_\mu = 2\, p_f^2 \left|F_{VP}(q^2)\right|^2 , \tag{B.33}$$

where $p_f = \hat{p}(q^2, m_V^2, m_P^2)$ and the HLS dependent factors were absorbed in the form-factor F_{VP}. Using this current we obtain the cross-section

$$\sigma(e^+e^- \to VP) = \frac{4\pi\alpha_{\rm em}^2}{3s^{3/2}} p_f^3 \left|F_{VP}(q^2)\right|^2 , \tag{B.34}$$

and the vector meson decay width

$$\Gamma(e^+e^- \to V \to VP) = \frac{1}{12\pi} p_f^3 |F_{VP}(q^2)|^2 . \tag{B.35}$$

The form-factors of all these channels can be calculated using eq. (B.30), where the sum over the intermediate vector meson resonances V include all vector mesons that contribute to that corresponding mode, as listed in table 2.2.

B.3.4 Three pseudoscalar mesons

The three pseudoscalar meson current can also be viewed as a VP current followed by a $V \to PP$ decay, as we mention in the last $\mathcal{H} = VP$ current subsection. However, the kinematics are very different since VP is a two-body process while $P_1P_2P_3$ involves three bodies, resulting in different expressions for the cross-section and decay width. The channels with three pseudoscalar mesons that we considered here are $\mathcal{H} = 3\pi, \eta\pi\pi, \eta'\pi\pi$ and $KK\pi$. In Figure B.3 we show the two diagrams that contribute to the 3π current, one of them correspond to the dominant contribution via the $\rho \to \pi^+\pi^-$ decay, and the other represents a small amplitude that proceeds via the G-parity violating decay $\omega \to \pi^+\pi^-$.

In appendix A we already obtained an expression for the three pseudoscalar current, eq. (A.36), which originated from the inclusion of the WZW term. Using this equation, we can express the current in momentum space as

$$J^\mu = \varepsilon^{\mu\nu\rho\sigma} p_{1,\nu} p_{2,\rho} p_{3,\sigma} F_{P_1P_2P_3}(p_1, p_2, p_3) , \tag{B.36}$$

where $p_{1,2,3}$ represent the final state momenta and the pre-factors were again absorbed in the form-factor. Likewise, we can arrive in the same result using the VVP vertex eq. (A.50).

In the case where the Breit-Wigner functions that appear in the form-factor only depend on one mass variable $m_{ij} = (p_i + p_j)$, we can integrate over the other one, as we did in eq. (B.5),

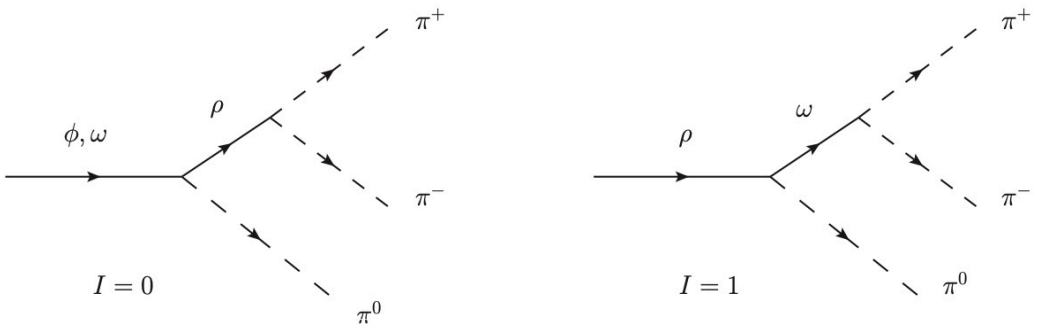

Figure B.3: Diagrams that contribute to the $\mathcal{H} = \pi^+\pi^-\pi^0$ current. In the left we show the dominant isospin $I = 0$ component while in the right the G-parity violating isospin $I = 1$ component.

such that

$$\begin{aligned} \mathrm{d}\Phi_3(-J_\mu J^\mu) &= \frac{1}{(2\pi)^3}\frac{1}{16s}\mathrm{d}m_{12}^2 \int (-J_\mu J^\mu)\,\mathrm{d}m_{23}^2 \\ &= \frac{s^{1/2}}{48\pi^3}\frac{\mathrm{d}m_{12}^2}{m_{12}}\hat{p}^3(m_{12}^2, m_1^2, m_2^2)\hat{p}^3(s, m_{12}^2, m_3^2)|F_{P_1P_2P_3}(p_1,p_2,p_3)|^2 \,. \end{aligned} \tag{B.37}$$

We can use this result to obtain the final expression for the cross-section in eq. (2.9) and decay width in eq. (2.10)

$$\mathrm{d}\sigma = \frac{\alpha_{\mathrm{em}}^2}{18\pi s^{3/2}}\frac{\mathrm{d}m_{12}^2}{m_{12}}\hat{p}^3(m_{12}^2, m_1^2, m_2^2)\hat{p}^3(s, m_{12}^2, m_3^2)|F_{P_1P_2P_3}(p_1,p_2,p_3)|^2 \,, \tag{B.38}$$

$$\mathrm{d}\Gamma = \frac{1}{288\pi^3}\frac{\mathrm{d}m_{12}^2}{m_{12}}\hat{p}^3(m_{12}^2, m_1^2, m_2^2)\hat{p}^3(s, m_{12}^2, m_3^2)|F_{P_1P_2P_3}(p_1,p_2,p_3)|^2 \,. \tag{B.39}$$

The form-factor of the 3π current was based on the model from [108], while the form-factors of $\eta\pi\pi$ and $\eta'\pi\pi$ are from [115, 193, 206]. Finally, the $KK\pi$ mode proceeds via the decay chain $e^+e^- \to KK^* \to K(K\pi)$. The possible final states are obtained through isospin relations, given by eq. (B.21) of section B.2, and the $KK\pi$ form-factor corresponds to a sum of Breit-Wigner amplitudes, as described in [19].

B.3.5 Two pseudoscalar mesons and a vector meson

The channels with two pseudoscalars and one vector meson are the $\mathcal{H} = \omega\pi\pi, \phi\pi\pi, K^*K\pi$ original channels for which we performed the parametrizations and fit. In appendix C we describe in detail how we model each one of these modes and also show the fit values and statistics.

Here, we just mention that the hadronic current for the VPP current can be written as

$$J^{\mu} = \left(g^{\mu\nu} - \frac{q^{\mu}q^{\nu}}{q^2} \right) \varepsilon^{*}_{V,\nu}(p_V) F(q^2) \,, \tag{B.40}$$

where $q = \sqrt{s} = p_V + p_1 + p_2$, according to eq. (2.15), and the form-factor already includes the Breit-Wigner propagator of the resonant vector meson and other possible intermediate states. In the case where F only depends on one mass variable, we can integrate over the other one in the phase-space element, resulting in

$$\begin{aligned} \mathrm{d}\Phi_3(-J_\mu J^\mu) =& \frac{1}{(2\pi)^3}\frac{1}{16s}\int \mathrm{d}m_{12}^2 \mathrm{d}m_{23}^2 (-J^\mu J_\mu) \\ =& \frac{3}{32\pi^3\sqrt{\hat{s}}}\frac{\mathrm{d}m_{12}^2}{m_{12}} \left(1 + \frac{\hat{p}^2(s, m_{12}^2, m_V^2)}{3m_V^2} \right) \hat{p}(s, m_{12}^2, m_V^2)\hat{p}(m_{12}^2, m_{P_1}^2, m_{P_2}^2)|F(s)|^2 \,, \end{aligned} \tag{B.41}$$

which we can use to calculate the cross-section in eq. (2.9) and the decay width in eq. (2.10)

$$\mathrm{d}\sigma = \frac{\alpha_{\mathrm{em}}^2}{4\pi s^{5/2}}\frac{\mathrm{d}m_{12}^2}{m_{12}} \left(1 + \frac{\hat{p}^2(s, m_{12}^2, m_V^2)}{3m_V^2} \right) \hat{p}(s, m_{12}^2, m_V^2)\hat{p}(m_{12}^2, m_{P_1}^2, m_{P_2}^2)|F(s)|^2 \,, \tag{B.42}$$

$$\mathrm{d}\Gamma = \frac{1}{64\pi^3\hat{s}}\frac{\mathrm{d}m_{12}^2}{m_{12}} \left(1 + \frac{\hat{p}^2(s, m_{12}^2, m_V^2)}{3m_V^2} \right) \hat{p}(s, m_{12}^2, m_V^2)\hat{p}(m_{12}^2, m_{P_1}^2, m_{P_2}^2)|F(s)|^2 \,. \tag{B.43}$$

Before concluding, it is important to mention that, as explained in appendix A, in the low-energy limit where $m_V^2 \gg q^2$, or, in other words, where $q^2 \to 0$, we should always recover the ChPT theory predictions with only photon-pseudoscalar meson couplings. This is ensured by the form-factor normalization condition that $F(q^2) \to 1$ for $q^2 \to 0$, which is valid for all the presented form-factors in this section.

Let us also remark that, although all the decay width expressions obtained in this section apply for SM decays $e^+e^- \to V \to \mathcal{H}$, it is easy to re-express the decay formulas considering the hadronic decays of the new light mediator $e^+e^- \to Z_Q \to \mathcal{H}$. To this end, we only need to interpret the COM squared energy s as the square of new mediator mass $m_{Z_Q}^2$ and also re-scale the SM quark coupling into the quark coupling with the new light mediator, as expressed in eq. (2.11). We used this prescription in order to obtain the light mediator hadronic decay widths in our calculations.

Appendix C

Calculation of the New Hadronic Modes

Besides the hadronic modes considered in [19], that we describe in appendix B, we also included four new channels in this dissertation. These channels, marked as 'new' in table 2.2, are relevant in the higher energy region close to 2 GeV. In order to describe them, we follow the steps depicted in section 2.2, *i.e.* we identified the intermediate structures, then we collected the experimental data and performed a fit following a specific parametrization in terms of vector mediators. For the fit, we used the python package `IMinuit` [100]. Below, we provide additional details concerning the specific parametrization and the obtained fit values for each one of these channels. The cross-section and decay widths of these channels, together with the form-factor expressions, can be found in the package DELIVER [70], available at https://github.com/preimitz/DeLiVeR

C.1 $\mathcal{H} = \omega\pi\pi$

The $\omega\pi\pi$ final state can be divided into a charged mode $\omega\pi^+\pi^-$ and a neutral mode $\omega\pi^0\pi^0$, that dominantly lead to the five pion final state combinations $2(\pi^+\pi^-)\pi^0$ and $\pi^+\pi^-3\pi^0$, respectively. This channel is formed by one vector meson and two pseudoscalar mesons, such that we can use the parametrization of the hadronic current given by eq. (2.15)

$$J^{\mu}_{\omega\pi\pi} = \left(g^{\mu\nu} - \frac{q^\mu q^\nu}{q^2}\right) \varepsilon^*_{V,\nu} F_{\omega\pi\pi}(q^2)\,, \tag{C.1}$$

where $q = p_\omega + p_{\pi_1} + p_{\pi_2}$. We will not consider possible intermediate substructures, such as $\omega f_0(980) \to \omega\pi^+\pi^-$ [54] and $b_1(1285)\pi \to \omega\pi\pi$ [207], since so far they have not been clearly seen in the data.

Parameter	Fit Value	Parameter	Fit Value
$m_{\omega''}$	$1.661 \pm 0.007\,\text{GeV}$	$\Gamma_{\omega''}$	$0.398 \pm 0.021\,\text{GeV}$
$a_{\omega''}$	2.73 ± 0.09	$\varphi_{\omega''}$	0 (fixed)
$\chi^2/\text{n.d.f.} = 1.67$			

Table C.1: Fit values for the $e^+e^- \to \omega\pi\pi$ current and the corresponding chi-square of the fit. The phase was fixed during the fit to $\varphi_{\omega''} = 0$.

For the parametrization of the form-factor, we will use a G-parity symmetry argument to conclude that only isospin $I = 0$ mediators are allowed. Therefore, we assume a point-like $\omega \to \omega\pi\pi$ interaction and the form-factor can be written as

$$F_{\omega\pi\pi} = \sum_{V=\omega''} \frac{a_V m_V^2 e^{i\varphi_V}}{m_V^2 - s - i\sqrt{s}\Gamma_V}\,, \tag{C.2}$$

where a_V, m_V, φ_V and Γ_V are the vector meson amplitude, mass, phase and decay width. According to the data, which we extracted from [53–55], the only relevant vector meson that can describe this channel is $V = \omega''$, which corresponds to the $\omega(1650)$ meson. Table C.1 lists the fit parameters obtained with the `IMinuit` python package and figure C.1 shows the best fit curve together with the hadronic data.

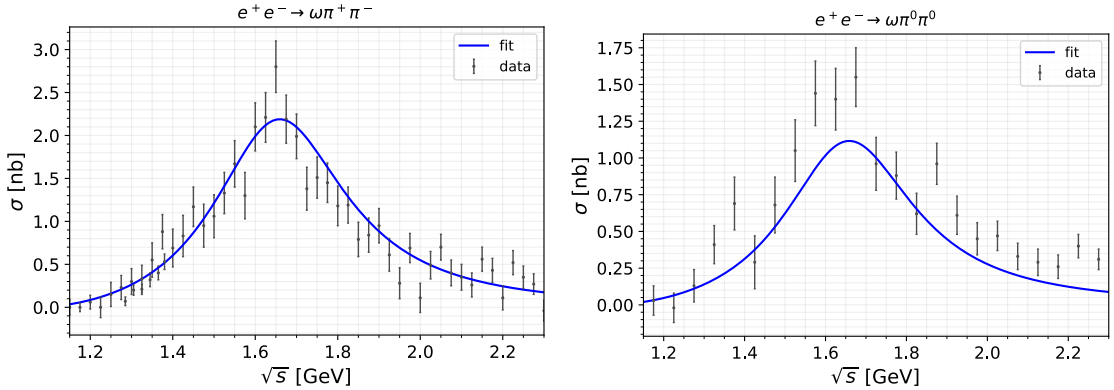

Figure C.1: Cross-section for the charged $\omega\pi^+\pi^-$ (left panel) and neutral $\omega\pi^0\pi^0$ (right panel) hadronic final states. The blue curve shows the best fit solution to the cross-section, obtained considering the fit values of table C.1. The black points and error bars represent data from [53–55].

C.2 $\mathcal{H} = K^*(892)K\pi$

In order to describe the $KK\pi\pi$ final state we took into account two different channel substructures. The first and dominant one was the $K^*(892)K\pi$ channel, and the second is a minor $\phi\pi\pi$ contribution. For the case of the $K^*(892)K\pi$ channel, we consider the most relevant combinations $K^{*0}K^{\pm}\pi^{\mp}$, $K^{*\pm}K_S\pi^{\mp}$ and $K^{*\mp}K^{\pm}\pi^0$ decaying into $K_SK^{\pm}\pi^{\mp}\pi^0$, and $K^{*0}K^{\pm}\pi^{\mp}$ decaying into $K^+K^-\pi^+\pi^-$.

The $K^*(892)K\pi$ mode is another example of a $\mathcal{H} = VPP$ current. As we saw, this type of channel can be described with the hadronic current of eq. (2.15), however, since we are dealing with kaons, in order to calculate the vector meson contributions in the form-factor we need to use isospin symmetry arguments, as described in section B.2. For illustration, let us consider the process $K^{*+}K^-\pi^0 \to K_SK^-\pi^+\pi^0$, which proceeds via the decay $K^{*+} \to K_S\pi^+$. Following the same method outlined in section B.2, we can first write the tensor product of K_S and π^+ isospin eigenstates as

$$\begin{aligned}
\left|K_S^0\right\rangle \otimes \left|\pi^+\right\rangle &= \frac{1}{\sqrt{2}}\left(\left|K^0\right\rangle - \left|\bar{K}^0\right\rangle\right) \otimes \left|\pi^+\right\rangle \\
&= \frac{1}{\sqrt{2}}(|1/2,-1/2\rangle - |1/2,+1/2\rangle) \otimes |1,+1\rangle \\
&= \frac{1}{\sqrt{2}}\sqrt{\frac{2}{3}}\,|1/2,+1/2\rangle + \dots \\
&= \frac{1}{\sqrt{3}}\left|K^{*+}\right\rangle + \dots
\end{aligned} \tag{C.3}$$

where we used the usual convention for the definition of the short-lived neutral kaon ('K-short') $K_S^0 = (K^0 - \bar{K}^0)/\sqrt{2}$ together with the Clebsh-Gordon coefficients. Now, we can write the full process tensor product by using the coefficient of the $K^{*+} \to K_S\pi^+$ decay

$$\begin{aligned}
\left|K_S^0\pi^+\right\rangle \otimes \left(\left|K^-\right\rangle \otimes \left|\pi^0\right\rangle\right) &= \frac{1}{\sqrt{3}}\,|1/2,+1/2\rangle \otimes (|1/2,-1/2\rangle \otimes |1,0\rangle) \\
&= \frac{1}{3}\left(\frac{1}{\sqrt{2}}\,|1,0\rangle - \frac{1}{\sqrt{2}}\,|0,0\rangle\right) \\
&= \frac{1}{\sqrt{18}}(A_1 - A_0)\,,
\end{aligned} \tag{C.4}$$

where we neglected other isospin in the calculation and in the last line we already converted the isospin states into the amplitudes that will appear in the form-factor. Hence, using isospin symmetry assumptions we end up with the magnitude and relative sign of the $I = 0$ and $I = 1$ amplitudes, which correspond to ϕ and ρ contributions, respectively. We can generalize this

calculation to all the other $K^*(892)K\pi$ states listed above, resulting in the following form-factors

$$\begin{aligned}
K^{*0}K^{\pm}\pi^{\mp} \to K_S K^{\pm}\pi^{\mp}\pi^0 : F_{(K^{*0}K^{\pm}\pi^{\mp})^n} &= \frac{1}{\sqrt{18}}(A_1 + A_0)\,, \\
K^{*\pm}K_S\pi^{\mp} \to K_S K^{\pm}\pi^{\mp}\pi^0 : F_{K^{*\pm}K_S\pi^{\mp}} &= \frac{1}{\sqrt{18}}(A_1 - A_0)\,, \\
K^{*\mp}K^{\pm}\pi^0 \to K_S K^{\pm}\pi^{\mp}\pi^0 : F_{K^{*\pm}K^{\mp}\pi^0} &= \frac{1}{\sqrt{18}}(A_1 - A_0)\,, \\
K^{*0}K^{\pm}\pi^{\mp} \to K^+K^-\pi^+\pi^- : F_{(K^{*0}K^{\pm}\pi^{\mp})^c} &= \sqrt{\frac{2}{9}}(A_1 + A_0)\,,
\end{aligned}$$

where we denote the form-factor of the $K^{*0}K^{\pm}\pi^{\mp}$ state decaying into the neutral (charged) $K_S K^{\pm}\pi^{\mp}\pi^0$ ($K^+K^-\pi^+\pi^-$) with a *n* (*c*) superscript and the isospin amplitudes are given by

$$\begin{aligned}
A_0 &= \sum_{\phi} \frac{a_\phi e^{i\varphi_\phi} m_\phi^2}{m_\phi^2 - s - i m_\phi \Gamma_\phi}\,, \\
A_1 &= \sum_{\rho} \frac{a_\rho e^{i\varphi_\rho} m_\rho^2}{m_\rho^2 - s - i m_\rho \Gamma_\rho}\,.
\end{aligned} \tag{C.5}$$

$K_S K^{\pm}\pi^{\mp}\pi^0$		$K^+K^-\pi^+\pi^-$	
Parameter	Fit Value	Parameter	Fit Value
$m_{\phi'}$	1.7 GeV (fixed)	$m_{\phi'}$	1.65 GeV (fixed)
$a_{\phi'}$	2.49 ± 0.6	$a_{\phi'}$	4.52 ± 0.5
$\Gamma_{\phi'}$	0.3 GeV (fixed)	$\Gamma_{\phi'}$	0.103 ± 0.009
$\varphi_{\phi'}$	1.02 ± 0.09	$\varphi_{\phi'}$	π (fixed)
$m_{\rho''}$	1.898 ± 0.012 GeV	$m_{\rho''}$	1.842 ± 0.011 GeV
$a_{\rho''}$	13.5 ± 0.5	$a_{\rho''}$	15.7 ± 1.0
$\Gamma_{\rho''}$	0.504 ± 0.021 GeV	$\Gamma_{\rho''}$	0.403 ± 0.016 GeV
$\varphi_{\rho''}$	0 (fixed)	$\varphi_{\rho''}$	0.000 ± 0.006
$\chi^2/\text{n.d.f.} = 2.68$		$\chi^2/\text{n.d.f.} = 1.59$	

Table C.2: Values obtained by the fit to the $e^+e^- \to K^*K\pi \to K_S K^{\pm}\pi^{\mp}\pi^0$ current (left) and to the $e^+e^- \to K^*K\pi \to K^+K^-\pi^+\pi^-$ current (right). The parameters marked as 'fixed' were fixed to the displayed values during the fit procedure.

To perform the fits of the $K^*K\pi \to K_S K^{\pm}\pi^{\mp}\pi^0$ and $K^{*0}K^{\pm}\pi^{\mp} \to K^+K^-\pi^+\pi^-$ processes

we used data from BaBar [56, 57]. The vector meson resonances found by the fit to mediate these channels were $V = \phi', \rho''$, which correspond to the $\phi(1680)$ and $\rho(1700)$ mesons of PDG [2]. Table C.2 summarizes the obtained fit parameters and figure C.2 shows the curve of the best fit solution for each of these four $KK\pi\pi$ intermediate states.

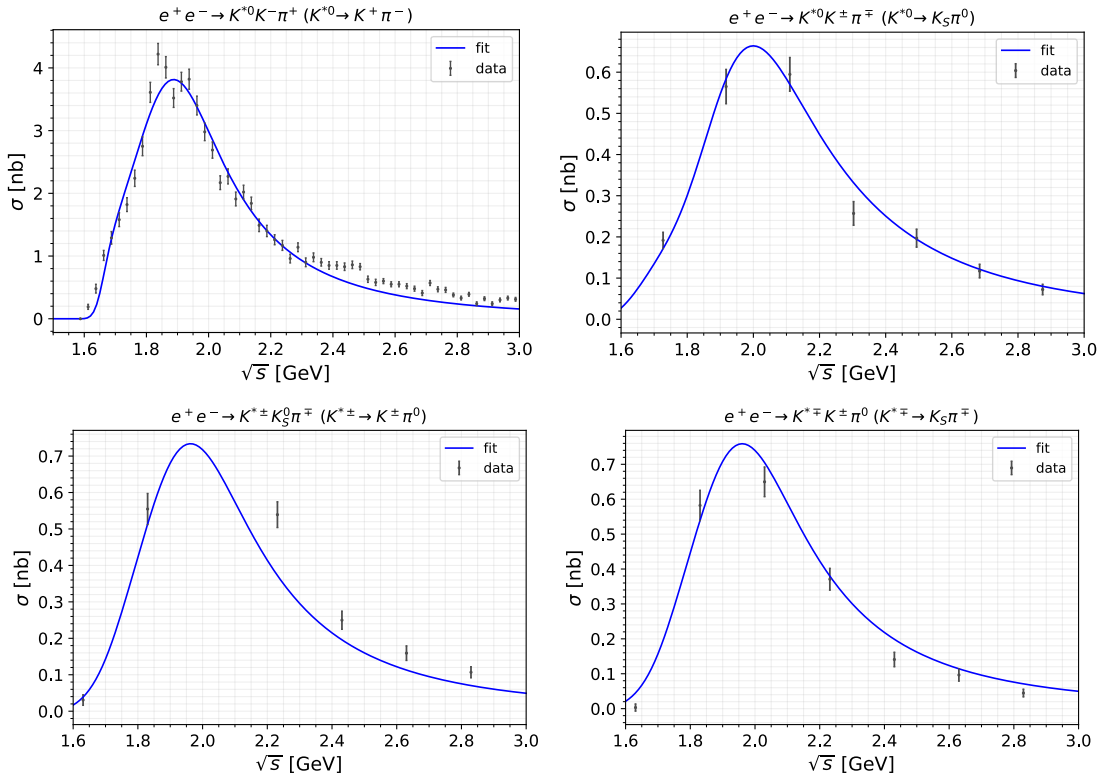

Figure C.2: Cross-section for the charged $K^{*0}K^\pm\pi^\mp$ (upper left panel), neutral $K^{*0}K^\pm\pi^\mp$ (upper right panel), $K^{*\pm}K_S\pi^\mp$ (lower left panel) and $K^{*\mp}K^\pm\pi^0$ (lower right panel) hadronic final states. The blue curve shows the best fit solution to the cross-section data, obtained considering the fit values of table C.2. The black points and error bars represent data from [56, 57].

C.3 $\mathcal{H} = \phi\pi\pi$

The $\phi\pi\pi$ channel is another example of a $\mathcal{H} = VPP$ current. This mode can be divided into a charged ($\phi\pi^+\pi^-$) and a neutral ($\phi\pi^0\pi^0$) component, that act as minor intermediate substructures of the final $K^+K^-\pi^+\pi^-$ and $K^+K^-\pi^0\pi^0$ channels, respectively, through the decay of the ϕ meson into two kaons, $\phi(1020) \to K^+K^-$.

In the relevant hadronic energy region, which extends from $0.2\,\mathrm{GeV}$ up to $\sim 2\,\mathrm{GeV}$, we can describe both $\phi\pi\pi$ states by the first two excited ϕ resonances, *i.e.* ϕ' and ϕ'', that correspond to

Parameter	Fit Value	Parameter	Fit Value
$m_{\phi'}$	$1.680 \pm 0.012\,\text{GeV}$	$m_{\phi''}$	$2.162 \pm 0.015\,\text{GeV}$
$a_{\phi'}$	1.44 ± 0.16	$a_{\phi''}$	0.69 ± 0.11
$\Gamma_{\phi'}$	$0.226 \pm 0.021\,\text{GeV}$	$\Gamma_{\phi''}$	$0.209 \pm 0.025\,\text{GeV}$
$\varphi_{\phi'}$	2.6 ± 0.4	$\varphi_{\phi''}$	0 (fixed)
$\chi^2/\text{n.d.f.} = 0.55$			

Table C.3: Values obtained by the fit for the $e^+e^- \to \phi\pi\pi$ current.

the $\phi(1680)$ and $\phi(2170)$ states, respectively. Hence, the form-factor will be given by

$$F_{\phi\pi\pi} = \sum_V \frac{a_V m_V^2 e^{i\varphi_V}}{m_V^2 - s - i\sqrt{s}\Gamma_V} \,, \tag{C.6}$$

with $V = \phi', \phi''$. The data used for the fit was taken from [56, 58] and the values of the parameters extracted from the fit are shown in table C.3. One can find the curve of the best fit for both charged and neutral modes, together with the corresponding data points, in figure C.3.

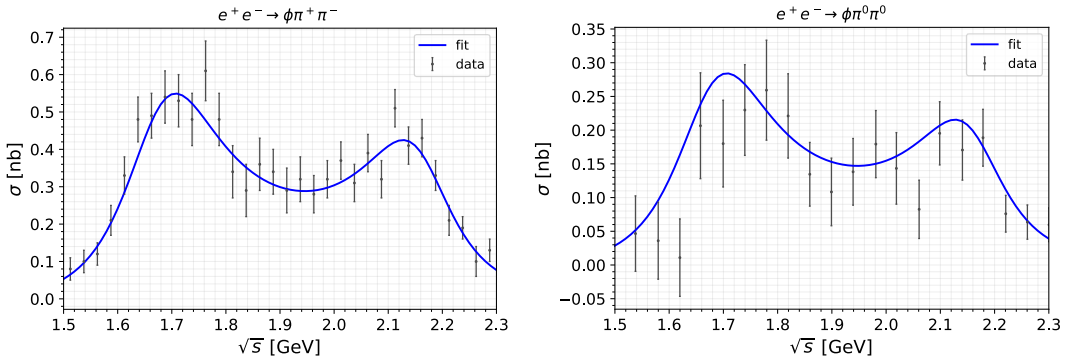

Figure C.3: Cross-section for the charged $\phi\pi^+\pi^-$ (left panel) and neutral $\phi\pi^0\pi^0$ (right panel) hadronic final states. The blue curve shows the best fit solution to the cross-section, obtained considering the fit parameters of table C.3. The black points and error bars represent data from [56, 58].

C.4 $\mathcal{H} = 6\pi$

Finally, in the case of the 6π channel we considered a charged $3(\pi^+\pi^-)$ and a neutral $2(\pi^+\pi^-\pi^0)$ contribution. For this particular channel, we cannot use Breit-Wigners to identify which resonances contribute since the available data does not indicate any clear intermediate structure. Hence, we can only describe the 6π channel by the inclusion of decays of many dif-

$3(\pi^+\pi^-)$		$2(\pi^+\pi^-\pi^0)$	
Parameter	Fit Value	Parameter	Fit Value
$m_{\rho'''}$	1.88 GeV (fixed)	$m_{\rho'''}$	1.86 GeV (fixed)
$a_{\rho'''}$	$0.0037 \pm 0.0005\,\mathrm{GeV}^{1/2}$	$a_{\rho'''}$	$-0.0072 \pm 0.0009\,\mathrm{GeV}^{1/2}$
$\Gamma_{\rho'''}$	0.13 GeV (fixed)	$\Gamma_{\rho'''}$	0.16 GeV (fixed)
$\varphi_{\rho'''}$	0.367 (fixed)	$\varphi_{\rho'''}$	-0.052 (fixed)
c_0	$0.0153 \pm 0.0029\,\mathrm{GeV}^{1/2}$	c_0	$-0.028 \pm 0.009\,\mathrm{GeV}^{1/2}$
c_1	$-1.082 \pm 0.017\,\mathrm{GeV}^{(5/2-a)}$	c_1	$2.4 \pm 0.7\,\mathrm{GeV}^{(5/2-a)}$
b	1.40 ± 0.01 GeV	b	1.54 ± 0.32 GeV
a	0.89 ± 0.04	a	0.85 ± 0.23
m_0	1.262 ± 0.012 GeV	m_0	1.20 ± 0.04 GeV
$\chi^2/\mathrm{n.d.f.} = 0.6$		$\chi^2/\mathrm{n.d.f.} = 0.7$	

Table C.4: Values of the parameters obtained by the best fit to the $e^+e^- \to 3(\pi^+\pi^-)$ current (left) and $e^+e^- \to 2(\pi^+\pi^-)\pi^0\pi^0$ current (right) cross-section data. The fixed values of $m_{\rho'''}$, $\Gamma_{\rho'''}$ and $\varphi_{\rho'''}$ were taken from [59].

ferent vector states. Following [59, 208], the fit of the 6π cross-section was made according to the parametrization given by

$$\sigma_{6\pi} = \frac{4\pi\alpha^2}{s^{3/2}} \left(\frac{a_V m_V^2 e^{i\varphi_V}}{s - m_V^2 + i\sqrt{s}\Gamma_V} + A_{\mathrm{cont}} \right)^2 , \tag{C.7}$$

where

$$A_{\mathrm{cont}} = c_0 + c_1 \frac{e^{-b/(\sqrt{s}-m_0)}}{(\sqrt{s}-m_0)^{2-a}} \tag{C.8}$$

is a Jacob-Slansky amplitude [209] that accounts for the mixture of several broad resonances and the parameters c_0, c_1, a, b, m_0 are free variables. Using G-parity symmetry arguments we can identify the resonance contribution V with the higher excitation of the ρ vector meson, namely $V = \rho'''$, which correspond to the PDG particle $\rho(1900)$. Table C.4 exhibits the values of the free parameters obtained by our fit using the parametrization described above and the data from [59]. The best fit solution to the cross-section data points, for both charged and neutral 6π modes, can be found in figure C.4.

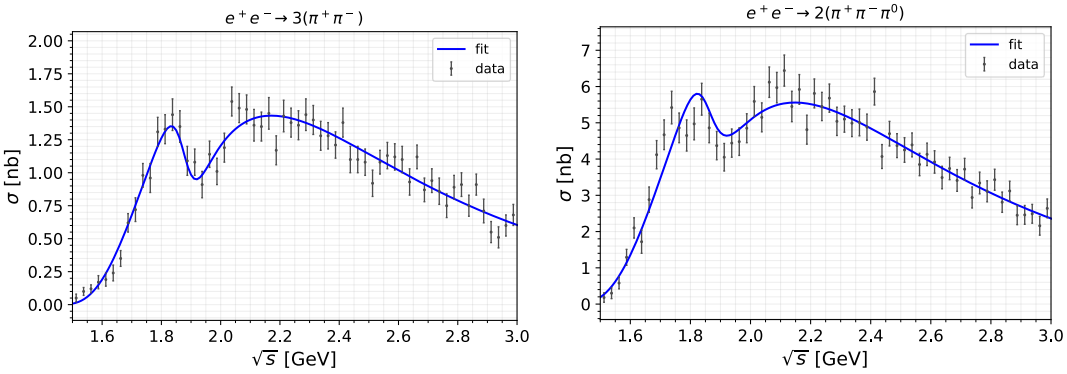

Figure C.4: Cross-section for the charged $3(\pi^+\pi^-)$ (left panel) and neutral $2(\pi^+\pi^-\pi^0)$ (right panel) hadronic final states. The blue curve shows the best fit solution to the cross-section, obtained considering the parameterization described in eq. (C.7) and (C.8) and the fit values of table C.4. The black error bars represent data from BaBar [59].

Appendix D

Additional Plots

In this appendix we will provide additional relevant plots and figures that we choose to omit from the main text, in order to avoid repetition.

D.1 Branching Ratios

In section 3.2 we show several branching ratio plots considering different $U(1)_Q$ models. Here we will also exhibit the plots for the $B - 3L_\mu$ and $B - L_e - 2L_\tau$, that can be found in figure D.1.

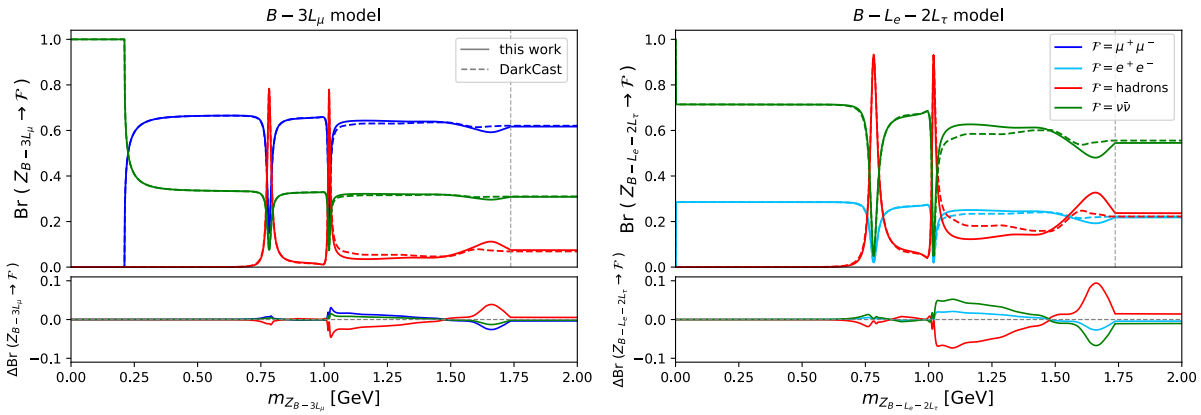

Figure D.1: Branching ratio of the vector boson mediator Z_Q decaying into electrons (light blue), muons (dark blue), hadrons (red) and neutrinos (green) for the $B - 3L_\mu$ (left) and $B - L_e - 2L_\tau$ (right) models. The solid (dashed) lines correspond to this dissertation (DARKCAST) results. In the lower panel of each figure we show the branching ratio difference between the two calculations.

Bibliography

[1] P. Ilten, Y. Soreq, M. Williams, and W. Xue, "Serendipity in dark photon searches," JHEP **06** (2018) 004, arXiv:1801.04847 [hep-ph].

[2] **Particle Data Group** Collaboration, P. A. Zyla et al., "Review of Particle Physics," PTEP **2020** no. 8, (2020) 083C01.

[3] **SND** Collaboration, M. N. Achasov et al., "Study of the reaction $e^+e^- \to \pi^0\gamma$ with the SND detector at the VEPP-2M collider," Phys. Rev. D **93** no. 9, (2016) 092001, arXiv:1601.08061 [hep-ex].

[4] **CLEO** Collaboration, T. K. Pedlar et al., "Precision measurements of the timelike electromagnetic form-factors of pion, kaon, and proton," Phys. Rev. Lett. **95** (2005) 261803, arXiv:hep-ex/0510005.

[5] M. N. Achasov et al., "Measurements of the parameters of the $\phi(1020)$ resonance through studies of the processes $e^+e^- \to K^+K^-$, K_SK_L, and $\pi^+\pi^-\pi^0$," Phys. Rev. D **63** (2001) 072002, arXiv:hep-ex/0009036.

[6] M. N. Achasov et al., "Experimental study of the reaction e+ d- $\to$ K(S)K(L) in the energy range s**(1/2) = 1.04-GeV divided by 1.38-GeV," J. Exp. Theor. Phys. **103** no. 5, (2006) 720–727, arXiv:hep-ex/0606057.

[7] F. Mane, D. Bisello, J. C. Bizot, J. Buon, A. Cordier, and B. Delcourt, "Study of the Reaction $e^+e^- \to K^0_SK^0_L$ in the Total Energy Range 1.4-GeV to 2.18-GeV and Interpretation of the K^+ and K^0 Form-factors," Phys. Lett. B **99** (1981) 261–264.

[8] **CMD-3** Collaboration, E. A. Kozyrev et al., "Study of the process $e^+e^- \to K^0_SK^0_L$ in the center-of-mass energy range 1004–1060 MeV with the CMD-3 detector at the VEPP-2000 e^+e^- collider," Phys. Lett. B **760** (2016) 314–319, arXiv:1604.02981 [hep-ex].

[9] **BaBar** Collaboration, J. P. Lees et al., "Cross sections for the reactions $e^+e^- \to K^0_S K^0_L$, $K^0_S K^0_L \pi^+\pi^-$, $K^0_S K^0_S \pi^+\pi^-$, and $K^0_S K^0_S K^+K^-$ from events with initial-state radiation," Phys. Rev. D **89** no. 9, (2014) 092002, arXiv:1403.7593 [hep-ex].

[10] **CMD-2** Collaboration, R. R. Akhmetshin et al., "Measurement of $e^+e^- \to \phi \to K^+K^-$ cross section with the CMD-2 detector at VEPP-2M Collider," Phys. Lett. B **669** (2008) 217–222, arXiv:0804.0178 [hep-ex].

[11] **BaBar** Collaboration, J. P. Lees et al., "Precision measurement of the $e^+e^-ßK^+K^-(\gamma)$ cross section with the initial-state radiation method at BABAR," Phys. Rev. D **88** no. 3, (2013) 032013, arXiv:1306.3600 [hep-ex].

[12] **BaBar** Collaboration, J. P. Lees et al., "Study of the $e^+e^- \to K^+K^-$ reaction in the energy range from 2.6 to 8.0 GeV," Phys. Rev. D **92** no. 7, (2015) 072008, arXiv:1507.04638 [hep-ex].

[13] M. N. Achasov et al., "Measurement of the $\mathrm{e^+e^- \to K^+K^-}$ cross section in the energy range $\sqrt{\mathrm{s}} = 1.05 - 2.0$ GeV" Phys. Rev. D **94** no. 11, (2016) 112006, arXiv:1608.08757 [hep-ex].

[14] **BaBar** Collaboration, B. Aubert et al., "Measurements of $e^+e^- \to K^+K^-\eta$, $K^+K^-\pi^0$ and $K^0_s K^\pm \pi^\mp$ cross- sections using initial state radiation events," Phys. Rev. D **77** (2008) 092002, arXiv:0710.4451 [hep-ex].

[15] **BaBar** Collaboration, J. P. Lees et al., "Cross sections for the reactions $e^+e^- \to K^0_S K^0_L \pi^0$, $K^0_S K^0_L \eta$, and $K^0_S K^0_L \pi^0\pi^0$ from events with initial-state radiation," Phys. Rev. D **95** no. 5, (2017) 052001, arXiv:1701.08297 [hep-ex].

[16] M. N. Achasov et al., "Measurement of the $\mathrm{e^+e^- \to K_S K_L \pi^0}$ cross section in the energy range $\sqrt{\mathrm{s}} = 1.3 - 2.0$ GeV" Phys. Rev. D **97** no. 3, (2018) 032011, arXiv:1711.07143 [hep-ex].

[17] D. Bisello et al., "Observation of an isoscalar vector meson at approximately = 1650-MeV/c**2 in the e+ e- → K anti-K pi reaction," Z. Phys. C **52** (1991) 227–230.

[18] F. Mane, D. Bisello, J. C. Bizot, J. Buon, A. Cordier, and B. Delcourt, "Study of $e^+e^- \to K^0_S K^\pm \pi^\mp$ in the 1.4-GeV to 2.18-GeV Energy Range: A New Observation of an Isoscalar Vector Meson ϕ' (1.65-GeV)," Phys. Lett. B **112** (1982) 178–182.

[19] T. Plehn, P. Reimitz, and P. Richardson, "Hadronic Footprint of GeV-Mass Dark Matter," SciPost Phys. **8** (2020) 092, arXiv:1911.11147 [hep-ph].

[20] **APEX** Collaboration, S. Abrahamyan et al., "Search for a New Gauge Boson in Electron-Nucleus Fixed-Target Scattering by the APEX Experiment," Phys. Rev. Lett. **107** (2011) 191804, arXiv:1108.2750 [hep-ex].

[21] **A1** Collaboration, H. Merkel et al., "Search for Light Gauge Bosons of the Dark Sector at the Mainz Microtron," Phys. Rev. Lett. **106** (2011) 251802, arXiv:1101.4091 [nucl-ex].

[22] H. Merkel et al., "Search at the Mainz Microtron for Light Massive Gauge Bosons Relevant for the Muon g-2 Anomaly," Phys. Rev. Lett. **112** no. 22, (2014) 221802, arXiv:1404.5502 [hep-ex].

[23] G. Bernardi et al., "Search for Neutrino Decay," Phys. Lett. B **166** (1986) 479–483.

[24] J. Blumlein et al., "Limits on neutral light scalar and pseudoscalar particles in a proton beam dump experiment," Z. Phys. C **51** (1991) 341–350.

[25] J. Blumlein et al., "Limits on the mass of light (pseudo)scalar particles from Bethe-Heitler e+ e- and mu+ mu- pair production in a proton - iron beam dump experiment," Int. J. Mod. Phys. A **7** (1992) 3835–3850.

[26] **CHARM** Collaboration, F. Bergsma et al., "Search for Axion Like Particle Production in 400-GeV Proton - Copper Interactions," Phys. Lett. B **157** (1985) 458–462.

[27] **LSND** Collaboration, C. Athanassopoulos et al., "Evidence for muon-neutrino $\rightarrow$ electron-neutrino oscillations from pion decay in flight neutrinos," Phys. Rev. C **58** (1998) 2489–2511, arXiv:nucl-ex/9706006.

[28] M. Bauer, P. Foldenauer, and J. Jaeckel, "Hunting All the Hidden Photons," JHEP **07** (2018) 094, arXiv:1803.05466 [hep-ph].

[29] J. D. Bjorken, R. Essig, P. Schuster, and N. Toro, "New Fixed-Target Experiments to Search for Dark Gauge Forces," Phys. Rev. D **80** (2009) 075018, arXiv:0906.0580 [hep-ph].

[30] S. Andreas, C. Niebuhr, and A. Ringwald, "New Limits on Hidden Photons from Past Electron Beam Dumps," Phys. Rev. D **86** (2012) 095019, arXiv:1209.6083 [hep-ph].

[31] **BaBar** Collaboration, J. P. Lees et al., "Search for a Dark Photon in e^+e^- Collisions at BaBar," Phys. Rev. Lett. **113** no. 20, (2014) 201801, arXiv:1406.2980 [hep-ex].

[32] A. Anastasi et al., "Limit on the production of a low-mass vector boson in $e^+e^- \to U\gamma$, $U \to e^+e^-$ with the KLOE experiment," Phys. Lett. B **750** (2015) 633–637, arXiv:1509.00740 [hep-ex].

[33] **KLOE-2** Collaboration, D. Babusci et al., "Limit on the production of a light vector gauge boson in phi meson decays with the KLOE detector," Phys. Lett. B **720** (2013) 111–115, arXiv:1210.3927 [hep-ex].

[34] **LHCb** Collaboration, R. Aaij et al., "Search for Dark Photons Produced in 13 TeV pp Collisions," Phys. Rev. Lett. **120** no. 6, (2018) 061801, arXiv:1710.02867 [hep-ex].

[35] **LHCb** Collaboration, R. Aaij et al., "Search for $A' \to \mu^+\mu^-$ Decays," Phys. Rev. Lett. **124** no. 4, (2020) 041801, arXiv:1910.06926 [hep-ex].

[36] **NA48/2** Collaboration, J. R. Batley et al., "Search for the dark photon in π^0 decays," Phys. Lett. B **746** (2015) 178–185, arXiv:1504.00607 [hep-ex].

[37] **KLOE-2** Collaboration, D. Babusci et al., "Search for light vector boson production in $e^+e^- \to \mu^+\mu^-\gamma$ interactions with the KLOE experiment," Phys. Lett. B **736** (2014) 459–464, arXiv:1404.7772 [hep-ex].

[38] **KLOE-2** Collaboration, A. Anastasi et al., "Combined limit on the production of a light gauge boson decaying into $\mu^+\mu^-$ and $\pi^+\pi^-$," Phys. Lett. B **784** (2018) 336–341, arXiv:1807.02691 [hep-ex].

[39] **BaBar** Collaboration, J. P. Lees et al., "Search for Invisible Decays of a Dark Photon Produced in e^+e^- Collisions at BaBar," Phys. Rev. Lett. **119** no. 13, (2017) 131804, arXiv:1702.03327 [hep-ex].

[40] **NA62** Collaboration, E. Cortina Gil et al., "Search for production of an invisible dark photon in π^0 decays," JHEP **05** (2019) 182, arXiv:1903.08767 [hep-ex].

[41] **NA64** Collaboration, D. Banerjee et al., "Search for invisible decays of sub-GeV dark photons in missing-energy events at the CERN SPS," Phys. Rev. Lett. **118** no. 1, (2017) 011802, arXiv:1610.02988 [hep-ex].

[42] **NA64** Collaboration, D. Banerjee et al., "Search for vector mediator of Dark Matter production in invisible decay mode," Phys. Rev. D **97** no. 7, (2018) 072002, arXiv:1710.00971 [hep-ex].

[43] D. Banerjee et al., "Dark matter search in missing energy events with NA64," Phys. Rev. Lett. **123** no. 12, (2019) 121801, arXiv:1906.00176 [hep-ex].

[44] **BESIII** Collaboration, M. Ablikim et al., "Dark Photon Search in the Mass Range Between 1.5 and 3.4 GeV/c^2," Phys. Lett. B **774** (2017) 252–257, arXiv:1705.04265 [hep-ex].

[45] **TEXONO** Collaboration, M. Deniz et al., "Measurement of Nu(e)-bar -Electron Scattering Cross-Section with a CsI(Tl) Scintillating Crystal Array at the Kuo-Sheng Nuclear Power Reactor," Phys. Rev. D **81** (2010) 072001, arXiv:0911.1597 [hep-ex].

[46] M. Lindner, F. S. Queiroz, W. Rodejohann, and X.-J. Xu, "Neutrino-electron scattering: general constraints on Z' and dark photon models," JHEP **05** (2018) 098, arXiv:1803.00060 [hep-ph].

[47] S. Bilmis, I. Turan, T. M. Aliev, M. Deniz, L. Singh, and H. T. Wong, "Constraints on Dark Photon from Neutrino-Electron Scattering Experiments," Phys. Rev. D **92** no. 3, (2015) 033009, arXiv:1502.07763 [hep-ph].

[48] D. Geiregat, G. Wilquet, U. Binder, H. Burkard, U. Dore, W. Flegel, H. Grote, T. Mouthuy, H. Overås, J. Panman, R. Santacesaria, P. Vilain, K. Winter, G. Zacek, V. Zacek, R. Beyer, F. Büsser, C. Foos, L. Gerland, T. Layda, F. Niebergall, G. Rädel, P. Stähelin, T. Voss, D. Favart, G. Grégoire, E. Knoops, P. Gorbunov, E. Grigoriev, V. Khovansky, A. Maslennikov, A. Rozanov, W. Lippich, A. Nathaniel, A. Staude, M. Caria, B. Eckart, A. Ereditato, R. Iasevoli, V. Palladino, P. Strohlin, A. Capone, D. De Pedis, E. Di Capua, A. Frenkel-Rambaldi, P. Loverre, G. Piredda, and D. Zanello, "First observation of neutrino trident production," Physics Letters B **245** no. 2, (1990) 271–275. https://www.sciencedirect.com/science/article/pii/037026939090146W.

[49] D. Barney, "CMS Detector Slice." CMS Collection., Jan, 2016.

[50] **ATLAS** Collaboration, G. Aad et al., "The ATLAS Experiment at the CERN Large Hadron Collider," JINST **3** (2008) S08003.

[51] D. Curtin, R. Essig, S. Gori, and J. Shelton, "Illuminating Dark Photons with High-Energy Colliders," JHEP **02** (2015) 157, arXiv:1412.0018 [hep-ph].

[52] **ATLAS** Collaboration, G. Aad et al., "Search for Higgs bosons decaying into new spin-0 or spin-1 particles in four-lepton final states with the ATLAS detector with 139 fb^{-1} of pp collision data at $\sqrt{s} = 13$ TeV," JHEP **03** (2022) 041, arXiv:2110.13673 [hep-ex].

[53] **CMD-2** Collaboration, R. R. Akhmetshin et al., "Study of the process e+ e- → pi+ pi- pi+ pi- pi0 with CMD-2 detector," Phys. Lett. B **489** (2000) 125–130, arXiv:hep-ex/0009013.

[54] **BaBar** Collaboration, B. Aubert et al., "The e+ e- → 2(pi+ pi-) pi0, 2(pi+ pi-) eta, K+ K- pi+ pi- pi0 and K+ K- pi+ pi- eta Cross Sections Measured with Initial-State Radiation," Phys. Rev. D **76** (2007) 092005, arXiv:0708.2461 [hep-ex]. [Erratum: Phys.Rev.D 77, 119902 (2008)].

[55] **BaBar** Collaboration, J. P. Lees et al., "Study of the reactions $e^+e^- \to \pi^+\pi^-\pi^0\pi^0\pi^0\gamma$ and $\pi^+\pi^-\pi^0\pi^0\eta\gamma$ at center-of-mass energies from threshold to 4.35 GeV using initial-state radiation," Phys. Rev. D **98** no. 11, (2018) 112015, arXiv:1810.11962 [hep-ex].

[56] **BaBar** Collaboration, J. P. Lees et al., "Cross Sections for the Reactions e+e- → K+ K- pi+pi-, K+ K- pi0pi0, and K+ K- K+ K- Measured Using Initial-State Radiation Events," Phys. Rev. D **86** (2012) 012008, arXiv:1103.3001 [hep-ex].

[57] **BaBar** Collaboration, J. P. Lees et al., "Measurement of the $e^+e^- \to K^0_S K^\pm\pi^\mp\pi^0$ and $K^0_S K^\pm\pi^\mp\eta$ cross sections using initial-state radiation," Phys. Rev. D **95** no. 9, (2017) 092005, arXiv:1704.05009 [hep-ex].

[58] **Belle** Collaboration, C. P. Shen et al., "Observation of the phi(1680) and the Y(2175) in e+e- → phi pi+ pi-," Phys. Rev. D **80** (2009) 031101, arXiv:0808.0006 [hep-ex].

[59] **BaBar** Collaboration, B. Aubert et al., "The $e^+e^- \to 3(\pi^+\pi^-), 2(\pi^+\pi^-\pi^0)$ and $K^+K^-2(\pi^+\pi^-)$ cross sections at center-of-mass energies from production threshold to 4.5-GeV measured with initial-state radiation," Phys. Rev. D **73** (2006) 052003, arXiv:hep-ex/0602006.

[60] **ATLAS** Collaboration, G. Aad et al., "Observation of a new particle in the search for the Standard Model Higgs boson with the ATLAS detector at the LHC," Phys. Lett. B **716** (2012) 1–29, arXiv:1207.7214 [hep-ex].

[61] **CMS** Collaboration, S. Chatrchyan et al., "Observation of a New Boson at a Mass of 125 GeV with the CMS Experiment at the LHC," Phys. Lett. B **716** (2012) 30–61, arXiv:1207.7235 [hep-ex].

[62] C. Csáki and P. Tanedo, "Beyond the Standard Model," in 2013 European School of High-Energy Physics, pp. 169–268. 2015. arXiv:1602.04228 [hep-ph].

[63] R. Zukanovich Funchal, B. Schmauch, and G. Giesen, "The Physics of Neutrinos," arXiv:1308.1029 [hep-ph].

[64] **Super-Kamiokande** Collaboration, Y. Fukuda et al., "Evidence for oscillation of atmospheric neutrinos," Phys. Rev. Lett. **81** (1998) 1562–1567, arXiv:hep-ex/9807003.

[65] S. M. Faber and R. E. Jackson, "Velocity dispersions and mass-to-light ratios for elliptical galaxies.," **204** (Mar., 1976) 668–683.

[66] E. Corbelli and P. Salucci, "The Extended Rotation Curve and the Dark Matter Halo of M33," Mon. Not. Roy. Astron. Soc. **311** (2000) 441–447, arXiv:astro-ph/9909252.

[67] D. Clowe, M. Bradac, A. H. Gonzalez, M. Markevitch, S. W. Randall, C. Jones, and D. Zaritsky, "A direct empirical proof of the existence of dark matter," Astrophys. J. Lett. **648** (2006) L109–L113, arXiv:astro-ph/0608407.

[68] **Planck** Collaboration, P. A. R. Ade et al., "Planck 2015 results. XIII. Cosmological parameters," Astron. Astrophys. **594** (2016) A13, arXiv:1502.01589 [astro-ph.CO].

[69] G. Bertone and D. Merritt, "Dark matter dynamics and indirect detection," Mod. Phys. Lett. A **20** (2005) 1021, arXiv:astro-ph/0504422.

[70] A. L. Foguel, P. Reimitz, and R. Z. Funchal, "A Robust Description of Hadronic Decays in Light Vector Mediator Models," arXiv:2201.01788 [hep-ph].

[71] P. Fayet, "A la recherche d'un nouveau boson de spin un," Nuclear Physics B **187** no. 1, (1981) 184–204. https://www.sciencedirect.com/science/article/pii/055032138190122X.

[72] P. Fayet, "Effects of the spin-1 partner of the goldstino (gravitino) on neutral current phenomenology," Physics Letters B **95** no. 2, (1980) 285–289. https://www.sciencedirect.com/science/article/pii/0370269380904888.

[73] L. B. Okun, "LIMITS OF ELECTRODYNAMICS: PARAPHOTONS?," Sov. Phys. JETP **56** (1982) 502.

[74] P. Galison and A. Manohar, "TWO Z's OR NOT TWO Z's?," Phys. Lett. B **136** (1984) 279–283.

[75] M. Pospelov, "Secluded U(1) below the weak scale," Phys. Rev. D **80** (2009) 095002, arXiv:0811.1030 [hep-ph].

[76] B. Holdom, "Two U(1)'s and Epsilon Charge Shifts," Phys. Lett. B **166** (1986) 196–198.

[77] M. Raggi and V. Kozhuharov, "Results and perspectives in dark photon physics," Riv. Nuovo Cim. **38** no. 10, (2015) 449–505.

[78] M. Fabbrichesi, E. Gabrielli, and G. Lanfranchi, "The Dark Photon," arXiv:2005.01515 [hep-ph].

[79] M. Graham, C. Hearty, and M. Williams, "Searches for Dark Photons at Accelerators," Ann. Rev. Nucl. Part. Sci. **71** (2021) 37–58, arXiv:2104.10280 [hep-ph].

[80] M. Battaglieri et al., "US Cosmic Visions: New Ideas in Dark Matter 2017: Community Report," in U.S. Cosmic Visions: New Ideas in Dark Matter. 7, 2017. arXiv:1707.04591 [hep-ph].

[81] H. Georgi, P. H. Ginsparg, and S. L. Glashow, "Photon Oscillations and the Cosmic Background Radiation," Nature **306** (1983) 765–766.

[82] M. Pospelov, A. Ritz, and M. B. Voloshin, "Secluded WIMP Dark Matter," Phys. Lett. B **662** (2008) 53–61, arXiv:0711.4866 [hep-ph].

[83] A. Kamada, K. Kaneta, K. Yanagi, and H.-B. Yu, "Self-interacting dark matter and muon $g-2$ in a gauged $\mathrm{U}(1)_{L_\mu - L_\tau}$ model," JHEP **06** (2018) 117, arXiv:1805.00651 [hep-ph].

[84] D. Borah, M. Dutta, S. Mahapatra, and N. Sahu, "Muon (g−2) and XENON1T excess with boosted dark matter in Lμ−Lτ model," Phys. Lett. B **820** (2021) 136577, arXiv:2104.05656 [hep-ph].

[85] S. Singirala, S. Sahoo, and R. Mohanta, "Light dark matter, rare B decays with missing energy in $L_\mu - L_\tau$ model with a scalar leptoquark," arXiv:2106.03735 [hep-ph].

[86] I. Holst, D. Hooper, and G. Krnjaic, "The Simplest and Most Predictive Model of Muon $g-2$ and Thermal Dark Matter," arXiv:2107.09067 [hep-ph].

[87] B. Batell, J. L. Feng, M. Fieg, A. Ismail, F. Kling, R. M. Abraham, and S. Trojanowski, "Hadrophilic Dark Sectors at the Forward Physics Facility," arXiv:2111.10343 [hep-ph].

[88] N. Arkani-Hamed, D. P. Finkbeiner, T. R. Slatyer, and N. Weiner, "A Theory of Dark Matter," Phys. Rev. D **79** (2009) 015014, arXiv:0810.0713 [hep-ph].

[89] T. Araki, J. Heeck, and J. Kubo, "Vanishing Minors in the Neutrino Mass Matrix from Abelian Gauge Symmetries," JHEP **07** (2012) 083, arXiv:1203.4951 [hep-ph].

[90] S. H. Seo and Y. D. Kim, "Dark Photon Search at Yemilab, Korea," JHEP **04** (2021) 135, arXiv:2009.11155 [hep-ph].

[91] J. J. Sakurai, "Theory of strong interactions," Annals Phys. **11** (1960) 1–48.

[92] N. M. Kroll, T. D. Lee, and B. Zumino, "Neutral Vector Mesons and the Hadronic Electromagnetic Current," Phys. Rev. **157** (1967) 1376–1399.

[93] T. D. Lee and B. Zumino, "Field Current Identities and Algebra of Fields," Phys. Rev. **163** (1967) 1667–1681.

[94] S. Tulin, "New weakly-coupled forces hidden in low-energy QCD," Phys. Rev. D **89** no. 11, (2014) 114008, arXiv:1404.4370 [hep-ph].

[95] A. Deur, S. J. Brodsky, and G. F. de Teramond, "The QCD Running Coupling," Nucl. Phys. **90** (2016) 1, arXiv:1604.08082 [hep-ph].

[96] P. A. Baikov, K. G. Chetyrkin, J. H. Kuhn, and J. Rittinger, "Adler Function, Sum Rules and Crewther Relation of Order $\mathcal{O}(\alpha_s^4)$: the Singlet Case," Phys. Lett. B **714** (2012) 62–65, arXiv:1206.1288 [hep-ph].

[97] R. Essig et al., "Working Group Report: New Light Weakly Coupled Particles," in Community Summer Study 2013: Snowmass on the Mississippi. 10, 2013. arXiv:1311.0029 [hep-ph].

[98] J. Alexander et al., "Dark Sectors 2016 Workshop: Community Report," 8, 2016. arXiv:1608.08632 [hep-ph].

[99] A. Berlin, N. Blinov, G. Krnjaic, P. Schuster, and N. Toro, "Dark Matter, Millicharges, Axion and Scalar Particles, Gauge Bosons, and Other New Physics with LDMX," Phys. Rev. D **99** no. 7, (2019) 075001, arXiv:1807.01730 [hep-ph].

[100] H. Dembinski, P. Ongmongkolkul, C. Deil, D. M. Hurtado, H. Schreiner, M. Feickert, Andrew, C. Burr, J. Watson, F. Rost, A. Pearce, L. Geiger, B. M. Wiedemann, C. Gohlke, Gonzalo, J. Drotleff, J. Eschle, L. Neste, M. E. Gorelli, M. Baak, O. Zapata, and odidev, "scikit-hep/iminuit: v2.8.4," Oct., 2021. https://doi.org/10.5281/zenodo.5561211.

[101] G. Rodrigo, H. Czyz, J. H. Kuhn, and M. Szopa, "Radiative return at NLO and the measurement of the hadronic cross-section in electron positron annihilation," Eur. Phys. J. C **24** (2002) 71–82, arXiv:hep-ph/0112184.

[102] H. Czyż, P. Kisza, and S. Tracz, "Modeling interactions of photons with pseudoscalar and vector mesons," Phys. Rev. D **97** no. 1, (2018) 016006, arXiv:1711.00820 [hep-ph].

[103] **KLOE** Collaboration, F. Ambrosino et al., "Measurement of $\sigma(e^+e^- \to \pi^+\pi^-\gamma(\gamma)$ and the dipion contribution to the muon anomaly with the KLOE detector," Phys. Lett. B **670** (2009) 285–291, arXiv:0809.3950 [hep-ex].

[104] **BaBar** Collaboration, B. Aubert et al., "Precise measurement of the e+ e- $\to$ pi+ pi- (gamma) cross section with the Initial State Radiation method at BABAR," Phys. Rev. Lett. **103** (2009) 231801, arXiv:0908.3589 [hep-ex].

[105] **BaBar** Collaboration, J. P. Lees et al., "Precise Measurement of the $e^+e^- \to \pi^+\pi^-(\gamma)$ Cross Section with the Initial-State Radiation Method at BABAR," Phys. Rev. D **86** (2012) 032013, arXiv:1205.2228 [hep-ex].

[106] H. Czyz, A. Grzelinska, and J. H. Kuhn, "Narrow resonances studies with the radiative return method," Phys. Rev. D **81** (2010) 094014, arXiv:1002.0279 [hep-ph].

[107] **BaBar** Collaboration, B. Aubert et al., "Study of $e^+e^- \to \pi^+\pi^-\pi^0$ process using initial state radiation with BaBar," Phys. Rev. D **70** (2004) 072004, arXiv:hep-ex/0408078.

[108] H. Czyz, A. Grzelinska, J. H. Kuhn, and G. Rodrigo, "Electron-positron annihilation into three pions and the radiative return," Eur. Phys. J. C **47** (2006) 617–624, arXiv:hep-ph/0512180.

[109] **BaBar** Collaboration, J. P. Lees et al., "Initial-State Radiation Measurement of the $e^+e^- > \pi^+\pi^-\pi^+\pi^-$ Cross Section," Phys. Rev. D **85** (2012) 112009, arXiv:1201.5677 [hep-ex].

[110] **BaBar** Collaboration, J. P. Lees et al., "Measurement of the $e^+e^- \to \pi^+\pi^-\pi^0\pi^0$ cross section using initial-state radiation at BABAR," Phys. Rev. D **96** no. 9, (2017) 092009, arXiv:1709.01171 [hep-ex].

[111] H. Czyz, J. H. Kuhn, and A. Wapienik, "Four-pion production in tau decays and e+e- annihilation: An Update," Phys. Rev. D **77** (2008) 114005, arXiv:0804.0359 [hep-ph].

[112] M. N. Achasov et al., "Study of the e+ e- $\to$ eta gamma process with SND detector at the VEPP-2M e+ e- collider," Phys. Rev. D **74** (2006) 014016, arXiv:hep-ex/0605109.

[113] M. N. Achasov et al., "Measurement of the e+ e- $\to \eta\pi^+\pi^-$ cross section with the SND detector at the VEPP-2000 collider," Phys. Rev. D **97** no. 1, (2018) 012008, arXiv:1711.08862 [hep-ex].

[114] **BaBar** Collaboration, J. P. Lees et al., "Study of the process $e^+e^- \to \pi^+\pi^-\eta$ using initial state radiation," Phys. Rev. D **97** (2018) 052007, arXiv:1801.02960 [hep-ex].

[115] H. Czyż, M. Gunia, and J. H. Kühn, "Simulation of electron-positron annihilation into hadrons with the event generator PHOKHARA," JHEP **08** (2013) 110, arXiv:1306.1985 [hep-ph].

[116] M. N. Achasov et al., "Updated measurement of the $e^+e^- \to \omega\pi^0 \to \pi^0\pi^0\gamma$ cross section with the SND detector," Phys. Rev. D **94** no. 11, (2016) 112001, arXiv:1610.00235 [hep-ex].

[117] **BaBar** Collaboration, J. P. Lees et al., "Cross sections for the reactions $e^+e^- \to K^0_S K^0_L \pi^0$, $K^0_S K^0_L \eta$, and $K^0_S K^0_L \pi^0 \pi^0$ from events with initial-state radiation," Phys. Rev. D **95** no. 5, (2017) 052001, arXiv:1701.08297 [hep-ex].

[118] M. N. Achasov et al., "Measurement of the $e^+e^- \to \omega\eta$ cross section below $\sqrt{s} = 2$ GeV," Phys. Rev. D **94** no. 9, (2016) 092002, arXiv:1607.00371 [hep-ex].

[119] M. N. Achasov et al., "Measurement of the e+e- $\to \eta K^+ K^-$ Cross Section by Means of the SND Detector," Phys. Atom. Nucl. **81** no. 2, (2018) 205–213.

[120] **BaBar** Collaboration, J. P. Lees et al., "Study of $e^+e^- \to p\bar{p}$ via initial-state radiation at BABAR," Phys. Rev. **D87** no. 9, (2013) 092005, arXiv:1302.0055 [hep-ex].

[121] **BESIII** Collaboration, M. Ablikim et al., "Measurement of the proton form factor by studying $e^+e^- \to p\bar{p}$," Phys. Rev. **D91** no. 11, (2015) 112004, arXiv:1504.02680 [hep-ex].

[122] **CLEO** Collaboration, T. K. Pedlar et al., "Precision measurements of the timelike electromagnetic form-factors of pion, kaon, and proton," Phys. Rev. Lett. **95** (2005) 261803, arXiv:hep-ex/0510005 [hep-ex].

[123] B. Delcourt et al., "Study of the Reaction $e^+e^- \to p\bar{p}$ in the Total Energy Range 1925-MeV - 2180-MeV," Phys. Lett. **86B** (1979) 395–398.

[124] M. Castellano, G. Di Giugno, J. W. Humphrey, E. Sassi Palmieri, G. Troise, U. Troya, and S. Vitale, "The reaction $e^+e^- \to p\bar{p}$ at a total energy of 2.1 gev," Nuovo Cim. **A14** (1973) 1–20.

[125] A. Antonelli et al., "The first measurement of the neutron electromagnetic form-factors in the timelike region," Nucl. Phys. **B517** (1998) 3–35.

[126] **E760** Collaboration, T. A. Armstrong et al., "Measurement of the proton electromagnetic form-factors in the timelike region at $8.9 - GeV^2 - 13 - GeV^2$," Phys. Rev. Lett. **70** (1993) 1212–1215.

[127] **E835** Collaboration, M. Ambrogiani et al., "Measurements of the magnetic form-factor of the proton in the timelike region at large momentum transfer," Phys. Rev. **D60** (1999) 032002.

[128] M. Andreotti et al., "Measurements of the magnetic form-factor of the proton for timelike momentum transfers," Phys. Lett. **B559** (2003) 20–25.

[129] V. Punjabi et al., "Proton elastic form-factor ratios to $Q^2 = 3.5\mathrm{GeV}^2$ by polarization transfer," Phys. Rev. **C71** (2005) 055202, arXiv:nucl-ex/0501018 [nucl-ex]. [Erratum: Phys. Rev.C71,069902(2005)].

[130] A. J. R. Puckett et al., "Final Analysis of Proton Form Factor Ratio Data at $\mathrm{Q}^2 = 4.0$, 4.8 and 5.6 GeV^2," Phys. Rev. **C85** (2012) 045203, arXiv:1102.5737 [nucl-ex].

[131] O. Gayou et al., "Measurements of the elastic electromagnetic form-factor ratio mu(p) G(Ep) / G(Mp) via polarization transfer," Phys. Rev. **C64** (2001) 038202.

[132] A. J. R. Puckett et al., "Recoil Polarization Measurements of the Proton Electromagnetic Form Factor Ratio to $Q^2 = 8.5\mathrm{GeV}^2$," Phys. Rev. Lett. **104** (2010) 242301, arXiv:1005.3419 [nucl-ex].

[133] A. J. R. Puckett et al., "Polarization Transfer Observables in Elastic Electron Proton Scattering at Q^2 =2.5, 5.2, 6.8, and 8.5 GeV^2," Phys. Rev. **C96** no. 5, (2017) 055203, arXiv:1707.08587 [nucl-ex]. [erratum: Phys. Rev.C98,no.1,019907(2018)].

[134] **A1** Collaboration, T. Pospischil et al., "Measurement of G(E(p))/G(M(p)) via polarization transfer at $Q^2 = 0.4 - \mathrm{GeV}/c^2$," Eur. Phys. J. **A12** (2001) 125–127.

[135] **Jefferson Laboratory E93-038** Collaboration, B. Plaster et al., "Measurements of the neutron electric to magnetic form-factor ratio G(En) / G(Mn) via the H-2(polarized-e, e-prime,polarized-n)H-1 reaction to $Q^2 = 1.45 - (\mathrm{GeV}/c)^2$," Phys. Rev. **C73** (2006) 025205, arXiv:nucl-ex/0511025 [nucl-ex].

[136] **BLAST** Collaboration, E. Geis et al., "The Charge Form Factor of the Neutron at Low Momentum Transfer from the H-2-polarized (e-polarized, e-prime n) p Reaction," Phys. Rev. Lett. **101** (2008) 042501, arXiv:0803.3827 [nucl-ex].

[137] L. Andivahis et al., "Measurements of the electric and magnetic form-factors of the proton from $Q^2 = 1.75\mathrm{GeV}/c^2$ to $8.83\mathrm{GeV}/c^2$," Phys. Rev. **D50** (1994) 5491–5517.

[138] H. Czyż, J. H. Kühn, and S. Tracz, "Nucleon form factors and final state radiative corrections to $e^+e^- \to p\bar{p}\gamma$," Phys. Rev. D **90** no. 11, (2014) 114021, arXiv:1407.7995 [hep-ph].

[139] M. Davier, A. Hoecker, B. Malaescu, and Z. Zhang, "Reevaluation of the hadronic vacuum polarisation contributions to the Standard Model predictions of the muon $g - 2$

and $\alpha(m_Z^2)$ using newest hadronic cross-section data," Eur. Phys. J. C **77** no. 12, (2017) 827, arXiv:1706.09436 [hep-ph].

[140] V. P. Druzhinin, S. I. Eidelman, S. I. Serednyakov, and E. P. Solodov, "Hadron Production via e+e- Collisions with Initial State Radiation," Rev. Mod. Phys. **83** (2011) 1545, arXiv:1105.4975 [hep-ex].

[141] K. Hagiwara, A. D. Martin, D. Nomura, and T. Teubner, "Predictions for g-2 of the muon and alpha(QED) (M**2(Z))," Phys. Rev. D **69** (2004) 093003, arXiv:hep-ph/0312250.

[142] M. R. Whalley, "A Compilation of data on hadronic total cross-sections in e+ e- interactions," J. Phys. G **29** (2003) A1–A133.

[143] F. Kling and S. Trojanowski, "Forward experiment sensitivity estimator for the LHC and future hadron colliders," Phys. Rev. D **104** no. 3, (2021) 035012, arXiv:2105.07077 [hep-ph].

[144] **FASER** Collaboration, A. Ariga et al., "FASER's physics reach for long-lived particles," Phys. Rev. D **99** no. 9, (2019) 095011, arXiv:1811.12522 [hep-ph].

[145] **FASER** Collaboration, A. Ariga et al., "Technical Proposal for FASER: ForwArd Search ExpeRiment at the LHC," arXiv:1812.09139 [physics.ins-det].

[146] **FASER** Collaboration, A. Ariga et al., "Letter of Intent for FASER: ForwArd Search ExpeRiment at the LHC," arXiv:1811.10243 [physics.ins-det].

[147] **FASER** Collaboration, H. Abreu et al., "Detecting and Studying High-Energy Collider Neutrinos with FASER at the LHC," Eur. Phys. J. C **80** no. 1, (2020) 61, arXiv:1908.02310 [hep-ex].

[148] J. A. Dror, R. Lasenby, and M. Pospelov, "New constraints on light vectors coupled to anomalous currents," Phys. Rev. Lett. **119** no. 14, (2017) 141803, arXiv:1705.06726 [hep-ph].

[149] J. A. Dror, R. Lasenby, and M. Pospelov, "Dark forces coupled to nonconserved currents," Phys. Rev. D **96** no. 7, (2017) 075036, arXiv:1707.01503 [hep-ph].

[150] G. Bellini et al., "Precision measurement of the 7Be solar neutrino interaction rate in Borexino," Phys. Rev. Lett. **107** (2011) 141302, arXiv:1104.1816 [hep-ex].

[151] R. Harnik, J. Kopp, and P. A. N. Machado, "Exploring nu Signals in Dark Matter Detectors," JCAP **07** (2012) 026, arXiv:1202.6073 [hep-ph].

[152] D. W. P. d. Amaral, D. G. Cerdeno, P. Foldenauer, and E. Reid, "Solar neutrino probes of the muon anomalous magnetic moment in the gauged $\mathrm{U}(1)_{L_\mu - L_\tau}$," JHEP **12** (2020) 155, arXiv:2006.11225 [hep-ph].

[153] M. Bauer, P. Foldenauer, and M. Mosny, "Flavor structure of anomaly-free hidden photon models," Phys. Rev. D **103** no. 7, (2021) 075024, arXiv:2011.12973 [hep-ph].

[154] C. Fanelli and M. Williams, "Photoproduction of leptophobic bosons," J. Phys. G **44** no. 1, (2017) 014002, arXiv:1605.07161 [hep-ph].

[155] S. Alekhin et al., "A facility to Search for Hidden Particles at the CERN SPS: the SHiP physics case," Rept. Prog. Phys. **79** no. 12, (2016) 124201, arXiv:1504.04855 [hep-ph].

[156] W. Bonivento et al., "Proposal to Search for Heavy Neutral Leptons at the SPS," arXiv:1310.1762 [hep-ex].

[157] **Belle-II** Collaboration, W. Altmannshofer et al., "The Belle II Physics Book," PTEP **2019** no. 12, (2019) 123C01, arXiv:1808.10567 [hep-ex]. [Erratum: PTEP 2020, 029201 (2020)].

[158] H. Ruegg and M. Ruiz-Altaba, "The Stueckelberg field," Int. J. Mod. Phys. A **19** (2004) 3265–3348, arXiv:hep-th/0304245.

[159] R. M. Schabinger and J. D. Wells, "A Minimal spontaneously broken hidden sector and its impact on Higgs boson physics at the large hadron collider," Phys. Rev. D **72** (2005) 093007, arXiv:hep-ph/0509209.

[160] S. Gopalakrishna, S. Jung, and J. D. Wells, "Higgs boson decays to four fermions through an abelian hidden sector," Phys. Rev. D **78** (2008) 055002, arXiv:0801.3456 [hep-ph].

[161] J. D. Wells, "How to Find a Hidden World at the Large Hadron Collider," arXiv:0803.1243 [hep-ph].

[162] S. Y. Choi, C. Englert, and P. M. Zerwas, "Multiple Higgs-Portal and Gauge-Kinetic Mixings," Eur. Phys. J. C **73** (2013) 2643, arXiv:1308.5784 [hep-ph].

[163] S. Gopalakrishna, "Hidden Sector Dark Matter and LHC Signatures," AIP Conf. Proc. **1200** no. 1, (2010) 778–781, arXiv:0909.5579 [hep-ph].

[164] J. Berger, K. Jedamzik, and D. G. E. Walker, "Cosmological Constraints on Decoupled Dark Photons and Dark Higgs," JCAP **11** (2016) 032, arXiv:1605.07195 [hep-ph].

[165] Y. Cui and F. D'Eramo, "Surprises from complete vector portal theories: New insights into the dark sector and its interplay with Higgs physics," Phys. Rev. D **96** no. 9, (2017) 095006, arXiv:1705.03897 [hep-ph].

[166] A. Falkowski, C. Gross, and O. Lebedev, "A second higgs from the higgs portal," Journal of High Energy Physics **2015** no. 5, (May, 2015) . http://dx.doi.org/10.1007/JHEP05(2015)057.

[167] **ALEPH, DELPHI, L3, OPAL, SLD, LEP Electroweak Working Group, SLD Electroweak Group, SLD Heavy Flavour Group** Collaboration, S. Schael et al., "Precision electroweak measurements on the Z resonance," Phys. Rept. **427** (2006) 257–454, arXiv:hep-ex/0509008.

[168] **CMS** Collaboration, "Measurements of the Higgs boson production and decay rates and constraints on its couplings from a combined ATLAS and CMS analysis of the LHC pp collision data at sqrt s = 7 and 8 TeV,".

[169] J. Alwall, R. Frederix, S. Frixione, V. Hirschi, F. Maltoni, O. Mattelaer, H. S. Shao, T. Stelzer, P. Torrielli, and M. Zaro, "The automated computation of tree-level and next-to-leading order differential cross sections, and their matching to parton shower simulations," JHEP **07** (2014) 079, arXiv:1405.0301 [hep-ph].

[170] A. Alloul, N. D. Christensen, C. Degrande, C. Duhr, and B. Fuks, "FeynRules 2.0 - A complete toolbox for tree-level phenomenology," Comput. Phys. Commun. **185** (2014) 2250–2300, arXiv:1310.1921 [hep-ph].

[171] **DELPHES 3** Collaboration, J. de Favereau, C. Delaere, P. Demin, A. Giammanco, V. Lemaître, A. Mertens, and M. Selvaggi, "DELPHES 3, A modular framework for fast simulation of a generic collider experiment," JHEP **02** (2014) 057, arXiv:1307.6346 [hep-ex].

[172] L. Buonocore, C. Frugiuele, and P. deNiverville, "Hunt for sub-GeV dark matter at neutrino facilities: A survey of past and present experiments," Phys. Rev. D **102** no. 3, (2020) 035006, arXiv:1912.09346 [hep-ph].

[173] **KOTO** Collaboration, J. K. Ahn et al., "Study of the $K_L \to \pi^0 \nu\bar{\nu}$ Decay at the J-PARC KOTO Experiment," Phys. Rev. Lett. **126** no. 12, (2021) 121801, arXiv:2012.07571 [hep-ex].

[174] **KOTO** Collaboration, C. Lin, "Recent Result on the Measurement of $K_L^0 \to \pi^0 \nu\bar{\nu}$ at the J-PARC KOTO Experiment," JPS Conf. Proc. **33** (2021) 011105.

[175] **CMS** Collaboration, S. Chatrchyan et al., "The CMS Experiment at the CERN LHC," JINST **3** (2008) S08004.

[176] **CMS** Collaboration, A. M. Sirunyan et al., "Performance of the CMS muon detector and muon reconstruction with proton-proton collisions at $\sqrt{s} = 13$ TeV," JINST **13** no. 06, (2018) P06015, arXiv:1804.04528 [physics.ins-det].

[177] D. Curtin et al., "Exotic decays of the 125 GeV Higgs boson," Phys. Rev. D **90** no. 7, (2014) 075004, arXiv:1312.4992 [hep-ph].

[178] T. Sjostrand, S. Mrenna, and P. Z. Skands, "A Brief Introduction to PYTHIA 8.1" Comput. Phys. Commun. **178** (2008) 852–867, arXiv:0710.3820 [hep-ph].

[179] E. Conte, B. Fuks, and G. Serret, "MadAnalysis 5, A User-Friendly Framework for Collider Phenomenology," Comput. Phys. Commun. **184** (2013) 222–256, arXiv:1206.1599 [hep-ph].

[180] A. Fowlie, "LHCO_reader: A new code for reading and analyzing detector-level events stored in LHCO format," arXiv:1510.07319 [hep-ph].

[181] **ATLAS** Collaboration, "Measurements of the properties of the Higgs-like boson in the four lepton decay channel with the ATLAS detector using 25 fb−1 of proton-proton collision data,".

[182] **CMS** Collaboration, S. Chatrchyan et al., "Measurement of the Properties of a Higgs Boson in the Four-Lepton Final State," Phys. Rev. D **89** no. 9, (2014) 092007, arXiv:1312.5353 [hep-ex].

[183] **CMS** Collaboration, A. Tumasyan et al., "Search for long-lived particles decaying into muon pairs in proton-proton collisions at $\sqrt{s}$ = 13 TeV collected with a dedicated high-rate data stream," JHEP **04** (2022) 062, arXiv:2112.13769 [hep-ex].

[184] T. Kitahara, T. Okui, G. Perez, Y. Soreq, and K. Tobioka, "New physics implications of recent search for $K_L \to \pi^0 \nu\bar{\nu}$ at KOTO," Phys. Rev. Lett. **124** no. 7, (2020) 071801, arXiv:1909.11111 [hep-ph].

[185] J. L. Feng, I. Galon, F. Kling, and S. Trojanowski, "Dark Higgs bosons at the ForwArd Search ExpeRiment," Phys. Rev. D **97** no. 5, (2018) 055034, arXiv:1710.09387 [hep-ph].

[186] J. L. Feng et al., "The Forward Physics Facility at the High-Luminosity LHC," in 2022 Snowmass Summer Study. 3, 2022. arXiv:2203.05090 [hep-ex].

[187] K. G. Wilson, "Confinement of Quarks," Phys. Rev. D **10** (1974) 2445–2459.

[188] T. Feldmann, "Quark structure of pseudoscalar mesons," Int. J. Mod. Phys. A **15** (2000) 159–207, arXiv:hep-ph/9907491.

[189] S. Scherer, "Introduction to chiral perturbation theory," Adv. Nucl. Phys. **27** (2003) 277, arXiv:hep-ph/0210398.

[190] S. Scherer and M. R. Schindler, "A Chiral perturbation theory primer," arXiv:hep-ph/0505265.

[191] J. Gasser and H. Leutwyler, "Chiral Perturbation Theory: Expansions in the Mass of the Strange Quark," Nucl. Phys. B **250** (1985) 465–516.

[192] E. Witten, "Global Aspects of Current Algebra," Nucl. Phys. B **223** (1983) 422–432.

[193] J. Wess and B. Zumino, "Consequences of anomalous Ward identities," Phys. Lett. B **37** (1971) 95–97.

[194] T. Fujiwara, T. Kugo, H. Terao, S. Uehara, and K. Yamawaki, "Nonabelian Anomaly and Vector Mesons as Dynamical Gauge Bosons of Hidden Local Symmetries," Prog. Theor. Phys. **73** (1985) 926.

[195] C. Kuang-chao, G. Han-ying, W. Ke, and S. Xing-chang, "On the gauge invariance and anomaly-free condition of the wess-zumino-witten effective action," Physics Letters B **134** no. 1, (1984) 67–69. https://www.sciencedirect.com/science/article/pii/0370269384909869.

[196] N. Pak and P. Rossi, "Gauged goldstone boson effective action from direct integration of bardeen anomaly," Nuclear Physics B **250** (12, 1985) 279–294.

[197] J. Bijnens, "Chiral perturbation theory and anomalous processes," Int. J. Mod. Phys. A **8** (1993) 3045–3105.

[198] M. Bando, T. Kugo, and K. Yamawaki, "On the Vector Mesons as Dynamical Gauge Bosons of Hidden Local Symmetries," Nucl. Phys. B **259** (1985) 493.

[199] M. Bando, T. Kugo, S. Uehara, K. Yamawaki, and T. Yanagida, "Is rho Meson a Dynamical Gauge Boson of Hidden Local Symmetry?," Phys. Rev. Lett. **54** (1985) 1215.

[200] M. Bando, T. Kugo, and K. Yamawaki, "Nonlinear Realization and Hidden Local Symmetries," Phys. Rept. **164** (1988) 217–314.

[201] K. Yamawaki, "Hidden Local Symmetry and Beyond," Int. J. Mod. Phys. E **26** no. 01n02, (2017) 1740032, arXiv:1609.03715 [hep-ph].

[202] M. Harada and K. Yamawaki, "Hidden local symmetry at loop: A New perspective of composite gauge boson and chiral phase transition," Phys. Rept. **381** (2003) 1–233, arXiv:hep-ph/0302103.

[203] H. B. O'Connell, B. C. Pearce, A. W. Thomas, and A. G. Williams, "$\rho - \omega$ mixing, vector meson dominance and the pion form-factor," Prog. Part. Nucl. Phys. **39** (1997) 201–252, arXiv:hep-ph/9501251.

[204] C. Bruch, A. Khodjamirian, and J. H. Kuhn, "Modeling the pion and kaon form factors in the timelike region," Eur. Phys. J. C **39** (2005) 41–54, arXiv:hep-ph/0409080.

[205] M. Davier, A. Hoecker, B. Malaescu, and Z. Zhang, "Reevaluation of the Hadronic Contributions to the Muon g-2 and to alpha(MZ)," Eur. Phys. J. C **71** (2011) 1515, arXiv:1010.4180 [hep-ph]. [Erratum: Eur.Phys.J.C 72, 1874 (2012)].

[206] G. Kramer, W. F. Palmer, and S. S. Pinsky, "Testing Chiral Anomalies With Hadronic Currents," Phys. Rev. D **30** (1984) 89.

[207] N. N. Achasov and A. A. Kozhevnikov, "Isoscalar resonances with J(PC) = 1– in e+ e- annihilation," Phys. Rev. D **57** (1998) 4334–4342, arXiv:hep-ph/9703397.

[208] N. N. Achasov and A. A. Kozhevnikov, "Rho primes in analyzing e+ e- annihilation, MARK III, LASS and ARGUS data," Phys. Rev. D **55** (1997) 2663–2671, arXiv:hep-ph/9609216.

[209] M. Jacob and R. Slansky, "Nova model of inclusive reactions," Phys. Rev. D **5** (Apr, 1972) 1847–1870. https://link.aps.org/doi/10.1103/PhysRevD.5.1847.